UNIVERSITY OF SOUTHAMPTON

FACULTY OF ENGINEERING, SCIENCE AND MATHEMATICS
School of Engineering Sciences

The Development of Zero-G Class Underwater Robots: Unrestricted Attitude Control using Control Moment Gyros

Blair Thornton

A Dissertation presented
in candidacy for the degree of
Doctor of Philosophy

May 2006

UNIVERSITY OF SOUTHAMPTON

ABSTRACT

FACULTY OF ENGINEERING, SCIENCE AND MATHEMATICS

SCHOOL OF ENGINEERING SCIENCES

Doctor of Philosophy

THE DEVELOPMENT OF ZERO-G CLASS UNDERWATER ROBOTS

by Blair Thornton

The ‘Zero-G’ is designated as a new class of underwater robot that is capable of unrestricted attitude control. A novel control scheme based on internal actuation using Control Moment Gyros (CMGs) is proposed to provide Zero-G Class Autonomous Underwater Vehicles (AUVs) with this unique freedom in control.

The equations of motion for a CMG actuated underwater robot are derived and a nonlinear feedback control law formulated based on energy considerations of the system’s coupled dynamics. Singularities, redundancy and null motion are discussed in the context of CMGs and a mathematical escapability condition is developed based on the differential geometry of null motion. A comprehensive geometric study of the singularities of a CMG pyramid is performed and together with considerations of the inverse kinematics of attitude control form the basis of a global steering law that exactly achieves the desired torques, whilst guaranteeing real-time singularity avoidance within a constrained workspace.

The development of the CMG actuated Zero-G Class underwater robot IKURA is described. This is the first Zero-G Class prototype and is the first application of CMGs to underwater robots. A series of experiments to demonstrate the practical application of CMGs and verify the associated theoretical developments is described. The open-loop dynamics of the system and the exactness and real-time applicability of the CMG steering law are verified. Experiments are carried out to assess the performance of the proposed control law by comparing the response of the robot to that using alternative control laws that neglect the hydrodynamic interactions of the body and the coupled motion of the CMGs and body respectively. The control law demonstrates a faster response with a smaller overshoot for less overall control activity than the alternative methods. The ability to actively stabilise the passively unstable translational dynamics of the robot are verified. Next, the unrestricted attitude control capability is confirmed with the robot demonstrating the necessary range of attitude control to adopt and maintain any attitude on the surface of a sphere. Finally, the ability to stabilise any attitude while translating in surge is confirmed with the robot performing vertically pitched diving and surfacing in surge.

This is the first time an underwater robot has performed such a manoeuvre. This research demonstrates that CMGs are capable of actively stabilising the passively unstable dynamics of an underwater robot with essentially zero-righting moment and are capable of providing it with unrestricted attitude control. The three-dimensional manoeuvring capabilities allow Zero-G Class underwater robots to plan and optimise their missions in a fully three-dimensional manner, in a way that has not been possible previously. This study concludes that the application of CMGs for attitude control opens up a path to develop sophisticated Zero-G Class underwater robots and their application to new fields of underwater research.

Acknowledgements

This research was carried out at the University of Southampton, UK, and the University of Tokyo, Japan, between October 2002 and March 2006 and was supported by the advanced research scholarship of the Monbukagakusho, Japanese Ministry of Education.

I am indebted to my supervisor, Dr. Stephen Turnock, for his enthusiasm, support and enduring optimism, and for the trust and freedom he gave me to explore my ideas. I thank Professor Geoff Roberts and Professor Eric Rogers for serving on my exam committee. I also wish to thank both the School of Engineering Sciences and the Oceanography Centre of the University of Southampton, especially Professors Grant Hearn, Gwyn Griffiths and Sandor Veres for sharing their time and for their continuing support.

I thank the Institute of Industrial Science at the University of Tokyo, especially Professor Tamaki Ura for welcoming me into his group and providing me with the exceptional research facilities of his laboratory. I owe a special debt of gratitude to Mr. Yoshiaki Nose, for his support in the design and construction of the physical and electronic hardware of IKURA. It is easy to appear courageous with someone stood poised to catch you when you fall. I would also like to thank Ms. Harumi Sugimatsu, Mr. Takashi Sakamaki and the members of the URA laboratory, Professors Rajendar Bahl, Hayato Kondo, Kazuo Ishii, Keisuke Watanabe, Dr. Youichi Kato and my fellow researchers Koichi Nose, Toshihiro Maki, Yann Epars, Takeshi Nakatani, Nicola Rohrseitz, Suguru Maiwa and Tomoki Inoue for their willingness to sacrifice their own time to help others. Thank you for providing an inspirational research environment that was so enjoyable to be a part of. I wish to extend my gratitude to the Central Workshop of the Institute of Industrial Science, the University of Tokyo, for the exceptional speed and quality in manufacturing the components of IKURA and its CMG system.

Above all, I thank my father Ken, who inspired me, much against his advice, to follow in his footsteps as an engineer. I thank him for teaching me that the only shortcut ever worth taking is to start at page one and keep going. I thank my mother Michiko, for teaching me her native language of Japanese, without her patience and persistence I would not have been able to take advantage of the time I spent conducting research in Japan. I thank my big sister Hisayo, whose love of the ocean and its majestic creatures, and even those that are just stuck on a rock, drew me to dedicate my studies to it. Finally, I thank Teruko, who has supported me over the period of this research, as my girlfriend, my fiancée and my wife.

Contents

List of Figures

List of Tables

Nomenclature

A	Projected cross-sectional area of the body	m^2
A_Z	Invariant part of the null motion quadratic Q_Z	
c_i	Unit vector along gyroscopic torque axis of ith CMG unit	
c_{i0}	Normalised gyroscopic torque vector at the nominal state	
c_{Si}	Torque vector of ith CMG unit at a singularity	
c^*	$\cos\beta$	
$\bar{c}$	Normalised gyroscopic torque matrix $[c_1, c_2, ..., c_N]$	
$\mathbf{C}$	CMG torque Jacobian	Nm s/rad
C_D	Drag coefficient	
$\mathbf{C}^*$	CMG torque Jacobian of constrained workspace	Nm s/rad
$\mathbf{C}^*_\times$	Coupled part of constrained Jacobian $\mathbf{C}^*$	Nm s/rad
$\mathbf{C}^*_o$	Direct part of constrained Jacobian $\mathbf{C}^*$	Nm s/rad
$\mathbf{e}_\mathbf{q}$	Difference between actual and desired quaternion vectors	
$\mathbf{e}_\omega$	Difference between actual and desired body angular velocity vectors	rad/s
E_Z	Null subspace with components $[e_{Z1}, e_{Z2}, ..., e_{ZN-2}]$	
$\mathbf{F}_\mathbf{b}$	Body-fixed reference frame with axes (x, y, z)	
F_{drag}	Linear drag	N
F_{ext}	External forces acting on the body	N
$\mathbf{F}_\mathbf{i}$	Inertially-fixed reference frame with axes $(\mathbf{i}, \mathbf{j}, \mathbf{k})$	
F_t	Thrust force from external actuators	N
g_i	Unit vector along gimbal axis of ith CMG unit	
$\bar{g}$	Gimbal axis matrix $[g_1, g_2, ..., g_N]$	
$\mathbf{G}$	Coefficient of second order CMG dynamics	Nm s^2/rad^2
$\mathbf{h}_{cmg}$	Momentum stored in CMG system	Nm s
h_i	Unit vector along flywheel spin axis of ith CMG unit	
h_{i0}	Normalised angular momentum vector at the nominal state	
h_{Si}	Angular momentum vector of ith CMG unit at a singularity	
h^*_i	Unit spin axis of ith CMG unit in constrained workspace	
$\bar{h}$	Normalised angular momentum matrix $[h_1, h_2, ..., h_N]$	
$\bar{h}_S$	Normalised singular angular momentum matrix $[h_{S1}, h_{S2}, ..., h_{SN}]$	
H	Normalised angular momentum vector of the CMG system	
$H_{x,y,z}$	x,y,z components of normalised CMG angular momentum vector	
i	CMG unit number	
$\mathbf{I}$	Identity matrix	
j	CMG unit number	

$\mathbf{J}_A$	Fluid added inertia	$\mathrm{kg\,m^2}$
$\mathbf{J}_c$	CMG inertia components about $\bar{c}$	$\mathrm{kg\,m^2}$
$\mathbf{J}_{cmg}$	CMG inertia matrix	$\mathrm{kg\,m^2}$
$\mathbf{J}_g$	CMG inertia components about $\bar{g}$	$\mathrm{kg\,m^2}$
$\mathbf{J}_h$	CMG inertia components about $\bar{h}$	$\mathrm{kg\,m^2}$
$\mathbf{J}_s$	Rigid body inertia	kg $\mathrm{m^2}$
$\mathbf{J}_{tot}$	Total inertia of the system	kg $\mathrm{m^2}$
k_{null}	CMG null gain	
k_q	Quaternion gain matrix	
k_ω	Body angular velocity gain matrix	
K	Gaussian curvature	
l	Characteristic length of the body	m
m	Total mass	kg
M	Largest invariant set in R	
$\mathbf{M}_A$	Fluid added mass	kg
$n_{i,j}$	Basis of null subspace $[c_{Si}\ c_{Sj}\ \mathbf{u}]$	
p_i	$\frac{1}{h_{Si}\mathbf{u}}$	
P	Diagonal matrix with elements p_i	
$\mathbf{P}$	Total linear momentum	$\mathrm{N\,s}$
$\mathbf{q}$	Quaternion vector to describe attitude in inertial frame	
$\mathbf{q}_d$	Desired quaternion vector	
$\bar{\mathbf{q}}$	Complex conjugate of quaternion vector	
Q	Quaternion transformation matrix	
$\mathbf{Q}$	Quaternion matrix-vector product	
Q_S	Singular surface quadratic	
Q_Z	Null motion quadratic	
$\bar{\mathbf{Q}}$	Complex conjugate of quaternion matrix-vector product	
$\hat{r}$	Location of centre of gravity with respect to centre of buoyancy	m
$\mathbf{r}$	A vector in the body frame	
$\mathbf{r}'$	A vector in the inertial frame	
r_b	Location of centre of buoyancy	m
r_g	Location of centre of gravity	m
r_i	Mean distance to the centre of rotation	m
R	Set of all points where $\dot{V}(\mathbf{x}) = 0$	
$\mathbf{R}$	Rotation matrix	
R_n	Reynolds number $\frac{ul}{\nu}$	
s^*	$\sin\beta$	
S_ϵ	Singular surface region with sign ϵ_i	
t	Time	s
$\mathbf{T}$	Total energy	J
$\mathbf{T}_{cmg}$	CMG system energy	J
$\mathbf{T}_l$	Fluid energy	J
$\mathbf{T}_s$	Rigid body energy	J

u	Body velocity vector	m/s
$\mathbf{u}$	Unit vector in the singular direction	
V	Lyapunov function	
$\bar{z}$	Variables of null subspace	
α	Steering parameter for yaw	rad
β	CMG pyramid skew angle	rad
β_λ	Angle of simple rotation	rad
γ	Steering parameter for pitch	rad
ϵ_i	Signature of relative orientation of ith CMG unit to $\mathbf{u}$	
η	Real part of quaternion vector $\mathbf{q}$	
θ_x	Roll angle in inertial frame	rad
θ_y	Pitch angle in inertial frame	rad
θ_z	Yaw angle in inertial frame	rad
κ	Null gain sensitivity parameter	
κ_1	Maximum curvature	
κ_2	Minimum curvature	
λ	Single axis of rotation with components $[\lambda_i, \lambda_j, \lambda_k]^T$	
ν	Kinematic viscosity of the fluid	m^2/s
ξ	Imaginary part of quaternion vector $\mathbf{q}$ with components $[\xi_i, \xi_j, \xi_k]^T$	
$\mathbf{\Pi}$	Total angular momentum	Nm s
ρ	Density of fluid	kg m^3
σ	Steering parameter for roll	rad
τ_{cmg}	CMG torque vector	Nm
τ_d	Damper like dissipative component of τ_u	Nm
τ_{drag}	Rotational drag vector	Nm
τ_{ext}	Vector of external torques acting on the body	Nm
τ_s	Spring like component of τ_u	Nm
τ_u	CMG system command torque	Nm
ϕ_i	Gimbal angle of ith CMG unit	rad
ϕ_j	Gimbal angle of jth CMG unit	rad
ϕ_{Si}	Gimbal angle of ith CMG unit at a singularity	rad
ϕ_{Zi}	Gimbal angle of ith CMG unit at a null condition	rad
ϕ^*	Steering parameters with components $[\sigma, \gamma, \alpha]^T$	rad
$\bar{\phi}$	Vector of CMG gimbal excursion angles $[\phi_1, \phi_2, ..., \phi_N]^T$	rad
$\bar{\phi}_S$	Vector of singular gimbal angles $[\phi_{S1}, \phi_{S2}, ..., \phi_{SN}]^T$	rad
$\bar{\phi}_Z$	Vector of null gimbal angles $[\phi_{Z1}, \phi_{Z2}, ..., \phi_{ZN}]^T$	rad
$\dot{\bar{\phi}}_d$	CMG gimbal steering rate command	rad/s
$\dot{\bar{\phi}}_Z$	CMG gimbal steering rate for null motion	rad/s
$\dot{\bar{\phi}}_\tau$	CMG inverse torque gimbal steering solution	rad/s
$\dot{\bar{\psi}}$	Flywheel spin rate matrix	rad/s
ω	Body angular velocity vector	rad/s
ω_d	Desired body angular velocity vector	rad/s
$\mathbf{\Omega}$	CMG rotation matrix	rad/s

Glossary

AUV	Autonomous Underwater Vehicle.
CMG	Control Moment Gyro.
Escapable singularity	A singularity that can be avoided through null motion.
Exact steering	Steering motion that generates a torque output that is equal to the command torque.
Gimbal vector	A unit vector in the gimbal direction.
IKURA	Internal Kinematic Underwater Robot Actuation.
Inescapable singularity	A singularity that cannot be crossed or avoided without generating undesired torque effects.
IPACS	Integrated Power and Attitude Control System.
Momentum vector	A unit vector parallel to the flywheel spin axis.
Null motion	Gimbal steering motion that keeps the angular momentum vector constant and so does not generate torque.
Real-time steering	A steering law that does not rely on knowledge of future instructions when generating its gimbal rate command.
SDA	Singular Direction Avoidance.
Singularity	Gimbal orientations where all momentum vectors are coplanar.
Singular surface	A surface formed by the total angular momentum vectors of all singular gimbal orientations.
Singular vector	A unit vector normal to the plane spanned by all torque vectors when the system is singular.
SR	Singularity-Robust.
Steering	Rotations of the gimbal in order to generate a command torque.
Torque vector	A unit vector parallel to the gyroscopic output torque.
Unrestricted attitude control	The ability to adopt and maintain any attitude on the surface of a sphere with a zero radius turning circle.
Workspace	Volume of available angular momentum vectors of a CMG system.

Preface

The ocean provides vast but finite natural resources that are vital for, and exists in harmony with, all life on earth. Exploration from its familiar shores to the unknown deep is essential to understand the behaviour of the ocean, discover what resources it offers and establish to what extent these can be exploited without destroying its fragile balance. However, underwater expeditions are riddled with complications and pose great dangers to the submersibles used. Therefore, unmanned underwater robots have attracted a great deal of attention from engineers and scientists as they can access remote underwater territories with no threat to human life. The future of ocean research points towards highly intelligent, untethered underwater robots to operate autonomously in geometrically complicated, cluttered and even enclosed environments. The increasingly ambitious requirements demand smaller and more agile underwater robots, pushing the performance envelope beyond the boundary of that offered by the traditional thrusters and fins used, and in particular calling for greater actuation capabilities at low speeds. This has seen research into alternative actuation techniques gain momentum.

Chapter 1

Introduction

1.1 Motivation and aims

The ocean is a vast three-dimensional environment and it follows that an ocean research tool, such as the Autonomous Underwater Vehicle (AUV), should ideally be able to move freely in any direction within its surroundings. The ability to adopt and maintain any attitude on the surface of a sphere with a zero radius turning circle would allow an intelligent underwater robot to approach its missions in a fully three-dimensional manner, optimising the use of its thrusters, sensors and power supply in a way that has not been possible previously. It is thought that, in addition to improving AUV performance, unrestricted attitude control will open up new fields of research where AUVs can be applied. The aim of this research is to develop a new class of 'Zero-G' AUV that is capable of unrestricted attitude control. This unique freedom in control is achieved through the pursuit of two complementary goals:

- the introduction of Control Moment Gyros (CMGs) as a new type of underwater actuator and
- the development of a novel unrestricted attitude control scheme, for a body with zero righting moment, based on internal momentum exchange using CMGs.

An AUV is a fully automated untethered underwater robot that is piloted by an internal computer. Onboard sensors assess its environment and this data is used to make intelligent decisions regarding the behaviour of the robot and to generate control signals to manoeuvre itself as required. An AUV carries its own power supply and forms a fully self-contained ocean exploration system. Once deployed there is no human interaction until the mission has been completed.

The last 25 years has seen AUVs evolve into two main classes. The most widely seen is the 'cruising' class that performs various large area observations [1–6]. These robots have lengths in the order of 4 to 10m and operate at a safe distance from their target, travelling predominantly in surge using a main thruster supplemented by fins and rudders for directional control. The demand for robots to operate closer to their targets and carry out detailed inspection, mapping and even manipulation tasks has seen the development of smaller and more agile 'hovering' class AUVs [7–9]. These typically have lengths between 1.5 to 2 m and operate at low speeds using multiple thrusters for independent control over several degrees of freedom so that they can cope with sudden changes in the geometry of the target. Underwater robotics is a diverse field and the various applications demand a number of different types of AUV in addition to the traditional main classes. Underwater gliders are extremely efficient in terms of power consumption and are capable of travelling long distances by varying their buoyancy, using foils to deflect fluid momentum and propel themselves through the open ocean [10, 11]. Other alternatives include biomimetic AUVs that draw inspiration from the actuation techniques of marine creatures [12, 13]. These often have articulated or flexible bodies that undulate to generate hydrodynamic forces to propel themselves through the water. More detailed discussions of underwater robots and their applications can be found in the following references [14–16]. To date, however, untethered underwater robots have relied on passive stability to maintain a useable orientation, applying limited or often no active control about the roll and pitch axes. This confines their motion to that along a series of two-dimensional planes through the water and thereby limits their applications.

The Zero-G is designated as a new class of underwater robot that is capable of approaching its missions in a truly three-dimensional manner. Coincident centres of gravity and buoyancy allow Zero-G Class underwater robots to adopt and maintain any attitude on the surface of a sphere as if in a zero gravity environment. However, this freedom in control comes at the cost of stability in roll and pitch. Therefore, the attitude control system must actively stabilise the necessary fast angular rotations about these axes as well as achieve the desired orientation. This requires a closed-loop attitude control system that can manage any orientation to provide independent control over all three rotational axes with a zero radius turning circle and demands a speed and resolution of control that cannot be achieved using traditional underwater actuation methods due to their slow response to control inputs.

Internal actuation devices present many advantages over traditional underwater actuators. Since they are contained within the body of the robot, they preserve the hydrodynamic integrity of its hull. Furthermore, they are protected from the harsh underwater environment and do not exert any external forces, which is of practical benefit when operating in proximity to loose surfaces or small creatures. In contrast to thrusters and fins that rely on relative fluid motion, internal actuators generate their own momentum and apply their control to the robot directly. Therefore, their performance is independent of external conditions and their control authority is maintained over the entire operating envelope, including low speed and even stationary conditions. This offers a speed and resolution of response that can surpass traditional actuation techniques and even those of nature. Such devices present their greatest advantage when used to complement traditional actuators, in particular the use of internal torque generators for attitude control greatly reduces the required number of thrusters and allows for simple and elegant design. It is contended that the control response offered by internal actuation techniques, specifically CMGs, opens a path to develop sophisticated Zero-G Class underwater robots and their application to new fields of underwater research.

1.2 Research background

Internal actuation devices such as controlled movable masses are used to provide roll and pitch control for buoyancy driven underwater gliders such as ALBAC [10] and SLOCUM [11]. In the latter case buoyancy is controlled by an electrically powered ballast pump, which in turn leads to propulsion. However, such devices cannot provide full control over all three rotational axes. The use of internal momentum exchange devices to control the attitude of underwater robots was suggested in 1998 by Leonard [17] and has been the subject of ongoing research [18–21] leading to the development of the underwater robot IAMBUS [22] in 2003 that uses reaction wheels to control its attitude. However, reaction wheels use a single motor for both the accumulation of angular momentum and generation of torque. This limits the magnitude of their output to that of the motor and also leads to saturation of the rotors as they reach their maximum rate. This poses significant difficulties for attitude control.

A CMG is a torque generator that consists of a flywheel mounted on a system of gimbals. Separate motors are used for the accumulation of momentum and generation of torque. The gyroscopic torque amplification offered by the momentum stored in the flywheels suggests that CMGs are capable of generating larger torques, with a faster response than equivalent reaction wheels and so they have been the subject of much research since they were first developed in 1966 [23]. Early research considered the application of CMGs for the attitude control of space vehicles [24–26] and this continues to be the main emphasis of research to date. This work considered theoretical issues such as the steering control of specific CMG configurations and the efficiency of these different arrangements, as well as more practical issues such as the physical assembly of the hardware and the implementation of software [27–34]. It was soon realised that CMG systems suffered a problem with singular orientations that can lead to a momentary loss of control. However, this problem could be overcome in double gimballed systems [35–38]. This led to the successful application of a CMG system in the US satellite Skylab, which consisted of three double gimbal CMG units [39, 40].

Single gimballed CMG systems pose several significant advantages over double gimballed devices. They are mechanically less complicated and are more efficient, generating larger torques due to their gyroscopic torque amplification property. However, they also suffer a serious problem with singular orientations that must be overcome if they are to be applied practically. The singularity problem was first identified by NASA in 1972 [32]. Margulies [41] formulated the geometric theory of singular surfaces in 1978 and was the first to identify null motion and thus the possibility of singularity avoidance in redundant single gimbal systems. In the same year Tokar described the shape and size of singular surfaces and considered the effects of gimbal limits [42–44]. One of Tokar's most significant contributions was in 1979 when he introduced the concept of locally escapable and inescapable singular surface regions [45]. He concluded that a system with six or more units contains no inescapable singular regions and thus has enough redundancy to solve any singularity problem. This led to the construction of a six unit single gimbal system for the Russian space station MIR [46]. However, due to the size and complexity of this system, efforts continued to assess the singularities of various other CMG configurations and propose methods for singularity avoidance in systems of limited redundancy. In particular, singularity avoidance in the minimally redundant four unit CMG pyramid was the focus of much attention due to its compact size and mechanical simplicity [47–53]. Many of these works considered singularity avoidance as a local problem, however, in 1987 Bauer [54] demonstrated that even though escapability is defined locally, local singularity avoidance methods can encounter inescapable singularities that could have been avoided in the first place, and so concluded that singularity avoidance should be treated as a global problem. However, a solution to perform real-time singularity avoidance whilst remaining exact to the commanded torque in systems of limited redundancy remained elusive.

It has been demonstrated that singularity avoidance can be achieved by relaxing some of the constraints on the system. In Vadali's method of preferred gimbal states [55] the real-time constraint is relaxed to allow knowledge of future instructions to be used when generating the steering command. Paradiso [56, 57] extended this concept to select predetermined gimbal paths based on extensive geometric studies. Bedrossian [58, 59] and later Oh [60] applied the singularity-robust (SR) method to relax the exactness constraint, allowing local output errors in order to pass singular regions. This concept was developed further in the singular direction avoidance (SDA) method of Ford [61] that reduces the permitted error. Kurokawa [62–64] approached the problem from a different perspective. Instead of avoiding singularities by relaxing the constraints on the system, additional constraints were imposed on gimbal motion to eliminate some singular regions and achieve exact and real-time steering in a restricted workspace. However, despite numerous applications for the three-axis attitude control of space vehicles, CMGs have not previously been applied to underwater robots.

1.3 Objectives

It is thought that the control response offered by single gimbal CMGs can form the basis for the development of Zero-G Class underwater robots and will lead to new fields of underwater research. However, extending the application of CMGs to underwater robots gives rise to complications associated with operating within a fluid environment. In particular, the viscous environment greatly complicates the dynamics and control of the robot, as well as demanding sustained torques that increase the likelihood of encountering problematic singular orientations. This research describes both theoretical and practical developments in order to realise Zero-G Class underwater robots and the associated CMG based control system to provide unrestricted attitude control. The theoretical steps are:

- derivation of a fully descriptive model for the dynamics of the system in any orientation,
- formulation of a three-axis attitude control law that is suitable for application to AUVs,
- analysis of the singularities and null motion of CMGs to develop a mathematical escapability condition and
- formulation of a steering law that exactly achieves the desired torques whilst guaranteeing real-time singularity avoidance.

Beyond the above problem formulation, the practical application of the control system is assessed using the CMG actuated, Zero-G Class underwater robot IKURA. This is an experimental platform developed as part of this research to verify the theoretical developments and to demonstrate unrestricted attitude control.

1.4 Organisation of thesis

This thesis is organised into ten chapters including this introduction. These detail both the theoretical and practical developments of this research. An additional four appendices are included to add depth and support the main body of the report. In Chapter 2 the main characteristics of CMG systems are discussed. A comparison of single and double gimbal systems is made together with an overview of different configurations. Finally, the basic structure of a CMG based attitude control system is described.

Chapter 3 derives the coupled equations of motion for a body, containing some system of CMGs, that is free to translate and rotate in a fluid environment. The fully descriptive dynamic equations are derived based on the energy of the complete system, accommodating fluid interactions and viscous effects. Quaternions are used to describe motion in the inertial frame of reference since their description is valid for all orientations. In Chapter 4 a three-axis attitude control law is formulated based on energy considerations of the system's dynamics. A Lyapunov assessment is carried out to ensure global asymptotic stability to the desired state. The non-linear control law developed takes into account the coupled dynamics of the CMG, body and fluid system.

Chapter 5 discusses singularities, redundancy and null motion in the context of CMGs and introduces the concept of steering law exactness. The differential geometry of singularities and null motion are considered to develop a mathematical escapability condition. This determines to what extent singularities can be avoided without generating any undesired torque effects. In Chapter 6 the mathematical tools developed in the previous chapter are applied to perform a comprehensive geometric study of the singularities of a minimally redundant CMG pyramid. This, together with considerations of the inverse kinematics of attitude control, forms the basis of a global steering law that rotates the gimbals to generate a torque exactly equal to that commanded by the control law, whilst guaranteeing real-time singularity avoidance within a constrained workspace.

Chapter 7 follows the development of the CMG actuated Zero-G Class underwater robot IKURA that provides an experimental platform to verify the theoretical developments. This is the first application of CMGs to underwater robots and so the practical considerations of the mechanical and electrical design of the system are discussed. This chapter is supported by Appendices A - C. Appendix A contains CAD drawings and some photos of IKURA and its CMG system. Appendix B contains details of the electrical design. The hydrodynamic and other modelling parameters used are presented in Appendix C.

Chapter 8 presents the results of a series of practical experiments performed to demonstrate the application of CMGs and verify the theoretical developments. The first series of experiments verifies the dynamic model of the system. Next, the exactness and real-time applicability of the CMG steering law is demonstrated. For convenience of instrumentation these experiments were performed on dry-land. This does not effect the validity of the results. The third series of experiments assess the performance of the complete control system. To allow for comparison tests were performed with two alternative control laws in addition to that developed in this work. The final experiment described in this chapter demonstrates the active stabilisation of a passively unstable surge manoeuvre using CMGs. These experiments were performed underwater using the experimental pool facilities of the URA laboratory at the University of Tokyo. Real-time video footage of the experiments can be found in Appendix D and is referred to in the text where relevant.

Chapter 9 focuses on the unrestricted attitude control and unique manoeuvring capabilities of this new Zero-G Class of underwater robot. The necessary range of yaw and pitch control to adopt and maintain any attitude on the surface of a sphere with a zero radius turning circle is demonstrated. Next, the ability to stabilise any attitude while translating in surge is verified practically in an experiment that involves vertically pitched diving and surfacing in surge. This is the first time an underwater robot has performed such a manoeuvre. Real-time video footage of the experiment can be found in Appendix D and is referred to in the text. The potential offered by the application of CMG technology to AUVs is reviewed and the implications for the future of underwater research discussed. Chapter 10 concludes this research and provides suggestions for future work.

Appendix D is a DVD that contains real-time video footage of the experiments carried out in this research. Instructions for use and the content of the DVD can be found in the text. Although all the relevant data is presented within the main body of this document, the author recommends viewing the DVD to support these results. In addition, the DVD also includes a poster and still images of IKURA and its components and a short trailer that illustrates the Zero-G concept. This can be viewed on any standard DVD player.

Chapter 2

CMG systems and attitude control

A CMG system is composed of a number of identical CMG units arranged in a defined configuration. Each unit consists of a flywheel mounted on an arrangement of actuated gimbals. Rotations of the gimbals change the direction of the flywheel angular momentum vector and this generates a gyroscopic torque that can be used to actuate the robot. There are two principal types of CMG unit; single and double gimbal. In both cases the direction of the torque generated changes with the gimbal angles and so typically a system composed of several units is required to achieve the desired torques. Thus the design of a CMG system involves not only the selection of a unit type, but also the selection of a system type, defined by the number of units and their configuration. In addition to the physical hardware, it is also necessary to develop a control system in order to realise three-axis attitude control.

2.1 CMG unit type

The two types of CMG unit, single and double gimbal, are illustrated in Fig. 2.1. In double gimbal devices (Fig. 2.1(a)), a flywheel is suspended inside two gimbal frames and so its momentum vector can be oriented in any direction. However, the multiple gimbal arrangement implies that some component of the output torque inevitably acts in the direction of at least one of the gimbals. This limits the speed and magnitude of the system's response as the gimbal actuators need to partially compensate for the gyroscopic torque produced. Therefore, the output of the system is limited by the torque available in the gimbal motors.

A single gimbal device (Fig. 2.1(b)) is constructed of a flywheel mounted normal to its spin axis on an actuated gimbal. These devices present a number of practical advantages as they are significantly less complicated than double gimbal arrangements. Furthermore, this type of unit is physically the most effective since the gyroscopic torque generated is transmitted radially across the bearings of the system with no component acting against the gimbal actuators. This combined with the gyroscopic torque amplification property means that large output torques can be achieved for relatively small inputs. This offers a fast and high resolution response. However, the flywheel momentum vector is restricted to a circular plane normal to the gimbal axis and this limitation in its motion presents significant difficulties for singularity avoidance. This problem is described later in Chapter 5.

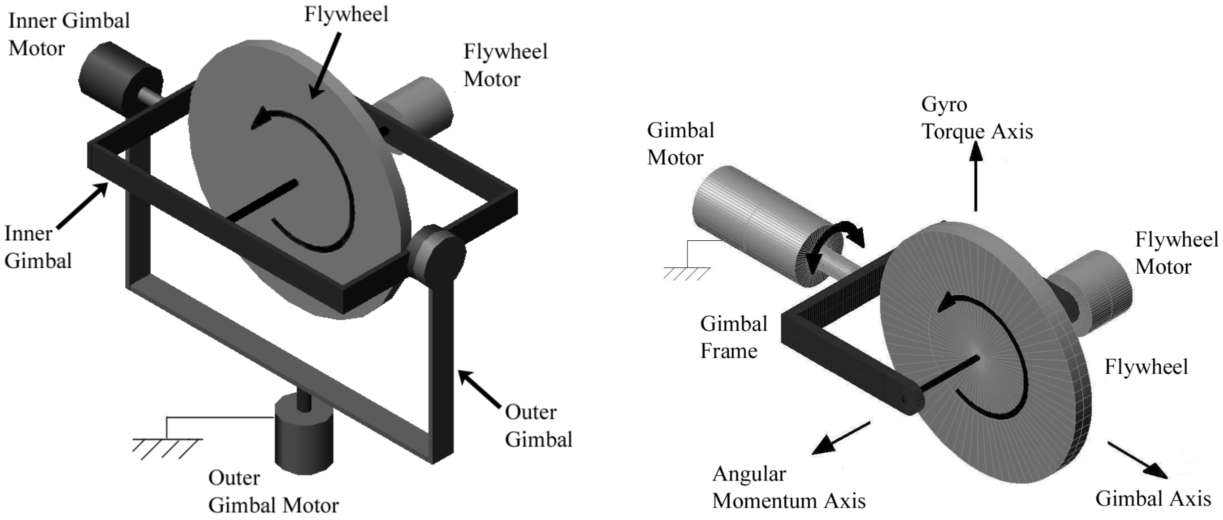

(a) Double gimbal unit (b) Single gimbal unit

Figure 2.1: CMG unit types

The size and weight of a CMG system depends not only on the size of the flywheels used, but also on the complexity of the gimbal mechanisms and the total number of units in the system. Although double gimbal devices are considerably larger and more complicated than single gimbal devices on a unit level, fewer units are required to achieve three-axis attitude control and thus they may be smaller and less complicated on a system level. Furthermore, singularity avoidance can be more easily achieved due to the freedom offered by the double gimbal mechanism. However, the limitations in the output torque implies that double gimbal units are more suitable for applications that require slow reorientations and attitude keeping in the presence of small disturbances. Despite the difficulties with singularities, the torque amplification property of single gimbal units makes them more suitable for achieving the fast response and agile reorientations sought in this research.

2.2 CMG system type

The generation of three-axis torque requires a cluster of identical CMG units arranged in a defined configuration. This allows the components of torque acting in the desired direction to be superimposed, while all other components cancel. The number of units and their configuration defines the size and shape of the operational momentum envelope, or workspace, of the system. This section provides a brief overview of various types of single gimbal CMG system.

The CMG system type is defined by the relative orientation of the principal axes of each CMG unit. For single gimbal systems this is specified by the gimbal axes g_i. Typically these systems have a certain degree of symmetry in their arrangement. This simplifies the mathematical calculations required to describe their motion and is also convenient for attitude control. There are two principal types of symmetry that are convenient for multi-axis attitude control; parallel and non-parallel symmetric.

2.2.1 Parallel symmetric

Parallel symmetric systems (Fig. 2.2) are also known as 'multiple' systems since they have more than one CMG unit on a single plane. An example of this type of system is the 'roof' type, illustrated in Fig. 2.2(a). This type of system has two rows of parallel CMG units and has been studied in [33] and [48]. Another example of a parallel symmetric system is the 'twin' type, illustrated in Fig. 2.2(b). This type of system has two parallel CMG units that are driven in opposite directions to produce torque about a single axis [27]. Three-axis attitude control can be achieved by using three orthogonal pairs of CMG twins. However, since the pairs works independently to generate torque about each axis the available momentum workspace is relatively small compared to systems that coordinate and manage the steering of all their units together.

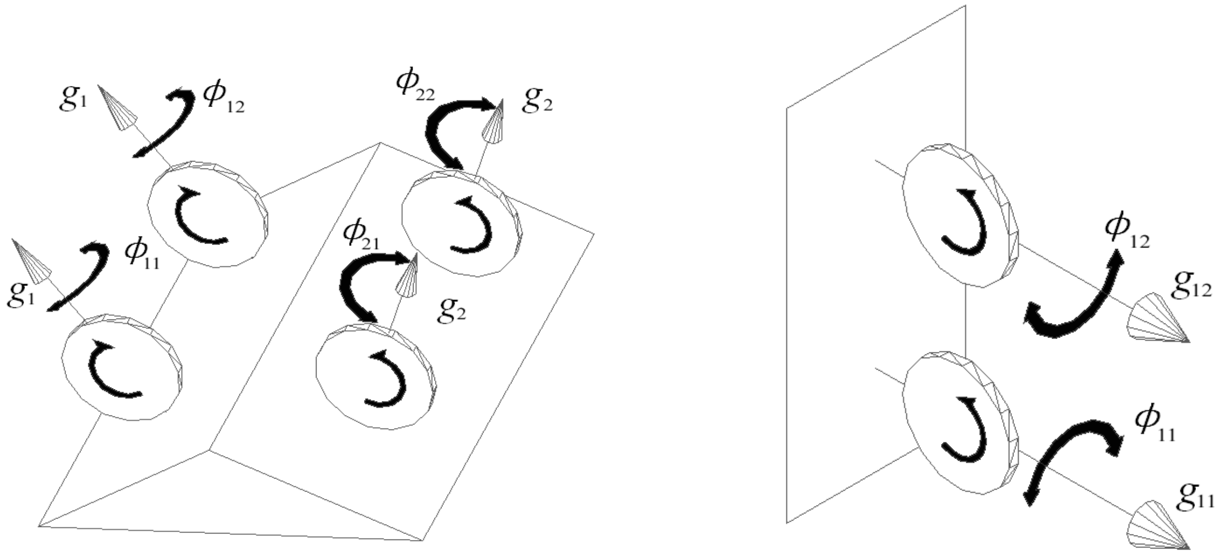

(a) Roof type system (b) Twin type system

Figure 2.2: Examples of parallel symmetric CMG systems

2.2.2 Non-parallel symmetric

Non-parallel symmetric systems (Fig. 2.3) are also known as 'independent' systems since they have no two CMG units with the same gimbal direction. These systems typically have their gimbal axes arranged in a conical array about some centre point. The four unit 'pyramid' (Fig. 2.3(a)) is the most widely researched CMG system as it is simple and its configuration is convenient for attitude control. However, this system is known to suffer significant problems with inescapable singularities. The six unit system of Tokar (Fig. 2.3(b)) has enough redundancy to completely solve the singularity problem [45] and has been applied in the Russian space station MIR [46]. However, the redundancy comes at the cost of the size and complexity of the system, which is not practical for underwater applications where strict dimensional, mass and computational restrictions apply. In this research a method to guarantee singularity avoidance in the minimally redundant CMG pyramid is sought.

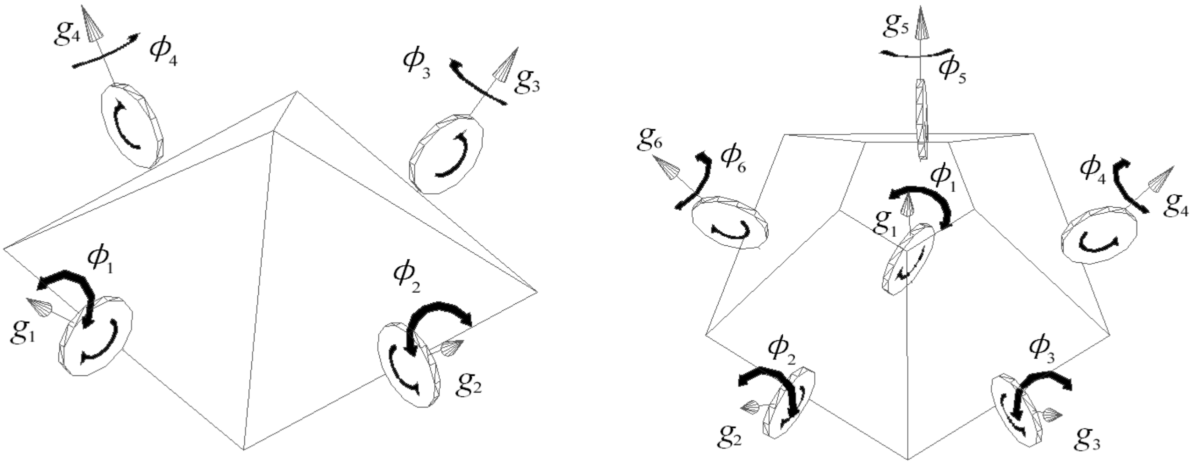

(a) Pyramid (b) Six unit system implemented in MIR

Figure 2.3: Examples of non-parallel symmetric CMG systems

2.3 Three-axis attitude control

The design of the CMG hardware determines the size of the momentum workspace. However, it is the control system implemented that governs how this workspace is used to achieve three-axis attitude control. Since CMGs rely on internal momentum exchange and have singularities, the conventional control techniques used in underwater robots cannot be applied directly. A general schematic for three-axis attitude control using any system of CMGs is presented in Fig. 2.4. The planned mission is executed by the navigation unit, which determines the states required to complete the mission. These, together with real-time measurements from the robot's sensors, form the inputs to the robot control law that determines the torques necessary to achieve the desired state. The main feature is that, in addition to the primary control law, a separate steering law is required to overcome the singularity problem and determine the gimbal motion necessary to generate the command torque. This forms a set of inputs for the robot, which responds through its electronics and physical dynamics.

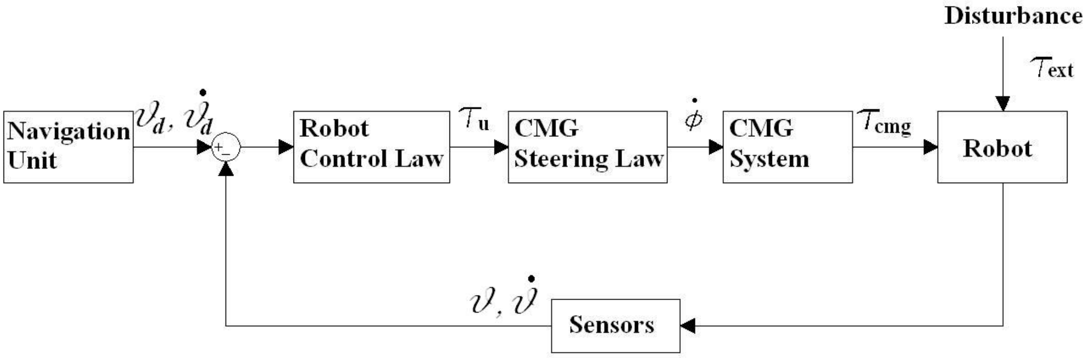

Figure 2.4: Three-axis attitude control using CMGs

Navigation unit: The missions of a Zero-G Class AUV should be planned and optimised in a three-dimensional manner according to the limitations set by the specification of the robot. The navigation unit determines the necessary attitudes and angular rates about all three rotational axes to complete a mission. The algorithms used must generate their commands whilst taking into consideration the momentum workspace of the CMG system. This does not limit the applications of the system if the CMG workspace is sized appropriately.

Robot control law: The desired states generated by the navigation unit are compared to those measured by the sensors of the robot in real-time. Their difference forms the inputs of the robot control law. This uses some dynamic model to determine the torques necessary to achieve the desired states. In this application it is essential that the model is valid for any orientation. The description of motion should take into account the dynamics of the robot, the CMGs and their coupled effects as well as the hydrodynamic interactions between the robot and its fluid environment. In an uncertain and constantly changing environment such as the ocean, it is important to ensure the control law is stable so that unforeseen disturbances do not cause significant degradation in the subsequent control performance.

CMG steering law: The steering law is a feed-forward unit that computes the gimbal rates necessary to produce the required torques calculated by the control law. It uses the gyroscopic amplification property of the CMGs to generate the desired torques whilst managing the redundancy of the system in real-time to avoid singular orientations. Its output is independent of the rest of the control system and forms the input signal that is sent directly to the CMG system. Therefore, it is essential that the output of the steering law remains exact to the required torque as any error in actuation may endanger the safety of the robot.

Momentum management and sizing: A CMG system does not produce angular momentum, but rather exchanges it with the robot. This can result in the accumulation of momentum in the CMGs during the manoeuvre and renders the momentum workspace finite. The design of the CMG system must take into account a number of different factors. Firstly, the basic size and shape of the workspace depends on the momentum stored in each CMG unit, the number of units and their configuration. At the same time however, a large percentage of the mass of a CMG system is composed of the gimbal mechanisms and so systems with fewer units are more efficient in terms of overall weight. Next, the steering law determines how the workspace is used and defines what areas of that workspace are available for attitude control. It is important that the system is designed to have a sufficient margin after the steering law has been implemented to overcome any disturbances during normal operation. One approach to manage the momentum is to use separate torque actuators to offload the momentum accumulated in the CMGs. This process must be carefully monitored and requires a momentum management unit to work in parallel with the control law. However, the use of additional actuators increases the overall size and complexity of the system, contradicting the concept of simplicity and minimal redundancy that is central to the design philosophy of Zero-G Class AUVs. Alternatively, the application of simple protocols during mission planning can avoid an excessive build up of momentum in the CMGs and greatly reduce the momentum required. This would allow the navigation unit to provide sufficient momentum management for the robot to successfully complete its missions without limiting its possible applications.

Chapter 3

System dynamics

This chapter develops a fully descriptive dynamic model for a rigid body that contains an arbitrary system of single gimbal CMGs and is immersed in a fluid. In contrast to previous CMG applications that consider a stationary body in space, this application considers a body moving through a viscous fluid and so the effects of translational motion and any hydrodynamic interactions must be accounted for. The discussion is restricted to a body with coincident centres of gravity and buoyancy as this concept is central to the development of underwater robots with unrestricted attitude control capabilities. The dynamic model is developed using Kirchhoff's equations of motion based on the dynamic energy of the complete CMG, body and fluid system. This approach was chosen as opposed to a conventional Newtonian approach [57, 61, 64] since the derivation is more concise and the concepts of energy used naturally lead on to the Lyapunov analysis in Chapter 4. Amongst the assumptions made by Kirchhoff's equations is that the fluid is inviscid. The limitations of this conservative analysis can be misleading as in reality viscous forces can greatly affect the dynamics. However, this is not restrictive as these equations can accommodate viscous effects, and any other inputs, which can be included as external forces and moments. In order to allow the body to adopt any orientation, quaternions are used to describe the attitude of the robot in the inertial reference frame as they contain no singularities in their description of motion.

3.1 Equations of motion

3.1.1 CMG motion

A CMG system is composed of a number of identical CMG units (Fig. 3.1) arranged in a defined configuration. For each unit the flywheel spins with an angular momentum vector along its axis of rotation h_i. For single gimbal units, the state of the system is defined by the angle ϕ_i about the gimbal axis g_i, which is orthogonal to the momentum axis. Rotations of the gimbal generate a gyroscopic torque that acts about the mutually orthogonal axis c_i and has a magnitude equal to the vector rate of change of the angular momentum stored. The unit vectors form a rotating coordinate system (Fig. 3.2) that tracks the nutation and precession of each CMG to follow its orientation. The relationship of the vectors is described by the following equation:

$$c_i = \frac{\partial h_i}{\partial \phi_i} = h_i \times g_i \tag{3.1}$$

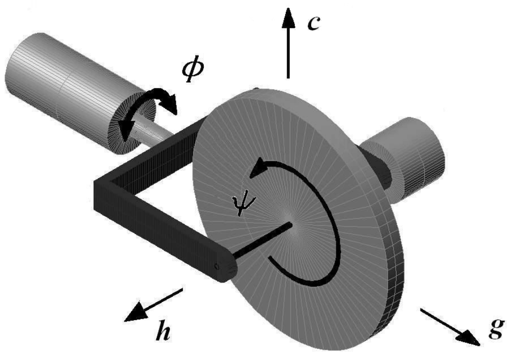

Figure 3.1: CMG unit vectors

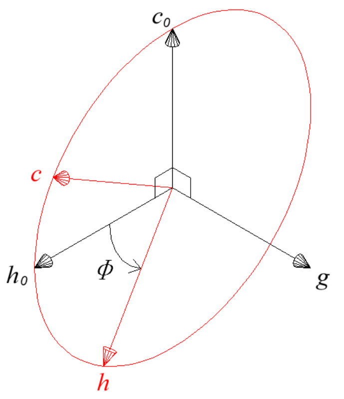

Figure 3.2: Rotating coordinate system

The gimbal axis g_i is fixed and the momentum and torque axes h_i and c_i vary as functions of the gimbal angle:

$$\begin{aligned} h_i &= h_{i0}\cos\phi_i - c_{i0}\sin\phi_i \\ c_i &= c_{i0}\cos\phi_i + h_{i0}\sin\phi_i \end{aligned}$$

where h_{i0} and c_{i0} are the nominal states of the system, as illustrated in Fig. 3.2.

Consider now the case of N identical CMG units in some fixed configuration. The orientation of each unit is defined by the vector of gimbal angles $\bar{\phi} = [\phi_1, \phi_2, ..., \phi_N]^T$, which defines the CMG state and specifies the gimbal, momentum and torque matrices $\bar{h}$, $\bar{g}$ and $\bar{c}$. The time derivatives of $\bar{h}$ and $\bar{c}$ vary as functions of the gimbal rates:

$$\begin{aligned} \dot{\bar{h}} &= -\bar{c}\,\mathrm{diag}(\dot{\bar{\phi}}) \\ \dot{\bar{c}} &= \bar{h}\,\mathrm{diag}(\dot{\bar{\phi}}) \end{aligned} \tag{3.2}$$

The energy of the CMG system can be expressed in matrix form:

$$\mathbf{T}_{cmg} = \frac{1}{2}\mathbf{\Omega}^T\mathbf{J}_{cmg}\mathbf{\Omega}$$

where $\mathbf{J}_{cmg}$ is the inertia of the CMGs. The inertia varies as the gimbals rotate and for single gimbal systems can be expressed:

$$\mathbf{J}_{cmg} = \bar{c}\mathbf{J}_c\bar{c}^T + \bar{g}\mathbf{J}_g\bar{g}^T + \bar{h}\mathbf{J}_h\bar{h}^T \tag{3.3}$$

The motion of the CMG system can be described by the rotation matrix:

$$\mathbf{\Omega} = \bar{g}\dot{\bar{\phi}} + \bar{h}\dot{\bar{\psi}}$$

where $\dot{\bar{\psi}}$ is the angular velocity of each flywheel. The angular momentum of the CMG system can be obtained by taking the derivative of the energy $\mathbf{T}_{cmg}$ with respect to $\mathbf{\Omega}$, as follows:

$$\begin{aligned}\mathbf{h}_{cmg} &= \frac{\partial \mathbf{T}}{\partial \Omega} = \mathbf{J}_{cmg}\Omega \\ &= \bar{g}\mathbf{J}_g\dot{\boldsymbol{\phi}} + \bar{h}\mathbf{J}_h\dot{\boldsymbol{\psi}} \end{aligned} \tag{3.4}$$

The torque of the CMG system can be expressed as a function of the gimbal rates by taking the time derivative of the angular momentum $\mathbf{h}_{cmg}$ and substituting in (3.2):

$$\tau_{cmg} = \dot{\mathbf{h}}_{cmg} = \bar{g}\mathbf{J}_g\ddot{\boldsymbol{\phi}} - \bar{c}\ \mathrm{diag}(\mathbf{J}_h\dot{\boldsymbol{\psi}})\dot{\boldsymbol{\phi}} \tag{3.5}$$

The first term describes the torque inputs required to rotate the gimbals and the second term describes the gyroscopic outputs generated. In most CMG applications the angular velocity of the flywheels is kept constant. This is highly efficient since the only power required to maintain the angular momentum is that to overcome friction. Furthermore, this implies that the magnitude of the output depends solely on the rotations of the gimbals. A large flywheel momentum ensures that the gyroscopic outputs are much greater than the torques required to actuate the gimbals. No component of the gyroscopic torques act in the flywheel or gimbal directions and so single gimbal CMGs are capable of a fast response to control inputs.

3.1.2 Coupled dynamics

Consider now a rigid body in which a system of N CMGs is placed. The total inertia of the system can be expressed:

$$\mathbf{J}_{tot} = \mathbf{J}_s + \mathbf{J}_{cmg} \tag{3.6}$$

where $\mathbf{J}_s$ is the inertia of the rigid body. The inertia of the CMG system varies with respect to the body-fixed reference frame, $\mathbf{F_b}$, with its axes (x, y, z) aligned with the principal axes of the body. The body is free to translate and rotate with respect to the inertially-fixed reference frame, $\mathbf{F_i}$, with the axes $(\mathbf{i}, \mathbf{j}, \mathbf{k})$. The coordinate system is illustrated in Fig. 3.3.

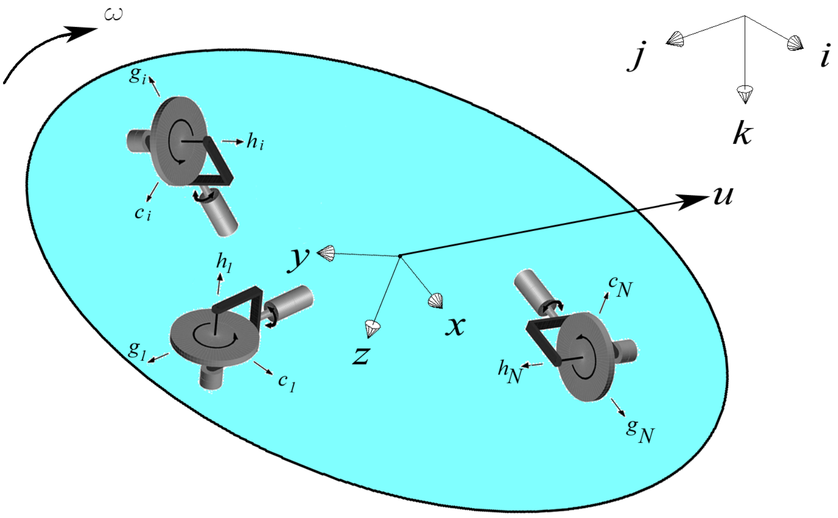

Figure 3.3: Coordinate system

The equations of motion of the system are derived based on Kirchhoff's equations. These provide a dynamic model of a neutrally buoyant rigid body translating and rotating in an infinite volume of fluid. The fluid is assumed to be irrotational, incompressible, inviscid and at rest at an infinitely distant boundary [65]. While these assumption initially seem restrictive, the equations can accommodate viscous effects, and any other unaccounted inputs, by appending them as external forces and moments. Kirchhoff's equations relate the dynamic energy of the system to the forces and moments that act on it:

$$\begin{aligned} \frac{d}{dt}\left(\frac{\partial \mathbf{T}}{\partial u}\right) + \omega \times \left(\frac{\partial \mathbf{T}}{\partial u}\right) &= F_{ext} \\ \frac{d}{dt}\left(\frac{\partial \mathbf{T}}{\partial \omega}\right) + \omega \times \left(\frac{\partial \mathbf{T}}{\partial \omega}\right) + u \times \left(\frac{\partial T}{\partial u}\right) &= \tau_{ext} \end{aligned} \tag{3.7}$$

where u and ω are the translational and rotational velocity components of the body (Fig. 3.3). The kinetic energy of a submerged body consists of both solid and fluid components [66]. The solid component is composed of the rigid body and CMG energy, and can be described:

$$\mathbf{T}_s = \frac{1}{2}\begin{pmatrix} u \\ \omega \\ \mathbf{\Omega} \end{pmatrix}^T \begin{pmatrix} m\mathbf{I} & -m\hat{r} & 0 \\ m\hat{r} & \mathbf{J}_{tot} & \mathbf{J}_{cmg} \\ 0 & \mathbf{J}_{cmg} & \mathbf{J}_{cmg} \end{pmatrix} \begin{pmatrix} u \\ \omega \\ \mathbf{\Omega} \end{pmatrix}$$

where m is the total mass of the rigid body and the CMGs. It is assumed that the CMGs are balanced so that rotations of the gimbals do not change the location of the centre of gravity $\hat{r}$, which remains constant with respect to the body-fixed coordinate frame. The discussion is restricted to a body with coincident centres of gravity and buoyancy where $\hat{r} = 0$ as this concept is central to the new class of underwater robot developed in this research. The consequences of this assumption are discussed in Chapter 8. The fluid energy component can be expressed as:

$$\mathbf{T}_l = \frac{1}{2}\begin{pmatrix} u \\ \omega \\ \Omega \end{pmatrix}^T \begin{pmatrix} \mathbf{M}_A & \mathbf{D}_A & 0 \\ \mathbf{D}_A & \mathbf{J}_A & 0 \\ 0 & 0 & 0 \end{pmatrix} \begin{pmatrix} u \\ \omega \\ \Omega \end{pmatrix}$$

where $\mathbf{M}_A$, $\mathbf{J}_A$ and $\mathbf{D}_A$ are the added mass, added inertia and added inertial coupling matrices associated with the potential flow. These terms depend on the external shape of the body and the choice of coordinate frame. The CMGs themselves make no contribution to the fluid energy since they are completely isolated from the external environment. The dynamics of the system are greatly simplified by choosing a body with three planes of symmetry with the body coordinate frame along its principal axes. This reduces $\mathbf{M}_A$, $\mathbf{J}_A$ to diagonal matrices and $\mathbf{D}_A$ to zero and thus fluid energy becomes uncoupled between the different degrees of freedom. This assumption is reasonable for the hull form chosen in this study, as discussed in Appendix C. The energy of the complete CMG, body and fluid system becomes:

$$\mathbf{T} = \mathbf{T}_s + \mathbf{T}_l = \frac{1}{2}\begin{pmatrix} u \\ \omega \\ \Omega \end{pmatrix}^T \begin{pmatrix} m\mathbf{I} + \mathbf{M}_A & 0 & 0 \\ 0 & \mathbf{J}_{tot} + \mathbf{J}_A & \mathbf{J}_{cmg} \\ 0 & \mathbf{J}_{cmg} & \mathbf{J}_{cmg} \end{pmatrix} \begin{pmatrix} u \\ \omega \\ \Omega \end{pmatrix} \tag{3.8}$$

The linear and angular momentum of the system can be obtained by taking the partial derivatives of the total energy with respect to u and ω:

$$\begin{aligned}\mathbf{P} &= \frac{\partial \mathbf{T}}{\partial u} = (m\mathbf{I} + \mathbf{M}_A)u \\ \mathbf{\Pi} &= \frac{\partial \mathbf{T}}{\partial \omega} = (\mathbf{J}_{tot} + \mathbf{J}_A)\omega + \mathbf{J}_{cmg}\Omega \end{aligned} \tag{3.9}$$

The final term $\mathbf{J}_{cmg}\Omega$ is the angular momentum of the CMGs derived earlier in (3.4). The fully descriptive equations for the translational and rotational dynamics of the system can be obtained by substituting these expressions into Kirchhoff's equations (3.7) to give:

$$\begin{aligned}\frac{d}{dt}[(\mathbf{mI} + \mathbf{M_A})\mathbf{u}] + \omega \times \mathbf{P} &= F_{ext} \\ \frac{d}{dt}[(\mathbf{J}_{tot} + \mathbf{J}_A)\omega + \mathbf{h}_{cmg}] + \omega \times \mathbf{\Pi} + u \times \mathbf{P} &= \tau_{ext}\end{aligned} \tag{3.10}$$

In the equation above the rigid body component of $\mathbf{J}_{tot}$ (3.6) is constant and so the derivative $\dot{\mathbf{J}}_{tot} = \dot{\mathbf{J}}_{cmg}$, which can be obtained by taking the derivative of (3.3) to give:

$$\dot{\mathbf{J}}_{cmg} = \dot{\bar{c}}\mathbf{J}_c\bar{c}^T + \bar{c}\mathbf{J}_c\dot{\bar{c}}^T + \dot{\bar{h}}\mathbf{J}_h\bar{h}^T + \bar{h}\mathbf{J}_h\dot{\bar{h}}^T$$

where the gimbal axes are fixed in the body. Substituting in the expressions for $\dot{\bar{h}}$ and $\dot{\bar{c}}$ derived in (3.2) gives:

$$\dot{\mathbf{J}}_{cmg} = \text{diag } \dot{\bar{\phi}}\bar{h}(\mathbf{J}_c - \mathbf{J}_h)\bar{c}^T + \text{diag } \dot{\bar{\phi}}\bar{c}(\mathbf{J}_c - \mathbf{J}_h)\bar{h}^T$$

Multiplying out the individual elements of the matrices gives the following form:

$$\dot{\mathbf{J}}_{cmg} = \sum_{i=1}^{N}(h_i(J_{ci} - J_{hi})\dot{\phi}_i c_i^T) + \sum_{i=1}^{N}(c_i(J_{ci} - J_{hi})\dot{\phi}_i h_i^T)$$

This can be expressed as a function of the gimbal rates:

$$\dot{\mathbf{J}}_{cmg} = [(h_1c_1^T + c_1h_1^T) \quad \ldots \quad (h_Nc_N^T + c_Nh_N^T)](\mathbf{J}_c - \mathbf{J}_h)\dot{\bar{\phi}} \tag{3.11}$$

Applying this result in (3.10) gives the translational and rotational dynamics of the system:

$$\begin{aligned}(\mathbf{mI} + \mathbf{M_A})\mathbf{u} &= -\omega \times \mathbf{P} + F_{ext} \\ (\mathbf{J}_{tot} + \mathbf{J}_A)\dot{\omega} &= -[(h_1c_1^T + c_1h_1^T)\omega \quad \ldots \quad (h_Nc_N^T + c_Nh_N^T)\omega](\mathbf{J}_c - \mathbf{J}_h)\dot{\bar{\phi}} \\ &\qquad -\omega \times \mathbf{\Pi} - u \times \mathbf{P} - \tau_{cmg} + \tau_{ext}\end{aligned} \tag{3.12}$$

The first term on the right of (3.12) describes the coupled effects of the change in inertia due to CMG motion as the body rotates. The second term describes the effects of the angular momentum as the body rotates. The third term describes the coupled effects of the translational dynamics on rotation, which is zero for a body with three planes of symmetry since the momentum $\mathbf{P}$ has no coupled terms. The fourth term, described in (3.5), accounts for the gimbal input and gyroscopic output torques of the CMG system.

The final term in (3.12) accounts for any externally applied forces and moments, thus no dynamic terms have been omitted from the equation. For the body with zero righting moment that is considered in this application, the final term includes the effects of other actuators and hydrodynamic drag, as described in Appendix C. In this application the CMG system actuates the rotational dynamics and so the external actuators can be arranged to generate thrust only with no rotational effects. Therefore, the external forces and moments are modelled as follows:

$$\begin{aligned} F_{ext} &= F_t + F_{drag} \\ \tau_{ext} &= \tau_{drag} \end{aligned}$$

These terms can be extended to accommodate non-coincident centres of gravity and buoyancy, as detailed in Appendix C, and any other external effects in a similar manner.

3.1.3 Viscosity

Kirchhoff's equations rely on the assumption that the fluid is inviscid and slips freely over the surface of the body. In reality, viscosity has an appreciable effect on the flow regime. This plays a significant role in the dynamics of the system, so much so that for bodies at large depths the contribution of potential damping is negligible in comparison [67]. In a viscous fluid, a layer of fluid adheres to the solid boundary and friction between the adjacent layers of fluid forms a thin boundary layer over the surface [68]. The relative flow velocity adjusts rapidly from zero at the surface of the body to the velocity of an effectively potential flow just outside the boundary layer. The velocity gradient of the boundary layer gives rise to viscous stresses that act on the surface of the body and retard its motion through skin friction. The boundary layer grows in the streamwise direction as flow is deflected away from the body to avoid accumulation. For non-planar surfaces, a pressure gradient exists along the boundary layer due to the centrifugal effect of flow around a curved body. In the case of an adverse pressure gradient the flow decelerates as the pressure increases along the body. In a sufficiently adverse pressure gradient the fluid cannot diffuse fast enough into the boundary layer and the flow separates from the body with the direction of flow over its surface reversed beyond the separation point. This forms a low pressure wake that gives rise to a retardant force on the body that is known as pressure drag.

The effects of viscus flow are highly dependant on the type of flow regime. Since boundary layers are composed of both laminar and turbulent regions, it is first necessary to determine the appropriate type of flow regime. Turbulent boundary layers generally exert more frictional drag on a surface than laminar boundary layers, but nevertheless often results in a smaller overall drag as they are less prone to separation [69]. An indicator of the dominant type of flow regime is the Reynolds number $R_n = \frac{ul}{\nu}$, where u is the velocity of the body, l is its characteristic length and ν is the kinematic viscosity of the fluid. This yields a Reynolds number of 2.2×10^5 for the robot developed in this research, which lies in the transition zone between laminar and turbulent flow. However, the hull form in this application is broken up by unavoidable protrusions and it is considered that these will trip the flow into a turbulent regime. This is discussed further in Appendix C.

Whilst the technology exists to analytically solve the Navier-Stokes equations and determine the exact effects of the hydrodynamic interactions, such calculations require sophisticated CFD packages and powerful computers and even then can take several days to solve. Therefore, with current technology, these equations are not suitable for application on-board AUVs since they must determine the effects of drag in real-time. Therefore, empirical models must be relied upon. While these models cannot predict with great accuracy all the interactions of an unsteady, three-dimensional flow regime over a self-propelled underwater body, they can capture the essential elements of flow and provide an effective tool to approximate the hydrodynamic forces that act on the body. The viscous drag can be expressed by the following standard empirical model:

$$\begin{aligned} F_{drag} &= -\frac{1}{2}\rho A C_D u|u| \\ \tau_{drag} &= -\frac{1}{2}\rho A \sum C_{Di} r_i^3 \omega|\omega| \end{aligned}$$

where ρ is the density of the surrounding fluid, A is the matrix of projected cross-sectional areas of the body, C_D is the drag coefficient of the body and r_i is the mean distance to the centre of rotation. A body with three planes of symmetry has a diagonal matrix of drag coefficients C_D and so there is no coupling between the different degrees of freedom. The assignment of appropriate values for C_D is essential to realistically model drag. The hydrodynamic calculations for the hull form used in this research can be found in Appendix C.

3.2 Conversion to the inertial frame

3.2.1 General formulation

A vector in the body-fixed reference frame can be expressed in the inertial reference frame using the general rotation equation:

$$\mathbf{r}' = \mathbf{R}\mathbf{r} \tag{3.13}$$

where the rotation matrix to map between any two frames of reference is given [67]:

$$\mathbf{R} = \cos\beta_\lambda \mathbf{I} + (1 - \cos\beta_\lambda)\lambda\lambda^T - \sin\beta_\lambda \hat{\lambda} \tag{3.14}$$

In this expression β_λ is the angle of simple rotation about the arbitrary single axis of rotation $\lambda = [\lambda_i, \lambda_j, \lambda_k]^T$ that would bring the body frame back to the inertial frame. The skew-symmetric operator $\hat{\lambda}$ is defined such that:

$$\hat{\lambda} = \begin{bmatrix} 0 & -\lambda_k & \lambda_j \\ \lambda_k & 0 & -\lambda_i \\ -\lambda_j & \lambda_i & 0 \end{bmatrix}$$

For unrestricted attitude control the mathematical description of attitude must not possess any numerical singularities. Therefore, a four-parameter quaternion method based on Euler parameters is used to describe the orientation of the body in the inertial frame of reference.

3.2.2 Quaternion rotations

A quaternion is an extended form of complex number that is composed of four units $[\mathbf{i}, \mathbf{j}, \mathbf{k}, \mathbf{1}]$ and is of unit magnitude. The imaginary part is made up of three orthogonal unit vectors $(\mathbf{i}, \mathbf{j}, \mathbf{k})$ and the real part is scalar. The quaternion vector is specified as:

$$\mathbf{q} = \xi_i \mathbf{i} + \xi_j \mathbf{j} + \xi_k \mathbf{k} + \eta$$

The quaternion components $[\xi_i, \xi_j, \xi_k, \eta]$ are real values that are defined as follows:

$$\mathbf{q} = \begin{pmatrix} \xi_i \\ \xi_j \\ \xi_k \\ \eta \end{pmatrix} = \begin{pmatrix} \xi \\ \eta \end{pmatrix} = \begin{pmatrix} \lambda \sin \frac{\beta_\lambda}{2} \\ \cos \frac{\beta_\lambda}{2} \end{pmatrix} \tag{3.15}$$

The representation is valid for any angle of β_λ. The parametrisation of a unit quaternion is subject to the following constraint:

$$\xi_i^2 + \xi_j^2 + \xi_k^2 + \eta^2 = 1 \tag{3.16}$$

This implies, since $|\mathbf{q}| = 1$, that the inverse of the quaternion is equal to its complex conjugate:

$$\mathbf{q}^{-1} = \bar{\mathbf{q}} = \begin{pmatrix} -\xi \\ \eta \end{pmatrix}$$

The rotation of any vector in space can be described by expressing the rotation matrix in terms of quaternions. It is first useful to observe the following trigonometric identities:

$$\begin{aligned} \cos \beta_\lambda =& \quad 2\cos^2 \tfrac{\beta_\lambda}{2} - 1 && = 2\eta^2 - 1 \\ (1 - \cos \beta_\lambda)\lambda\lambda^T =& \quad 2\sin^2 \tfrac{\beta_\lambda}{2} \lambda\lambda^T && = 2\xi\xi^T \\ \sin \beta_\lambda \hat{\lambda} =& \quad 2\sin \tfrac{\beta_\lambda}{2} \cos \tfrac{\beta_\lambda}{2} \hat{\lambda} && = 2\eta\hat{\xi} \end{aligned}$$

The rotation matrix (3.14) can be written in terms of quaternions:

$$\mathbf{R} = (2\eta^2 - 1)\mathbf{I} + 2\xi\xi^T - 2\eta\hat{\xi}$$

Substituting in the unitary constraint (3.16) gives the relation:

$$\mathbf{R} = (\eta^2 + (1 - \xi_i^2 - \xi_j^2 - \xi_k^2) - 1)\mathbf{I} + 2\xi\xi^T - 2\eta\hat{\xi}$$

to give the following quaternion form of the rotation matrix:

$$\mathbf{R} = (\eta^2 - \xi^T\xi)\mathbf{I} + 2\xi\xi^T - 2\eta\hat{\xi}$$

This can be expressed in component form as follows:

$$\mathbf{R} = \begin{bmatrix} \eta^2 + \xi_i^2 - \xi_j^2 - \xi_k^2 & 2(\xi_i\xi_j - \eta\xi_k) & 2(\xi_i\xi_k + \eta\xi_j) \\ 2(\xi_i\xi_j + \eta\xi_k) & \eta^2 - \xi_i^2 + \xi_j^2 - \xi_k^2 & 2(\xi_j\xi_k - \eta\xi_i) \\ 2(\xi_i\xi_k - \eta\xi_j) & 2(\xi_j\xi_k + \eta\xi_i) & \eta^2 - \xi_i^2 - \xi_j^2 + \xi_k^2 \end{bmatrix} \tag{3.17}$$

The mapping between two frames of reference can be described in terms of quaternions by substituting the quaternion form of the rotation matrix (3.17) into the general expression for the rotation of a vector (3.13). However, before the rotation of a rigid body can be described it is first necessary to determine the values of the quaternion components $[\xi_i, \xi_j, \xi_k, \eta]^T$.

3.2.3 Quaternion kinematic equations

This section details a full derivation of the quaternion differential equations to allow the quaternion components $[\xi_i, \xi_j, \xi_k, \eta]^T$ to be determined. In order to achieve this it is first useful to introduce the general matrix-vector products $\mathbf{Q}(\mathbf{q})$ and $\bar{\mathbf{Q}}(\mathbf{q})$ that describe the multiplication of any two quaternions [70]:

$$\begin{aligned} \mathbf{q}\mathbf{q}' &= \begin{pmatrix} \eta\mathbf{I} + \hat{\xi} & \xi \\ -\xi^T & \eta \end{pmatrix} \begin{pmatrix} \xi' \\ \eta' \end{pmatrix} = \mathbf{Q}(\mathbf{q})\mathbf{q}' \\ \mathbf{q}'\mathbf{q} &= \begin{pmatrix} \eta\mathbf{I} - \hat{\xi} & \xi \\ -\xi^T & \eta \end{pmatrix} \begin{pmatrix} \xi' \\ \eta' \end{pmatrix} = \bar{\mathbf{Q}}(\mathbf{q})\mathbf{q}' \end{aligned} \tag{3.18}$$

The quaternion rotation in (3.17) can be expressed in terms of the matrix-vector products:

$$\begin{pmatrix} \mathbf{R} & 0 \\ 0^T & 1 \end{pmatrix} = \begin{pmatrix} \eta\mathbf{I} + \hat{\xi} & \xi \\ -\xi^T & \eta \end{pmatrix} \begin{pmatrix} \eta\mathbf{I} + \hat{\xi} & -\xi \\ \xi^T & \eta \end{pmatrix} = \mathbf{Q}(\mathbf{q})\bar{\mathbf{Q}}(\bar{\mathbf{q}})$$

By associating the three-dimensional vector r with the imaginary part of the quaternion $\mathbf{r} = (r, 0)$, the above expression can be substituted into (3.13) to yield:

$$\mathbf{r}' = \mathbf{Q}(\mathbf{q})\bar{\mathbf{Q}}(\bar{\mathbf{q}})\mathbf{r}$$

The transformation can be expressed in terms of the quaternions by substituting in (3.18):

$$\mathbf{r}' = \mathbf{q}\mathbf{r}\bar{\mathbf{q}}$$

Taking the derivative of the inverse relation gives:

$$\begin{aligned} \mathbf{r} &= \bar{\mathbf{q}}\mathbf{r}'\mathbf{q} \\ \dot{\mathbf{r}} &= \dot{\bar{\mathbf{q}}}\mathbf{r}'\mathbf{q} + \bar{\mathbf{q}}\mathbf{r}'\dot{\mathbf{q}} \\ &= \dot{\bar{\mathbf{q}}}\mathbf{q}\mathbf{r}\bar{\mathbf{q}}\mathbf{q} + \bar{\mathbf{q}}\mathbf{q}\mathbf{r}\bar{\mathbf{q}}\dot{\mathbf{q}} \\ &= \dot{\bar{\mathbf{q}}}\mathbf{q}\mathbf{r} + \mathbf{r}\bar{\mathbf{q}}\dot{\mathbf{q}} \end{aligned} \tag{3.19}$$

where from (3.15) the following relationship for $\bar{\mathbf{q}}\mathbf{q}$ has been applied:

$$\begin{aligned} \bar{\mathbf{q}}\mathbf{q} &= \left(\cos\frac{\beta_\lambda}{2} - \lambda\sin\frac{\beta_\lambda}{2}\right)\left(\cos\frac{\beta_\lambda}{2} + \lambda\sin\frac{\beta_\lambda}{2}\right) \\ &= \cos^2\frac{\beta_\lambda}{2} - \lambda^2\sin^2\frac{\beta_\lambda}{2} \\ &= \cos^2\frac{\beta_\lambda}{2} + \sin^2\frac{\beta_\lambda}{2} \quad = 1 \end{aligned}$$

Similarly the products $\dot{\bar{\mathbf{q}}}\mathbf{q}$ and $\bar{\mathbf{q}}\dot{\mathbf{q}}$ can be expressed as purely imaginary values:

$$\begin{aligned}
\dot{\bar{\mathbf{q}}}\mathbf{q} &= \left(-\frac{1}{2}\sin\frac{\beta_\lambda}{2} - \frac{\lambda}{2}\cos\frac{\beta_\lambda}{2}\right)\left(\cos\frac{\beta_\lambda}{2} + \lambda\sin\frac{\beta_\lambda}{2}\right) = -\frac{\lambda}{2} \\
\bar{\mathbf{q}}\dot{\mathbf{q}} &= \left(\cos\frac{\beta_\lambda}{2} - \lambda\sin\frac{\beta_\lambda}{2}\right)\left(-\frac{1}{2}\sin\frac{\beta_\lambda}{2} + \frac{\lambda}{2}\cos\frac{\beta_\lambda}{2}\right) = \frac{\lambda}{2}
\end{aligned}$$

Therefore, $\dot{\bar{\mathbf{q}}}\mathbf{q} = -\bar{\mathbf{q}}\dot{\mathbf{q}}$. From (3.15) it can also be observed that the rotation by $\mathbf{q}$ represents the same rotation as $-\mathbf{q}$. Furthermore, it can be seen that both $\bar{\mathbf{q}}\dot{\mathbf{q}}$ and $\mathbf{r}$ have only imaginary parts and so their bottom rows are zero. Thus the following vector identities can be applied:

$$[a\ b\ c] = ab \times c = -c \times ab = a \times bc = -bc \times a$$

The derivation continues by using these results in (3.19) as follows:

$$\begin{aligned}
\dot{\mathbf{r}} &= \bar{\mathbf{q}}\dot{\mathbf{q}}\mathbf{r} - \mathbf{r}\bar{\mathbf{q}}\dot{\mathbf{q}} \\
&= \bar{\mathbf{q}}\dot{\mathbf{q}} \times \mathbf{r} - \mathbf{r} \times \bar{\mathbf{q}}\dot{\mathbf{q}} \\
&= \bar{\mathbf{q}}\dot{\mathbf{q}} \times \mathbf{r} + \bar{\mathbf{q}}\dot{\mathbf{q}} \times \mathbf{r} \\
&= 2\bar{\mathbf{q}}\dot{\mathbf{q}} \times \mathbf{r} \qquad (3.20)
\end{aligned}$$

Equation (3.20) is of the form:

$$\dot{\mathbf{r}} = \omega \times \mathbf{r}$$

This is a general expression that describes the rotational kinematics of any system, where ω is the angular rate of the body expressed with respect to the body-fixed reference frame. Therefore, it can be observed that the angular rate of the body in (3.12) relates to the quaternions and their derivative as follows:

$$\omega = 2\bar{\mathbf{q}}\dot{\mathbf{q}}$$

Observing that $\bar{\mathbf{q}}^{-1} = \mathbf{q}$, the inverse of the above expression gives the differential equations of the quaternion system:

$$\begin{aligned}
\dot{\mathbf{q}} &= \frac{1}{2}\mathbf{q}\omega \\
&= \frac{1}{2}\mathbf{Q}(\mathbf{q})\begin{pmatrix}\omega \\ 0\end{pmatrix}
\end{aligned}$$

Since the rotation ω has zero real part the last column of $\mathbf{Q}(\mathbf{q})$ can be discarded. Thus the following dynamic equation for the rate of change of the quaternions can be obtained:

$$\dot{\mathbf{q}} = Q(\mathbf{q})\omega \qquad (3.21)$$

The component form of the transform matrix is:

$$Q(\mathbf{q}) = \frac{1}{2}\begin{pmatrix} \eta & -\xi_k & \xi_j \\ \xi_k & \eta & -\xi_i \\ -\xi_j & \xi_i & \eta \\ -\xi_i & -\xi_j & -\xi_k \end{pmatrix}$$

3.2.4 Euler angle representation

Despite their many advantages, quaternion parameters do not carry any obvious physical meaning and so it is convenient to plan and record missions using Euler angles. The Euler angles $[\theta_x, \theta_y, \theta_z]$ directly correspond to the angles of roll, pitch and yaw respectively and this provides a more intuitive representation of attitude information for human interpretation. The quaternions calculated by the dynamic equations can be converted to Euler angles using the following equations:

$$\begin{aligned}
\theta_x &= \tan^{-1}\left(\frac{2(\xi_j\xi_k - \eta\xi_i)}{\eta^2 - \xi_i^2 - \xi_j^2 + \xi_k^2}\right) \\
\theta_y &= \sin^{-1}\left(-2(\xi_i\xi_k + \eta\xi_j)\right) \\
\theta_z &= \tan^{-1}\left(\frac{2(\xi_i\xi_j - \eta\xi_k)}{\eta^2 + \xi_i^2 - \xi_j^2 - \xi_k^2}\right)
\end{aligned}$$

Conversely, the attitude and angular rate measurements made by the sensors typically used by underwater robots are also provided in terms of Euler angles and so these must be converted to quaternions. This can be achieved using the following equation:

$$\begin{aligned}
\mathbf{q} &= q_{\theta_x} q_{\theta_y} q_{\theta_z} \\
&= \left(\cos\frac{\theta_x}{2} - \mathbf{i}\sin\frac{\theta_x}{2}\right)\left(\cos\frac{\theta_y}{2} - \mathbf{j}\sin\frac{\theta_y}{2}\right)\left(\cos\frac{\theta_z}{2} - \mathbf{k}\sin\frac{\theta_z}{2}\right)
\end{aligned}$$

This can be expressed in component form as:

$$\mathbf{q} = \begin{pmatrix} \xi_i \\ \xi_j \\ \xi_k \\ \eta \end{pmatrix} = \begin{pmatrix} \sin\frac{\theta_x}{2}\cos\frac{\theta_y}{2}\cos\frac{\theta_z}{2} - \cos\frac{\theta_x}{2}\sin\frac{\theta_y}{2}\sin\frac{\theta_z}{2} \\ \cos\frac{\theta_x}{2}\sin\frac{\theta_y}{2}\cos\frac{\theta_z}{2} + \sin\frac{\theta_x}{2}\cos\frac{\theta_y}{2}\sin\frac{\theta_z}{2} \\ \cos\frac{\theta_x}{2}\cos\frac{\theta_y}{2}\sin\frac{\theta_z}{2} - \sin\frac{\theta_x}{2}\sin\frac{\theta_y}{2}\cos\frac{\theta_z}{2} \\ \cos\frac{\theta_x}{2}\cos\frac{\theta_y}{2}\cos\frac{\theta_z}{2} + \sin\frac{\theta_x}{2}\sin\frac{\theta_y}{2}\sin\frac{\theta_z}{2} \end{pmatrix}$$

3.3 Summary

The fully descriptive equations of motion have been derived for a rigid body that contains an arbitrary system of single gimbal CMGs and is immersed in a fluid. In contrast to past derivations, these are formulated based on Kirchhoff's equations of motion to allow for a more natural transition into the Lyapunov analysis in the next chapter. Unlike previous CMG applications, this dynamic model takes into account the effects of translational motion and the hydrodynamic interactions of the body as well as the actuating effects of external thrusters. Quaternions are used to describe the attitude of the body in the inertial frame to provide the numerical freedom for the body to adopt any attitude on the surface of a sphere. In order that this can be physically achieved it is important for the body to have as near coincident centres of gravity and buoyancy as possible. However, this dynamic freedom in the orientation of the body raises questions concerning the stability of the system that can only be answered by the control system used.

Chapter 4

Control law

In an uncertain and constantly changing environment such as the ocean it is important to ensure that unforeseen disturbances do not cause significant degradations in the subsequent control performance. Furthermore, a body with zero righting moment is inherently unstable and particularly sensitive to disturbances and so must be actively stabilised by its control system. The area of control engineering links theory with physical reality and so for complex situations there often exist several ways in which to approach a particular problem. This chapter develops an attitude control law based on energy considerations of the complete CMG, body and fluid system described by the equations of motion developed in the previous chapter. Lyapunov's direct method is applied to assess the stability of the non-linear system taking into account the effects of viscous damping. This is used to design an asymptotically stable attitude control law that allows the robot to adopt any attitude in roll, pitch and yaw.

4.1 Lyapunov's direct method

Lyapunov's direct method assesses the stability of non-linear, autonomous systems by considering the time variation of a scalar energy-like function. A system can be described as autonomous if its closed-loop dynamics do not explicitly depend on time. In reality this concept is an idealised notion since the properties of any system change with time. However, in the case of an underwater robot these changes are slow and so can be neglected without causing any significant error, thus the dynamics of the robot can be described as both non-linear and autonomous. If engineering insight and physical properties are exploited, a Lyapunov analysis can allow for elegant and powerful control solutions to even the most complex problems:

Theorem 4.1 (Lyapunov's direct method [71]) *Assume that there exists a scalar function V of the state $\mathbf{x}$ with continuous first order derivatives such that:*

- $V(\mathbf{x}) > 0$ *for* $\mathbf{x} \neq 0$
- $V(\mathbf{x}) \longrightarrow \infty$ *as* $|\mathbf{x}| \longrightarrow \infty$
- $\dot{V}(\mathbf{x}) < 0$ *for* $\mathbf{x} \neq 0$

Satisfying these conditions ensures global asymptotic stability to the origin.

Lyapunov's direct method can demonstrate the global asymptotic stability of a system by finding a radially unbounded function of the system's dynamics that is positive definite and has a negative definite time derivative. An obvious challenge in applying this method is the formulation of an appropriate Lyapunov function V. There is no formal procedure for constructing this function although, for physical systems such as underwater robots, energy is often a good candidate [71].

The role of the CMGs is analogous to a system of springs and dampers that bring the body smoothly to the desired state. This analogy is formalised by defining the Lyapunov function based on appropriate potential and kinetic energy-like terms with respect to the desired state. The function chosen is similar to that chosen in Oh [60], but is extended to take into account the effects of added fluid inertia:

$$V(\mathbf{e_q}, \mathbf{e}_\omega) = \frac{1}{2}\mathbf{e_q}^T k_q \mathbf{e_q} + \frac{1}{2}\mathbf{e}_\omega^T(\mathbf{J}_{tot} + \mathbf{J}_A)\mathbf{e}_\omega \tag{4.1}$$

The states $\mathbf{e_q} = \mathbf{q} - \mathbf{q}_d$ and $\mathbf{e}_\omega = \omega - \omega_d$ are the attitude and angular velocity errors with respect to the desired state. The effect of the first term on the right hand side of the equation is analogous to a 'spring', describing the potential energy-like contribution with respect to the desired quaternion attitude. The effect of the second term is analogous to a 'damper', describing the kinetic energy-like contribution with respect to the desired angular velocity. Since k_q is a diagonal matrix of positive gains and the inertia of the system is always positive, the Lyapunov function is positive definite and the following conditions are satisfied:

$$\begin{aligned} &V(\mathbf{e_q}, \mathbf{e}_\omega) > 0 \quad for\ [\mathbf{e_q}, \mathbf{e}_\omega] \neq [0, 0] \\ &V(\mathbf{e_q}, \mathbf{e}_\omega) \rightarrow \infty \quad as\ |\mathbf{e_q}, \mathbf{e}_\omega| \rightarrow \infty \end{aligned}$$

The time derivative of the Lyapunov function can be obtained by differentiating (4.1) to give the following expression:

$$\dot{V}(\mathbf{e_q}, \mathbf{e}_\omega) \;\; = \;\; \mathbf{e}_q^T k_q \dot{\mathbf{e}}_q + \frac{1}{2}\mathbf{e}_\omega^T \dot{\mathbf{J}}_{tot}\mathbf{e}_\omega + \mathbf{e}_\omega^T \mathbf{J}_{tot}\dot{\mathbf{e}}_\omega$$

Using the relationship in (3.21) to express $\dot{\mathbf{e}}_q$ and recalling that $\dot{\mathbf{J}}_{tot} = \dot{\mathbf{J}}_{cmg}$ gives:

$$\dot{V}(\mathbf{e_q}, \mathbf{e}_\omega) \;\; = \;\; \mathbf{e}_q^T k_q Q(\mathbf{q})\mathbf{e}_\omega + \frac{1}{2}\mathbf{e}_\omega^T \dot{\mathbf{J}}_{cmg}\mathbf{e}_\omega + \mathbf{e}_\omega^T \mathbf{J}_{tot}\dot{\mathbf{e}}_\omega$$

Since the product in the first term equates to a scalar value:

$$\mathbf{e}_q^T k_q Q(\mathbf{q})\mathbf{e}_\omega = [\mathbf{e}_\omega^T Q^T(\mathbf{q}) k_q^T \mathbf{e_q}]^T = [\mathbf{e}_\omega^T Q^T(\mathbf{q}) k_q \mathbf{e_q}]$$

Therefore, the derivative can be written in the following form:

$$\dot{V}(\mathbf{e_q}, \mathbf{e}_\omega) = \mathbf{e}_\omega^T[Q^T(\mathbf{q}) k_q \mathbf{e_q} + \frac{1}{2}\dot{\mathbf{J}}_{cmg}\mathbf{e}_\omega + (\mathbf{J}_{tot} + \mathbf{J}_A)\dot{\mathbf{e}}_\omega]$$

The Lyapunov derivative can only be guaranteed negative by choosing the relationship:

$$k_\omega \mathbf{e}_\omega = -[Q^T(\mathbf{q}) k_q \mathbf{e_q} + \tfrac{1}{2}\dot{\mathbf{J}}_{cmg}\mathbf{e}_\omega + (\mathbf{J}_{tot} + \mathbf{J}_A)\dot{\mathbf{e}}_\omega] \tag{4.2}$$

where k_ω is a diagonal matrix of positive gains. Thus the Lyapunov derivative becomes:

$$\dot{V}(\mathbf{e_q}, \mathbf{e}_\omega) = -\mathbf{e}_\omega^T k_\omega \mathbf{e}_\omega \leq 0 \quad for\ [\mathbf{e_q}, \mathbf{e}_\omega] \neq [0, 0] \tag{4.3}$$

This describes the energy dissipated by the system. It can be seen that the system would be in equilibrium (i.e. $\dot{V} = 0$) at anywhere along $\mathbf{e}_\omega = 0$ even if $\mathbf{e_q} \neq 0$ and thus the Lyapunov derivative is only negative semi-definite. Although this ensures the stability of the system, this does not guarantee asymptotic stability to the desired state. A simple geometric interpretation of this condition is given in Fig. 4.1 that illustrates how the system can become stuck at any point along the $\mathbf{e}_\omega = 0$ axis as the Lyapunov energy V reduces to zero. Further analysis is required to show that the system will in fact, converge to the desired state.

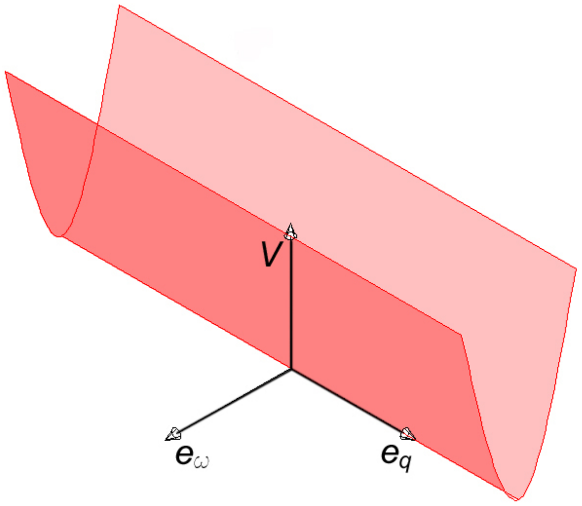

Figure 4.1: Lyapunov function with a negative semi-definite derivative

4.2 Global asymptotic stability

In control systems where the Lyapunov derivative $\dot{V}$ is only negative semi-definite, it is still possible to draw conclusions on asymptotic stability by extending Lyapunov's direct method and applying the invariance principle of La Salle:

Theorem 4.2 (La Salle's invariance principle [71]) *Consider a system where the scalar function V of the state $\mathbf{x}$ has continuous first order derivatives such that:*

- $V(\mathbf{x}) > 0$ *for* $\mathbf{x} \neq 0$
- $V(\mathbf{x}) \longrightarrow \infty$ *as* $|\mathbf{x}| \longrightarrow \infty$
- $\dot{V}(\mathbf{x}) \leq 0$ *over the whole state space*

Let R be the set of all points where $\dot{V}(\mathbf{x}) = 0$, and M be the largest invariant set in R. Then all solutions globally asymptotically converge to M as $t \rightarrow \infty$.

Asymptotic stability can be guaranteed by making sure that the origin $[\mathbf{e}_\omega, \mathbf{e}_\mathbf{q}] = [0, 0]$ is the largest invariant set in $\dot{V}(\mathbf{x}) = 0$. This can be achieved by developing a control law that ensures the conditions $\omega_d = \omega$ and $q_d = q$ are equivalent. In order to formulate such a control law, the expression for k_ω in (4.2) is expanded as follows:

$$k_\omega \mathbf{e}_\omega = -Q^T(\mathbf{q})k_q\mathbf{e}_\mathbf{q} - \frac{1}{2}\dot{\mathbf{J}}_{cmg}\omega_d + \frac{1}{2}\dot{\mathbf{J}}_{cmg}\omega - (\mathbf{J}_{tot} + \mathbf{J}_A)\dot{\omega}_d + (\mathbf{J}_{tot} + \mathbf{J}_A)\dot{\omega}$$

This can be rearranged to express the angular acceleration of the body in terms of the gains k_q and k_ω in the following form:

$$(\mathbf{J}_{tot} + \mathbf{J}_A)\dot{\omega} = k_\omega \mathbf{e}_\omega + Q^T(\mathbf{q})k_q\mathbf{e}_\mathbf{q} + \frac{1}{2}\dot{\mathbf{J}}_{cmg}(\omega_d - \omega) + (\mathbf{J}_{tot} + \mathbf{J}_A)\dot{\omega}_d$$

Substituting this expression into the equations for the rotational dynamics derived in (3.12) gives the condition:

$$Q^T(\mathbf{q})k_q\mathbf{e}_\mathbf{q} + k_\omega \mathbf{e}_\omega - \frac{1}{2}\dot{\mathbf{J}}_{cmg}(\omega + \omega_d) - (\mathbf{J}_{tot} + \mathbf{J}_A)\dot{\omega}_d - \omega \times \mathbf{\Pi} - u \times \mathbf{P} - \tau_{cmg} + \tau_{drag} = 0$$

This can be expanded by substituting in the expressions for τ_{cmg} in (3.5) and $\dot{\mathbf{J}}_{cmg}$ in (3.11) to form a condition for all terms explicitly dependant on gimbal motion:

$$\begin{aligned}\bar{g}\mathbf{J}_g\ddot{\bar{\phi}} - \bar{c}\ \mathrm{diag}(\mathbf{J}_h\dot{\bar{\psi}})\dot{\bar{\phi}} + \frac{1}{2}[(h_1c_1^T + c_1h_1^T)(\omega + \omega_d)\ \ldots\ (h_Nc_N^T + c_Nh_N^T)(\omega + \omega_d)](\mathbf{J}_c - \mathbf{J}_h)\dot{\bar{\phi}} \\ = Q^T(\mathbf{q})k_q\mathbf{e}_\mathbf{q} + k_\omega \mathbf{e}_\omega - (\mathbf{J}_{tot} + \mathbf{J}_A)\dot{\omega}_d - \omega \times \mathbf{\Pi} - u \times \mathbf{P} + \tau_{drag} \qquad (4.4)\end{aligned}$$

It can be observed from (3.9) and (3.4) that $\mathbf{\Pi}$ contains the term $\bar{g}\mathbf{J}_g\dot{\bar{\phi}} + \bar{h}\mathbf{J}_h\dot{\bar{\psi}}$ and thus varies with gimbal angles. However, in this application the momentum stored in the flywheels must be much larger than the gimbal momentum to achieve significant gyroscopic gains in torque, i.e: $\bar{h}\mathbf{J}_h\dot{\bar{\psi}} >> \bar{g}\mathbf{J}_g\dot{\bar{\phi}}$, and thus it is not unreasonable to assume that the momentum contribution due to rotations of the gimbals has a negligible effect on the dynamics of the system. The expression in (4.4) is of the form:

$$\mathbf{G}\ddot{\bar{\phi}} - \mathbf{C}\dot{\bar{\phi}} = \tau_u \qquad (4.5)$$

where $\mathbf{C}$ fully describes the non-linear first order dynamics of a CMG cluster in a rigid body and $\mathbf{G}$ accounts for the inertia of the CMGs about the gimbal axes. The magnitude of τ_u varies with the robot's attitude and angular rate errors, and represents the torque required from the CMGs to guarantee the stability of the system. Since the structure of the control system in Fig. 2.4 only requires the control law to compute the required torque, a candidate for the control law can be formulated based directly on the expressions in (4.4) and (4.5):

$$\tau_u = Q^T(\mathbf{q})k_q\mathbf{e}_\mathbf{q} + [k_\omega \mathbf{e}_\omega - (\mathbf{J}_{tot} - \mathbf{J}_A)\dot{\omega}_d - \omega \times \mathbf{\Pi} - u \times \mathbf{P} + \tau_{drag}] \qquad (4.6)$$

From the initial analogy it is known that a control law of the form, $\tau_u = \tau_s + \tau_d$ is sought. The candidate control law satisfies this structure where the first term constitutes τ_s, which acts like a spring to bring the robot to the desired state, and the remaining bracketed terms constitute τ_d, which is a dissipative term to achieve smooth and continuous motion.

The closed-loop stability of the system's dynamics with this control law can be assessed by letting $\tau_u = \tau_{cmg}$ in the dynamic equation (3.12), which gives the following condition:

$$
\begin{aligned}
&(\mathbf{J}_{tot} + \mathbf{J}_A)\dot{\mathbf{e}}_\omega + k_\omega \mathbf{e}_\omega + Q^T(\mathbf{q}) k_q \mathbf{e}_\mathbf{q} \\
&+[(h_1 c_1^T + c_1 h_1^T)\omega \ \ \ldots \ \ (h_N c_N^T + c_N h_N^T)\omega](\mathbf{J}_c - \mathbf{J}_h)\dot{\bar{\phi}} = 0
\end{aligned}
\tag{4.7}
$$

This indicates that for the system to remain in stable equilibrium where $\mathbf{e}_\omega \equiv \dot{\mathbf{e}}_\omega \equiv 0$, it is possible to guarantee $\mathbf{e}_q \equiv 0$ by ensuring that $\dot{\bar{\phi}} = 0$; i.e. the CMGs do not produce any torque. This is in fact a trivial condition since any actuating effect at this point would drive the system away from its desired state. It can be shown that this condition is satisfied by the candidate control law since when the system is in equilibrium at the origin $[\mathbf{e}_q, \mathbf{e}_\omega] = [0, 0]$ the torque computed by the control law is zero and so the gimbals are stationary; i.e. $\dot{\bar{\phi}} = 0$. The conditions satisfied by the control law can be expressed in terms of La Salle's invariance principle where it is known from (4.3) that $R \to [\mathbf{e}_q, 0]$ and from (4.7) that $M \to [0, 0]$ is the largest invariant set in $[\mathbf{e}_q, 0]$, thus:

(La Salle's invariance principle) $[\mathbf{e}_q, 0]$ *is the set of all points where* $\dot{V}(\mathbf{e}_q, \mathbf{e}_\omega) = 0$, *and* $[0, 0]$ *is the largest invariant set in* $[\mathbf{e}_q, 0]$. *Therefore, all solutions globally asymptotically converge to* $[0, 0]$ *as* $t \to \infty$.

The above analysis shows that the control law (4.6), illustrated in Fig. 4.2, satisfies the conditions of La Salle's invariance principle to guarantee the global asymptotic stability of the system to the desired state. This control law computes the torques required to achieve the desired robot state, where the sensitivity is tuned by the attitude and angular rate gains k_q and k_ω. In contrast to all previous applications the control law developed in this research takes into account the effects of translation and the hydrodynamic interactions of the body as well as the coupled dynamics of the CMG and body system.

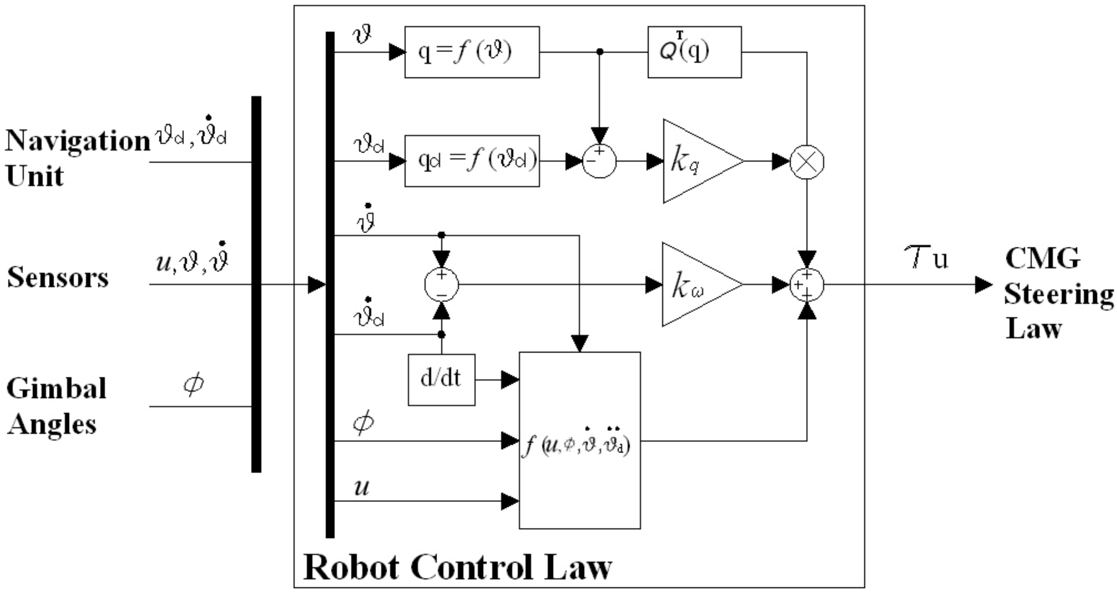

Figure 4.2: Attitude control law for a CMG actuated underwater robot

Chapter 5

Singularities and null motion

The greatest challenge in the application of single gimbal CMG systems is the inherent and serious problem of singular orientations. This chapter first defines the singularity problem and introduces the concept of null motion in redundant systems. This can be used to avoid singularities to some extent dependent of the degree of redundancy. The implications of singularities that are escapable and inescapable through null motion are discussed. A mathematical description of singularities and the corresponding singular angular momentum vectors is formulated. These form a smooth surface of singular vectors that can be visualised in the system's momentum workspace. Escapability is defined in terms of the differential geometry of the singular surface and its null motion. Finally, a method to distinguish between escapable and inescapable singularities is developed based on the Gaussian curvature of null motion.

5.1 Singularity problem

The singularity problem for single gimbal systems was first identified by NASA in 1972 [32]. A singularity occurs when the all the momentum vectors of the CMG system become coplanar. The system becomes unable to generate torque about the axis along this plane and this can results in a momentary loss of control authority. These singularities must be avoided in order to achieve smooth and continuous attitude control. The most basic CMG steering law makes the reasonable assumption that the momentum stored in the flywheels is large; i.e. $\mathbf{C} >> \mathbf{G}$ in (4.5). Thus the second order term in (4.4) becomes negligible and a particular solution for the desired torque can be computed by taking the pseudo-inverse of the $[N \times 3]$ Jacobian $\mathbf{C}$, to map the $[N \times 1]$ gimbal rate vector onto the $[3 \times 1]$ vector of desired torque:

$$\dot{\bar{\phi}}_\tau = -\mathbf{C}^T(\mathbf{C}\mathbf{C}^T)^{-1}\tau_u \tag{5.1}$$

This inverse steering solution uses the gyroscopic torque component of the CMGs to achieve the desired torque. However, the pseudo-inverse produces a minimum norm vector. This implies that once in its vicinity, a CMG unit will oscillate at an unreasonably high gimbal rate about the norm and become stuck in this direction. Although this has little effect on the torque generated, this behaviour encourages the formation of coplanar singular orientations.

5.2 Redundancy and null motion

The solution to the singularity problem lies in the system's null motion. Margulies [41] was the first to identify null motion and the possibility of singularity avoidance in redundant systems. Systems with more CMG units than controlled degrees of freedom have a dimensional redundancy that allows for motion of the gimbals by which all the momentum vectors exactly cancel and so no resultant torque is produced. This null motion can be used to avoid singular orientations to some extent. Whether complete singularity avoidance is possible depends on the degree of redundancy and how it is used. The linear combination of the inverse steering solution and null motion forms the general relationship that describes all possible CMG motions to exactly achieve a specific command torque.

$$\dot{\bar{\phi}}_d = \dot{\bar{\phi}}_\tau + k_{null}\dot{\bar{\phi}}_Z \tag{5.2}$$

This forms the basis of all singularity avoidance steering laws. However, difficulties arise from attempting to manipulate a cluster of single degree of freedom actuators to control motion about multiple axes. This limits the dimensions of null motion, which for three-axis control has an order of $N - 3$. It was first recognised by Tokar [45] that not all singularities can be avoided through null motion alone, and thus singularities can be classified as either:

- Escapable or
- Inescapable

Escapable singularities can be avoided through null motion without causing any undesired torque effects. However, inescapable singularities cannot be avoided through null motion alone and thus cannot be physically avoided without generating an error in torque. After the initial work of Margulies and Tokar, geometric studies by Paradiso [56] and Kurokawa [64] have formed a deeper understanding of the singularity problem and provide a useful tool for the analysis of potential solutions.

5.3 Geometric analysis of singularities

5.3.1 Singular surface

In a singular orientation the CMG angular momentum vectors are coplanar, thus the output torque has no component in the normal direction and no longer spans three-dimensional space. This implies that the transverse matrix $\bar{c}$ is not of full rank, and thus the following condition is satisfied:

$$\det(\bar{c}\bar{c}^T) = 0 \tag{5.3}$$

The degeneration of rank does not in general reduce to unity since this is only possible when all the gimbal axes lie on the same plane. Thus at a singularity the unit vector $\mathbf{u}$ in the singular direction, illustrated in Fig. 5.1, can be defined as follows:

$$\mathbf{u} = c_i \times c_j \qquad \text{where} \quad i \neq j$$

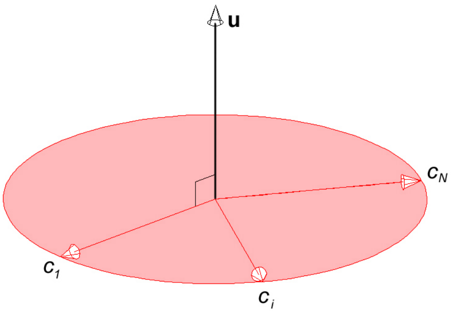

Figure 5.1: Singular direction vector

A singularity can be defined as any orientation that satisfies the following condition:

$$c_{Si}\mathbf{u} = 0 \qquad \text{where} \quad i = 1, 2, ..., N \tag{5.4}$$

For any given $\mathbf{u}$ there exist two possible singular angular momentum vectors h_{Si} and $-h_{Si}$, illustrated in Fig. 5.2, for each unit. The two cases can be distinguished by the following sign variable that represents the orientation of each unit with respect to the singular direction:

$$\epsilon_i = \frac{\mathbf{u}h_{Si}}{|\mathbf{u}h_{Si}|}$$

Thus each singular direction has a total of 2^N singular angular momentum vectors. These can be expressed in terms of the singular vector in the following manner [64]:

$$\bar{h}_S = \sum_{i=1}^{N} \epsilon_i \frac{(g_i \times \mathbf{u}) \times g_i}{|g_i \times \mathbf{u}|} \tag{5.5}$$

This equation represents a mapping from the singular orientations to a smooth and continuous surface of singular momentum vectors. The singular surface S_ϵ can be classified by the set of signs in ϵ, e.g. $(++-...+)$, into regions that correspond to different relative orientations of the units. If the direction of the units and the singular direction vector are reversed, i.e. $\epsilon \to -\epsilon$ and $\mathbf{u} \to -\mathbf{u}$, the angular momentum $\bar{h}_S$ remains the same and thus the surface regions S_ϵ and $S_{-\epsilon}$ are identical. Therefore, the system has a total of 2^{N-1} different singular regions that can be visualised in the momentum workspace of the system.

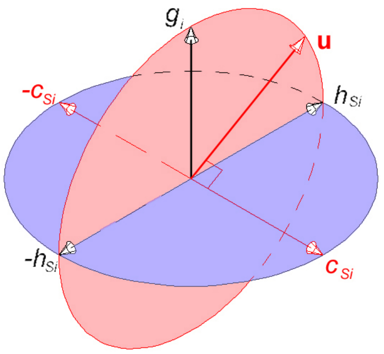

Figure 5.2: Singular angular momentums

5.3.2 Differential geometry and escapability

The discussion so far has demonstrated a method to plot the singular surface of a CMG system. However, this alone is not enough to determine the implications for CMG steering, which can only be achieved by distinguishing singularities that are escapable from those that are inescapable. This can be achieved by studying the effects of gimbal steering on the momentum of the singular system and examining the shape of its differential geometry [64].

The effects of infinitesimal changes in gimbal angle on the singular angular momentum vector can be determined by taking a second order Taylor series expansion in the immediate neighbourhood of the singular orientation $\bar{\phi}_S$:

$$\bar{h}(\bar{\phi}_S + d\bar{\phi}) = \bar{h}(\bar{\phi}_S) + \sum_{i=1}^{N} \frac{\partial \bar{h}}{\partial \phi_i} d\phi_i + \frac{1}{2} \sum_{i=1}^{N} \sum_{j=1}^{N} \frac{\partial^2 \bar{h}}{\partial \phi_i \phi_j} d\phi_i \phi_j + f(d\phi_i^3)$$

The change in angular momentum can be obtained:

$$\begin{aligned} \Delta \bar{h} &= \bar{h}(\bar{\phi}_S + d\bar{\phi}) - \bar{h}(\bar{\phi}_S) \\ &= \sum_{i=1}^{N} \frac{\partial \bar{h}}{\partial \phi_i} d\phi_i + \frac{1}{2} \sum_{i=1}^{N} \sum_{j=1}^{N} \frac{\partial^2 \bar{h}}{\partial \phi_i \phi_j} d\phi_i \phi_j \end{aligned}$$

where terms of third order and greater have been omitted. The first partial derivative is c_i by definition (3.1). At a singularity the following conditions are also satisfied:

$$\frac{\partial^2 \bar{h}}{\partial \phi_i \phi_j} = -h_i \quad \text{if } i = j \tag{5.6}$$

$$\frac{\partial^2 \bar{h}}{\partial \phi_i \phi_j} = 0 \quad \text{if } i \neq j \tag{5.7}$$

Therefore, the change in angular momentum can be expressed by the following quadratic:

$$\Delta \bar{h} = \sum_{i}^{N} c_i d\phi_i - \frac{1}{2} \sum_{i}^{N} h_i (d\phi_i)^2$$

By definition the first order term is orthogonal to $\mathbf{u}$ and so it follows that:

$$\begin{aligned} \Delta \bar{h} \mathbf{u} &= -\frac{1}{2} \mathbf{u} \sum_{i}^{N} h_i (d\phi_i)^2 \\ &= -\frac{1}{2} \sum_{i}^{N} \frac{(d\phi_i)^2}{p_i} \end{aligned} \tag{5.8}$$

The characteristics of the singularity can be examined by decomposing the quadratic into elements of its singular tangent bases. The singular element $d\bar{\phi}_S$ can be defined as the gimbal steering that maintains the singularity condition (5.4), and thus its derivative gives:

$$\frac{dc_{Si}}{d\phi_{Si}} \mathbf{u} + c_{Si} \frac{d\mathbf{u}}{d\phi_{Si}} = 0$$

From (5.6) it can be seen that $\frac{\partial c_{Si}}{\partial \phi_{Si}} = -h_{Si}$, thus the equation can be rearranged in the form:

$$c_{Si}\frac{d\mathbf{u}}{d\phi_{Si}} \;=\; h_{Si}\mathbf{u}$$

Since $p_i = \frac{1}{h_{Si}\mathbf{u}}$ the following expression for the singular element is obtained:

$$d\phi_{Si} = p_i c_{Si} d\mathbf{u} \tag{5.9}$$

The null element $d\bar{\phi}_Z$ can be defined as the gimbal steering that does not result in any change of the angular momentum vector. By rearranging the definition in (3.1), where the overall change in the angular momentum of the system $d\bar{h}$ is zero, the following expression for the null element is obtained:

$$\bar{c}d\bar{\phi}_Z = 0 \tag{5.10}$$

This expression forms the general definition of null motion. The change in gimbal angles can only be decomposed into components of $d\phi_{Zi}$ and $d\phi_{Si}$ if these elements are always orthogonal. This can be demonstrated using the definition in (5.9) as follows:

$$\begin{aligned}\sum_i^N d\phi_{Zi}d\phi_{Si} &= \sum_i^N d\phi_{Zi}(p_i c_{Si} d\mathbf{u}) \\ &= d\bar{\phi}_Z^T P \bar{c}^T d\mathbf{u} \\ &= (\bar{c}d\bar{\phi}_Z)^T P d\mathbf{u} \\ &= 0\end{aligned} \tag{5.11}$$

where in the final stage the condition in (5.10) has been used. In this derivation P is a $[N \times N]$ diagonal matrix with elements p_i. This result demonstrates that the elements $d\phi_{Zi}$ and $d\phi_{Si}$ are orthogonal.

The change in gimbal angle can be decomposed into the singular and null elements of its tangent subspace:

$$d\phi_i = d\phi_{Zi} + d\phi_{Si}$$

Based on this the angular momentum quadratic in (5.8) can be separated into components of its singular and null elements. The derivation continues, making use of the result in (5.11), as follows:

$$\begin{aligned}\Delta\bar{h}\mathbf{u} &= -\frac{1}{2}\sum_i^N \frac{(d\phi_{Zi} + d\phi_{Si})^2}{p_i} \\ &= -\frac{1}{2}\sum_i^N \frac{(d\phi_{Zi}^2 + d\phi_{Si}^2)}{p_i} \\ &= -\frac{1}{2}d\bar{\phi}_Z^T P^{-1} d\bar{\phi}_Z - \frac{1}{2}d\bar{\phi}_S^T P^{-1} d\bar{\phi}_S\end{aligned}$$

The two components of the quadratic are orthogonal and can be treated independently [64]:

$$\begin{aligned} Q_S &= -\frac{1}{2} d\bar{\phi}_S^T P^{-1} d\bar{\phi}_S \\ Q_Z &= -\frac{1}{2} d\bar{\phi}_Z^T P^{-1} d\bar{\phi}_Z \end{aligned} \tag{5.12}$$

The second order term Q_S represents the local curvature of the singular surface. Similarly, the second order term Q_Z represents the shape of the system's null motion that steers the gimbals away from the singular orientation. Since P^{-1} can be either positive or negative, but cannot be zero, the signature of Q_Z can only be either indefinite or definite. If Q_Z is of indefinite form, this implies that null motion is open ended, existing on both sides of the singularity as well as on the singularity itself. This means that the singularity is escapable through null motion alone since the gimbals can be steered away from the singularity without generating any undesired torque effects. If in contrast Q_Z is definite, this implies that null motion is closed, existing only on one side of the singularity. Furthermore, the system's null motion collapses into the singular point with no null motion at the singularity itself. Therefore, once in the vicinity of this kind of inescapable singularity, it cannot be crossed or avoided without generating undesired torque effects. Thus the signature of Q_Z defines whether the singularity can or cannot be avoided through null motion alone. This can be used to form the following condition that distinguishes the different types of singularity:

- Q_Z is indefinite - Escapable, or
- Q_Z is definite - Inescapable.

The quadratic and its derivative are continuous with respect to the gimbal angles and thus its signature is also continuous. This implies that the singularities form continuous escapable and inescapable areas over the singular surface.

5.3.3 Gaussian curvature and classification

Escapability has been defined based on the signature of Q_Z. However, it still remains to determine the signature to classify the escapable and inescapable singularities. This section develops a method to determine escapability that is more concise and direct than that presented in previous work [64]. The Gaussian curvature is an intrinsic property of any two-dimensional surface that provides useful insights into the shape of the surface in three-dimensional space. Its implications can be understood by considering the curve formed at the intersection of the surface with a flat plane that has an axis normal to the surface. As the plane rotates about the normal axis, the shape of the curve formed at the intersection with the surface changes and after a full rotation will have maximal and minimal extremes of curvature. These are known as the principal curvatures $[\kappa_1, \kappa_2]$ and their orientations are known as the principal planes. These are visualised in Fig. 5.3. Adopting the convention that outward curvature is positive, planes 1 and 2 contain the maximum and minimum principal curvatures respectively. The Gaussian curvature of the surface can be calculated by taking the product of the principal curvatures:

$$K = \kappa_1 \kappa_2$$

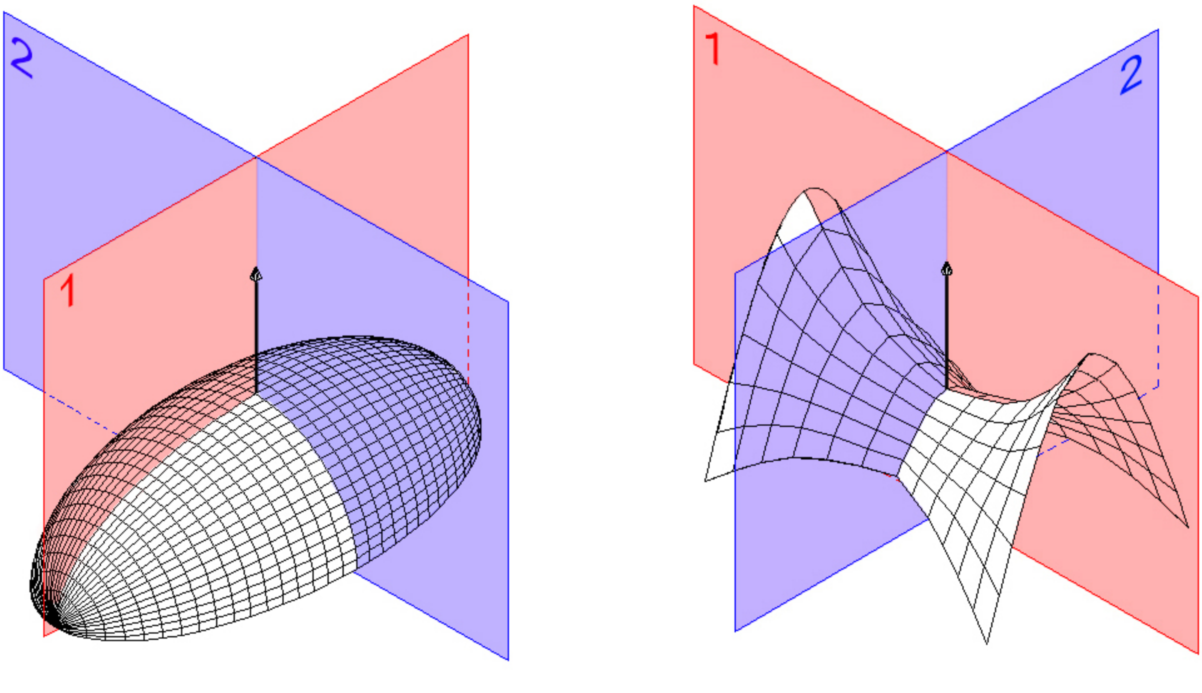

(a) Elliptic (b) Hyperbolic

Figure 5.3: CMG unit types

When applied to the null motion of a CMG system, the sign of the Gaussian curvature K indicates the shape of null motion and thus the signature of Q_Z can be determined. If K is positive the principal curvatures have the same sign and so the shape of null motion must be elliptic (Fig. 5.3(a)), terminating at the singular point. This form of null motion indicates that the signature of Q_Z is definite. If K is negative the principal curvatures have different signs and so the shape of null motion must be hyperbolic (Fig. 5.3(b)), bifurcating at the singular point. This form of null motion indicates that the signature of Q_Z is indefinite.

The Gaussian curvature of null motion can be determined by first defining the null element $d\bar{\phi}_Z$ of the tangent subspace in terms of any two independent torque vectors, for example c_{S1} and c_{S2}, of the singular system. In order to derive the basis of the null subspace, the following general expression for four arbitrary vectors in three-dimensional space is noted:

$$a[b\ c\ d] - b[c\ d\ a] + c[d\ a\ b] - d[a\ b\ c] = 0$$

It is also useful to observe the following vector relations for triple scalar products:

$$[a\ b\ c] = [b\ c\ a] = [c\ a\ b] = [a\ c\ b] = [b\ a\ c] = [c\ b\ a]$$

Substituting the vectors of the singular system c_{S1},c_{S2},c_{Si},$\mathbf{u}$ into the first relation gives:

$$c_{S1}[c_{S2}\ c_{Si}\ \mathbf{u}] - c_{S2}[c_{Si}\ \mathbf{u}\ c_{S1}] + c_{Si}[\mathbf{u}\ c_{S1}\ c_{S2}] - \mathbf{u}[c_{S1}\ c_{S2}\ c_{Si}] = 0 \quad \textit{where} \quad i = 3, ..., N$$

Since the vectors c_{S1}, c_{S2} and c_{Si} lie on the same plane the final term becomes zero. Using this result, together with the second vector relation, gives the following condition:

$$c_{S1}[c_{S2}\ c_{Si}\ \mathbf{u}] + c_{S2}[c_{Si}\ c_{S1}\mathbf{u}] + c_{Si}[c_{S1}\ c_{S2}\ \mathbf{u}] = 0$$

Defining the notation $n_{i,j} = [c_{Si}\ c_{Sj}\ \mathbf{u}]$ this condition can be expressed as:

$$n_{2,i}c_{S1} + n_{i,1}c_{S2} + n_{1,2}c_{Si} = 0$$

This forms a candidate for the basis of the null subspace that satisfies the condition for null motion (5.10). For a system of N units, the null subspace has an order of $N-2$ and the null elements can be expressed in terms of the candidate basis:

$$\begin{aligned} d\bar{\phi}_Z &= z_1 e_{Z1} + z_2 e_{Z2} + ... + z_{(N-2)} e_{ZN-2} \\ &= E_Z \bar{z} \end{aligned}$$

where $\bar{z}$ is a $[(N-2)\times 1]$ vector and E_Z is the $[N \times (N-2)]$ null subspace matrix. This can be expressed in component form as:

$$E_Z = \begin{bmatrix} e_{Z1} \\ e_{Z2} \\ \vdots \\ e_{Z(N-2)} \end{bmatrix} = \begin{bmatrix} n_{2,3} & n_{3,1} & n_{1,2} & 0 & \cdots & 0 \\ n_{2,4} & n_{4,1} & 0 & n_{1,2} & \cdots & 0 \\ \cdot & \cdot & \cdots & \cdot & & \\ n_{2,(N-2)} & n_{(N-2),1} & 0 & 0 & \cdots & n_{1,2} \end{bmatrix}$$

Substituting the basis into the expression for Q_Z in (5.12) gives:

$$Q_Z = -\frac{1}{2}\bar{z}^T E_Z^T P^{-1} E_Z \bar{z}$$

The signature of Q_Z is independent of the variable $\bar{z}$ and so is defined by the matrix:

$$A_Z = E_Z^T P^{-1} E_Z$$

where A_Z is a $[N \times N]$ matrix with maximum and minimum eigenvalues that represent the principal curvatures $[\kappa_1, \kappa_2]$. Thus the Gaussian curvature of null motion can be determined for all singular orientations as follows:

$$K = \kappa_1\kappa_2 = \max[\mathrm{Eig}(A_Z)]\min[\mathrm{Eig}(A_Z)] \tag{5.13}$$

This term does not vanish as P^{-1} cannot be zero. Therefore, every singular orientation can be classified based on the following condition:

- if $K < 0$ the singularity is escapable, else
- if $K > 0$ the singularity is inescapable.

This chapter has clarified the singularity problem and presented a method to geometrically represent the singular surface in the momentum space. A method to determine the Gaussian curvature of null motion has been developed to provide the geometric tools necessary to distinguish the escapable and inescapable singularities of any CMG system.

Chapter 6

Steering of a CMG pyramid

It is widely recognised that only systems with six or more CMG units have enough redundancy to solve the singularity problem. However, increased redundancy comes at the cost of the size and complexity of the system and so is impractical for underwater applications where strict dimensional, mass and computational restrictions apply. Conversely, a system of three-units has no redundancy and so its singular orientations cannot be avoided. Therefore, a method to guarantee singularity avoidance in a system of minimal redundancy, specifically the CMG pyramid, is sought. This chapter formulates a mathematical description for the dynamics of a CMG pyramid and its null motion. The mathematical tools developed in the previous chapter are applied to perform a comprehensive geometric study of the singularities of a CMG pyramid and assess their implications for attitude control. Different approaches to singularity avoidance are reviewed in the context of this application. The results of this analysis and global considerations of the inverse kinematics of attitude control form the basis of an exact and real-time steering law that is suitable for application to AUVs.

6.1 System definition

The CMG pyramid (Fig. 6.1) is a non-parallel type CMG system that consists of four units arranged symmetrically about its centre. The gimbal axis of each unit lies normal to the surface of a pyramid with a skew angle of β.

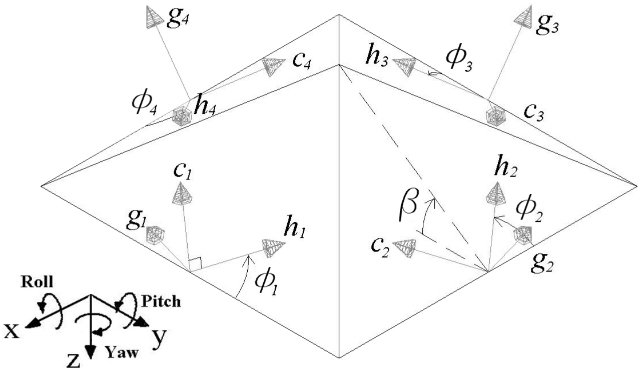

Figure 6.1: Four unit CMG pyramid

Adopting the convention that the gimbal angles are positive clockwise about the outward facing gimbal axes, the orientation of each unit can be defined by the gimbal angle matrix $\bar{\phi} = [\phi_1, \phi_2, \phi_3, \phi_4]^T$. Using the notation $s^* = \sin\beta$ and $c^* = \cos\beta$, the column vectors of the gimbal, momentum and torque matrices $\bar{g}$, $\bar{h}$ and $\bar{c}$ can be defined:

$$
\begin{aligned}
g_1 &= \begin{bmatrix} c^* \\ 0 \\ -s^* \end{bmatrix}, \quad g_2 = \begin{bmatrix} 0 \\ c^* \\ -s^* \end{bmatrix}, \quad g_3 = \begin{bmatrix} -c^* \\ 0 \\ -s^* \end{bmatrix}, \quad g_4 = \begin{bmatrix} 0 \\ -c^* \\ -s^* \end{bmatrix} \\
h_1 &= \begin{bmatrix} -c^*\sin\phi_1 \\ \cos\phi_1 \\ -s^*\sin\phi_1 \end{bmatrix}, \quad h_2 = \begin{bmatrix} -\cos\phi_2 \\ -c^*\sin\phi_2 \\ -s^*\sin\phi_2 \end{bmatrix}, \quad h_3 = \begin{bmatrix} c^*\sin\phi_3 \\ -\cos\phi_3 \\ -s^*\sin\phi_3 \end{bmatrix}, \quad h_4 = \begin{bmatrix} \cos\phi_4 \\ c^*\sin\phi_4 \\ -s^*\sin\phi_4 \end{bmatrix} \\
c_1 &= \begin{bmatrix} -c^*\cos\phi_1 \\ -\sin\phi_1 \\ -s^*\cos\phi_1 \end{bmatrix}, \quad c_2 = \begin{bmatrix} \sin\phi_2 \\ -c^*\cos\phi_2 \\ -s^*\cos\phi_2 \end{bmatrix}, \quad c_3 = \begin{bmatrix} c^*\cos\phi_3 \\ \sin\phi_3 \\ -s^*\cos\phi_3 \end{bmatrix}, \quad c_4 = \begin{bmatrix} -\sin\phi_4 \\ c^*\cos\phi_4 \\ -s^*\cos\phi_4 \end{bmatrix}
\end{aligned}
\tag{6.1}
$$

The system's null motion is defined by (5.10), which implies that the null motion $\dot{\bar{\phi}}_Z$ is orthogonal to the torque matrix $\bar{c}$. Since the non-singular columns of $\bar{c}$ span three-dimensional space, the null motion of the four unit system is only one-dimensional. This can be computed for each unit by taking the scalar triple product of the remaining torque vectors [41]:

$$
\dot{\bar{\phi}}_Z = [[c_2\ c_3\ c_4], -[c_3\ c_4\ c_1], [c_4\ c_1\ c_2], -[c_1\ c_2\ c_3]]^T \tag{6.2}
$$

6.2 Singularities of a CMG pyramid

6.2.1 Geometric analysis

A detailed geometric analysis of the singularities of a CMG pyramid is carried out using the mathematical tools developed in the previous chapter. Figs. 6.2-6.8 are generated by mapping a polar lattice of singular orientations to their corresponding angular momentum vectors using (5.5). The escapable and inescapable areas are distinguished using (5.13). The transformation is highly non-linear and results in complex shapes that are far from spherical, this can be seen in the exploded view of the complete singular surface in Fig. 6.8. Since the lattice of singular orientations used in the calculation is finite, it was not possible to create a continuous sheet of singularities and so these figures must be mentally interpolated to imagine their true structure. Despite the limitations in their representation the figures provide an accurate description of the singular surface, allowing for a deeper understanding of their implications for attitude control.

The singular surface is plotted for a skew angle of $\beta = \cos^{-1} 1/\sqrt{3}$, which has a near spherical momentum envelope and so equal control authority about all three rotational degrees. The escapable and inescapable areas are plotted in red and black respectively. For clarity of presentation the inescapable areas are plotted alongside the complete singular surface regions where appropriate. The system has a total of eight singular regions that are classified according to the number of reversed units [56].

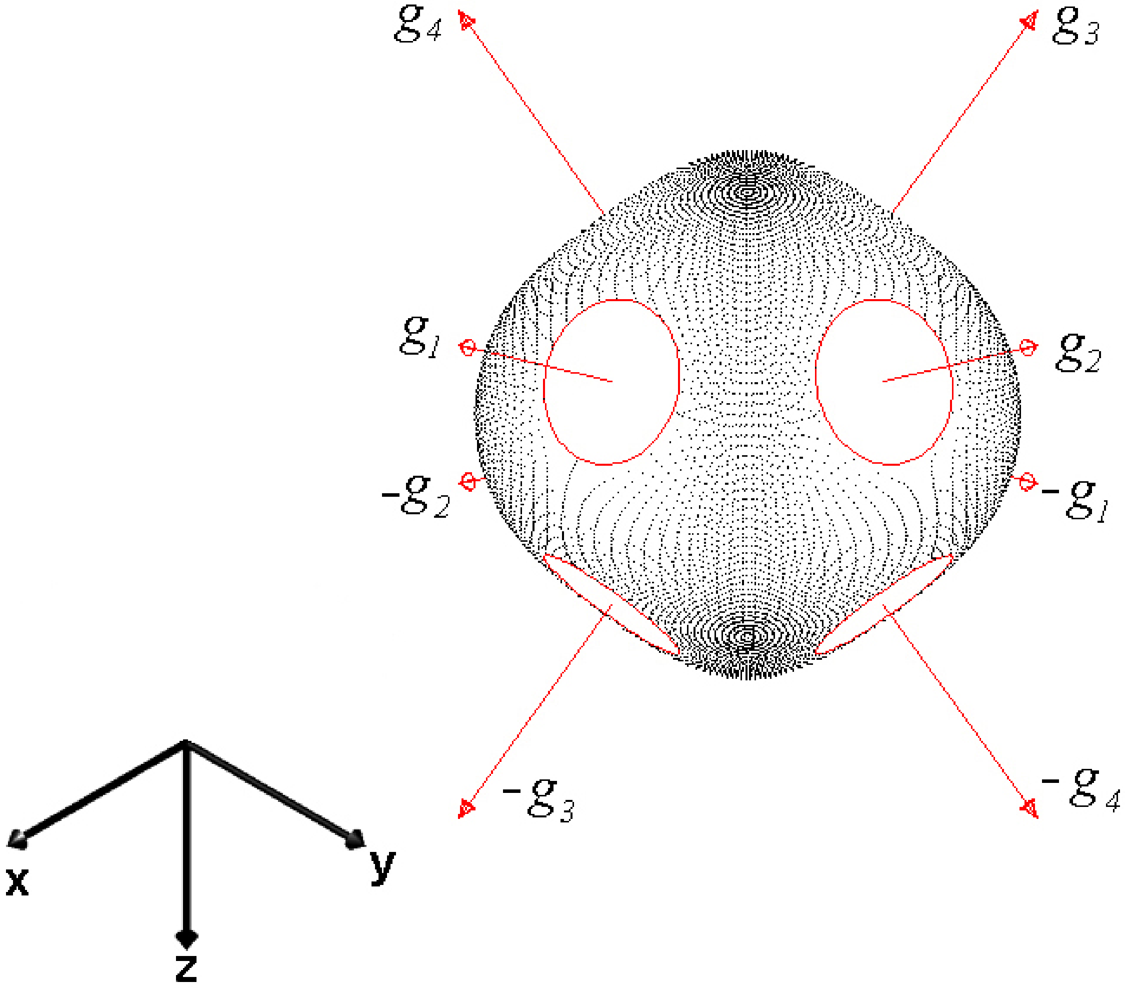

Figure 6.2: Isometric view of S_{++++}

No reversed units

The surface region S_{++++}, shown in Fig. 6.2, is formed when the momentum vectors of each unit project positively onto the singular direction and so represents a relatively straightforward mapping that forms a spherical envelope. This external singular region is trivially inescapable as it represents the maximum amplitude of the momentum stored in the system, forming the boundary of the momentum workspace. As the momentum vectors rotate about each gimbal axis, the singular vectors form a unit circle about $\mathbf{u} = \pm g_i$. These form a total of eight unit circles that appear as holes in the singular surface region. This is a general characteristic of all singular regions, each having 2^N edges that form holes in their surface. These indicate where each region reaches the boundary of its definition as the signature ϵ_i of one of the unit's momentum vectors flips and changes direction. This is most easily recognised in this external region because of its simple structure.

One reversed unit

Regions with one negative ϵ_i form the outer singular zone. This zone is composed of the four regions S_{-+++}, S_{+-++}, S_{++-+} and S_{+++-} that can be mapped onto each other by a series of 90° rotations about the z-axis. Fig. 6.3 shows a xz-plane view of the region S_{-+++}.

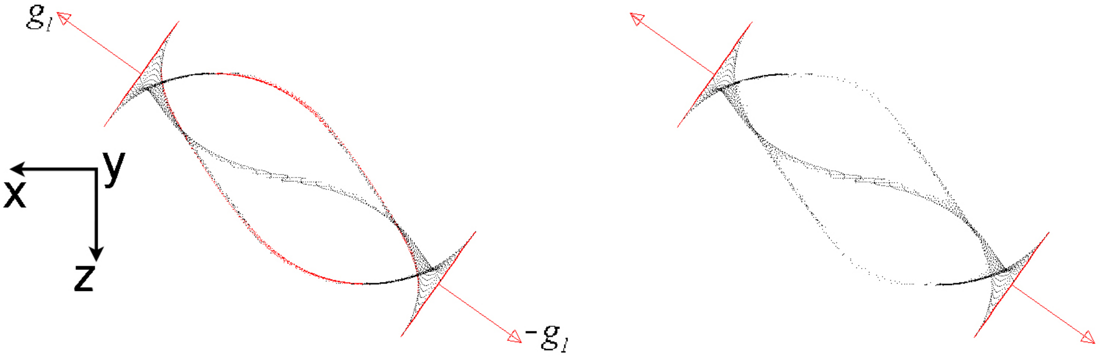

Figure 6.3: xz-plane view of S_{-+++} with inescapable singularities duplicated on right

As the singular direction approaches one of the gimbal axes, the momentum vector of the corresponding parallel unit is almost orthogonal to the singular direction. Therefore, it has a small contribution that reduces to zero when the singular direction is aligned with the gimbal axis. As this happens the opposing unit, which has its gimbal axis normal to the singular direction, must compensate for the near normal momentum vector and this reduces the overall momentum capacity of the system. Therefore, the singular region obtained is relatively small in size and is far from spherical. The characteristics of this region are somewhat difficult to discern due to its highly complex shape. However, close inspection reveals that each region forms a petal aligned with the reversed gimbal axis. The base of each petal develops into three thin strips that twist along the gimbal axes to form a symmetrical petal at the opposing end. These petals fill the holes in S_{++++} (Fig. 6.2) and form part of the external envelope. It can be seen that the inescapable areas penetrate some way into the momentum workspace. Fig. 6.4 shows an xz-plane view of S_{-+++} and S_{++-+}. The strips of these regions and those of S_{+-++} and S_{+++-} intersect at six regularly spaced nodes about the momentum origin, four of which are on the vertices of a square in the xy-plane and the other two are located symmetrically along the z-axis to form the corners of a regular octahedron.

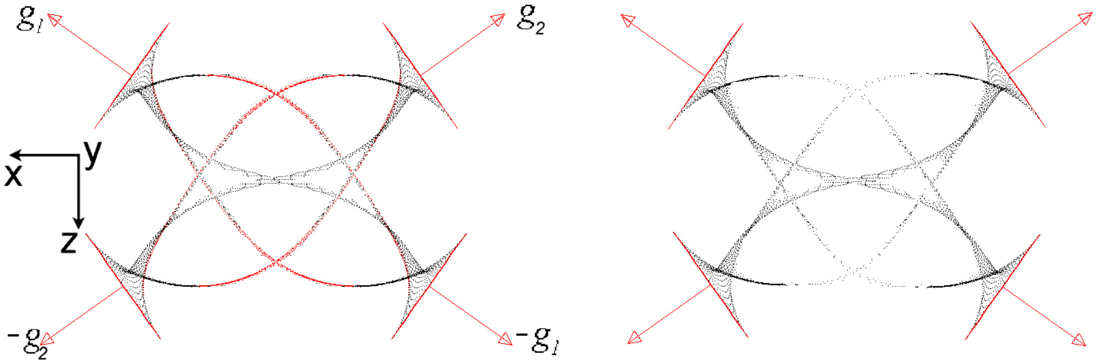

Figure 6.4: xz-plane view of S_{-+++} and S_{++-+}

Two reversed units

Regions with two negative ϵ_i form the inner singular zone. At these singular regions, components of the momentum vectors of all four units cancel and this greatly limits the overall momentum capacity. The regions obtained form the smallest part of the singular surface that fits within the outer singular zone and has no part in contact with the external envelope. These regions have complex shapes that have several inflections, however, their overall form is closer to a sphere than the outer singular zone.

There are two types of region in this zone. Fig. 6.5 shows the regions S_{--++} and S_{+--+} that are formed when adjacent units are reversed. These regions form a complex ridged shape. The ridges join the strips of the outer singular zone (Fig. 6.4). It can be seen that this shape has considerable inescapable areas that are heavily concentrated along the xy-plane.

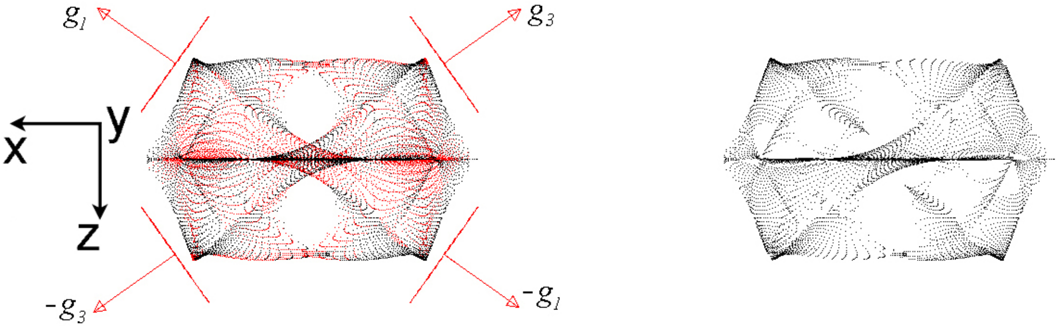

Figure 6.5: xz-plane view of S_{--++} and S_{+--+}

The region S_{-+-+} formed by reversing opposite units is shown in Fig. 6.6. Again this shape has several ridges that join the strips of the outer singular zone (Fig. 6.4). This region has the smallest momentum capacity in the z-direction as the components of all units cancel. However, this region is mostly escapable, only becoming inescapable towards its extremities.

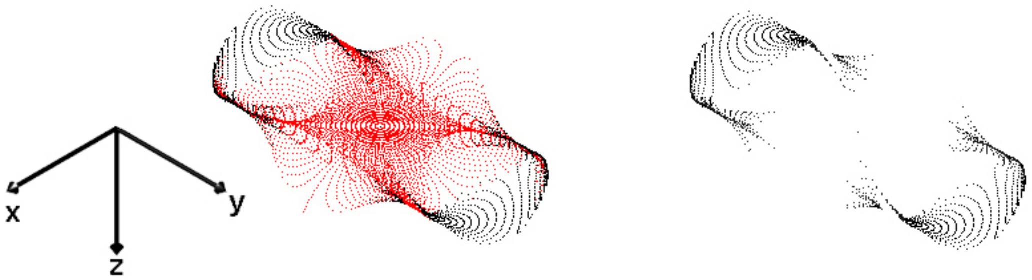

Figure 6.6: Isometric view of S_{-+-+}

Continuous Surface

Each singular region has eight holes that form the boundary of its definition where the sign ϵ_i of one of the units changes and the surfaces becomes part of a different region. Each boundary is shared by two regions and this implies that all the regions must fit together to form a smooth and continuous singular surface of closed form. The manner in which the different regions join together is illustrated in Fig. 6.7 that shows an xz-section of the singular surface as different regions are added. It can be seen that the outer zone fills in the holes in the external envelope and that the inner zone patches the void spaces left by the strips of the outer zone. This figure reveals that the central inescapable parts visible in the xz-plane of S_{-+++} and S_{++-+} in Fig. 6.4 are located in the extreme $\pm y$ directions of the momentum envelope as they are not visible in the xz-section in Fig 6.7(b). This also indicates that the octahedron formed by the intersecting singular regions described previously is oriented in the same manner as the pyramid in (Fig. 6.1) mirrored about its base.

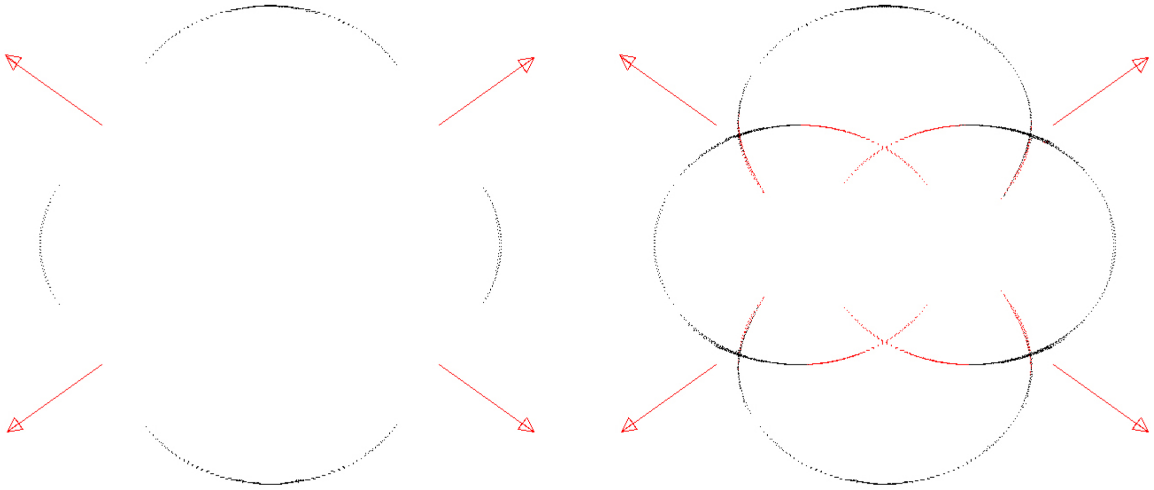

(a) Envelope S_{++++} (b) Outer regions S_{-+++} and S_{++-+}

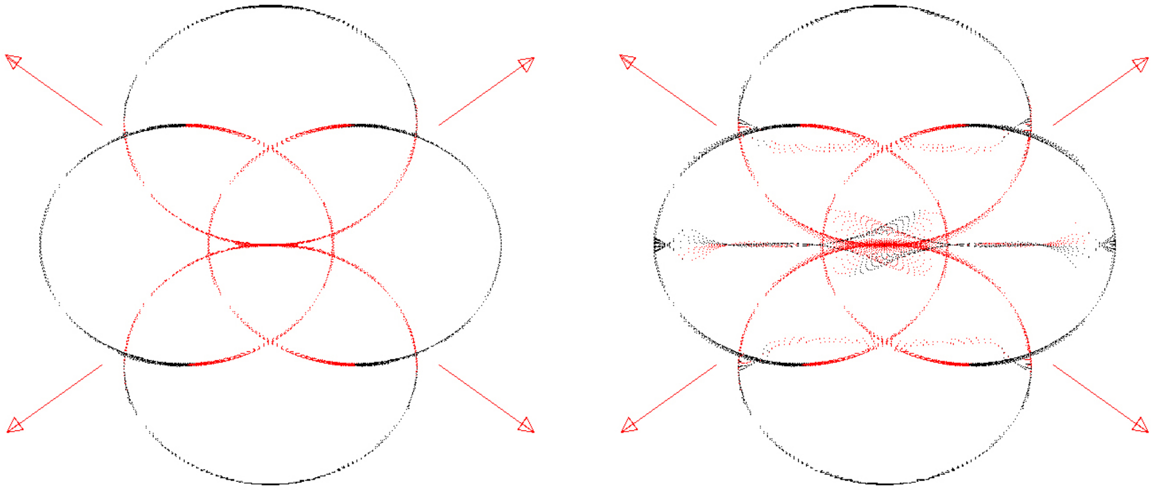

(c) Inner region S_{-+-+} (d) Complete surface

Figure 6.7: xz-sections of the continuous singular surface

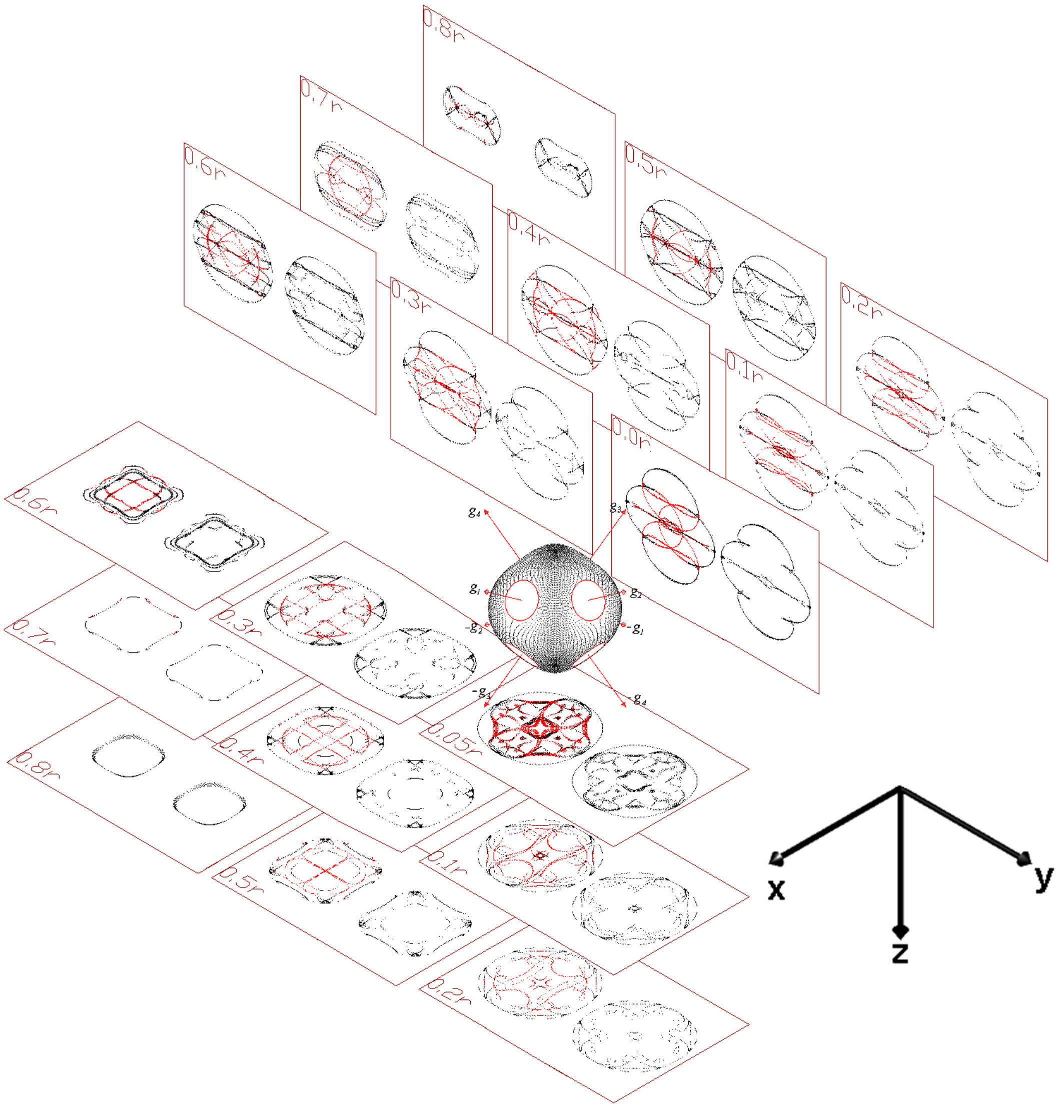

Figure 6.8: Exploded view of the complete singular surface

6.2.2 Implications for attitude control

The analysis has shown that the minimally redundant system contains inescapable singularities through which no steering law can remain exact. Fig. 6.8 is an exploded view of the complete singular surface of a minimally redundant CMG pyramid. Various cross sections of this surface are projected in the x and z directions. This illustrates how the singular regions join to form a smooth and continuous surface of singular momentum vectors. Although there exists large volumes with no singularities, the system contains locally inescapable singular areas. These are distributed in a complex manner and cannot be easily overcome by real-time steering and momentum management algorithms. The inescapable areas of the outer singular zone and those of S_{-+-+} are located near the envelope of the system and so do not have a significant detrimental effect on attitude control. However, the inescapable areas of S_{--++} and S_{+--+} enclose the origin with a significant concentration on the xy-plane. This has serious implications for attitude control, in particular degrading control about the roll and pitch axes.

6.3 Singularity avoidance

The pyramid configuration is convenient for attitude control as its symmetrical nature allows for independent actuation about all three rotational axes. Furthermore, its compact size and mechanical simplicity make it suitable for underwater applications. However, the minimal redundancy of the system poses significant challenges for singularity avoidance. The likelihood of encountering singularities is magnified as sustained torques are required to overcome the viscous resistance of the fluid. This section discusses specific singularity avoidance algorithms while the next section considers their suitability for underwater applications.

Escapable singularities can be avoided using a steering law of the form (5.2), where the assignment of null motion is regulated using the gain variable k_{null}. This is typically achieved using the gradient method, which maximises an objective function W of the gimbal angles that is zero at a singularity and otherwise positive. This can be achieved by selecting the variables of k_{null} to keep the derivative of the function positive:

$$k_{null} = f\left(\frac{\partial W}{\partial \phi}\right)$$

The following candidate function was proposed in [36] and successfully applied to double gimbal systems:

$$W = \sqrt{\det(\mathbf{C}\mathbf{C}^T)}$$

Various other gradient functions have also been proposed [46, 49, 50]:

$$\begin{aligned} W &= \min\left(\frac{1}{|\mathbf{d}_i|}\right) \\ W &= \min(s_i) \\ W &= \sum_j^N \sum_i^N |c_i \times c_j|^2 \end{aligned}$$

where $\mathbf{d}_i$ is a row vector of the pseudo-inverse function in (5.1) and s_i is the singular value of the Jacobian $\mathbf{C}$. However, whilst gradient methods can effectively assign null motion to pass escapable singularities, they cannot avoid inescapable singularities where no null motion exists and so encounter considerable difficulties in single gimbal systems of limited redundancy [45].

The singularity problem applies to any system with limited redundancy that aims to perform exact and real-time steering. In this context, exactness implies that the steering law generates an output that is equal to the commanded torque. A strictly real-time steering law does not rely on knowledge of future instructions when generating its steering command. There are three methods to overcome this problem:

- relax the exactness condition,
- relax the real-time condition or
- restrict the workspace.

6.3.1 Relaxed exactness

One approach towards singularity avoidance is to relax the exactness constraint and permit local errors in order to pass singular areas. This can be achieved by modifying the steering law (5.1) to enable calculation of the inverse Jacobian even at a singular point. A general solution to restrict the output torque error to singular areas can be obtained [41]:

$$\dot{\phi}_\tau = -\mathbf{C}^T(\mathbf{C}\mathbf{C}^T + k\mathbf{u}^T\mathbf{u})^{-1}\tau_u$$

This maintains an exact solution when the command τ_u is normal to the singular direction $\mathbf{u}$ and minimises the error elsewhere as its output is equal to the projection of the commanded torque onto the plane normal to the singular direction.

An extension of this concept is the SR method, originally developed for robot manipulators [72], and applied to CMGs in [59] and later in [60]:

$$\dot{\phi}_\tau = -\mathbf{C}^T(\mathbf{C}\mathbf{C}^T + a\mathbf{I})^{-1}\tau_u$$

where $a = a_0 e^{-\det(\mathbf{C}\mathbf{C}^T)}$. Therefore, the output error increases rapidly as a singularity is approached and is negligible elsewhere. This allows any singular orientation to be avoided.

The SDA method of Ford [61] is an extension of the SR method that uses singular value decomposition to further minimise the output torque errors. The Jacobian $\mathbf{C}$ is decomposed into a diagonal matrix of its singular values $\mathbf{S}$ by the unitary matrices $\mathbf{U}$ and $\mathbf{V}$:

$$\mathbf{S} = \mathbf{UCV} = \begin{bmatrix} s_1 & 0 & 0 & 0 & \dots & 0 \\ 0 & s_2 & 0 & 0 & \dots & 0 \\ 0 & 0 & s_3 & 0 & \dots & 0 \end{bmatrix} \quad \textit{where} \quad s_1 > s_2 > s_3$$

These singular values represent the maximum input to output ratios of $\mathbf{C}$, which forms an ellipse in three-dimensional space. At a singularity, the outputs no longer span three-dimensional space with the rank of $\mathbf{C}$ reducing to two as s_3 becomes zero. Therefore, singularities can be avoided by preventing $s_3 = 0$. However, the SR method modifies all three singular values:

$$\mathbf{S}_{SR} = \begin{bmatrix} \frac{s_1}{s_1+a} & 0 & 0 & 0 & \dots & 0 \\ 0 & \frac{s_2}{s_2+a} & 0 & 0 & \dots & 0 \\ 0 & 0 & \frac{s_3}{s_3+a} & 0 & \dots & 0 \end{bmatrix}$$

whereas the SDA method modifies only the critical singular value:

$$\mathbf{S}_{SDA} = \begin{bmatrix} s_1 & 0 & 0 & 0 & \dots & 0 \\ 0 & s_2 & 0 & 0 & \dots & 0 \\ 0 & 0 & \frac{s_3}{s_3+a} & 0 & \dots & 0 \end{bmatrix}$$

where $a = a_0 e^{-k_\sigma \sigma_3^2}$ and σ_3 is a normalised function of s_3. This results in less modification of the Jacobian $\mathbf{C}$ and thus smaller errors in the output torque. However, these methods do not explicitly distinguish escapable and inescapable singularities and so produce an error in the output even where an exact solution is possible.

6.3.2 Relaxed time constraint

The null motion in the vicinity of an escapable singularity is hyperbolic and so bifurcates into two seperate paths at the singular point. In some cases one of these path leads to an inescapable singularity during the remainder of the manoeuvre, whereas the other does not [64]. Therefore, even though escapability is defined locally, local singularity avoidance algorithms can encounter inescapable singularities that could have been avoided in the first place had some global approach been used [54]. However, unless future commands are known, there is no method of knowing which of the paths to select. One solution is to relax the real-time constraint and allow knowledge of future instructions to be used when generating the steering command.

In Vadali [55], a set of preferred gimbal angles are prepared based on the direction of the manoeuvre to be performed. Before each manoeuvre, the gimbals are adjusted from the origin to the preferred gimbal angles in order to maximise the momentum available before the system encounters an inescapable singularity. However, this method relies on the assumption that at the end of each manoeuvre the CMG angular momentum vector returns to the origin. This implies that this approach is not general and is not robust when subject to disturbance.

In Paradiso [56], a stronger assumption is made and this concept is extended to select predetermined gimbal paths. These paths to avoid inescapable singularities are computed off-line before the mission. This approach assumes that a particular steering command will result in a unique attitude response and so relies on the assumption that there are no disturbances present. Furthermore, this approach requires all the manoeuvres that will be performed during the mission to be foreseen and planned in advance.

6.3.3 Restricted workspace

This approach allows for both exact and real-time steering by excluding inescapable singularities from the momentum workspace. However, any reduction in the workspace reduces the torque available for control and so it is necessary to determine the largest continuous workspace that contains no inescapable singularities. It can be seen from Fig. 6.8 that simply excluding all inescapable singularities from the workspace would only leave a small fraction of the momentum available for use. This would result in an unacceptably inefficient use of the system and is too severe a restriction.

Kurokawa [62,64] developed a method to avoid problems with singularities by globally restricting the momentum workspace. Instead of allowing the CMGs to steer freely, some rules of steering were developed to eliminate as many inescapable singularities as possible whilst keeping the largest viable volume of the workspace intact. After an extensive geometric analysis, it was concluded that a suitable workspace could be achieved by algebraically restricting gimbal steering by one degree of freedom. This method guarantees that the inversion from the system's momentum $\bar{h}$ to its gimbal angles $\bar{\phi}$ is unique and continuous within some range of the constrained system, which determines the size and shape of the restricted workspace.

6.4 Exact and real-time steering

The behaviour of an AUV cannot be foreseen since they operate in an unknown environment using sensors to react to their surroundings. A steering law for application to AUVs must be strictly real-time and remain exact to the command, as any error in actuation may endanger the safety of the robot. Therefore, a method to exclude all inescapable singularities from the momentum workspace is sought. An appropriate restriction on gimbal steering is developed based on global considerations of the inverse kinematics of attitude control.

6.4.1 Inverse kinematics and workspace restriction

The gyroscopic torque of the CMGs corresponds to the velocity of the angular momentum vector in the three-dimensional momentum space and is generated about the path taken. If the nominal state is defined at the momentum origin, where all gimbal angles are zero, attitude control can be achieved by moving the momentum vector along a path parallel to its principal axes using the following steering commands:

$$\sigma = \begin{bmatrix} \sigma \\ 0 \\ -\sigma \\ 0 \end{bmatrix}, \gamma = \begin{bmatrix} 0 \\ \gamma \\ 0 \\ -\gamma \end{bmatrix}, \alpha = \begin{bmatrix} \alpha \\ \alpha \\ \alpha \\ \alpha \end{bmatrix}$$

where the corresponding motion of the momentum vector is illustrated in Fig. 6.9. The steering parameters σ, γ, and α independently govern roll, pitch and yaw.

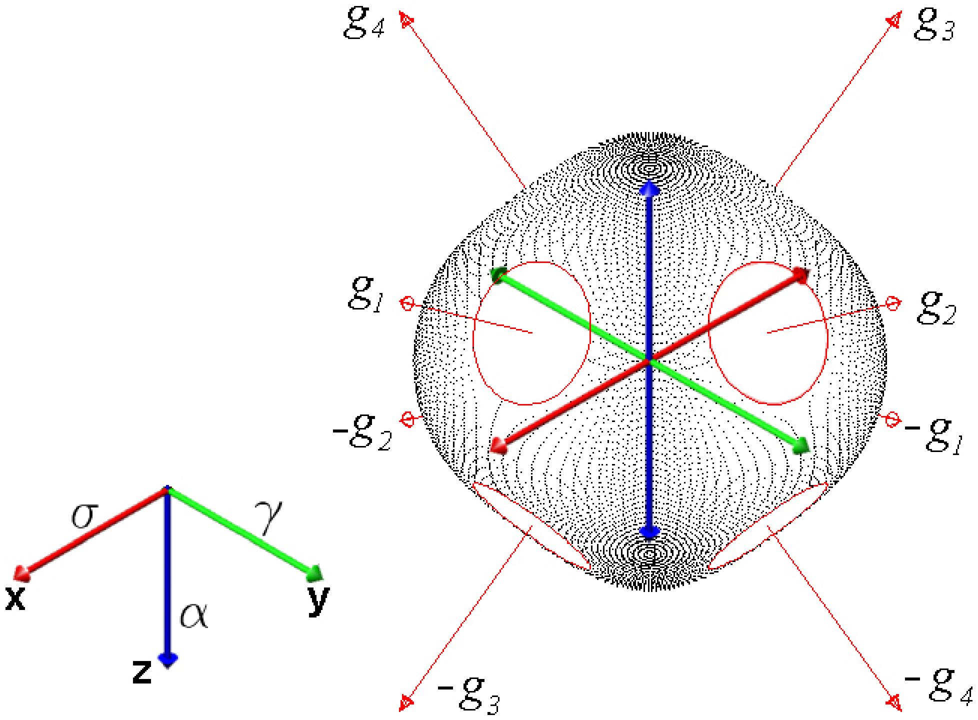

Figure 6.9: Inverse kinematics of attitude control from the nominal state

These three steering parameters can be used to couple the motion of the four independent CMG units:

$$\bar{\phi} = [\alpha + \sigma, \alpha + \gamma, \alpha - \sigma, \alpha - \gamma]^T \tag{6.3}$$

This algebraically constrains gimbal motion by one degree of freedom and imposes the restraining condition:

$$\phi_1 - \phi_2 + \phi_3 - \phi_4 = 0 \tag{6.4}$$

This eliminates many of the singular regions discussed previously, greatly simplifying the kinematics of the system and globally restricting the workspace in a manner that is ideal for attitude control. Substituting (6.3) into the expression for $\bar{h}$ defined in (6.1) gives the constrained angular momentum vector $\bar{h}^*$. Taking the sum of each component gives the following analytical solution for the normalised momentum of the constrained workspace:

$$\begin{aligned} H = \Sigma_i^N h_i^* &= \begin{bmatrix} -c^* \sin(\alpha + \sigma) - \cos(\alpha + \gamma) + c^* \sin(\alpha - \sigma) + \cos(\alpha - \gamma) \\ \cos(\alpha + \sigma) - c^* \sin(\alpha + \gamma) - \cos(\alpha - \sigma) + c^* \sin(\alpha - \gamma) \\ -s^* \sin(\alpha + \sigma) - s^* \sin(\alpha + \gamma) - s^* \sin(\alpha - \sigma) - s^* \sin(\alpha - \gamma) \end{bmatrix} \\ &= 2 \begin{bmatrix} -c^* \cos\alpha \sin\sigma + \sin\alpha \sin\gamma \\ -\sin\alpha \sin\sigma - c^* \cos\alpha \sin\gamma \\ -s^* \sin\alpha(\cos\sigma + \cos\gamma) \end{bmatrix} \end{aligned} \tag{6.5}$$

Fig. 6.10 shows xy-sections of the restricted workspace at various points along the z-axis.

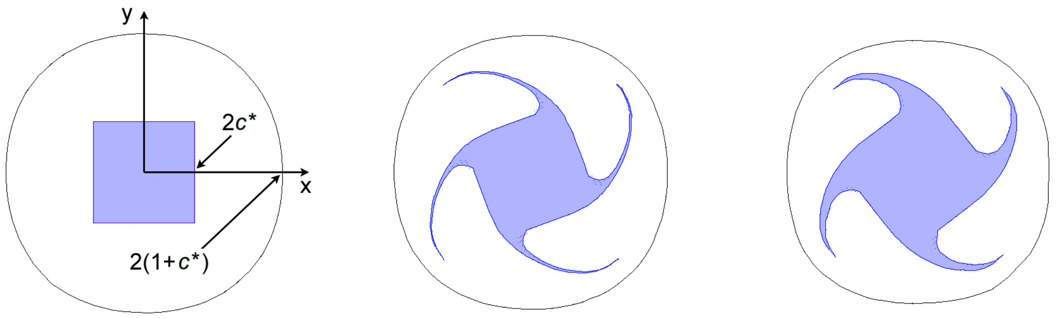

(a) $H_z = 0$ (b) $H_z = 0.1H_{zmax}$ (c) $H_z = 0.2H_{zmax}$

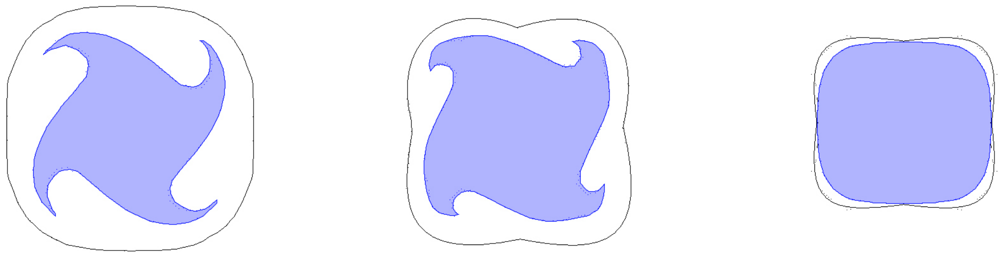

(d) $H_z = 0.3H_{zmax}$ (e) $H_z = 0.4H_{zmax}$ (f) $H_z = 0.6H_{zmax}$

Figure 6.10: xy-sections of the constrained (shaded) and unconstrained (outlined) workspace

The constrained workspace is shown in relation to the envelope of the unrestricted system that is outlined in each cross section. The momentum envelope maintains its original dimension in the z-direction and has at least one third the dimensions in the x and y directions. If the system operates near its envelope it is necessary to account for the irregular shape of its boundary. However, these curved branches correspond to specific manoeuvring patterns that are neither practical nor realistic in this application. Furthermore, these branches are thin and contribute little to the overall momentum capacity of the system. These can therefore be eliminated without any significant degradation in performance. This can be achieved by using the following model of the momentum in the z-direction:

$$H_z = -2s^* \sin\alpha \quad for \quad |H_z| \leq 0.5H_{zmax}$$

The resulting constrained workspace is illustrated in Fig. 6.11. The dimensions are limited to $\pm 2c^*$ in the pure x and y directions when $H_z = 0$ and to $\pm 4s^*$ in the z-direction. The relative dimensions of the workspace can be adjusted to suit the requirements of the application by changing the skew angle, where $\beta = \tan^{-1} 1/2$ provides almost equal control authority about the x,y and z axes. The most important feature of this workspace is that the only inescapable singularities are those that form its external boundary. Therefore, it is possible to guarantee exact and real-time steering while operating within this constrained workspace.

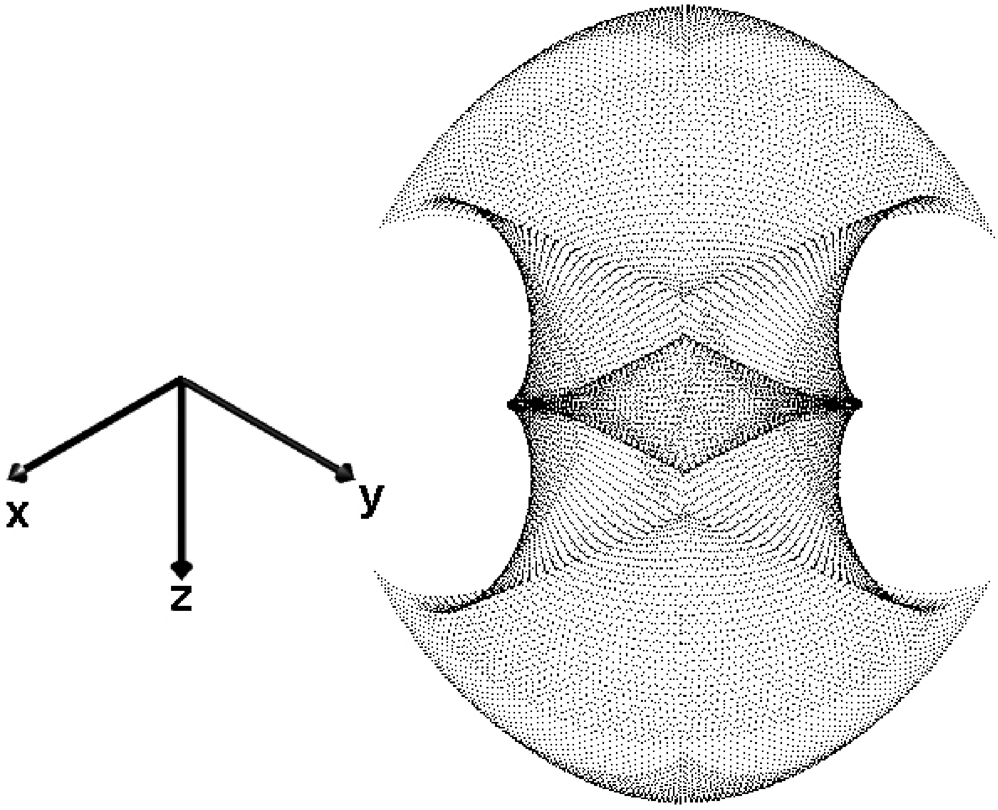

Figure 6.11: Isometric view of the constrained workspace

6.4.2 Global steering law

A global steering solution for exact and real-time singularity avoidance can be obtained by constraining the system to operate within the restricted workspace of Fig. 6.11. This can be implemented by applying relationship (6.3) to equation (4.5) and formulating a steering law based on the parameters σ, γ and α. This algebraically constrains gimbal steering by one degree of freedom and imposes the restraining condition in equation (6.4). The solution for the desired torque becomes:

$$\dot{\phi}^* = -(\mathbf{C}^*)^{-1}\tau_u \tag{6.6}$$

The steering parameter $\phi^* = [\sigma, \gamma, \alpha]^T$ and its derivative have the same dimensions as the vector of desired torque and so the constrained Jacobian $\mathbf{C}^*$ is a $[3 \times 3]$ square matrix with an inverse that can be computed directly. The following condition must be satisfied:

$$\mathbf{C}^*\dot{\phi}^* \;=\; \mathbf{C}\dot{\bar{\phi}}$$

The expression for $\mathbf{C}$ can be decomposed into its direct and coupled parts as follows:

$$(\mathbf{C}^*_o + \mathbf{C}^*_\times)\dot{\phi}^* \;=\; (\mathbf{C}_o + \mathbf{C}_\times)\dot{\bar{\phi}}$$

The first term can be expanded by using (4.4) and substituting in (6.1) and (6.3) to give:

$$\begin{aligned}
\mathbf{C}^*_o\dot{\phi}^* \;&=\; -\bar{c}\ \mathrm{diag}(\mathbf{J}_h\dot{\bar{\psi}})\dot{\bar{\phi}} \\
&=\; \mathbf{J}_h\dot{\bar{\psi}} \begin{bmatrix} -c^*\cos(\alpha+\sigma) & \sin(\alpha+\gamma) & c^*\cos(\alpha-\sigma) & -\sin(\alpha-\gamma) \\ -\sin(\alpha+\sigma) & -c^*\cos(\alpha+\gamma) & \sin(\alpha-\sigma) & c^*\cos(\alpha-\gamma) \\ -s^*\cos(\alpha+\sigma) & -s^*\cos(\alpha+\gamma) & -s^*\cos(\alpha-\sigma) & -s^*\cos(\alpha-\gamma) \end{bmatrix} \begin{bmatrix} \dot{\alpha}+\dot{\sigma} \\ \dot{\alpha}+\dot{\gamma} \\ \dot{\alpha}-\dot{\sigma} \\ \dot{\alpha}-\dot{\gamma} \end{bmatrix} \\
&=\; \mathbf{J}_h\dot{\bar{\psi}} \begin{bmatrix} -2c^*\cos\alpha\cos\sigma\dot{\sigma} + 2\sin\alpha\cos\gamma\dot{\gamma} + 2(c^*\sin\alpha\sin\sigma + \cos\alpha\sin\gamma)\dot{\alpha} \\ -2\sin\alpha\cos\sigma\dot{\sigma} - 2c^*\cos\alpha\cos\gamma\dot{\gamma} + 2(c^*\sin\alpha\sin\gamma - \cos\alpha\sin\sigma)\dot{\alpha} \\ 2s^*\sin\alpha\sin\sigma\dot{\sigma} + 2s^*\sin\alpha\sin\gamma\dot{\gamma} - 2(s^*\cos\alpha\cos\sigma + s^*\cos\alpha\cos\gamma)\dot{\alpha} \end{bmatrix} \\
&=\; -2\mathbf{J}_h\dot{\bar{\psi}} \begin{bmatrix} c^*\cos\alpha\cos\sigma & -\sin\alpha\cos\gamma & -(c^*\sin\alpha\sin\sigma + \cos\alpha\sin\gamma) \\ c^*\cos\alpha\cos\gamma & \sin\alpha\cos\sigma & (\cos\alpha\sin\sigma - c^*\sin\alpha\sin\gamma) \\ -s^*\sin\alpha\sin\sigma & -s^*\sin\alpha\sin\gamma & (s^*\cos\alpha\cos\sigma + s^*\cos\alpha\cos\gamma) \end{bmatrix} \begin{bmatrix} \dot{\sigma} \\ \dot{\gamma} \\ \dot{\alpha} \end{bmatrix}
\end{aligned}$$

Similarly the second term can be expanded to give:

$$\mathbf{C}^*_\times\dot{\phi}^* = \frac{1}{2}[(h_1c_1^T + c_1h_1^T)(\omega+\omega_d)\ \ldots\ (h_Nc_N^T + c_Nh_N^T)(\omega+\omega_d)](\mathbf{J}_c - \mathbf{J}_h)\dot{\bar{\phi}} = 0$$

This expression is zero for CMG systems that are symmetrical about the principal axes of the body, since $(h_ic_i^T + c_ih_i^T)$ becomes zero. Thus the constrained steering law (6.6) becomes:

$$\dot{\phi}^* = \frac{1}{2\mathbf{J}_h\dot{\bar{\psi}}} \begin{bmatrix} c^*\cos\alpha\cos\sigma & -\sin\alpha\cos\gamma & -(c^*\sin\alpha\sin\sigma + \cos\alpha\sin\gamma) \\ c^*\cos\alpha\cos\gamma & \sin\alpha\cos\sigma & (\cos\alpha\sin\sigma - c^*\sin\alpha\sin\gamma) \\ -s^*\sin\alpha\sin\sigma & -s^*\sin\alpha\sin\gamma & (s^*\cos\alpha\cos\sigma + s^*\cos\alpha\cos\gamma) \end{bmatrix}^{-1} \tau_u \tag{6.7}$$

Once the steering parameter rates have been computed the gimbal rate commands can be obtained as follows:

$$\dot{\bar{\phi}} = [\dot{\alpha} + \dot{\sigma}, \dot{\alpha} + \dot{\gamma}, \dot{\alpha} - \dot{\sigma}, \dot{\alpha} - \dot{\gamma}]^T$$

Similarly the steering parameters in (6.7) can be determined from the measured gimbal angles using the following equations:

$$\alpha = \frac{\phi_1 + \phi_2 + \phi_3 + \phi_4}{4}, \qquad \sigma = \frac{\phi_1 - \phi_3}{2}, \qquad \gamma = \frac{\phi_2 - \phi_4}{2}$$

In practical applications it is possible that condition (6.4) is violated as the frequency of the control system is finite. In these situations null motion can be used to bring the system back to this condition using the following null gain:

$$k_{null} = -\kappa(\phi_1 - \phi_2 + \phi_3 - \phi_4)$$

where the sensitivity is tuned by adjusting κ. A schematic of the steering law is illustrated in Fig. 6.12.

This steering law guarantees exact and real-time steering within a restricted workspace. This is a simple solution to the complex problem of singularity avoidance that eliminates the problem of internal singularities by applying algebraic constraints on gimbal motion. The uniqueness of its response is guaranteed by limiting the domain of the three steering parameters σ, γ, and α to within $\pm\pi/2$, ensuring the repeatability of the system's performance and limiting the gimbal angles to within $\pm 90^\circ$. This is of significant practical importance as it prevents multiple rotations of the gimbals, which is often overlooked in simulations and would require complicated mechanisms for actuation of the flywheels and serve no useful purpose. The steering law not only simplifies the design of the hardware, but also simplifies the implementation in software as the matrix inversion does not require the real-time computation of a complicated pseudo-inverse Jacobian and thus reduces the burden on the processors used in the AUV.

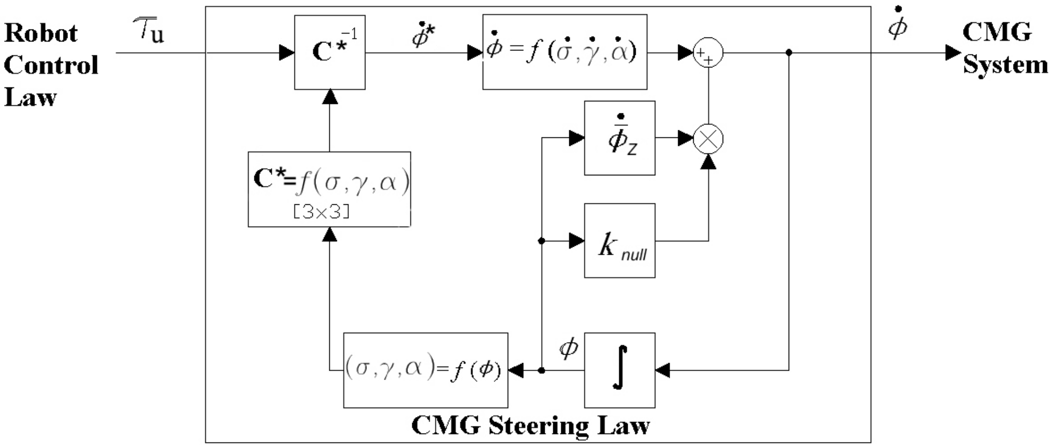

Figure 6.12: Global steering law

Chapter 7

Development of a Zero-G Class underwater robot

This chapter follows the design and construction of the CMG actuated Zero-G Class underwater robot IKURA. IKURA is an experimental platform developed as part of this research to verify the associated theoretical developments, assess the practical application of the control system and to demonstrate unrestricted attitude control and three-dimensional manoeuvering capabilities. This is the first application of CMGs to underwater robots and so the practical considerations of the mechanical and electrical design of the system are discussed. This chapter is supported by Appendices A - C. Appendix A contains CAD drawings and photographs of IKURA and its CMG system. Appendix B contains details of the electronic design, signals and circuitry. The hydrodynamic parameters are presented together with other modelling parameters in Appendix C.

7.1 Zero-G classification

A Zero-G Class underwater robot is defined as any underwater robot that can:

- adopt and maintain any attitude on the surface of a sphere with a zero radius turning circle and
- actively stabilise any attitude while translating in surge.

It should be noted that these points are not intended to specify the entire design of a complete AUV system, but simply outline the primary requirements for the attitude control capabilities of this new class of underwater robot. To satisfy the first point, the robot should ideally have coincident centres of gravity and buoyancy and thus zero righting moment. Unrestricted attitude control can be provided by the proposed CMG based method. The robot should be capable of fast, on the spot reorientations to offer sufficiently agile manoeuvrability to meet its specification. An example of the specification used in this research is detailed in the next section. The second point can be satisfied by equipping the robot with a single thruster to actuate surge. This is not restrictive as missions can be approached in a fully three-dimensional manner by making use of the attitude control capabilities.

Beyond the above specification, Zero-G Class underwater robots should be considerably smaller than most existing AUVs. The primary reason for this is to allow missions to be carried out in geometrically complicated, cluttered and even enclosed environments. A small size not only allows for greater agility, but also allows the robot to manoeuvre in confined spaces. Furthermore, compactness allows the robot to be handled manually. This is of great practical advantage since although the missions of an AUV are autonomous, the preparation for their deployment is, for the most part, far from it. Typically AUVs weigh in excess of 150kg and can weigh several tonnes, therefore their deployment requires large crewed support vessels equipped with cranes and other machinery. This involves a large number of people and is not only expensive, but requires a great deal of time and effort spent organising the missions. A discussion concerning possible Zero-G applications can be found in Chapter 9.

7.2 IKURA

The Internal Kinematic Underwater Robot Actuation system, or IKURA, shown in Fig. 7.1, was constructed in June 2005 and is the first Zero-G Class underwater robot. This is also, to the knowledge of the author, the first application of CMGs to underwater robots. It should be noted that IKURA is a prototype, designed to provide an experimental platform to verify the theoretical developments presented and demonstrate the unique freedom in attitude control offered by CMGs. At this stage IKURA is not intended to be a complete AUV system and thus its specification primarily relates to control about the rotational axes. The CMG system must provide sufficient control authority from the nominal state so that the robot can:

- rotate $\pm 180^{\circ}$ in yaw, starting and finishing at rest in $6\,\mathrm{s}$,
- rotate $\pm 90^{\circ}$ in pitch, starting and finishing at rest in $3\,\mathrm{s}$ and
- stabilise any roll angle.

Figure 7.1: Photo of the Zero-G Class underwater robot IKURA

IKURA is made up of a cylindrical body with hemispherical ends. Its hull is compact with a length of 0.5 m, a diameter of 0.22 m and a total mass of 17.0 kg. This includes 3.5 kg of ballast that can be used to adjust the centre of gravity of the robot. The locations of the centres of gravity and buoyancy, calculated in Appendix C, are coincident, indicating that the robot theoretically has zero righting moment. The robot is equipped with a single thruster to actuate surge and thus satisfies the conditions for Zero-G classification. Since the CMGs are completely contained within the hull they preserve its hydrodynamic integrity and maintain symmetry about its major axes. Therefore, the robots motion is essentially uncoupled between different degrees of freedom. Furthermore, the CMGs have no fluid interactions of their own, which greatly simplifies the hydrodynamic behaviour of the robot.

7.2.1 Pressure hull

IKURA has a single pressure hull that is illustrated in Fig. 7.2. The hull consists of an acrylic pipe of length 280 mm and external diameter 220 mm with acrylic domes at either end. The three parts of the pressure hull are sealed using AS(APR)568-173 rubber O-rings and fastened using YMV12745-T-230 V-band couplings. The cylindrical part of the hull has three Fisher DEE-1031A010 connectors, which can be used for thrusters, external sensors and a tether cable. A cradle mechanism rotates freely about the pitch axis of the hull. If a tether is used, the cable can be fixed to the cradle arm and so any pull from the cable will act through the centre of the robot and thus eliminate any rotational pitch effects that would act on it. The pressure hull is designed to comply with a depth rating of 20 m using Japan International Shipping standards as this is the depth rating of the connectors used. Considerable margins have been added to allow for the large internal forces generated by the CMG system. The minimum wall thickness is 8.5 mm with reinforced mountings to rigidly fix the CMG system inside the cylindrical section of the hull.

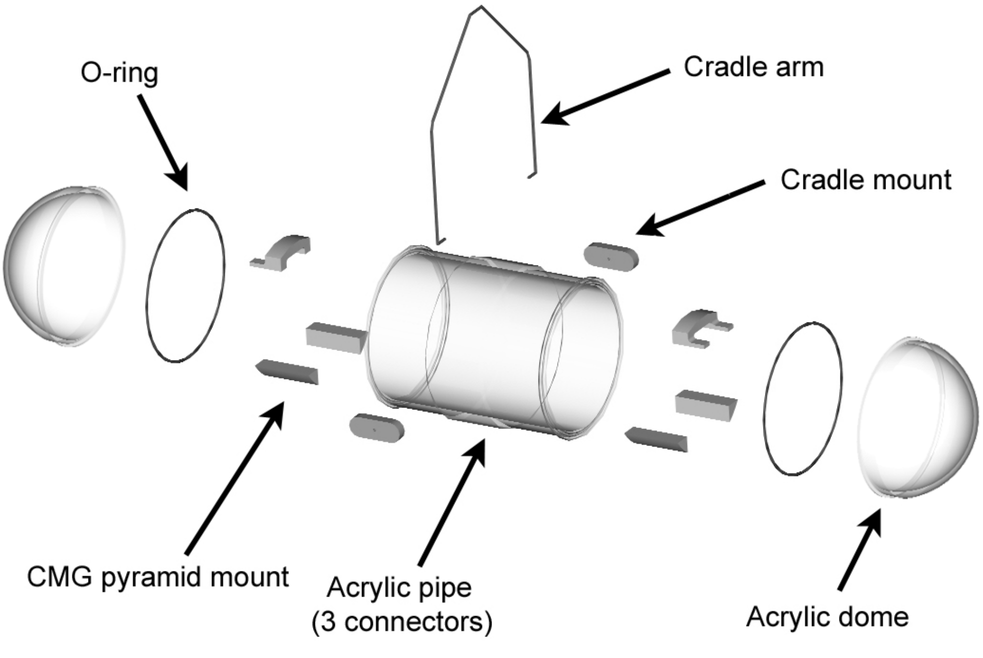

Figure 7.2: Construction of the pressure hull

7.2.2 CMG system

IKURA contains a cluster of four CMG units that are arranged in a pyramid configuration, as shown in Fig. 7.3. This provides independent roll, pitch and yaw actuation. A skew angle of $\beta = \cos^{-1}\sqrt{1/3}$ was chosen to provide greater control authority in yaw than in pitch when using the proposed steering law. The shape of the pyramid is stretched to fit the pressure hull, however, angular symmetry is maintained about its centre and so there are no detrimental effects on its performance as an actuator.

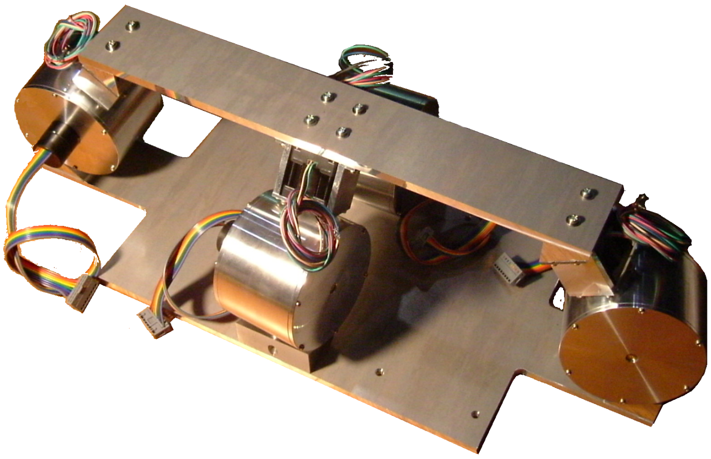

Figure 7.3: Photo of the CMG pyramid

The CMGs are sized based on the predictions of numerical simulations that used an optimised bang-bang control law, as detailed in Appendix C. The minimum angular momentum required to meet the specification within the constrained workspace was computed to be 3.8 Nms with a maximum required torque of 0.47 Nm. Although it is desirable to have the flywheel rates as fast as possible, high speeds introduce practical problems such as vibration and wear in the bearings. To ensure reliability the system is designed to meet its specification at under 30% of its maximum rotational speed. A fast mechanical response and high resolution of control are achieved by using high torque servos to steer the gimbals. The parameters of the CMG system are specified in Table 7.2.

CMG Parameters	Value
Skew angle	54.7°
Gimbal torque	0.58 Nm (Futaba S9550)
Flywheel diameter	68 mm
Flywheel mass	825 g (Brass)
Flywheel inertia	6.38×10^{-4} kgm^2
Flywheel max. rate	50,000 rpm (Maxon EC22-169007)
Output torque $[roll, pitch, yaw]$	$\sim [1, 1, 3]$ Nm
Maximum momentum stored	13.4 Nms
Maximum energy stored	35 kJ

Table 7.1: Physical parameters of the CMG pyramid

The construction of each CMG unit is illustrated in Fig. 7.4. Since the physical dimensions of the CMG system are limited by the space restrictions of the pressure hull, it is desirable for the flywheels to be made out of as dense a material as possible. However, the material must also be non-magnetic and strong enough to withstand the large gyroscopic torques produced. Brass, with a density of $8450\,\mathrm{kgm^{-3}}$, was chosen as a suitable material. The flywheels rotate at speeds of up to $50,000\,\mathrm{rpm}$ and so care was taken to ensure the safety of their design. Each flywheel is supported at both ends to evenly transmit the gyroscopic torque to an aluminium gimbal frame. The gimbal frame is a cylindrical drum that encloses the flywheel and isolates it from the rest of the system. The flywheel is mounted on the shaft of a high speed motor that is fixed to the active lid of the gimbal frame. A bearing in the passive lid supports the opposite end of the flywheel shaft. The skew angle is set by a wedge at either end of each CMG unit. A servo fixed to the active wedge is used to rotate the gimbal. A bearing in the passive wedge supports a shaft on the gimbal frame to evenly transmit the torques generated.

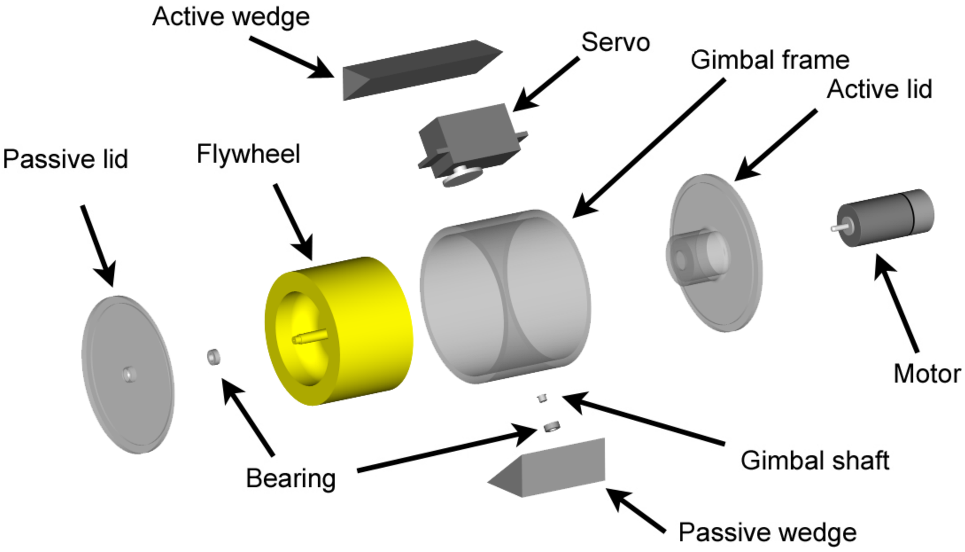

Figure 7.4: Construction of a CMG unit

The pyramid is formed by fixing the CMG units to two plates as shown in Fig. 7.3. However, the system is only held together by the bearings of each gimbal and so relies on being fixed to the pressure hull for rigidity (Fig. 7.5). Appendix A contains CAD drawings of the CMGs.

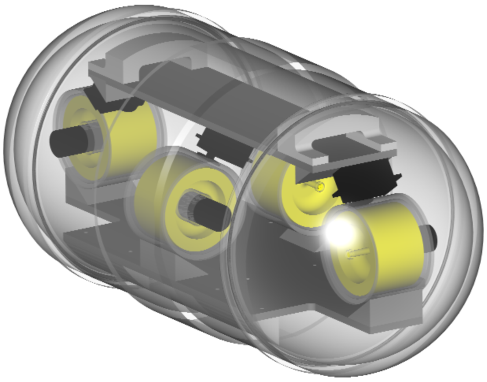

Figure 7.5: CMG pyramid fixed inside the pressure hull

7.2.3 Thruster

A simple thruster unit (Fig. 7.6) was constructed to provide actuation in surge. The thruster is designed to be long and slender to reduce resistance. Also it is desirable to have the propeller as far from the main body of the robot as possible to allow a smoother flow into the propeller when advancing in surge. This also reduces the effects of the wake acting against the body when the robot reverses. The thruster is driven by a 10 W DC motor that is placed in a pressure vessel with a mechanically sealed drive shaft to rotate the propeller. A magnetic coupling system was considered to be unnecessary since the depth rating of the mechanical seal is greater than the 20 m depth limit of the electrical connectors used in the hull of the robot. The thruster can generate a maximum thrust of 4.5 N in the forward and 3.5 N in the reverse direction at a rotational speed of ±900 rpm in bollard-pull conditions. Details of the thruster model used in this study can be found in Appendix C.

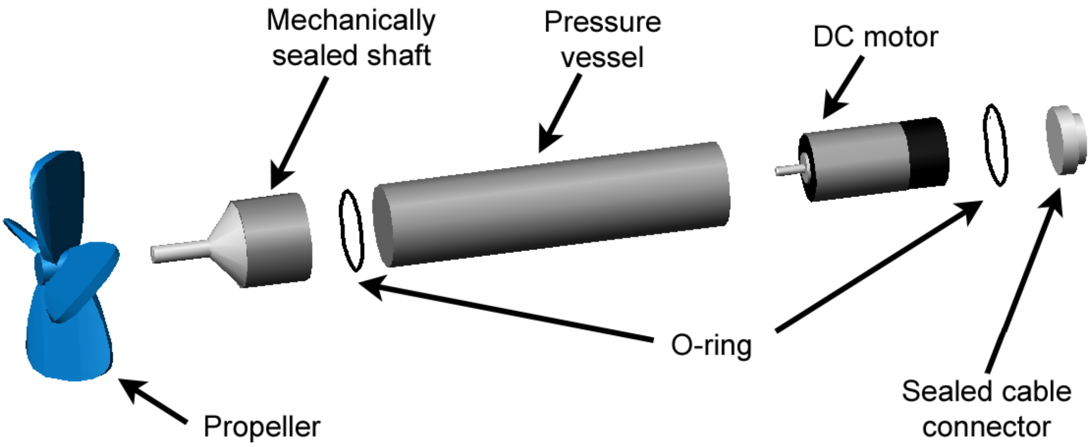

Figure 7.6: Construction of the thruster unit

The thruster is mounted on the main body of the hull using a steel tripod arrangement as shown in Fig. 7.7. Since the robot has no righting moment the reaction to the roll moment generated by the thruster is of great concern. Therefore, the thruster mount was designed with a large surface area in the roll direction to provide some resistance to limit this effect. For post-prototype designs the use of a contra-rotating propeller is recommended. Further details of the design can be found in CAD drawings in Appendix A.

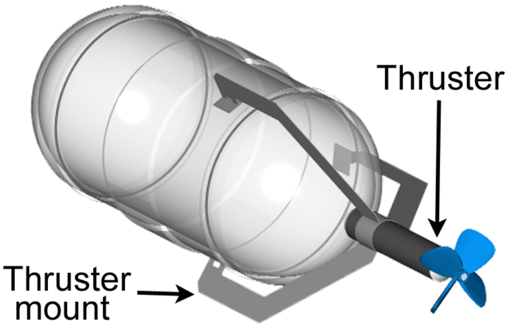

Figure 7.7: Thruster unit mounted on the pressure hull

7.3 Electronics and control

The control system is realised using a single chip micro-controller. This generates the appropriate signals for the CMG flywheel, servo and thruster drivers based on the measurements of a three-axis attitude and rate sensor. The arrangement of these components is shown in Fig. 7.8. Details of the electrical hardware and circuitry can be found in Appendix B.

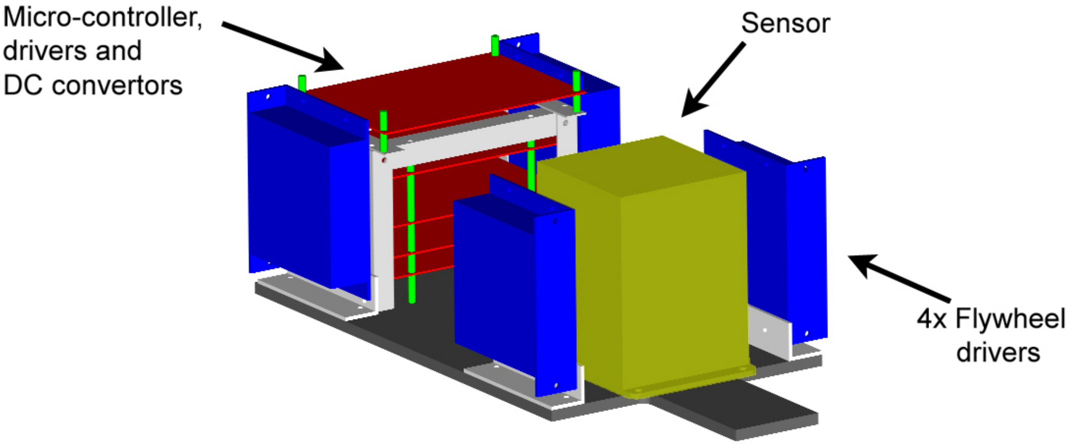

Figure 7.8: Arrangement of electronics

7.3.1 Sensors

The robot's triaxial attitudes and angular rates are measured at a sampling frequency of 50 Hz using an Attitude and Heading Rate Sensor (AHRS). This sensor has a larger range in roll than in pitch and so is fixed normal to its standard orientation in the hull. Thus the AHRS roll, pitch and yaw measurements correspond to the pitch, roll and yaw dynamics of the robot. Table 7.2 shows the sensing capabilities in the body frame. These are output as 12 bit analogue signals between ±4.096 V. The signals are converted to the appropriate measurements using the following equations:

$$\begin{aligned}\dot{\theta} &= \text{Range} \times 1.5 \times \frac{V_{out}}{2 \times 4.096}\\ \theta &= \text{Range} \times \frac{V_{out}}{2 \times 4.096}\end{aligned}$$

These signal are converted so that they can be read by the 10 bit 0 - 5 V A/D convertors on the micro-controller. The circuitry for this conversion is illustrated in Appendix B.

Measurement	Range	Accuracy
roll (^{o})	±90	$< \pm 0.75$
pitch (^{o})	±180	$< \pm 0.75$
yaw (^{o})	±180	$< \pm 1.5$
roll, pitch, yaw rate (^{o}/s)	±100	$< \pm 1.0$

Table 7.2: Sensing capabilities of IKURA

7.3.2 Drivers

Flywheel motor: The angular velocity of each flywheel is individually monitored by a closed-loop digital driver that uses three Hall sensors in the motor to regulate its speed. These have a 28 V power supply. The motor speed is controlled by an 8 bit 0 - 5 V analogue signal that is generated by the micro-controller. The speed of the flywheels can be determined as follows:

$$\dot{\psi} \;=\; \frac{k_{\dot{\psi}} \times V_{in} \times V_{D/A}}{5}$$

where $k_{\dot{\psi}}$ is the speed constant of the motor. This was experimentally determined to be 2150 rpm/V. V_{in} is the supply voltage and $V_{D/A}$ is the signal from the micro-controller. A separate I/O signal is used to apply an electronic brake to stop the flywheels from rotating. Details of the experiment and circuitry used to control the flywheels can be found in Appendix B.

Gimbal servo: The servos used to rotate the gimbals define the resolution of the attitude control system. The servos have a 5 V power supply and are controlled using four 16 bit PWM signals generated by the micro-controller. The servo angle is controlled by the width of a pulse that is sent every 22 ms. The angle can be determined as follows:

$$\phi \;=\; \frac{\pi}{2} \times \frac{\mathrm{PWM} - \mathrm{PWM}_0}{\mathrm{PWM}_\mathrm{R}}$$

where PWM is the length of each pulse. PWM_0 is the pulse length for a zero excursion angle, which was practically determined to be 1480 μs. The pulse range was found to be $\pm 700\,\mu$s and thus $\mathrm{PWM}_\mathrm{R} = 1400\,\mu$s. Further details of the PWM signal are given in Appendix B.

Thruster: The direction and rate of the thruster's rotation are controlled by an I/O signal and an 8 bit PWM signal respectively. The thruster has a 10 V power supply. The rotational rate of the thruster can be calculated as follows:

$$n \;=\; d \times \frac{k_n \times V_{in} \times \mathrm{PWM}}{\mathrm{PWM}_1}$$

where d is $+1$ when the I/O is 1 and -1 when I/O is 0 and k_n is the motor speed constant when loaded. This was experimentally determined to be 93.4 rpm/V. PWM is the width of the pulse sent and PWM_1 is the period of the pulse. Further details of the experiment and the control signals can be found in Appendix B.

7.3.3 Micro-controller

The robot is controlled by a 16 bit Hitachi H8/3067 single-chip micro-controller. This is programmed in C++ and compiled using a host computer. The compiled program is downloaded to the micro-controller through a serial cable. This has a H8/300H CPU core unit that uses a real-time operating system with a clock rate of 20 MHz. A watchdog timer is used to control the system at a frequency of 10 Hz. Information can be transmitted via a RS232 serial communication port to a user interface on a host PC to be monitored in real-time.

7.3.4 Power

The various different supply voltages are distributed via a number of DC-DC convertors. These ensure that each of the electrical devices receives the correct voltage supply. The voltage and power requirements of each of the components is presented in Appendix B. The overall power requirement of the robot is shown in Table 7.3. The operational power consumption of 20 W is for a constant flywheel rate of $\dot{\psi} = 10,000$ rpm with steady propulsion at a thruster rate of 450 rpm. The peak power consumption for the maximum acceleration of the flywheels and the thruster is about 100 W. What may seem like a drawback of the system is the energy required initially to accelerate the flywheels. However, this can be carried out prior to each deployment using an external power source. Furthermore, since this energy is stored in the rotation of the flywheels it can in theory be used to power the robot during its missions. This idea of using flywheels as a mechanical battery was suggested for use on-board spacecraft by Roes [73] in 1961. With this approach it may be possible to perform short missions with no chemical battery at all. Unlike conventional batteries the energy stored is not sensitive to temperature change and has no memory effect. Another practical advantage is that the remaining energy can be accurately calculated by measuring the angular velocity of the flywheels. However, this is beyond the scope of this research and in the experiments described power is supplied to the robot through a tether cable using an external source.

Component	Operational power	Peak power
Sensors and CPU	4 W	4 W
CMG system	14 W	82 W
Thruster	2 W	10 W
Total	20 W	$\sim$ 100 W

Table 7.3: Operational and peak power consumption of IKURA

7.4 Specification

The underwater robot IKURA is the first prototype of the Zero-G Class and is the first application of CMGs to underwater robots. This forms a unique platform with which to demonstrate unrestricted attitude control and three-dimensional manoeuvring. The structure of the control system is presented in Fig. 7.9. The complete construction of IKURA is illustrated in Fig. 7.10 and the overall specification is given in Table 7.4.

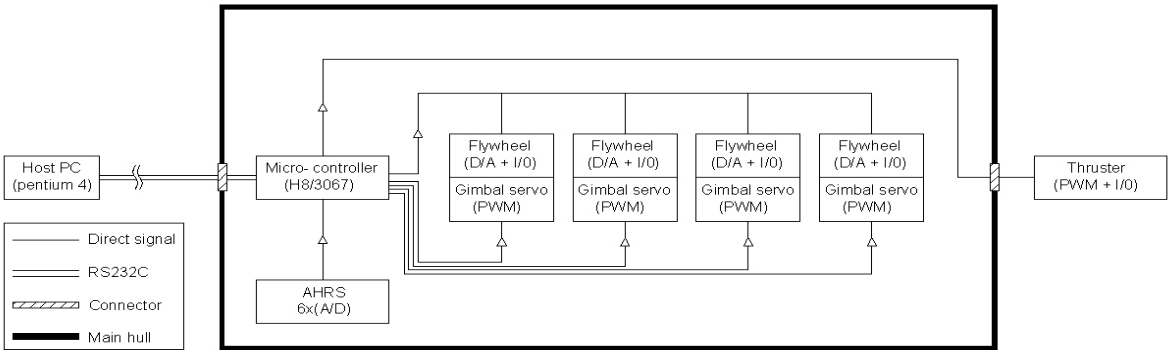

Figure 7.9: Structure of the control system

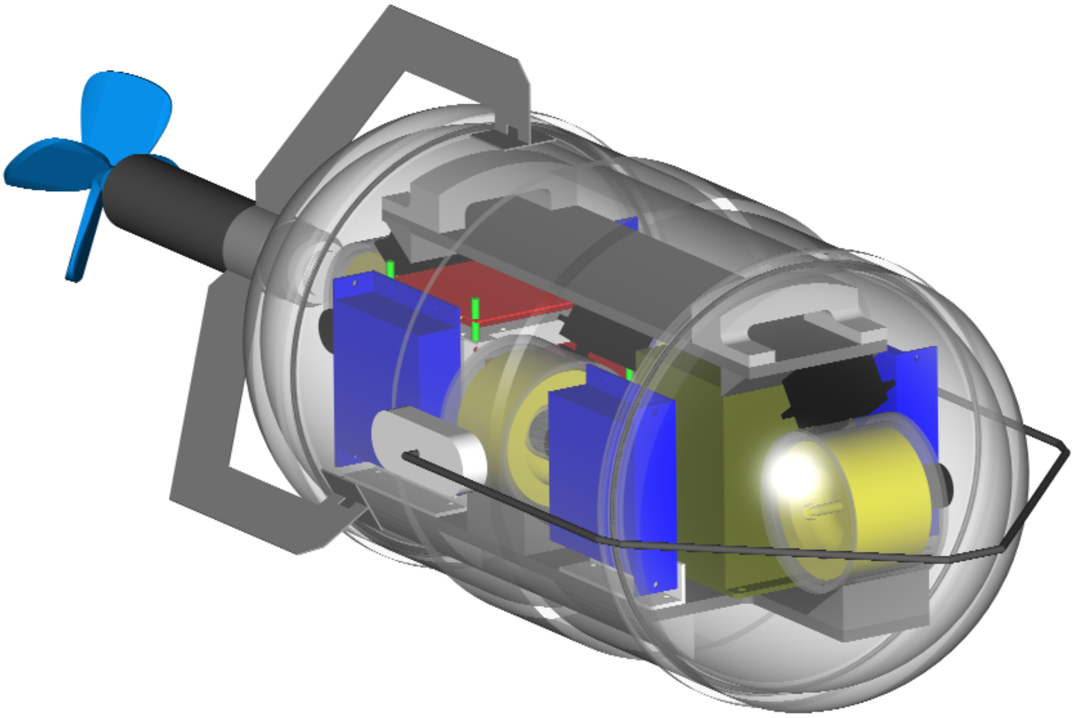

Figure 7.10: Construction diagram of IKURA

Classification	Zero-G
Objective Capabilities	Investigation of CMG and Zero-G applications Unrestricted attitude control and 3D missions
Hull length Hull diameter Mass	500 mm 220 mm 17.0 kg
Max. depth Max. speed Max. slew rate	20 m 0.5 m/s 45 °/s
CPU Sensor	H8/3067 Cross-Bow AHRS-400CA
Translation Rotation	Thruster (surge) CMG pyramid (roll, pitch, yaw)
Max. energy stored in CMGs Power consumption	35 kJ 20 W (∼ 100 W for accel.)

Table 7.4: Specification of IKURA

Chapter 8

Experimental verification

This chapter verifies the theoretical developments of this research and demonstrates the practical application of CMGs to Zero-G Class underwater robots. A series of experiments is performed to assess the:

- actuation capabilities of the CMG system,
- dynamics and control of the CMG and body system and
- dynamics, control and stabilisation of the complete CMG, body and fluid system.

To clarify the first point the torque developed by the CMG system is assessed. Next, the exactness and real-time applicability of the steering law are investigated to demonstrate the practical aspects of using CMGs for actuation. In both cases the torque generated by the CMG system was measured using an array of cantilevered strain gauges. For convenience of instrumentation both experiments were performed on land.

To elucidate the second point a series of experiments was performed to assess the open-loop dynamics and the closed-loop control of the CMG and body system in the presence of a disturbance. These experiments were performed on land with the CMG pyramid mounted on a thrust bearing so that it was free to rotate in yaw. The robustness of the control law to the disturbance of the bearing is verified.

Finally, the performance of the CMG, body and fluid system is verified to demonstrate the practical applicability of the complete control system to Zero-G Class underwater robots. These experiments were performed with the underwater robot IKURA in the experimental pool facilities of the URA laboratory at the University of Tokyo. The experiments assess the open-loop attitude response to a series of gimbal rate inputs and the closed-loop control performance of the underwater robot using the proposed control law. During the experimental work, as confidence in reliability grew the flywheel speeds were steadily increased up to the recommended operational rate for this system of 10,000 rpm. The results are presented in a different sequence to the work so this steady increase is not apparent. However, the speed of the flywheels is not a critical parameter in the verification of the theory presented. Details of the hydrodynamic model used are presented in Appendix C. To allow for comparison the second series of experiments was performed with two alternative control laws in addition to that developed in this research. Finally, the ability to stabilise the passively unstable, unsteady self-propelled translational dynamics of a Zero-G Class underwater robot are assessed. Video footage experimental work can be found in Appendix D.

8.1 CMG actuation

The performance of CMGs as an actuator is assessed by measuring the torque developed by the CMG system and investigating the exactness and real-time applicability of the steering law. The torque generated was measured using an array of cantilevered strain gauges. These were calibrated before each experiment by applying a known force at a measured distance along the cantilever. A plan view of the experimental setup is illustrated in Fig. 8.1. For convenience of instrumentation these experiments were performed on land with the CMG pyramid mounted on a thrust bearing so that it was free to rotate in yaw. This does not make the results of the experiments any less valid since the torque generated by the CMG system is independent of its environment and is applied directly to the body of the robot.

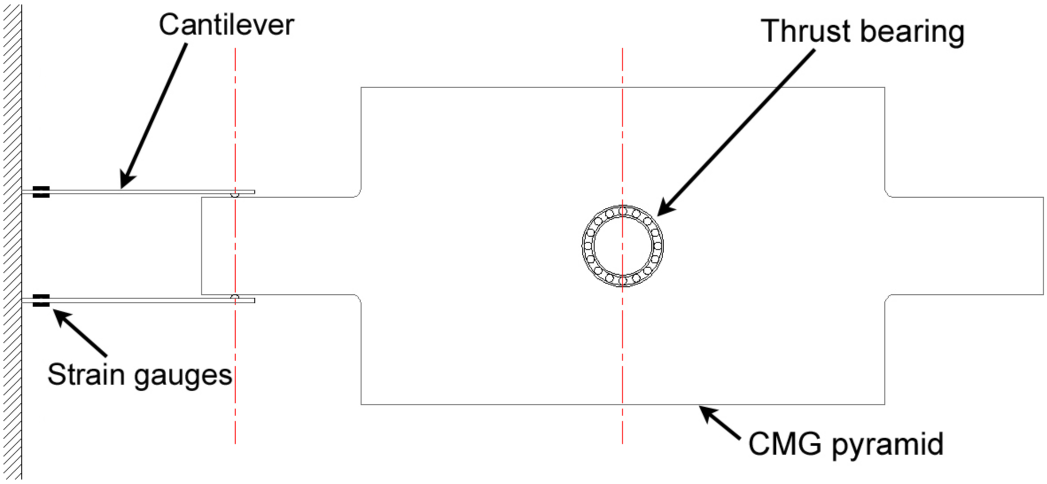

Figure 8.1: Setup for measurement of the torque generated by the CMG system

8.1.1 Gyroscopic torque output

In the first experiment the torque generated by the CMG system in response to an open-loop gimbal rate command is measured and compared to the theoretical torque calculated using (3.5). Fig. 8.2 shows the response of the system to a gimbal rate command of $\pm 8\,^{\circ}/\mathrm{s}$ that covers the entire range of gimbal excursion angles between $\pm 90\,^{\circ}$ where the flywheel angular velocity $\dot{\psi}$ is set to 5000 rpm. The torque generated by the system has a cosinusoidal relationship with the gimbal excursion angles and shows good agreement with the torque computed on-line by the micro-controller in real-time. The 6.0% loss in magnitude is of an acceptable order considering mechanical disturbances such as friction, vibrations and flywheel imbalance. Recalling from (5.4) that a singularity occurs when $\det(\bar{c}\bar{c}^T) = 0$, the parameter $\det(\bar{c}\bar{c}^T)$ can be used to indicate how far the system is from a singular orientation. This is described further in the next experiment. It can be seen that there is a singularity when all the units have a $90\,^{\circ}$ excursion angle. At this point the momentum vector in the z-direction reaches its maximum normalised value of $4s^*$ and so no torque can be generated in this direction. These results confirm the dynamic equations derived for the CMG system.

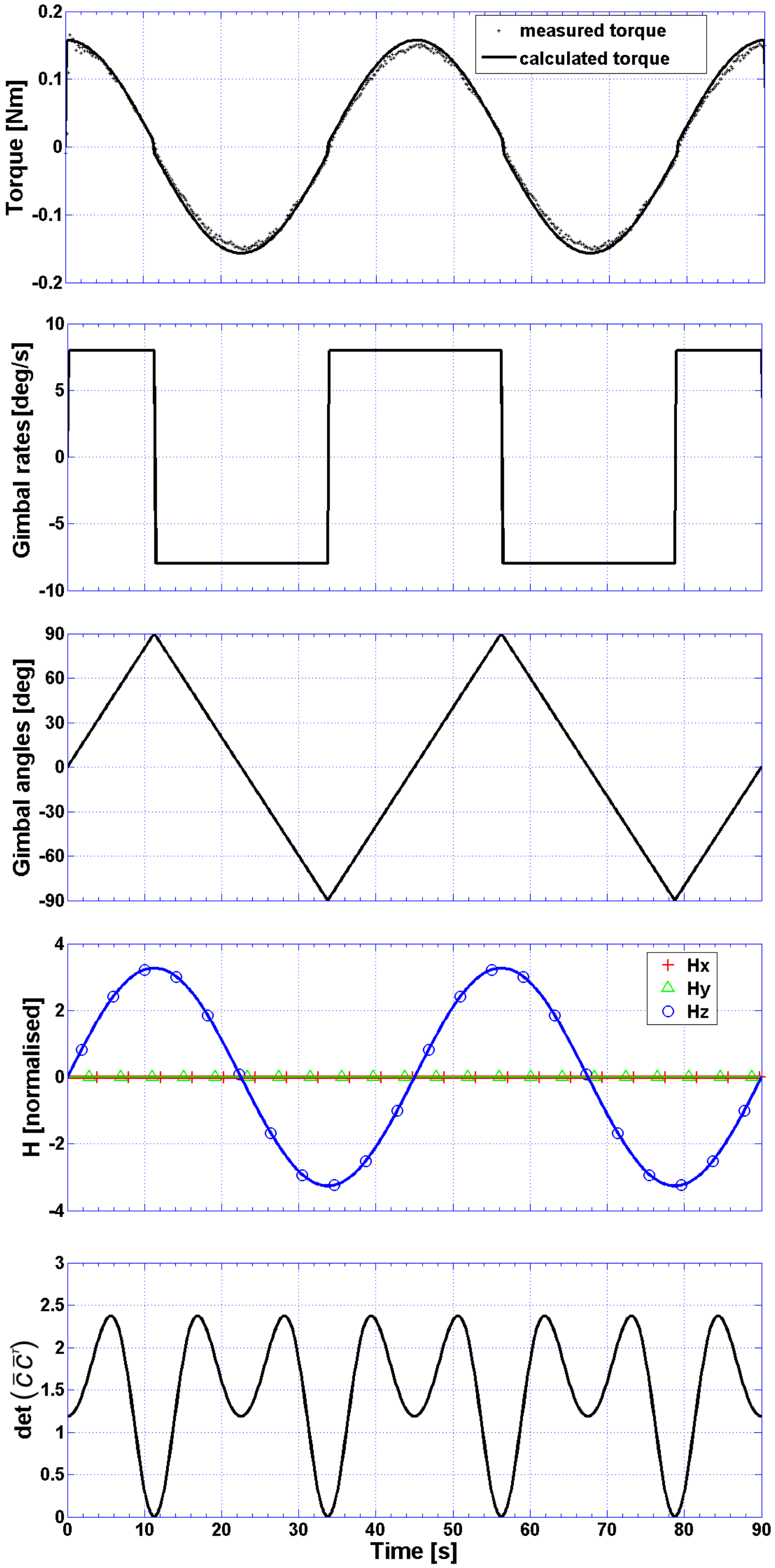

Figure 8.2: Comparison of measured and theoretical torque output with $\dot{\psi} = 5000\,\text{rpm}$

8.1.2 Steering law exactness

The exactness and real-time applicability of the steering law in (6.7) is assessed by measuring the step response of the system to an open-loop torque command. Fig. 8.4 shows the response of the system to a command torque of 0.07 Nm for a flywheel rate of 5000 rpm. The steering law responds immediately to generate the command torque. The brief transient period is due to the finite acceleration of the servos used to steer the gimbals. The measured torque is maintained within 6.0% of that commanded until the system reaches the workspace envelope where no further torque can be generated in the desired direction. As the momentum in z-direction increases, the system becomes less singular with $\det(\bar{c}\bar{c}^T)$ increasing as the distance to the nearest singularity becomes further. This is illustrated graphically in Fig. 8.3, which shows the position of the normalised momentum vector in the constrained workspace. Beyond a certain point $\det(\bar{c}\bar{c}^T)$ starts to decrease as the system approaches the singular momentum envelope in the z-direction, eventually becoming singular where $\det(\bar{c}\bar{c}^T) = 0$.

The gimbal rates determined by the steering law increase exponentially with the excursions of the gimbals. A limit of 25 °/s is imposed to prevent unreasonable gimbal rate commands being executed near singular orientations. This can cause a drop off in the torque generated near singularities, but is not restrictive as the only singularities in this workspace are those that form the boundary of the momentum envelope. Operation of the system near these regions does not pose any significant practical advantage since the system soon reaches the boundary of its operational envelope. Some losses in torque are recorded beyond 50 ° excursion with rapid degeneration beyond 70 °. These losses occur before the gimbal rate limit is reached and are due to the sampling frequency of the control system, which at 10 Hz becomes unable to keep up with rapidly changing gimbal rate commands.

The results of the experiment verify that the proposed steering law is both exact and applicable in real-time. The errors described are due to the practical implementation of the steering law in a finite system. These can be overcome by increasing the frequency of the control system or by increasing the flywheel rate to avoid operation at large gimbal excursions. However, these limitations are not restrictive since the system is designed to meet its specification well within the boundary of its maximum momentum envelope.

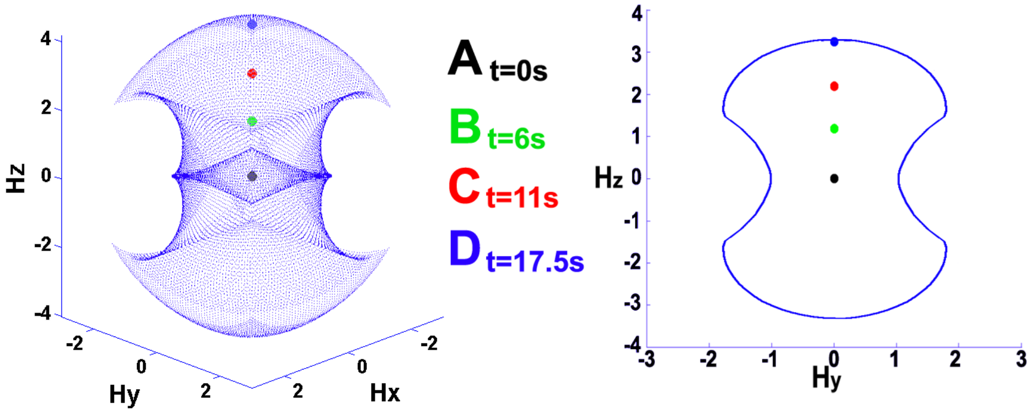

Figure 8.3: Geometric representation of the momentum vector in the constrained workspace

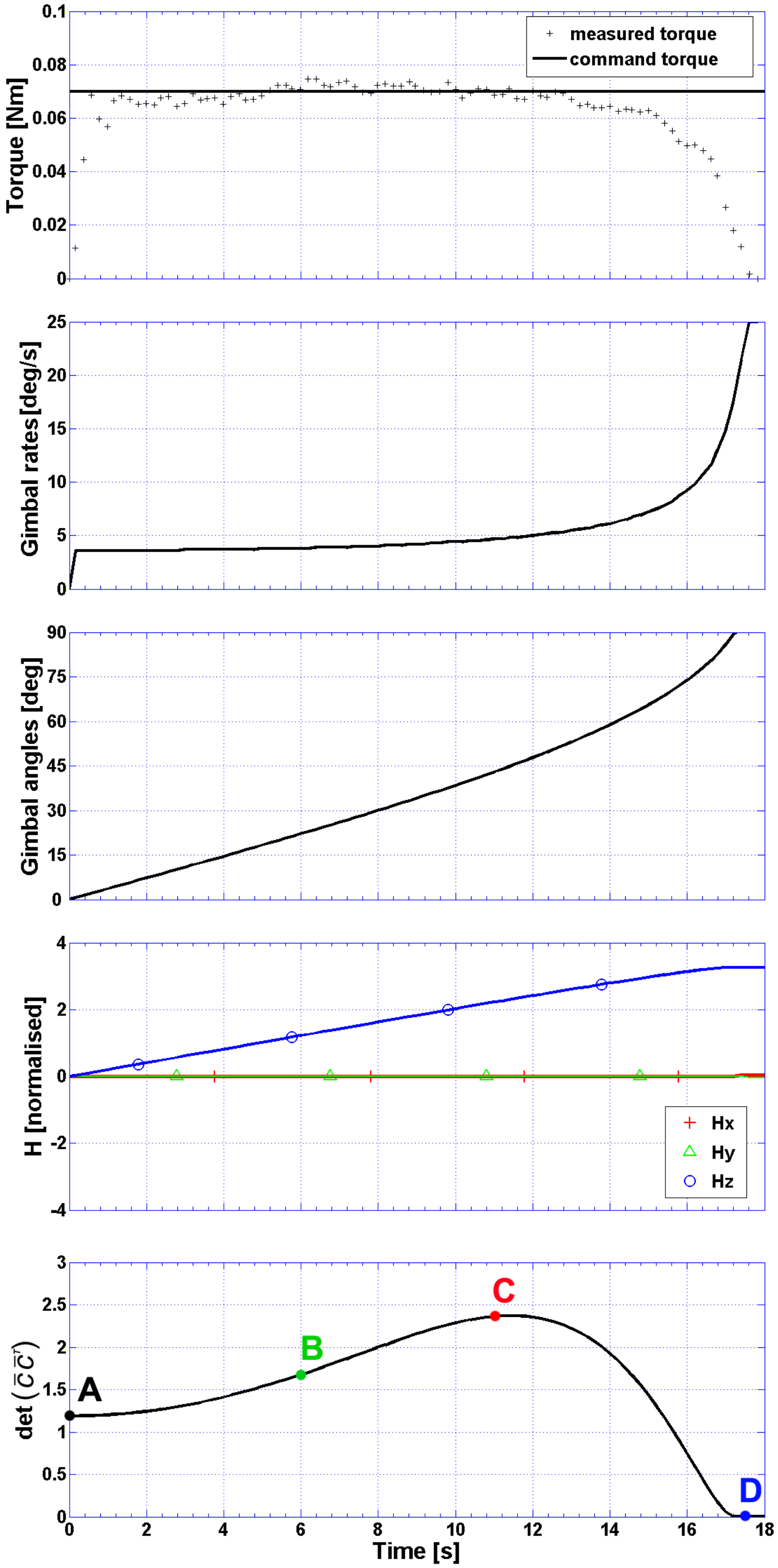

Figure 8.4: Verification of steering law exactness with $\dot{\psi} = 5000\,\mathrm{rpm}$

8.2 Dry-land dynamics

A series of experiments was performed to assess the open and closed-loop dynamics of the CMG and body system in the presence of a disturbance. The experiments were performed on land with the CMG pyramid mounted on a bearing that was free to rotate in yaw. Attitude and angular rate measurements were made using an AHRS unit (see Table 7.2) fixed within the system where average readings were taken at 10 Hz to filter noise. The setup is illustrated in Fig. 8.5 and experimental video footage can be found in Appendix D.

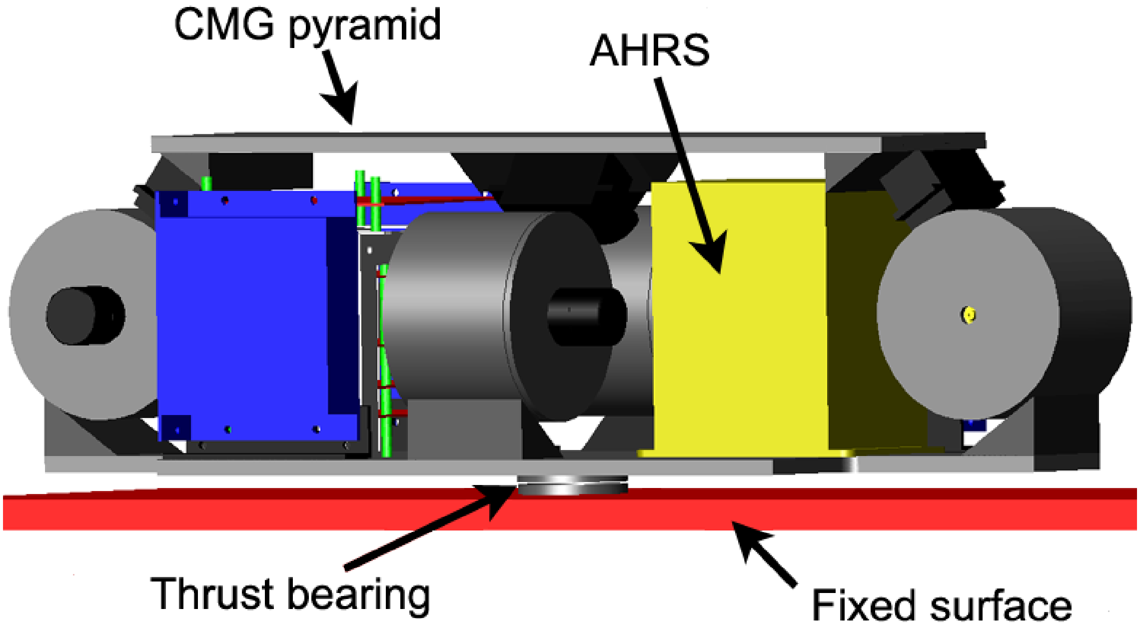

Figure 8.5: Setup for assessment of dry-land dynamics and control

8.2.1 Open-loop dynamics

The first series of experiments assess the open-loop attitude response of the CMG and body system to gimbal rate inputs. Fig. 8.6 shows the attitude response of the system in the presence of a disturbance due to friction in the thrust bearing. A gimbal rate command of $\pm 10\,^{\circ}/\mathrm{s}$ is sent to cover the range of excursion angles between $\pm 90\,^{\circ}$ for two cycles. The angular velocity of the flywheels is 1000 rpm and the torque generated is determined using (3.5). The system's attitude and angular rate response are highly non-linear. The results indicate that friction in the bearing has a significant impact on the dynamics of the system.

The dynamics of the system simulated using (3.12) with the bearing modelled as described in Appendix C shows a reasonable agreement with the measured response. The errors in simulation are due to unmodelled vibrations in the CMG pyramid as the direction of the gyroscopic torque changes. This can be seen in the video footage in Appendix D. This occurs as the CMG pyramid relies on being fixed to the robot's hull for rigidity. Although the vibrations cause modelling difficulties in this experiment, the problem is overcome when the system is rigidly fixed inside the body of the robot. The results of the experiment support the validity of the attitude dynamics derived for the CMG and body system.

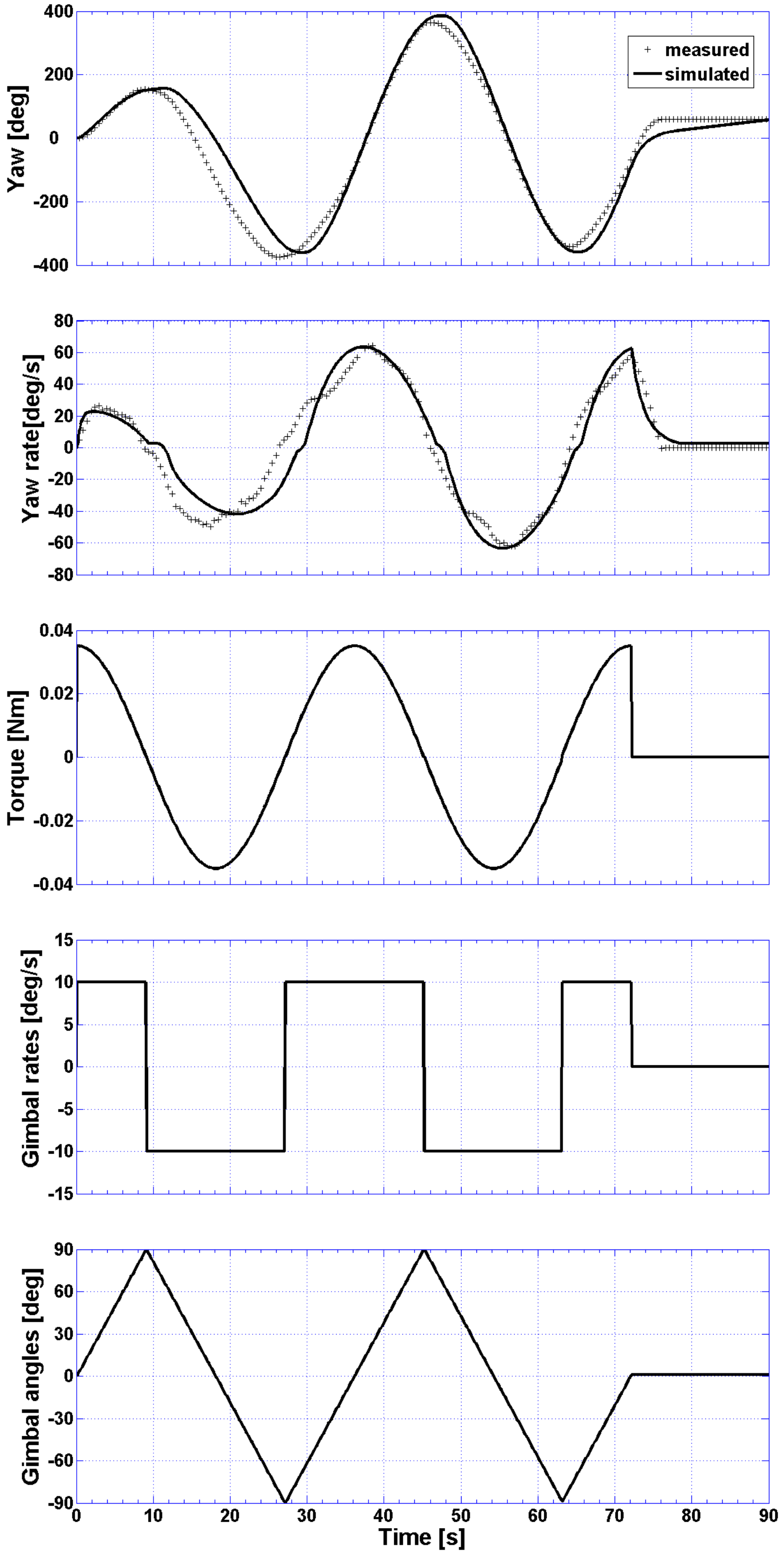

Figure 8.6: Dry land open-loop response in the presence of a disturbance with $\dot{\psi} = 1000\,\text{rpm}$

8.2.2 Closed-loop control

The performance of the attitude control law (4.6) developed in Section 4.2 is analysed by measuring the response of the system to an angular state command in the presence of a known disturbance. The control law does not model the non-linear dynamic effects of the bearing or the effects of vibrations of the system. These have been discussed in the previous section and are treated as disturbances in this experiment. Appropriate control gains were determined experimentally with the final values optimised at $[k_\omega, k_q] = [0.4, 1.0]$ for this setup.

Step response

This experiment investigates the response of the system to a step attitude command of 15 °. The navigation unit (Fig. 2.4) computes the desired angular rate as a function of the distance to the desired angle. The attitude response of the system is plotted in Fig. 8.7. The system takes 1.0 s to first reach the target yaw angle with a small overshoot of 1 ° before finally converging 2.4 s after the initial command. The maximum torque generated by the CMG system is 0.135 Nm. This is sustained for 0.3 s corresponding to a momentum impulse of 0.04 Nms. The experiment demonstrates a rapid response that converges to the desired state and this suggests that the system may be robust against the un-modelled disturbances.

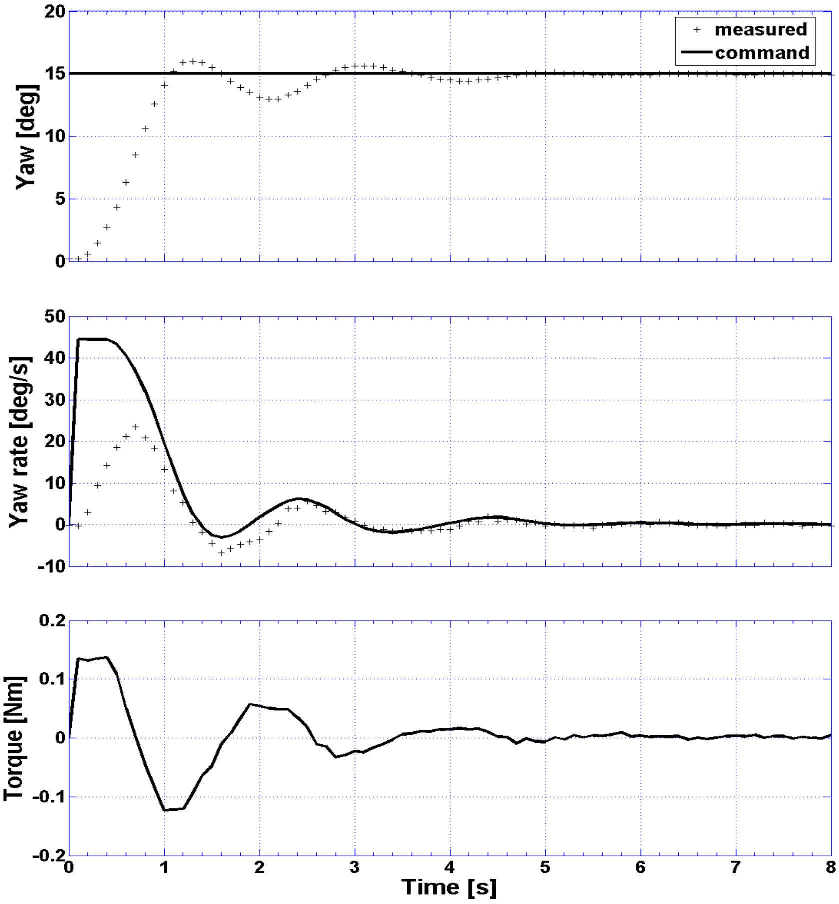

Figure 8.7: Dry-land step control response in the presence of a disturbance

The response of the CMG system for a flywheel rate of 3000 rpm is plotted in Fig. 8.8. The system respond rapidly to generate the required torque. The initial absolute error in the torque generated reaches 1×10^{-3} Nm, which is 0.7% of that commanded by the control law. This is due to finite accelerations of the gimbals in practical implementations. Beyond this initial transient the mean torque error remains exact to within 0.1×10^{-3} Nm. The maximum gimbal rate is 11.5 °/s with a maximum excursion angle of 6 °. The final excursion after the manoeuvre is 3 °. The angular momentum and $\det(\bar{c}\bar{c}^T)$ plots show that the system performs this manoeuvre while operating well within the boundary of its operational envelope.

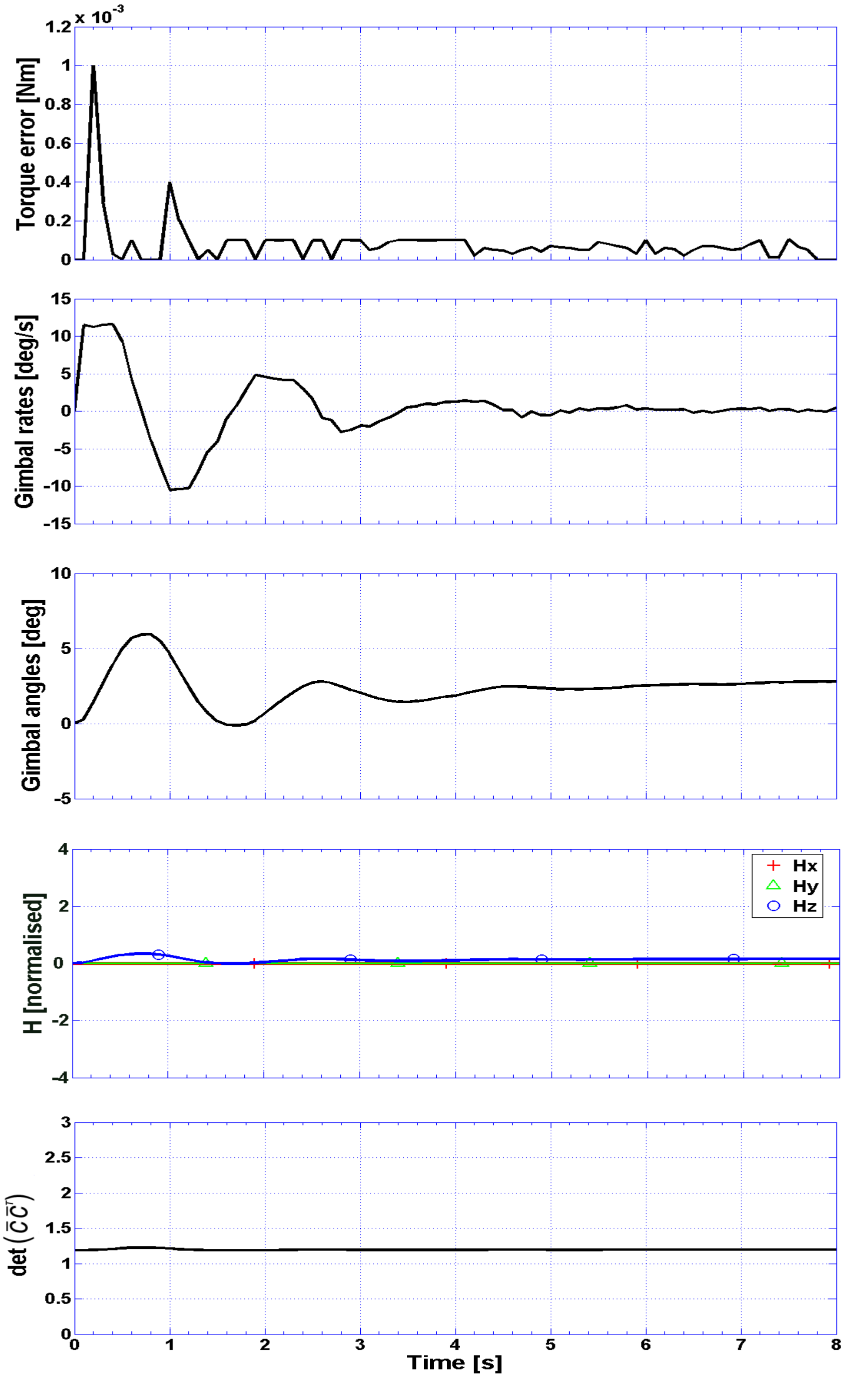

Figure 8.8: Step response CMG steering with $\dot{\psi} = 3000$ rpm

Ramp response

For practical implementation the navigation unit computes a ramp signal to the target attitude in order to limit the response of the control law. This experiment investigates the response of the system to an attitude command of 180 ° with a maximum yaw rate of 50 °/s. Fig. 8.9 shows the attitude response of the system and the torque generated by the CMGs. The system first reaches its target attitude in 3.5 s with an overshoot of 10 ° before converging 5 s after the initial command. The desired rate is first reached in 0.3 s, overshooting the command by 15 °/s before converging to the desired rate 1.4 s after the command. The maximum torque generated by the CMGs is 0.45 Nm to first accelerate the system to the desired rate and to bring the system to a halt once the target attitude is reached. The motion of the CMGs is plotted in Fig. 8.10. The maximum absolute error in torque is 7×10^{-3} Nm, which is 1.5% of that commanded by the control law. This is due to the finite gimbal accelerations and is larger than in the previous experiment as greater accelerations are required to achieve the maximum gimbal rates of 23.0 °/s and −20.0 °/s. The largest gimbal excursion during the manoeuvre is 17 ° with a final excursion of 13 ° after the manoeuvre has been completed. The angular momentum and $\det(\bar{c}\bar{c}^T)$ plots show that the system operates within 19% of the momentum workspace for a flywheel rate of $\dot{\psi} = 3000$ rpm.

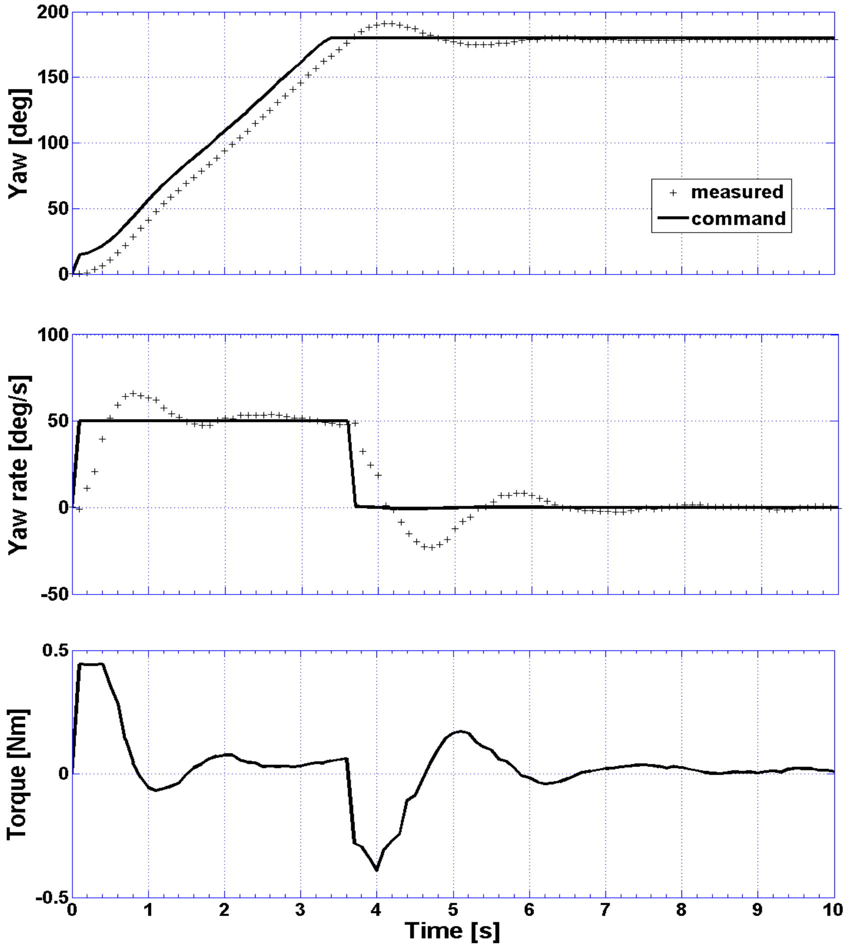

Figure 8.9: Dry-land ramp control response in the presence of a disturbance

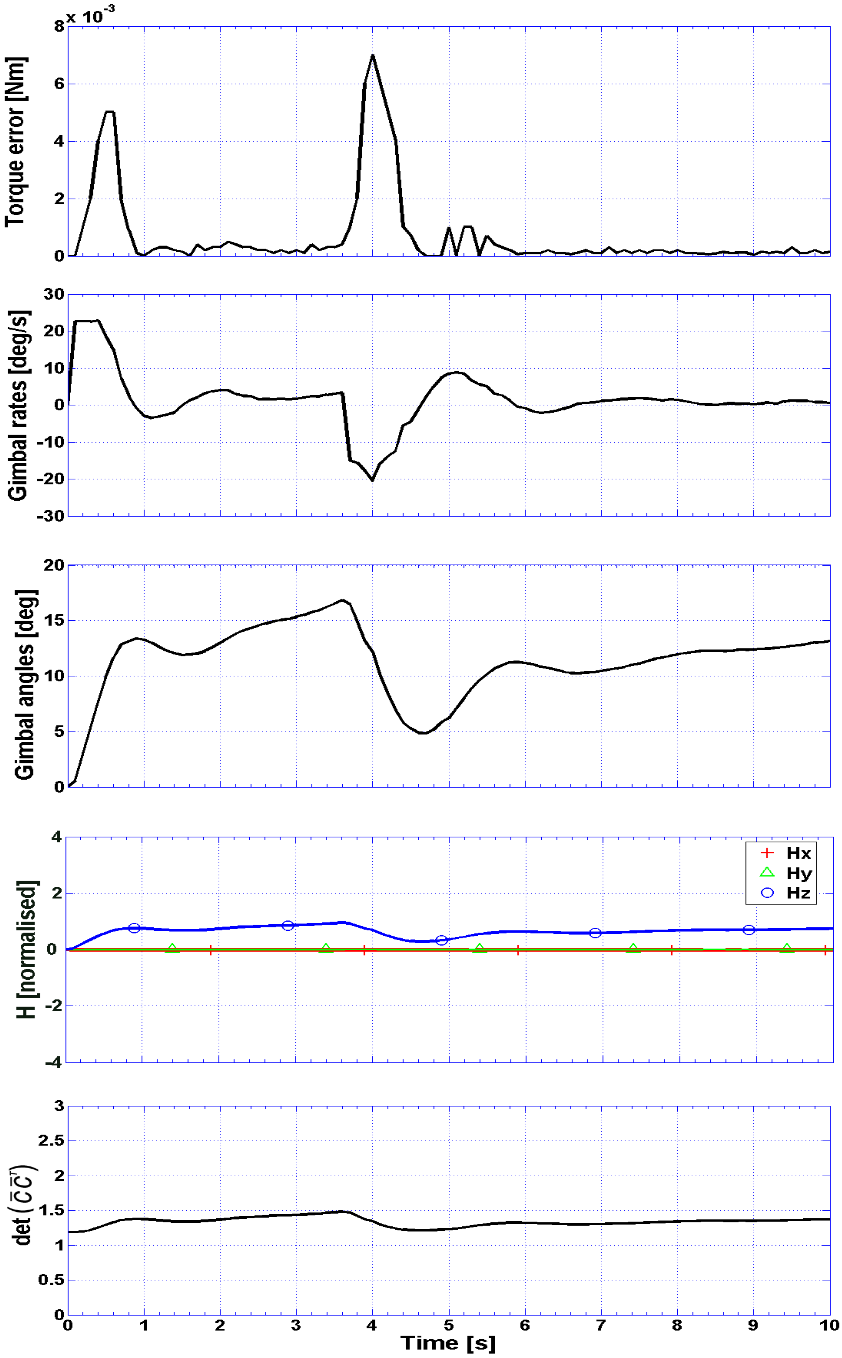

Figure 8.10: Ramp response CMG steering with $\dot{\psi} = 3000\,\text{rpm}$

Discussion of results

The CMG system operates well within the momentum workspace to generate the command torques determined by the control law to achieve a more than acceptable attitude response with no offset error. The control law is robust to the non-linear dynamic disturbance of the bearing and due to the vibrations of the system. These disturbances are functions of the speed and acceleration of the system and so in this respect are somewhat similar to the dynamic effects associated with operating within a viscous fluid. The results are promising, indicating that the control law may also be robust to the types of unmodelled disturbances that can be expected when using a simplified model of viscous flow in the control law.

8.3 Underwater dynamics

A series of underwater experiments was carried out to verify the theoretical developments and demonstrate the practical application of Zero-G Class underwater robots. These were performed using the Zero-G prototype IKURA in the experimental pool facilities of the URA laboratory at the University of Tokyo. During these experiments two tethers were attached as pictured in Fig. 8.11. One of these is a safety line and the other is used to supply power and to transmit information to a host PC. Experiments were first performed to verify the open-loop dynamics of the complete CMG, body and fluid system. Next, the performance of the proposed control law is assessed by comparing its closed-loop response with two alternative control laws. Finally, an experiment was performed to assess the ability of the CMG system to stabilise the passively unstable self-propelled translational dynamics of a Zero-G Class underwater robot. Video footage of this experiment can be found in Appendix D.

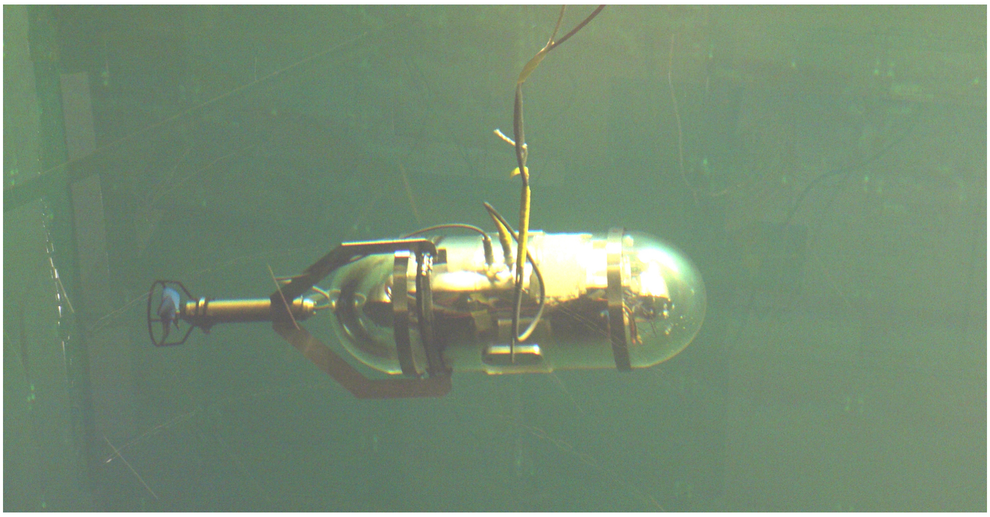

Figure 8.11: IKURA in the $8 \times 8 \times 8\,\mathrm{m}$ test tank facility of the URA laboratory

8.3.1 Open-loop dynamics

The open-loop attitude response of the robot to a series of gimbal rate inputs was experimentally assessed. The measured response is compared to that determined by the dynamic model (3.12) where the added mass and drag coefficients of the robot are determined in Appendix C.

Yaw dynamics

Fig. 8.12 shows the open-loop response of the robot to two cycles of a cosinusoidal torque input about the yaw axis. The simulated response has a reasonable correlation with that measured, accurately modelling the phase dynamics. However, the simulation consistently over-predicts the yaw rate with a maximum value of $37\,^{\circ}/\mathrm{s}$ compared to a maximum measured value of $32\,^{\circ}/\mathrm{s}$. This corresponds to a yaw rate error of 16% and this results in a growth in the attitude error as the experiment progresses. Since the experiment was performed in a controlled environment the only likely explanation is that these effects are due to the tether. The two cables twist as the robot rotates and this retards yaw motion. Any initial twist in the cables would have a tendency to unwind and this would explain the drift observed in the measured yaw. However, a further investigation would be necessary to confirm this point.

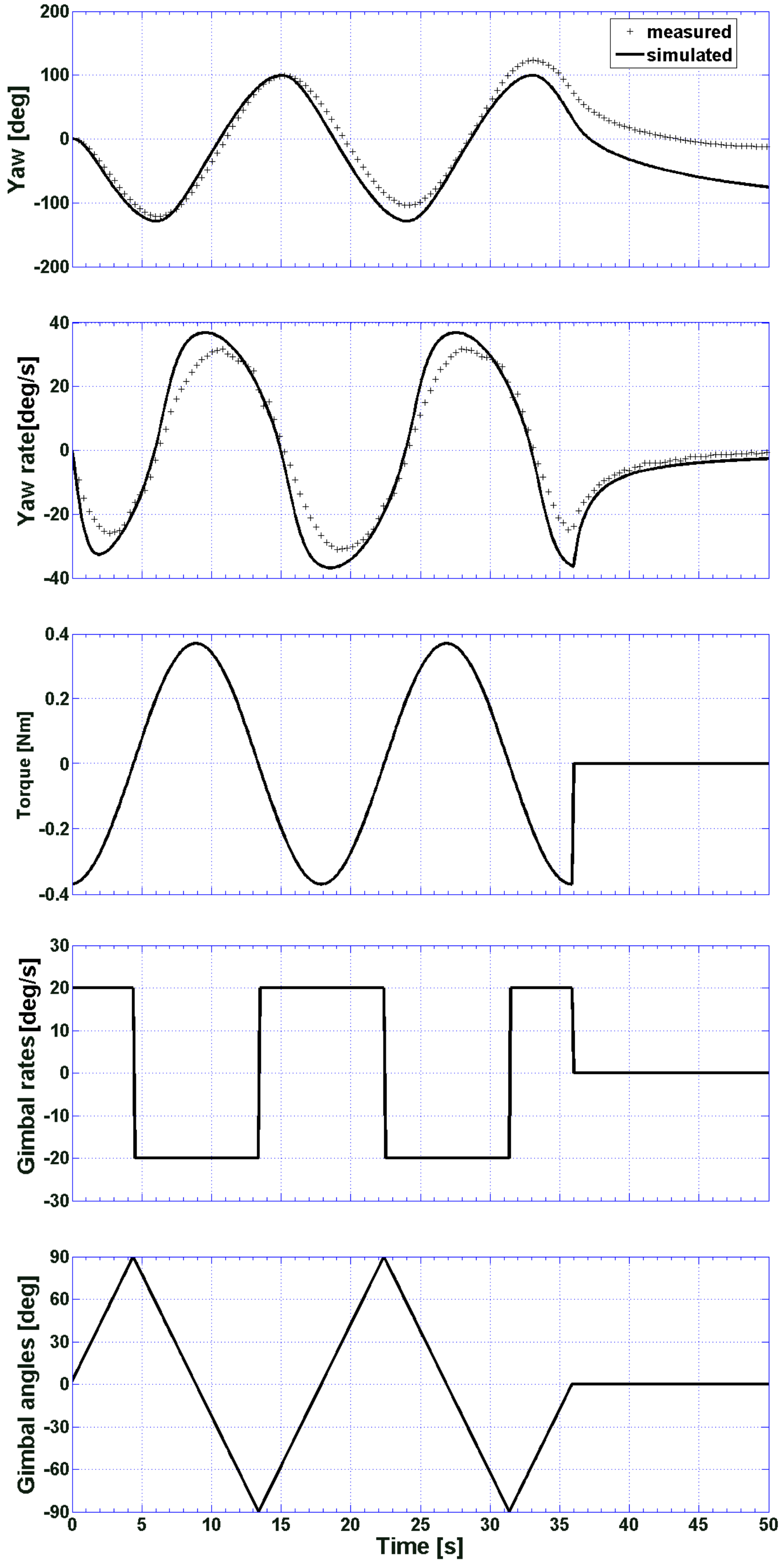

Figure 8.12: Underwater robot open-loop yaw response with $\dot{\psi} = 5000\,\text{rpm}$

Pitch dynamics

Fig. 8.13 shows the open-loop response of the robot to two cycles of a cosinusoidal torque input about the pitch axis. The measured response indicates that the robot does not have absolutely coincident centres of gravity and buoyancy. A reasonable simulated response can be achieved by modelling a righting lever of 0.4 mm as discussed in Appendix C. The simulated response initially shows good agreement with the actual attitude and angular rate measurements. However, as the robot pitches in the positive direction with its nose down, the thruster mount comes into contact with the cradle mechanism when the robot reaches 70 °, which occurs at $t = 14\,\mathrm{s}$ and $t = 32\,\mathrm{s}$. This causes oscillations in the angular rate measured and stops the robot from pitching further and this accounts for the significant deviation from the simulated dynamics. However, when the robot pitches with its nose up, it reaches -90° and shows a much closer agreement with the simulation. This indicates that the effects of the tether on the pitch dynamics are negligible due to the cradle mechanism described in the previous chapter.

The motion of the CMGs is plotted in Fig. 8.14. The CMG units on the y-axis steer in opposite directions to move the angular momentum vector in the y-direction to generate a pitching torque. The momentum vector has a maximum normalised value of $2c^*$ in this direction that occurs when the two CMG units reach their maximum excursion. This is illustrated in the $\det(\bar{c}\bar{c}^T)$ plot and in the geometric representation of the momentum vector. These imply that the system is more prone to becoming singular in pitch than in yaw.

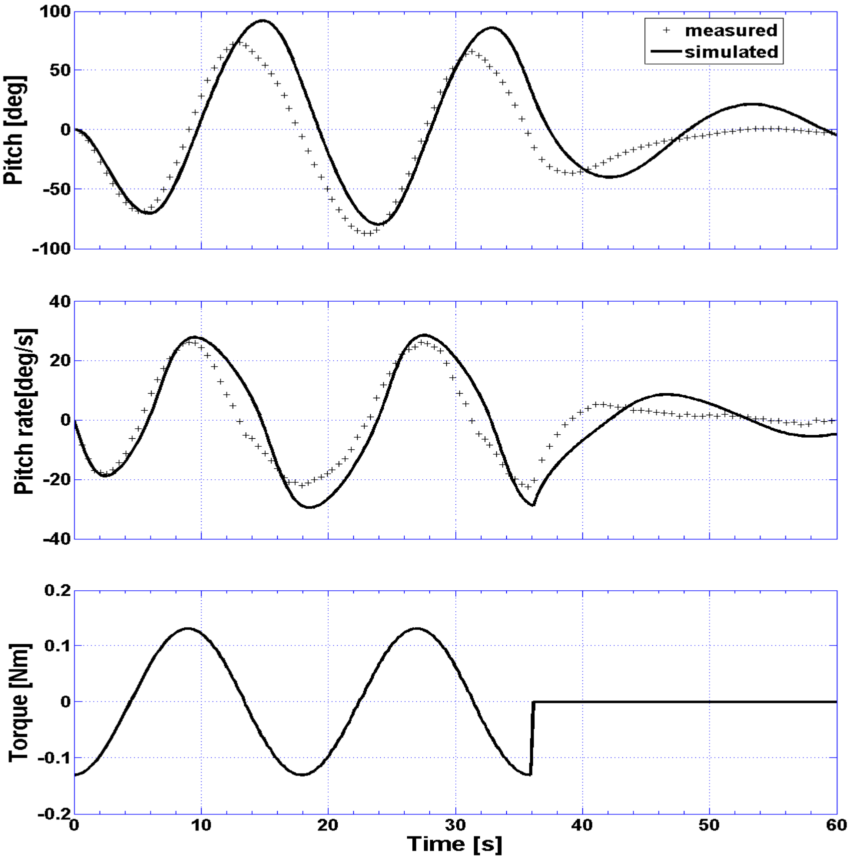

Figure 8.13: Underwater robot open-loop pitch response

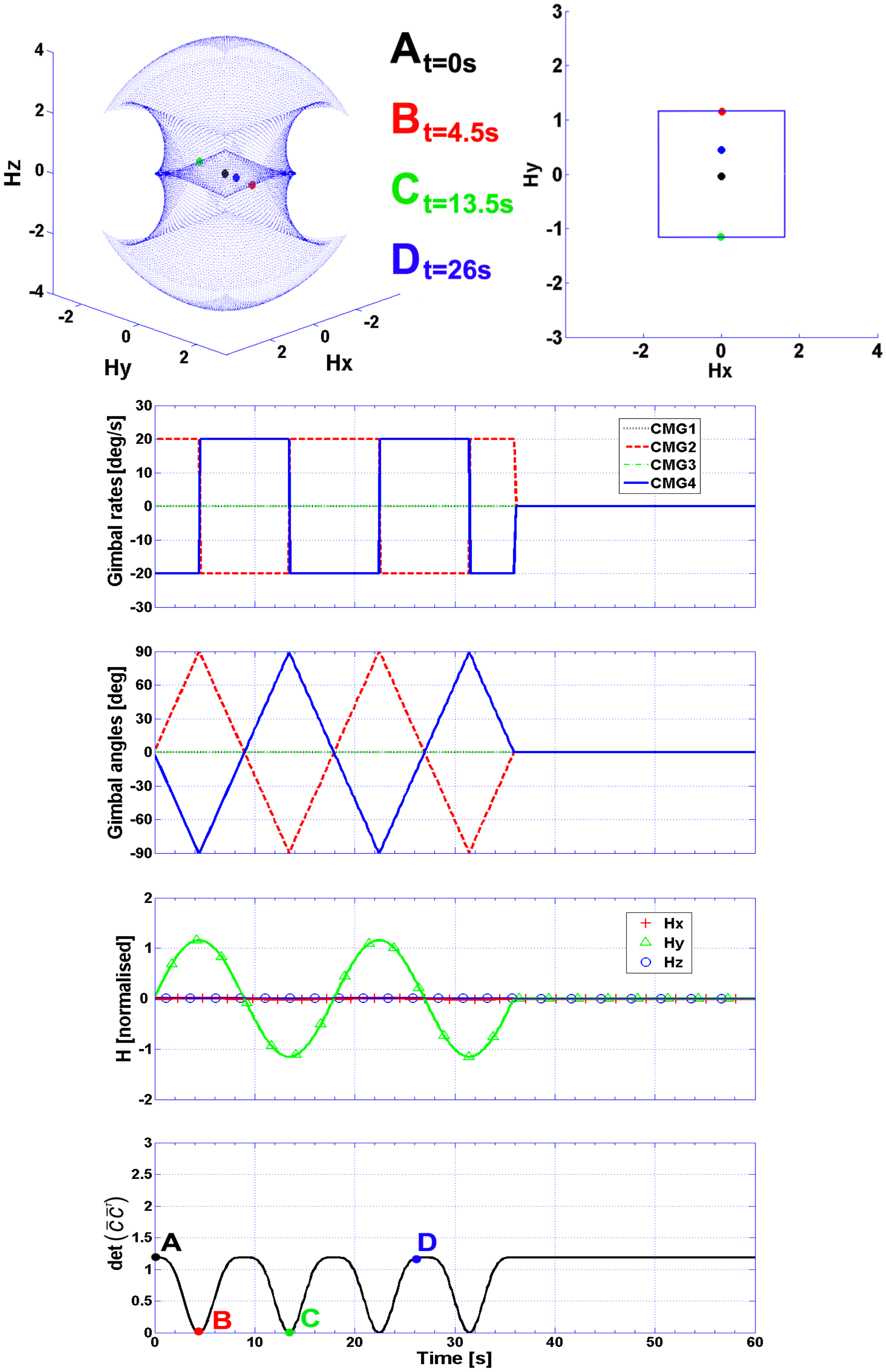

Figure 8.14: Pitch dynamics CMG steering with $\dot{\psi} = 5000\,\text{rpm}$

8.3.2 Closed-loop control

The closed-loop response of the complete CMG, body and fluid system is assessed in a series of underwater experiments using the proposed control law (PC) (4.6). To allow for comparison the experiments were repeated under identical conditions with two alternative control laws:

$$\begin{aligned}\tau_{u_A} &= \mathbf{Q}^T(\mathbf{q})k_q\mathbf{e_q} + k_\omega\mathbf{e}_\omega \\ \tau_{u_B} &= \mathbf{Q}^T(\mathbf{q})k_q\mathbf{e_q} + [k_\omega\mathbf{e}_\omega - \mathbf{J}_{tot}\dot{\omega}_d - \omega \times \mathbf{\Pi} - u \times \mathbf{P}]\end{aligned}$$

The first of these, Control law A (CA), is a PD controller that generates its command based only on the error in state. This control law is the feedback part of PC and neglects any feedforward modelling of the dynamics. The second, Control law B (CB), also takes into account the dynamics of the CMG and body but, in contrast to PC, does not account for the hydrodynamic interactions of the body. An extensive parametric study determined the appropriate control gains for the system in both pitch and yaw to be $[k_q, k_\omega] = [0.5, 0.3]$.

Yaw control

Fig. 8.15 shows the response of the robot to a 30 ° step yaw command. The yaw rate command plotted is that computed for the response of the robot using PC. By modelling the coupled dynamics of the CMG and body, both PC and CB achieve a faster response than CA with an initial peak in torque due to the sudden change in the body rate command in $\dot{\omega}_d$. The slower response of CA results in oscillations in the attitude response and so the robot takes longer to stabilise at the desired state. By modelling the hydrodynamic interactions of the body, PC generates marginally larger torques than CB to achieve a faster dynamic response.

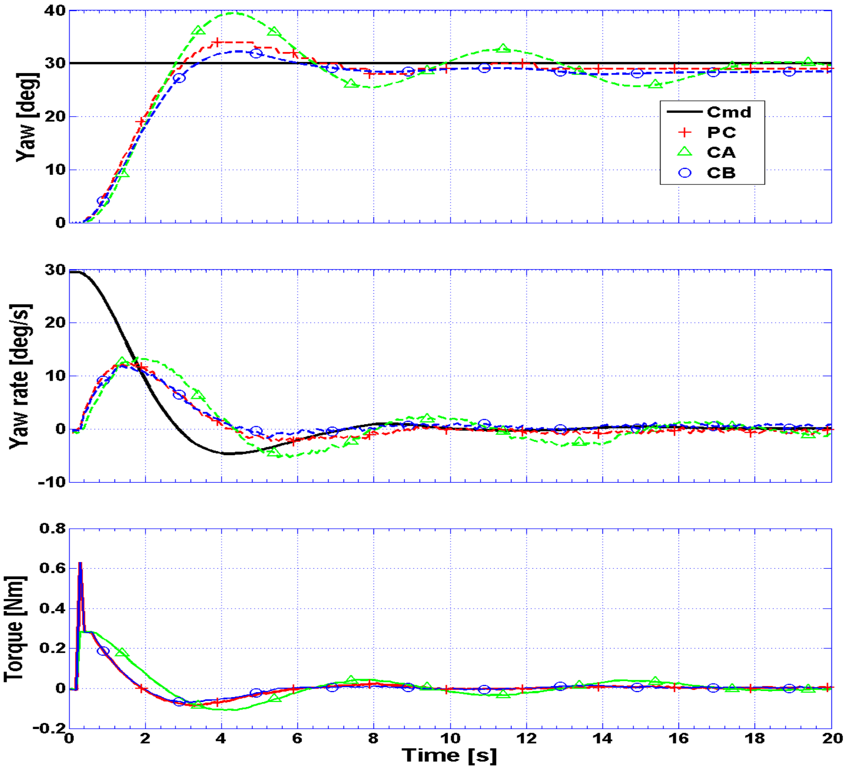

Figure 8.15: Underwater robot step yaw control

Fig. 8.16 shows the response of the CMGs. The steps in the torque profiles for PC and CB are due to the numerically imposed gimbal rate limit of 20 °/s that was set to protect the system. After the initial acceleration of the gimbals, the CMGs steer smoothly with a negligible difference between the desired torque and that generated. The control behaviour of PC results in the smallest gimbal excursions and gives the most efficient use of the system, with 20% less motion of the momentum vector than CB. All three control laws fall marginally short of the desired yaw attitude with an offset of 2 ° using PC. The momentum of the system continues to change at the final state and a constant torque is exerted towards the command state. This equilibrium can be explained by the previously discussed torque effect of the tether twisting, which cancels the torque generated by the system. Unlike the dynamic disturbance of the bearing and the viscous forces, the cable has a static effect that causes this offset.

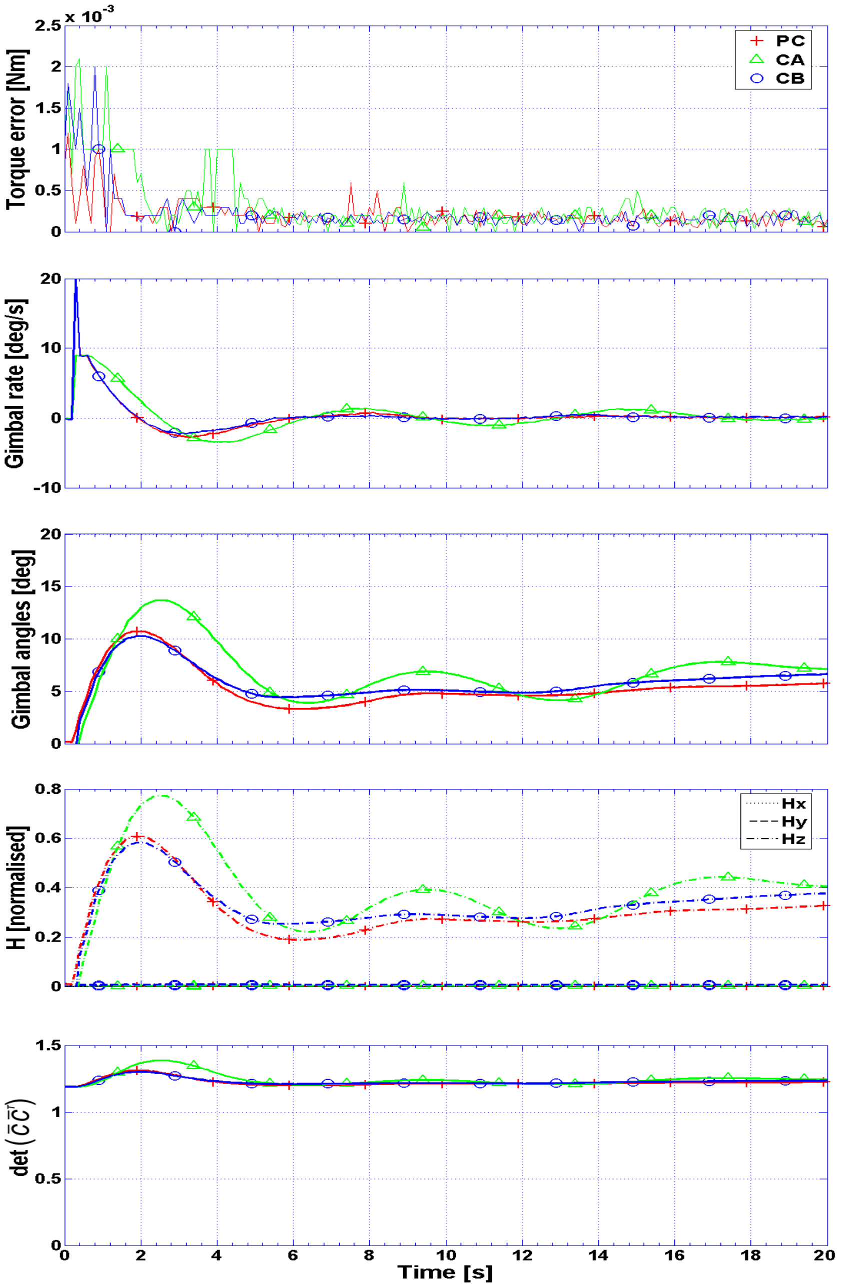

Figure 8.16: Yaw control CMG steering with $\dot{\psi} = 8000\,\mathrm{rpm}$

Pitch control

Fig. 8.17 shows the pitch response of the robot using the three different control laws. A command is sent for the robot to first adopt a horizontal pitch angle and then a step command to pitch 30° is sent with the command pitch rate calculated as a function of the attitude error. The command pitch rate computed for the robot's response using PC is shown. The results show a similar trend to the previous yaw control experiment. The attitude dynamics with CA are oscillatory due to the slower torque response of the control law compared to PC and CB. Again the torques generated with PC and CB have an initial peak due to the derivative of the body rate command $\dot{\omega}_d$. In this case however, CB struggles to reach its final state. By modelling the hydrodynamic interactions of the robot, PC generates larger torques than CB when the robot first accelerates and when it rotates at large rates to achieve a superior response by overcoming the hydrodynamic added inertia and viscous drag respectively. Fig. 8.18 shows that this behaviour results in significantly smaller gimbal excursions than CA and CB, with 30% less motion of the momentum vector than CB. In each case the robot's attitude falls short of the command with an offset of 3° using PC. As the robot maintains its attitude the CMG system continues to exert a constant torque. Since the experiments were carried out in a controlled environment with no currents or waves, the only explanation is that the robot has a small righting moment that works against the CMG system. This confirms the findings of Section 8.3.1.

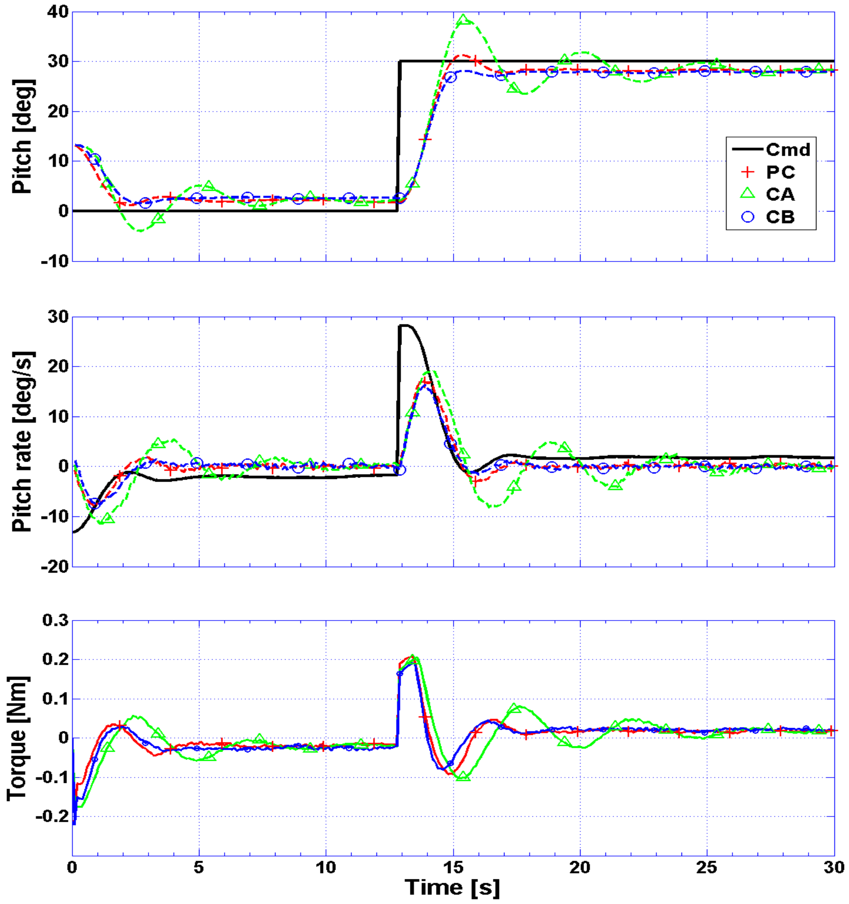

Figure 8.17: Underwater robot step pitch control

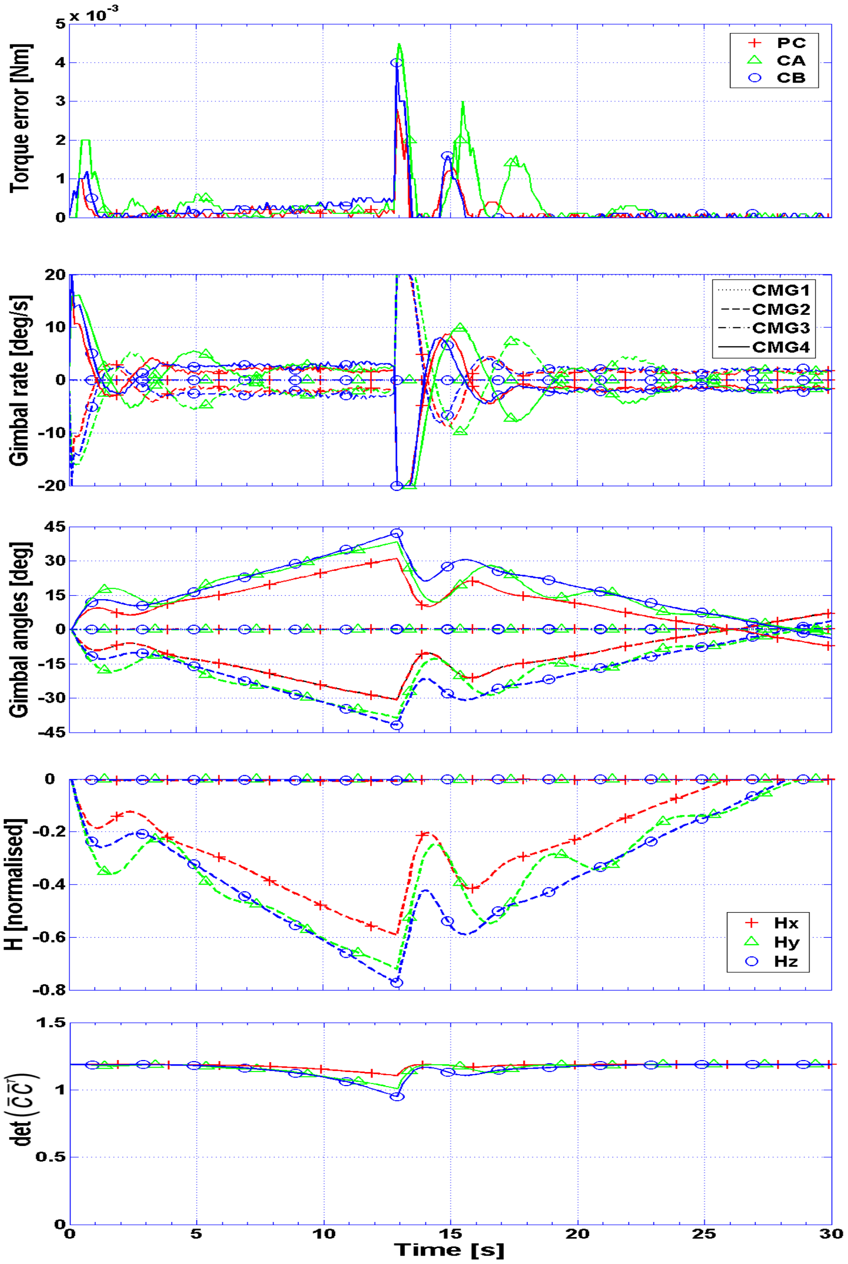

Figure 8.18: Pitch control CMG steering with $\dot{\psi} = 8000\,\text{rpm}$

Discussion of results

In the experiments the attitude using PC falls 2° short of the command in yaw and 3° short of the command pitch due to the static disturbance of the tether and the righting moment respectively. It is reasonable to assume that this will not pose a problem for yaw control in untethered operation. The static attitude offset can be overcome by including an integral error term in the control law. However, the system would still have to resist the righting moment and the CMGs would eventually reach the boundary of their operating envelope. A superior solution is to eliminate or at least reduce the righting moment that forms the root of the problem. Despite these problems the analysis shows that the proposed method takes advantage of the coupled behaviour of the CMG, body and fluid system to make more efficient use of the system, achieving a superior control response with 20% less overall control activity in yaw and 30% less in pitch than the alternative control laws.

8.3.3 Stabilision of unsteady self-propelled translational dynamics

The final experiment in this chapter verifies the ability of the control system to actively stabilise the passively unstable, unsteady self-propelled translational dynamics of a Zero-G Class underwater robot. This requires a fast response and a high resolution of attitude control and is essential for the practical application of Zero-G Class underwater robots. Video footage of this experiment can be found in Appendix D.

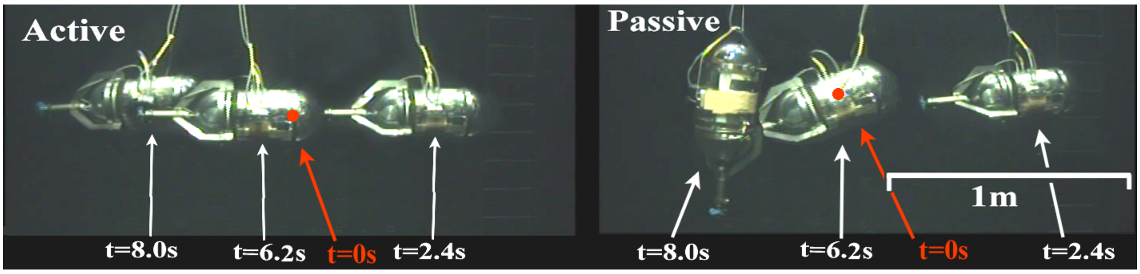

Figure 8.19: Image sequence of the actively stabilised and passive surge response

Fig. 8.19 is an image sequence taken by an underwater camera that compares the actively stabilised and passive response of the robot to identical thruster inputs as shown in Fig. 8.20. The image shows how the cradle mechanism rotates to eliminate the torque effects of the tether about the robot's pitch axis. In the passive case the flywheels are stationary and so the CMGs are inactive. In the active case the flywheels rotate at 10, 000 rpm and the CMG system responds to actively stabilise the robot's attitude during the manoeuvre.

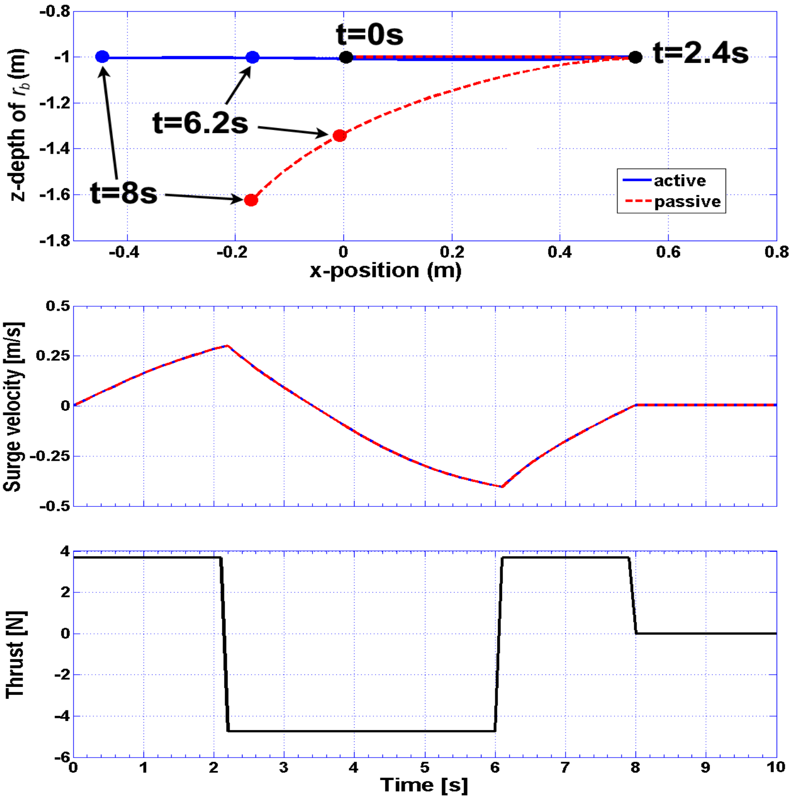

Figure 8.20: Actively stabilised and passive translational dynamics

The position of the centre of buoyancy is computed in real-time using the dynamic model (3.12) with actual attitude and angular rate measurements. The parameters for the translational dynamic model are developed in Appendix C. Inspection of Fig. 8.19 using the length of the robot as a reference in the visual images shows that the translational dynamics computed on-line are reasonable. The passive response is unstable and Fig. 8.21 shows that the robot pitches to 70 ° and yaws to 45 °. In the active case the CMG system responds to stabilise the robot's attitude during the manoeuvre, generating torques in the order of 0.1 Nm to stabilise the attitude response of the robot to within ±3 °. The reaction to the torque exerted by the thruster causes the robot to roll. Although this effect is relatively small it may be problematic for real-life applications and must be either overcome through active stabilisation using the CMGs, or eliminated by using a contra-rotating propeller to actuate surge.

a.) Attitude

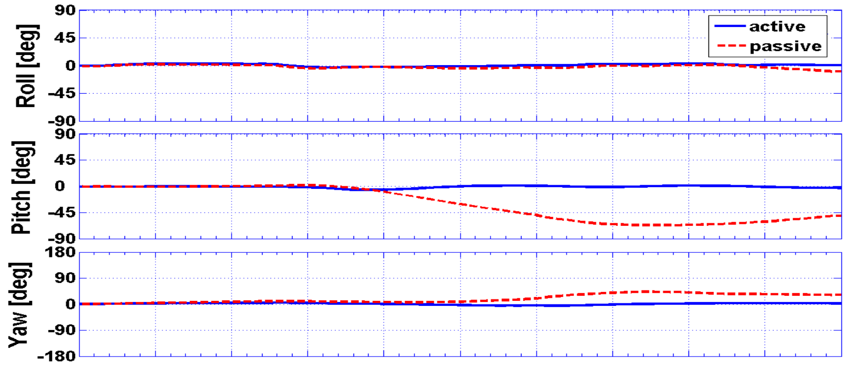

b.) Angular rate

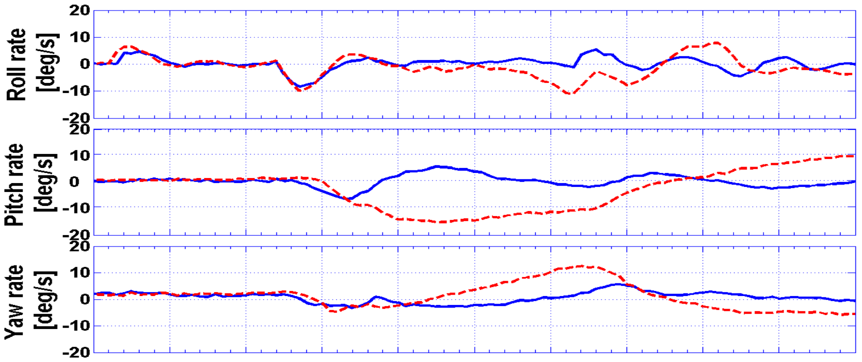

c.) Torque

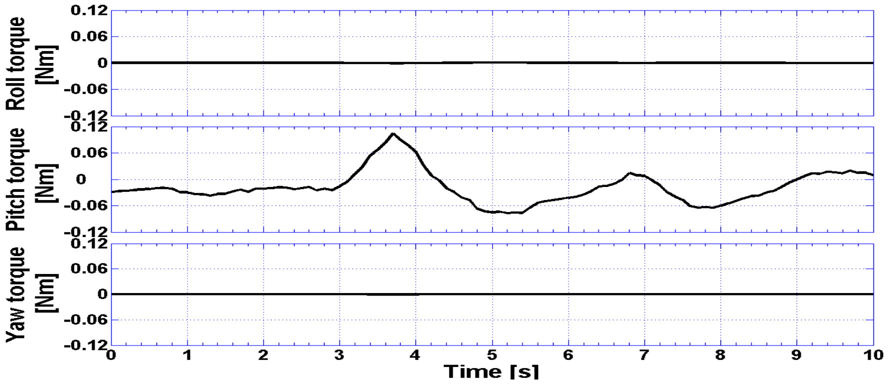

Figure 8.21: Actively stabilised and passive attitude response

Fig 8.22 shows that the system responds smoothly to generate the necessary torque. The total absolute error in the torque generated about all three rotational axes is within 2×10^{-3} Nm of that determined by the control law. This error is 2% of the torque generated by the system and is due to the finite accelerations of the gimbals. The maximum gimbal rate is 10 °/s and the system operates well within the limits of the constrained workspace.

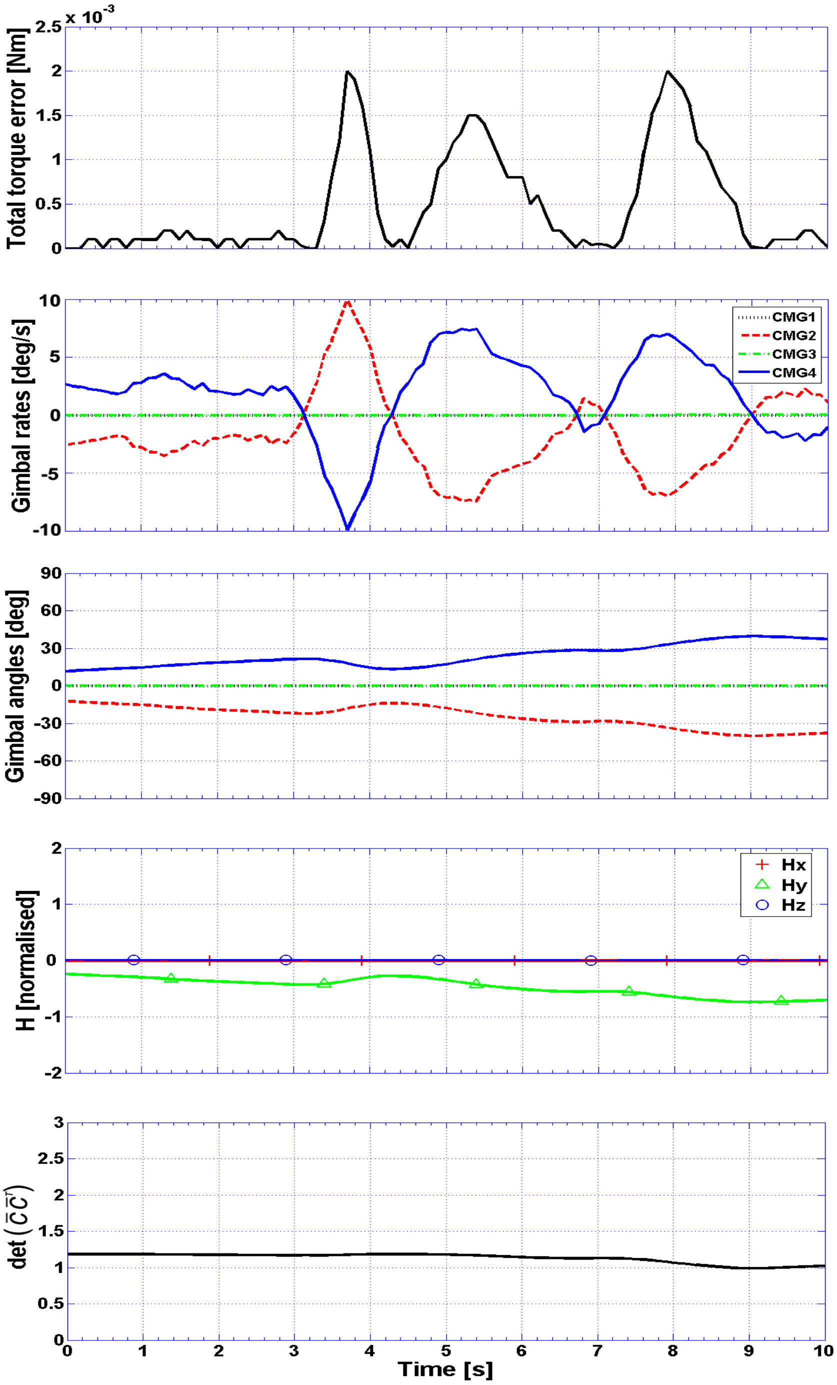

Figure 8.22: CMG steering for active stabilisation of surge with $\dot{\psi} = 10,000\,\text{rpm}$

The results of this analysis verify that the CMG based attitude control system has a sufficiently fast and high resolution of response to actively stabilise the passively unstable, unsteady self-propelled translational dynamics of a Zero-G Class underwater robot.

8.4 Summary

The experiments performed in this chapter verify the theoretical developments of this research and demonstrate the practical application of Zero-G Class underwater robots. The actuation capabilities of the CMG system have been assessed, with the results confirming the validity of the CMG equations and demonstrating that the steering law developed is applicable in real-time and remains exact to the desired torque. In practical applications errors of up to 8×10^{-3} Nm can be expected due to the finite accelerations of the gimbals. This corresponds to less than 2% of the torque generated in the experiments performed, which is more than acceptable for this scale of application. This error is a function of the limits on gimbal acceleration and so depends on the ratio of the torque available in the servos used to actuate the gimbals and the inertia of the CMGs about the gimbal axes. However, it is possible to reduce this error and by increasing the flywheel rates to directly reduce the required gimbal accelerations. The dynamic equations for the CMG and body system have been assessed in dry-land experiments. The control system demonstrates a fast response and high resolution of attitude control and is robust to the dynamic disturbance due to non-linear bearing friction and the vibrations of the system.

The equations of motion for the CMG, body and fluid system have been verified in underwater experiments. Difficulties in yaw and pitch control arise from the static disturbance of the tether and the righting moment respectively. These cause a static offset in the closed-loop step response of the robot's attitude. It is suggested that this can be overcome by including an integral error term in the control law in future applications. However, these disturbances place a significant burden on the attitude control system and it is important to eliminate or at least reduce these static effects. In the case of yaw it is reasonable to assume that this will not pose a problem for control in untethered operation. In the case of pitch control there are a number of practical difficulties encountered when attempting to achieve coincident centres of gravity and buoyancy in a robot with moving internal parts. One suggestion is to use electronically controlled moveable internal masses to calibrate the centre of gravity of the robot once it is in the water. Despite these problems the analysis shows that the proposed method takes advantage of the coupled behaviour of the CMG, body and fluid system to make a more efficient use of the system, achieving a superior control response for 20 - 30% less overall control activity than the alternative control laws. Finally, the ability of the system to actively stabilise the passively unstable, unsteady self-propelled translational dynamics of a Zero-G Class underwater robot has been verified.

The experiments demonstrate that, in contrast to traditional underwater actuators, the actuating effect of CMGs is independent of their environment as they generate torque using only the momentum stored in their flywheels. The CMG system demonstrates a speed and resolution of attitude control that is essential for the practical application of Zero-G Class underwater robots and it is difficult to envisage how this could be otherwise achieved. The experiments establish that CMGs form an ideal basis for the attitude control system of Zero-G Class AUVs. The advantages of the new manoeuvring capabilities offered by the application of CMGs in Zero-G Class underwater robots are demonstrated in the next chapter.

Chapter 9

Zero-G manoeuvring and implications for underwater research

Typically underwater robots rely on passive stability to maintain a useable orientation. This limits their attitude to a circle in yaw and confines their motion to that along a series of two-dimensional planes. This chapter demonstrate the unrestricted attitude control and three-dimensional manoeuvring capabilities of Zero-G Class underwater robots. First, a series of on the spot attitude control manoeuvres are performed to demonstrate the necessary range of control for a Zero-G to adopt any attitude on the surface of a sphere. Next, the robot demonstrates a three-dimensional approach to mission planning by performing a vertically pitched diving and surfacing manoeuvre in surge. The implications of the unique manoeuvring capabilities for underwater research using AUVs and the potential offered by the application of CMGs to Zero-G Class underwater robots are discussed.

9.1 Unrestricted attitude control

This section describes experiments to demonstrate the unrestricted attitude control capabilities of Zero-G Class underwater robots, where unrestricted attitude control has been defined earlier as the ability to adopt and maintain any attitude on the surface of a sphere with a zero radius turning circle. This requires the robot to be capable of ±180° yaw and ±90° pitch control. Video footage of the experiment can be found in Appendix D.

Yaw manoeuvre

In this experiment the robot performs a series of 45° rotations to cover the range of yaw angles between ±180° in order to demonstrates the necessary range of yaw for unrestricted attitude control. The sequence of images in Fig. 9.1 shows a series of plan views of the experiment taken by a camera mounted on a crane above the robot and images taken by an underwater camera. The image sequence shows that the robot is capable of performing a full rotation in yaw. It can be seen that the manoeuvre is performed with an effectively zero radius turning circle. The attitude response of the robot and the torque generated by the CMG system are plotted in Fig. 9.2.

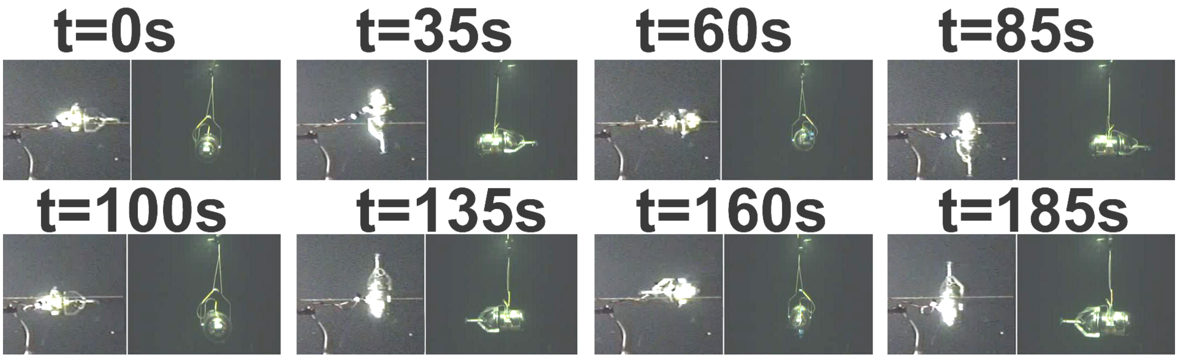

Figure 9.1: Image sequence of ±180° yaw manoeuvre with plan and side views

As each step of the yaw command is executed the robot responds smoothly, accelerating and decelerating to adopt and maintain the desired attitude. The control system generates a peak torque with a magnitude of 0.6 Nm each time a new command is sent. The performance of the system is consistent despite the changing gimbal angles, as shown in Fig. 9.3.

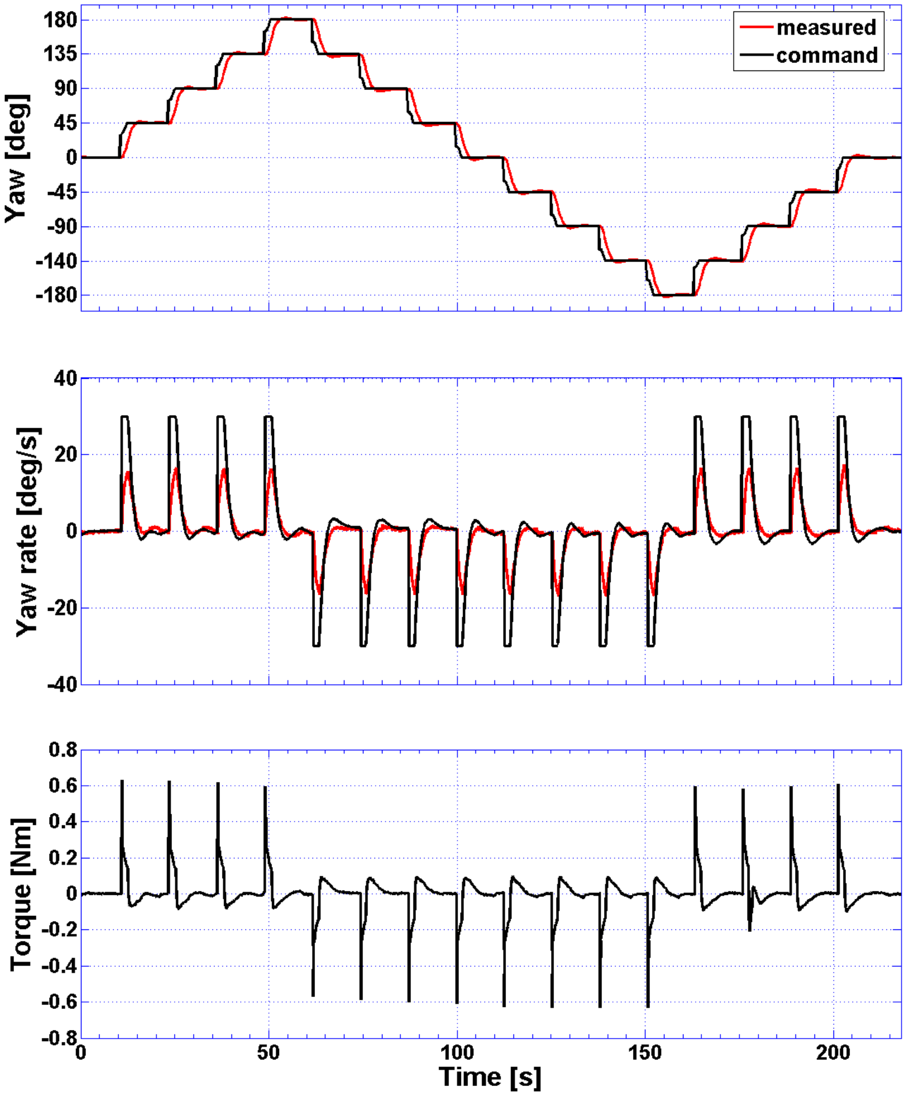

Figure 9.2: Control response for ±180° yaw manoeuvre in steps of 45°

The system operates within the constrained workspace for a flywheel rate of $\dot{\psi} = 8000\,\text{rpm}$ with a maximum gimbal excursion of 30 °. The gimbal rates reach the 20 °/s limit imposed to protect the system. The steering law keeps the torque generated to within $8 \times 10^{-3}\,\text{Nm}$, 1.3%, of the command torque. This error is due to the finite accelerations of the gimbals.

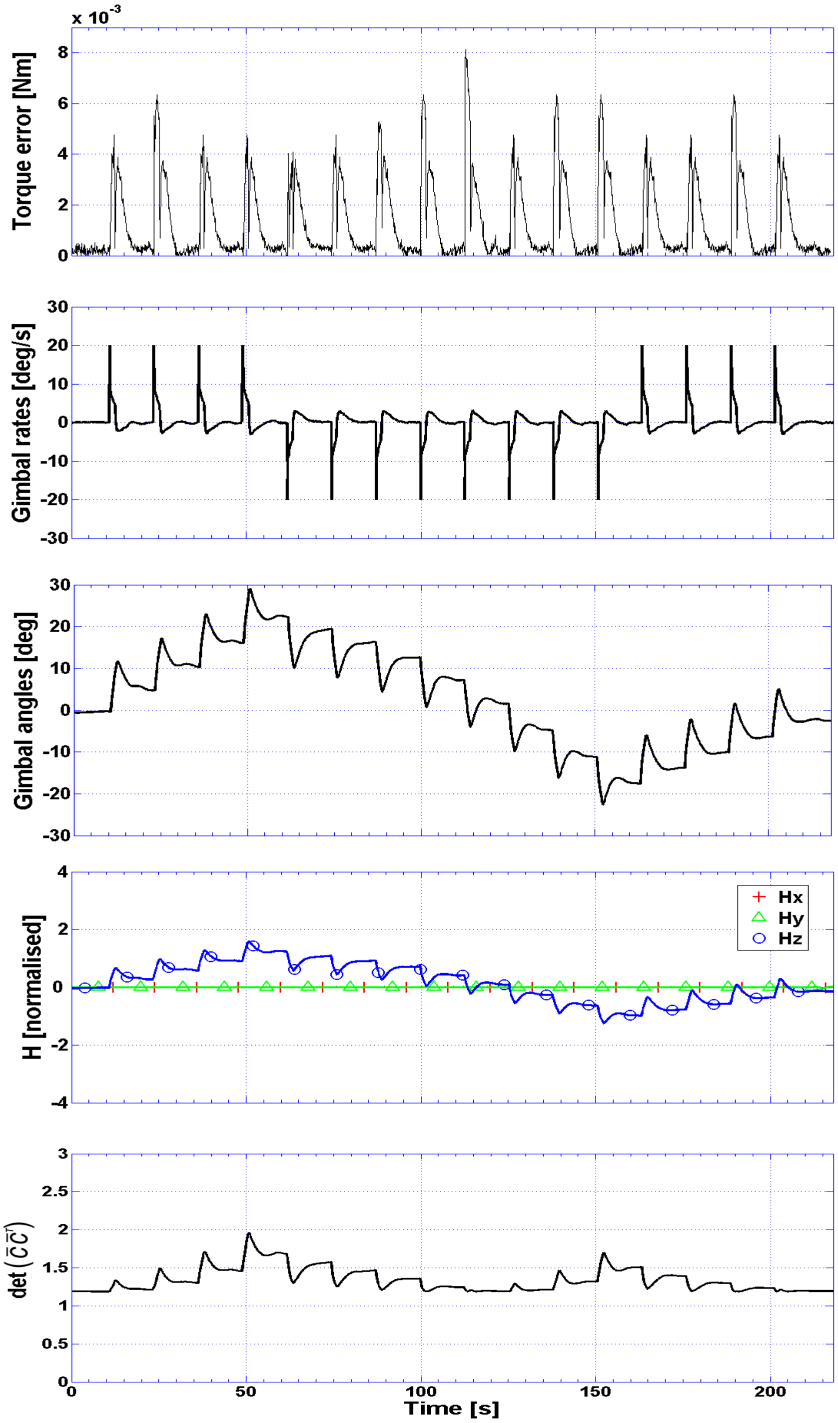

Figure 9.3: Yaw manoeuvre CMG steering with $\dot{\psi} = 8000\,\text{rpm}$

This experiment was performed in 45 ° steps to demonstrate a reliable and repeatable control response despite changes in the state of the CMG system. The robot is capable of performing a full rotation in yaw with a zero radius turning circle while operating at 5.3% of its maximum momentum capacity and so can adopt and maintain any attitude in yaw.

Pitch manoeuvre

In this experiment the robot adopts ±90° vertical pitch angles to demonstrate the necessary range of pitch for unrestricted attitude control. Since quaternions are used to describe the robot's attitude there are no singularities in the control law. Fig. 9.4 shows an image sequence taken by an underwater camera. Complete video footage can be found in Appendix D.

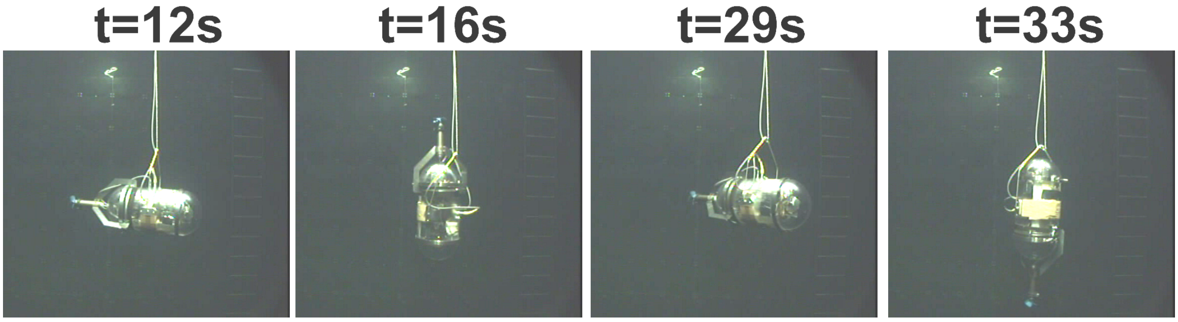

Figure 9.4: Image sequence of ±90° pitch manoeuvre

The robot first adopts a horizontal attitude before pitching to 90° with its nose down. As the robot pitches the thruster mount comes into contact with the cradle mechanism and exerts a moment on the robot. However, the control system responds rapidly to stabilise any oscillations in the robot's attitude. The robot then pitches to $-90°$ with its nose up, finally righting itself to complete the manoeuvre. The attitude response of the robot and the torque generated by the CMG system are plotted in Fig. 9.5.

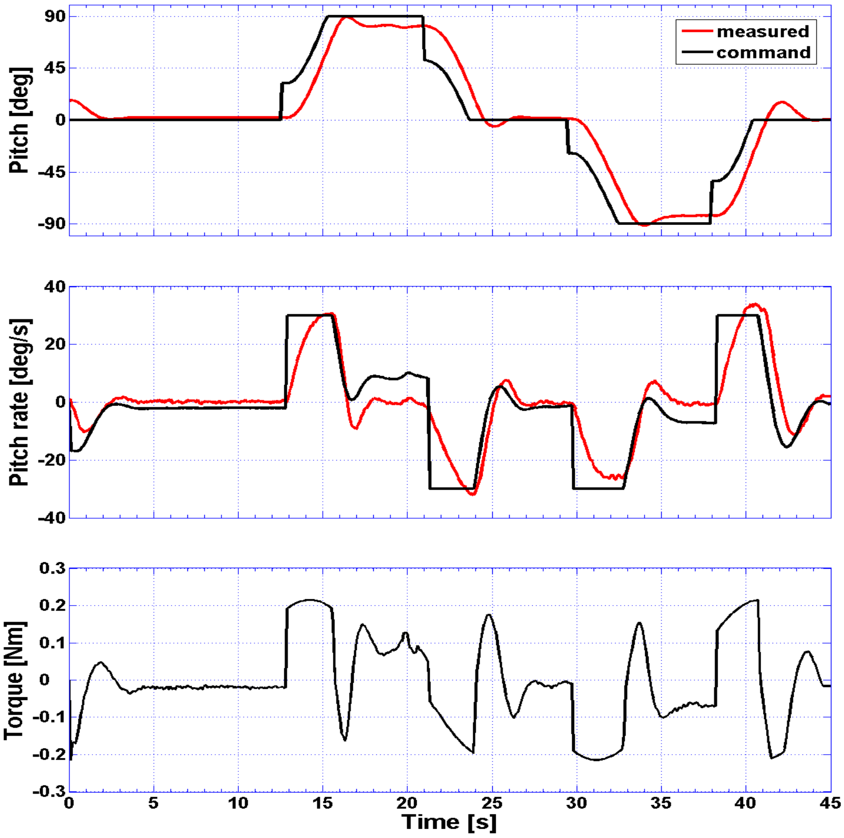

Figure 9.5: Control response for ±90° pitch manoeuvre

The robot reaches a maximum pitch rate of 30 °/s with the CMG system exerting torques in the order of 0.2 Nm to adopt a vertical pitched angle in just over 3 s. The attitude held falls slightly short of 90 ° due to the righting moment discussed in the previous chapter. When pitched the system exerts a constant torque of 0.07 Nm. This confirms the findings of Section 8.3.1, indicating that the robot has a righting moment of 0.4 mm and this places a significant strain on the CMG system. Although the system is capable of performing this manoeuvre with a flywheel rate of 8000 rpm, Fig. 9.6 shows that $\det(\bar{c}\bar{c}^T)$ becomes small with the CMG system closely approaching the boundary of the constrained workspace.

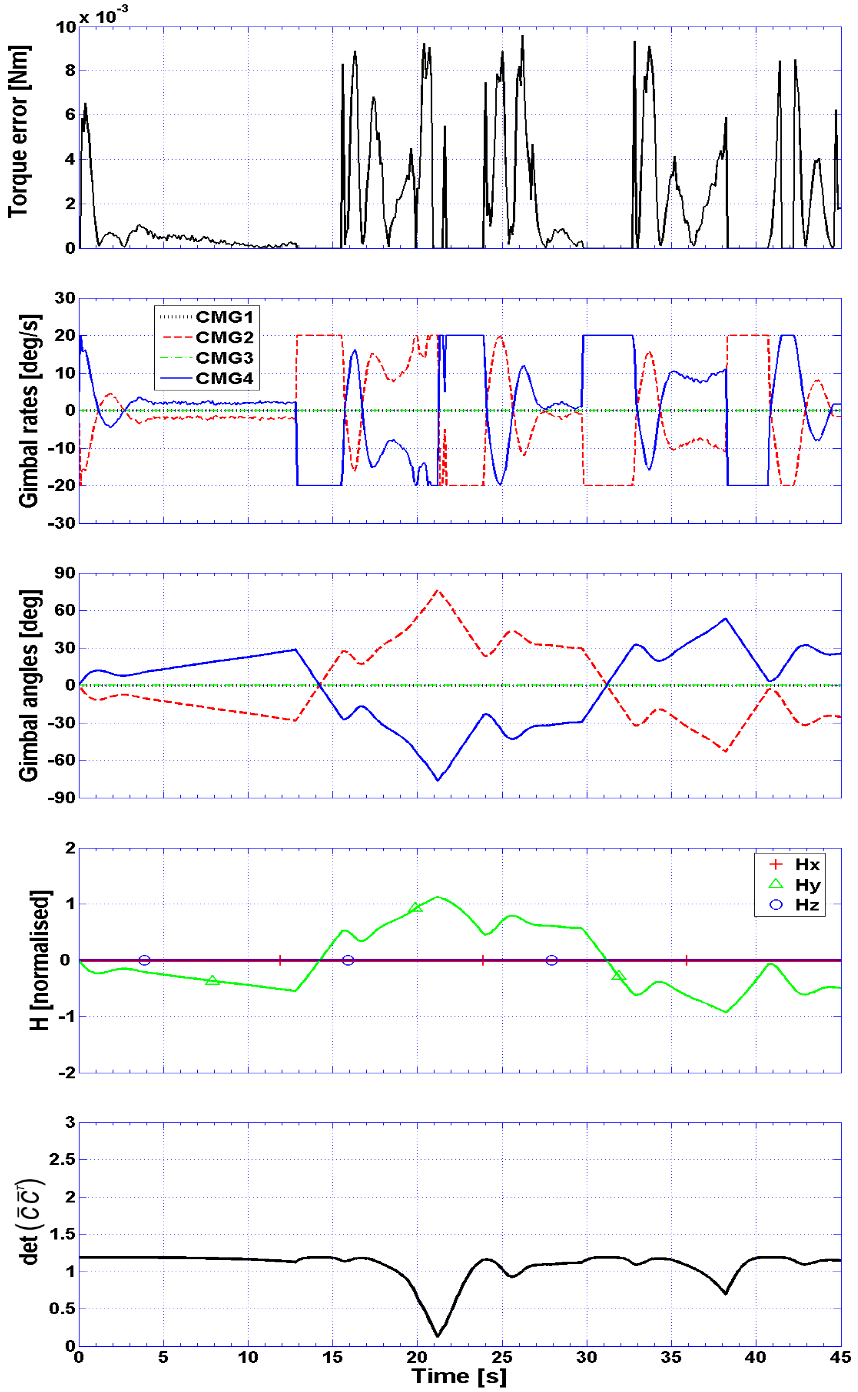

Figure 9.6: Pitch manoeuvre CMG steering with $\dot{\psi} = 8000\,\text{rpm}$

Discussion of results

The experiments demonstrate the necessary range of attitude control in yaw and pitch for the robot to adopt any attitude on the surface of a sphere with a zero radius turning circle. This freedom in attitude control allows Zero-G Class underwater robots to plan and optimise their missions in a three-dimensional manner in a way that has not been possible previously. Furthermore, the fast on the spot attitude control capabilities demonstrated are essential if Zero-G Class underwater robots are to be applied in geometrically complicated, cluttered and even enclosed environments where reorientations must be performed in confined spaces.

The non-coincident centres of gravity and buoyancy cause an offset error in the static attitude response of the robot. It has been suggested in the previous chapter that this can be overcome by including an integral error term in the control law in future applications. However, the non-zero righting moment places a significant burden on the attitude control system. It is possible to sufficiently overcome this problem for practical applications by operating the flywheels at a higher rate to increase the momentum envelope. However, in a finite system the CMGs will eventually reach the boundary of their operating envelope when holding non-horizontal attitudes and it is important to take realistic measures to balance the internal moving parts and reduce the righting moment that forms the root of the problem.

9.2 Vertically pitched diving and surfacing in surge

This section demonstrates how a Zero-G Class underwater robot can plan and optimise its missions in a three-dimensional manner. Fig 9.7 shows an image sequence of the experiment taken by an underwater camera. This is the first time an underwater robot has performed vertically pitched diving and surfacing in surge. Video footage can be found in Appendix D.

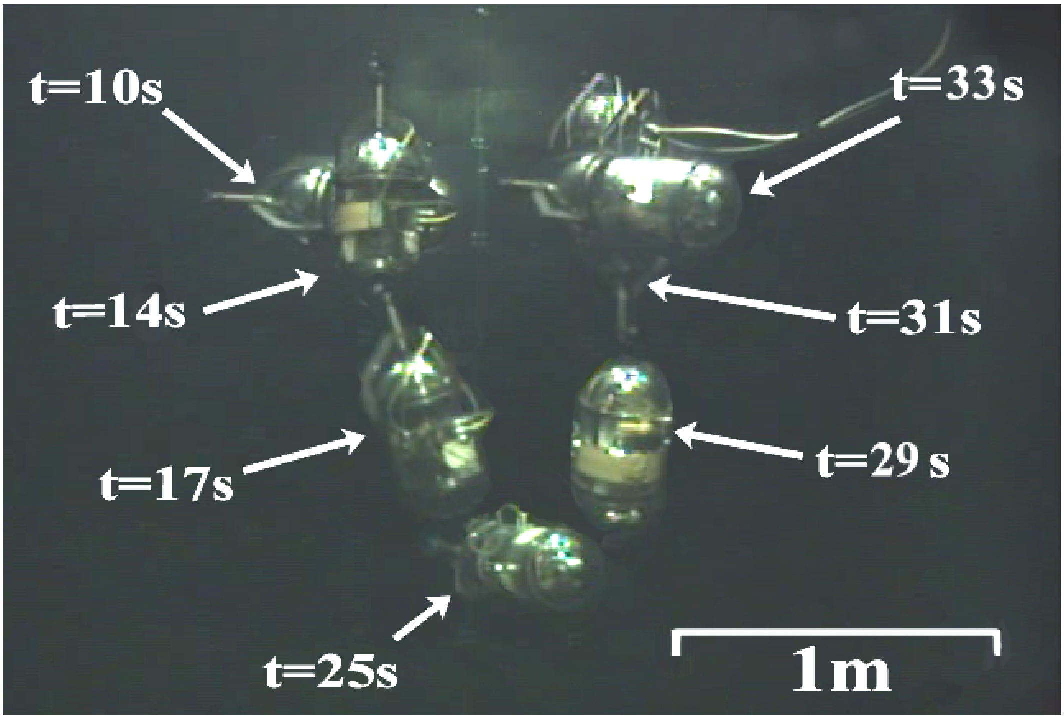

Figure 9.7: Image sequence of a vertically pitched diving and surfacing manoeuvre

The robot first adopts a horizontal attitude before pitching to 90 ° with its nose down and diving vertically in surge. It then holds a horizontal attitude before pitching to -90 ° with its nose up to surface vertically. Finally, the robot rights itself to complete the manoeuvre. The roll and yaw dynamics of the robot were not controlled during the experiment due to the unreliability of the attitude sensor's measurements about these axes at near vertical pitch angles. Clearly the use of alternative sensors must be investigated. The CMG system exerts the necessary torques to reorientate the robot and actively stabilise its attitude as it propels itself through the water. The position data in Fig. 9.8 is computed in real-time by the robot using the dynamic model (3.12) with actual attitude and angular rate measurements. Using the length of the robot as a reference in the image sequence it can be seen that the simulated translational dynamics are reasonable.

Fig. 9.9 shows the attitude response of the robot during the experiment. The CMG system exerts a torque in the order of 0.2 Nm during the pitching manoeuvre to adopt a vertical pitch angle. As the robot propels itself at a vertically pitched orientation, the reaction to the torque exerted by the thruster causes the robot to roll. This can be seen in Fig. 9.7 and in the video footage in Appendix D. It follows that when the robot rights itself after having rolled when vertically pitched, its heading angle will have changed. This effect explains the large yaw angles observed and also accounts for the large yaw rate recorded by the sensor each time the robot rights itself. This can be overcome by actively stabilising roll motion using the CMGs or by using a contra-rotating propeller to actuate surge as discussed in Section 8.3.3.

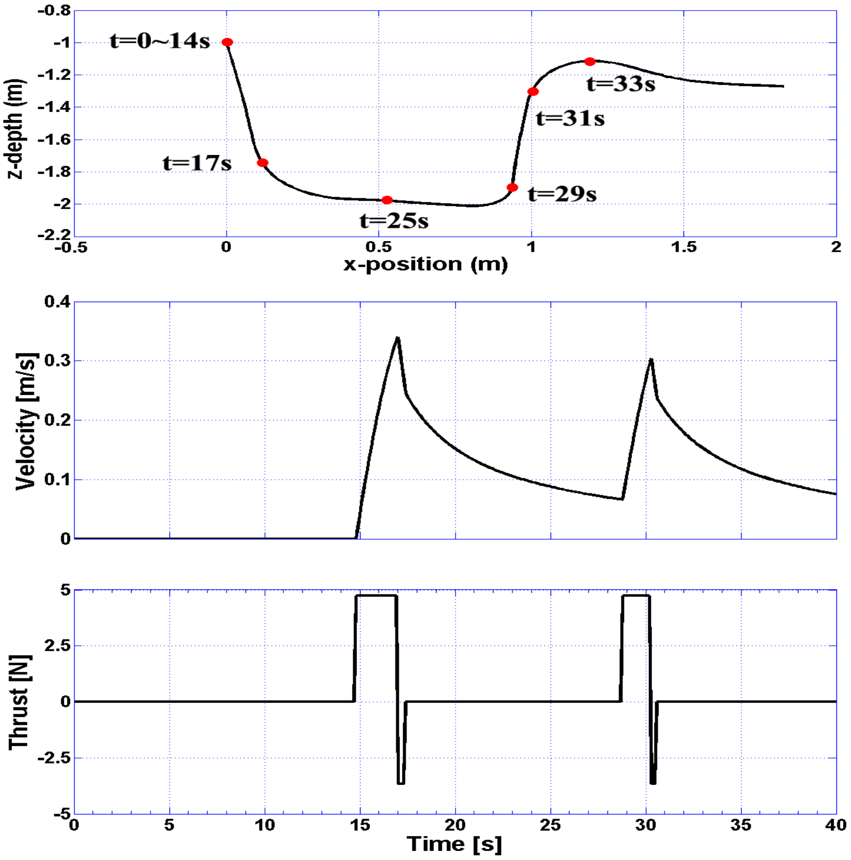

Figure 9.8: Translational dynamics during the diving manoeuvre

a.) Attitude

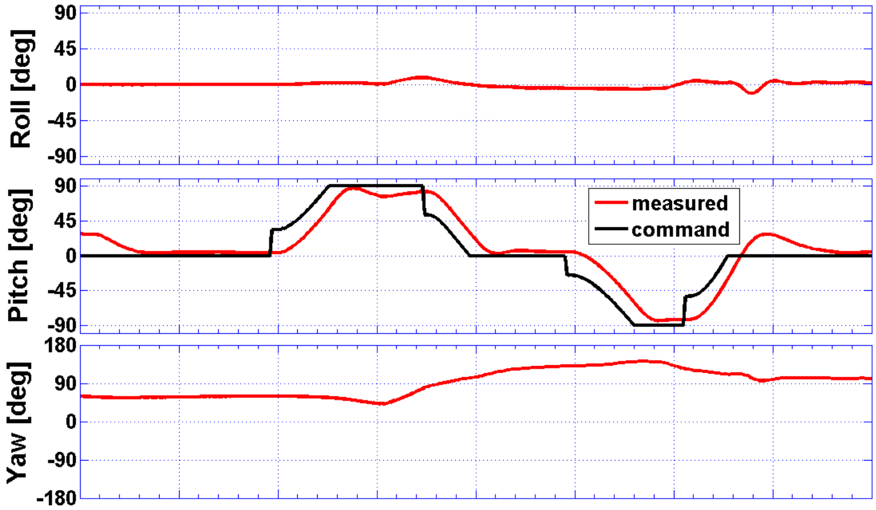

b.) Angular rate

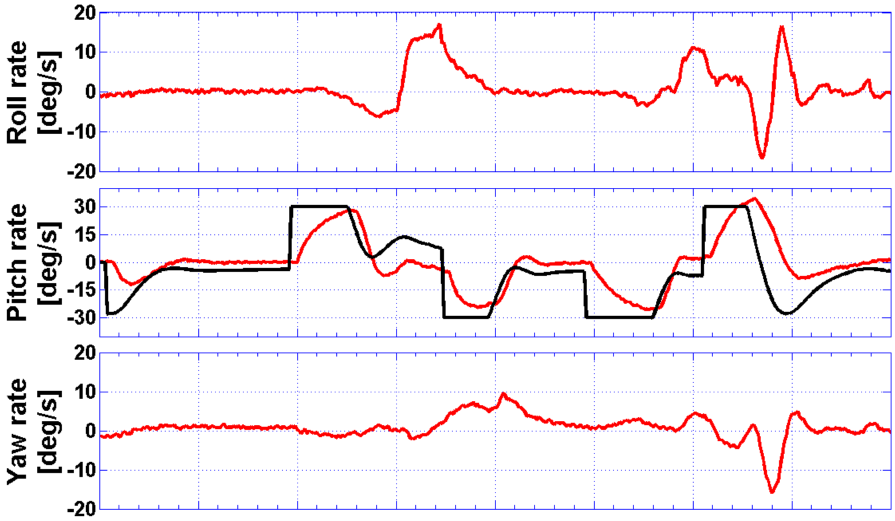

c.) Torque

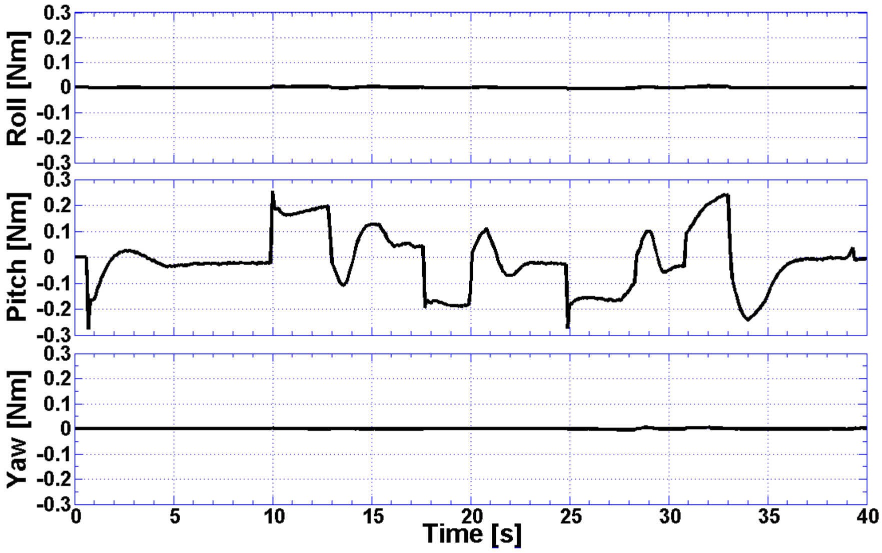

Figure 9.9: Attitude dynamics during the diving manoeuvre

Fig. 9.10 shows the steering response of the CMG system for a flywheel rate of $\dot{\psi} = 10,000\,\text{rpm}$. The flywheels rotate 25% faster than in the vertical pitching manoeuvre described in the previous section and so the gimbal rates required to generate the same magnitude torque are smaller. This results in smaller gimbal excursions during the manoeuvre and the system operates further within the momentum envelope and has a larger value of $\det(\bar{c}\bar{c}^T)$.

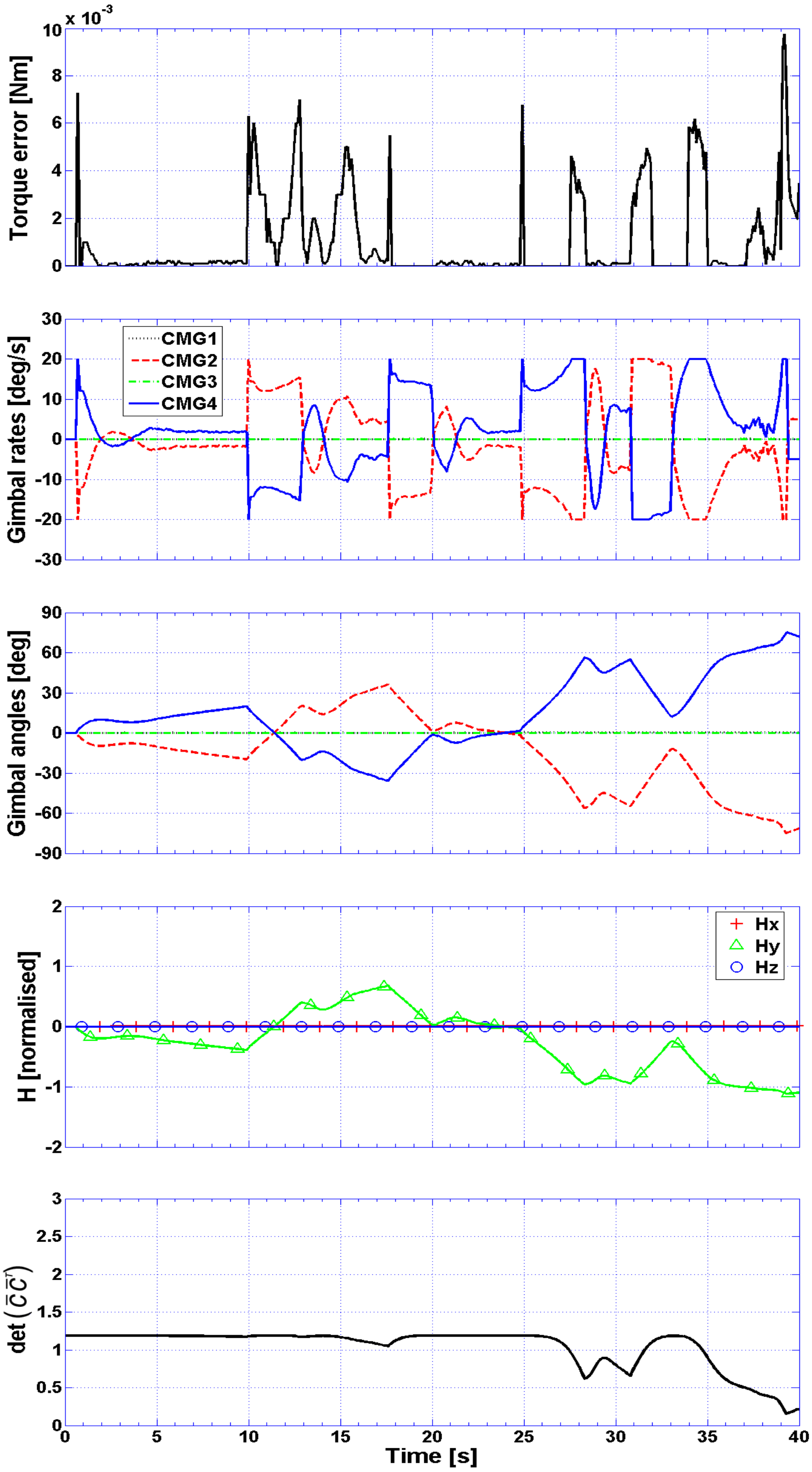

Figure 9.10: Diving manoeuvre CMG steering with $\dot{\psi} = 10,000\,\text{rpm}$

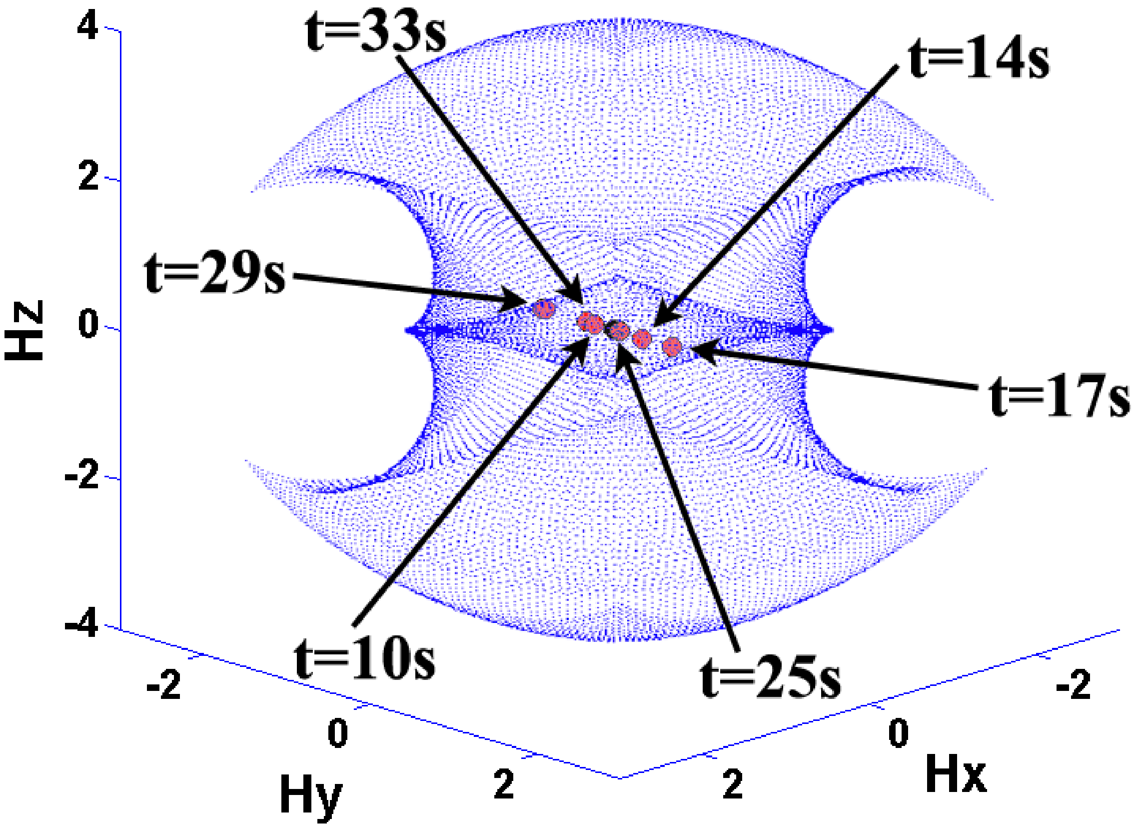

Figure 9.11: Geometric representation of momentum vector during the diving manoeuvre

The geometric representation in Fig. 9.11 illustrates the motion of the normalised CMG momentum vector to generate the required torques during the experiment. It can be seen that the momentum vector stays within the boundaries of the constrained workspace.

Discussion of results

This is, to the knowledge of the author, the first time an underwater robot has performed vertically pitched diving and surfacing in surge. The CMG system stores enough momentum at a flywheel rate of 10, 000 rpm to adopt a vertically pitched attitude and overcome the non-coincident centres of gravity and buoyancy of the robot used in this experiment. The CMG system demonstrates a fast response and high resolution of control to actively stabilise the robot's attitude as it propels itself through the water in vertically pitched surge. This clearly indicates that the CMG system is capable of stabilising any attitude on the surface of a sphere as the robot translates in surge.

The unrestricted attitude control capabilities allow the robot to take full advantage of its single thruster and perform three-dimensional manoeuvres that have not been possible previously. This is efficient in terms of both speed and power since the robot travels only in its principal mode of translation. The unrestricted attitude control and unique manoeuvring capabilities demonstrated in this experiment allow the missions of a Zero-G Class underwater robot to be planned and optimised in a fully three-dimensional manner.

9.3 Implications for underwater robot research

The application of CMGs to Zero-G Class underwater robots has several important implications for underwater research using AUVs. The unrestricted attitude control and unique manoeuvreing capabilities allow Zero-G Class underwater robots to approach their missions in a truly three-dimensional manner, optimising the use of their thrusters, sensors and power supply in a way that has not been possible previously. In addition to improving AUV efficiency, this opens up new fields of research where AUVs can be applied. This section discusses the implications of CMG technology on Zero-G design and provides suggestions for the types of missions in which this new class of underwater robot could be applied.

9.3.1 Zero-G design

The freedom in attitude control offered by CMGs allows Zero-G Class underwater robots to manoeuvre freely in any direction whilst travelling only in their principal mode of translation. This is often seen in nature and is efficient both in terms of performance and design. Since the robot can adopt and maintain any attitude it only requires a single thruster to actuate surge. Having just a single mode of translation minimises the number of sensors required for navigation and obstacle avoidance as in principal, the robot only requires perceptional sensors in the direction of travel. Since the CMG system is contained within the body of the robot, it is physically protected and does not exert any external forces that may agitate loose surfaces or small creatures. This highly integrated form preserves the hydrodynamic integrity of the hull and allows for simple and elegant design.

The idea of using the flywheels as a mechanical battery was introduced in Section 7.3.4. As stated it may be possible to perform short missions with no chemical battery at all. Specifically in the case of CMGs, this combines energy storage and attitude control in a single device, known as an Integrated Power and Attitude Control System, or IPACS, as suggested by Will [74] in 1974. This, together with the highly efficient three-dimensional approach to missions, minimises the necessary number of components and indicates that Zero-G Class underwater robots can be considerably smaller than conventional AUVs.

9.3.2 Zero-G missions

The concept of minimal redundancy is central to the design philosophy of Zero-G Class underwater robots. This not only applies their physical design, but also extends to their missions. It is envisaged that Zero-G Class AUVs will perform 20-30 minute inspections of targets that have been located prior to deployment. The short mission time suggests that the robot would not require any source of power other than the energy stored in their flywheels. These can be accelerated to their operational speed in a matter of minutes and this can be performed on board a support vessel using an external power source immediately prior to each deployment. Since no gases are produced this can be performed without opening the pressure hull. This combined with the ease of handling for deployment and recovery due to the small size of the robot, allows for a rapid turnaround that would allow a number deployments to be made in quick succession when inspecting large, or multiple targets.

The small size and highly integrated design combined with the high manoeuvrability at low speeds allows for manoeuvring in confined spaces, making Zero-G Class AUVs ideal for operation in geometrically complicated, cluttered and even enclosed environments. This allows Zero-G Class AUVs to perform missions that have so far eluded AUVs. Potential applications include tracking the dives of marine animals such as whales, turtles and even penguins and ranges to visual surveys of man-made structures such as oil rigs, subsea oil wells, submerged ruins and even the inside of sunken wrecks. It is hoped that the increased agility and operational envelope will ultimately lead to an increase in the commercial and scientific value of AUVs.

Chapter 10

Conclusions and future work

The aim of this research has been the development of a new class of Zero-G underwater robot that is capable of approaching its missions in a fully three-dimensional manner. This requires the ability to perform on the spot rotations to adopt and maintain any attitude on the surface of a sphere as if in a zero gravity environment and the ability to actively stabilise any attitude while translating in surge. To achieve this CMGs have been introduced as a new type of underwater actuator and a novel control scheme has been developed based on internal momentum exchange.

10.1 Original contributions and summary

This is the first application of CMGs to underwater robots and so it has been necessary to develop a dynamic model of a rigid body, containing an arbitrary system of single gimbal CMGs, that is free to translate and rotate in a viscous fluid. This has been derived using Kirchhoff's equations of motion, which is more concise than the Newtonian derivations of previous works. This is the first time that the translational dynamics of a CMG system have been modelled and that the coupled effects of translation have been accounted for in the rotational dynamics. Furthermore, the hydrodynamic interactions of the body have also been included in the form of added mass, added inertia and viscous drag together with the effects of other actuators. The equations have been restricted to a body with coincident centres of gravity and buoyancy as this concept is central to this research. However, for completeness, a method to incorporate gravity effects into the model has been presented. In order to describe any orientation, the attitude of the body is converted to the inertial frame using quaternions since they contain no singularities in their description of motion.

The freedom in attitude control offered by having coincident centres of gravity and buoyancy raises questions concerning the stability of the system. This has been assessed based on energy considerations of the complete CMG, body and fluid system using Lyapunov's direct method. The results of this analysis forms the basis of a globally asymptotically stable feedback attitude control law that determines the torques necessary for the robot to adopt and maintain any attitude in roll, pitch and yaw. In contrast to all previous CMG applications, the control law developed in this research takes into account the effects of translation, the added inertia and the viscous hydrodynamic interactions of the body as well as the coupled dynamics of the CMG and body system.

The greatest challenge in the application of single gimbal CMG systems is the inherent and serious problem of singular orientations that can result in a momentary loss of control authority. This research has presented a method to geometrically represent the singularities of a CMG system based on previous work by Kurokawa [64]. A new method has been developed to classify escapable and inescapable singularities based on the Gaussian curvature of null motion that is determined using the eigenvalues of a characteristic function. This is more simple and direct than the method presented by Kurokawa that indirectly deduces escapability using a number of different conditions. A comprehensive geometric study of a minimally redundant CMG pyramid has been performed and the graphical assessment is the first such study to explicitly distinguish between escapable and inescapable singularities for the complete singular surface. The study has demonstrated why no exact, real-time steering law can guarantee singularity avoidance over the entire workspace. The implications of this on attitude control have been discussed and it was concluded that a steering law for application to AUVs must be applicable in real-time and must remain exact, guaranteeing that the torque developed by the CMG system is always equal to that demanded by the control law. A global steering law that satisfies these conditions has been formulated based on the method of workspace restriction developed by Kurokawa. This research has presented a formal method to derive the appropriate algebraic constraining condition, filling in gaps in the logic of the previously mentioned work that pioneered this technique, based on global considerations of the inverse kinematics of attitude control.

The underwater robot IKURA, developed as part of this research, is the first prototype of the Zero-G Class and is the first application of CMGs to underwater robots. Practical considerations of its mechanical and electrical design have been discussed and a series of dry-land and underwater experiments performed to verify the associated theoretical developments. In particular, the actuation capabilities of the CMG system and the exactness and real-time applicability of the steering law have been verified by physical measurements of the torque generated. The dynamic equations for the complete CMG, body and fluid system have been verified in a series of underwater experiments, though difficulties were encountered due to the tether and the non-coincident centres of gravity and buoyancy of the robot used. The control law developed has demonstrated robustness to certain types of unmodelled disturbances, such as the effects of non-linear bearing friction and vibrations of the system. However, problems were encountered due to the hydrostatic righting moment of the body and the presence of a tether that caused a small, bounded offset in the robot's closed-loop attitude response. It has been suggested that this can be overcome by adding an integral error term in the control law, though this remains to be verified experimentally. Despite these problems experiments have demonstrated that the control law developed in this research takes advantage of the coupled behaviour of the CMG, body and viscous fluid interactions to make a more efficient use of the system, achieving a superior control response for 20% less overall control activity in yaw and 30% less activity in pitch than two alternative control laws that neglect the dynamics of the system and the fluid interactions of the body respectively. Finally, the ability of the system to actively stabilise the passively unstable, unsteady self-propelled translational dynamics of a Zero-G Class underwater robot has been verified experimentally.

The ability to perform on the spot rotations to adopt and maintain any attitude on the surface of a sphere has been verified with the robot demonstrating the necessary range of attitude control by performing $\pm 180^{\circ}$ rotations in yaw and adopting $\pm 90^{\circ}$ vertical pitch angles with a zero radius turning circle. The ability to stabilise any attitude while translating in surge has been practically verified with the CMG system demonstrating a fast response and high resolution of control to actively stabilise the robot's attitude as it propels itself through the water when pitched vertically. This is the first time an underwater robot has performed vertically pitched diving and surfacing in surge.

10.2 Conclusions

This research establishes CMGs as a new type of underwater actuator that offers a speed and resolution of response that is independent of the fluid environment and cannot be achieved using traditional actuation methods. A novel control scheme has been developed based on internal momentum exchange using CMGs that provides the necessary range and resolution of control about all three rotational degrees to allow Zero-G Class underwater robots to adopt and maintain any attitude on the surface of a sphere with a zero radius turning circle and to actively stabilise any attitude while translating in surge.

The unrestricted attitude control and unique manoeuvring capabilities demonstrated in this research allow Zero-G Class underwater robots to plan and optimise their missions in a fully three-dimensional manner, taking advantage of their thrusters, sensors and power supply in a way that has not been possible previously. This allows Zero-G Class underwater robots to manoeuvre in confined spaces and so operate in geometrically complicated, cluttered and even enclosed environments to perform missions that have so far eluded AUVs. The prototype Zero-G Class underwater robot IKURA forms a unique platform with which to investigate potential applications and explore new fields of underwater research.

10.3 Future work

This work has formed the foundations for research into Zero-G Class AUVs and their applications. There remain a number of unresolved issues and potential areas for future research. One area that should be investigated is the formal assessment of the robustness of the control law. During the experiments carried out in this work a static offset was observed in the robot's closed-loop attitude response, suggesting that the control law is not robust to some types of disturbance. Twisting of the tether and non-coincident centres of gravity and buoyancy have been identified as possible sources for these errors and, although future applications should focus on untethered operation, investigations of both the tethered and untethered dynamics should be performed for a variety of known righting levers to provide valuable insights to confirm these points and investigate the sensitivity to these parameters. It has been suggested that these disturbances may be overcome by incorporating an integral error term in the control law, however, it still remains to assess the robustness of such a control law. Furthermore, it is recommended that the dynamic response of the system using alternative robust control techniques, such as sliding control, is also investigated to improve the overall performance of the system.

A number of recommendations can be made concerning post-prototype design. Firstly, the use of a contra-rotating propeller is recommended to eliminate any roll effects when actuating surge. Secondly, the use of angular rate based attitude sensors such as vibration, ring-laser or fibre-optic gyros is recommended as magnetic heading measurements were found to encounter difficulties when the robot adopted near vertical pitch angles. The accumulation of dead-reckoning error is not expected to cause practical difficulties for this application due to the short mission times. Finally, although investigations into robustness may elucidate the offset errors in control, non-coincident centres of gravity and buoyancy place a significant burden on the CMG system and will eventually cause it to reach the boundary of its operational envelope when holding non-horizontal attitudes. As such it is essential that this issue is formally addressed for post-prototype design and that realistic measures are taken to reduce the righting moment that forms the root of this problem. It is recommended that a system of moveable internal masses is used to automatically calibrate the centre of gravity of the robot once it is in the water. Although it may not be possible to completely eliminate the righting moment, it may be possible to sufficiently reduce it to overcome this problem for practical applications. It follows that any increase in the actuating capabilities of the CMG system would further improve the performance of the system in overcoming this difficulty.

The next major target in the development of Zero-G Class technology is to investigate the use of the energy mechanically stored in the flywheels to power the robot during its missions. This would combine energy storage and attitude control in a single device, allowing Zero-G Class AUVs to carry out their missions without the use of any other source of power. The implementation of this system requires a number of practical and also theoretical developments. Firstly, a generator must be attached to the flywheel axes to distributed the energy stored to the electrical system. Furthermore, flywheel rate measurements must be used accurately determine the remaining energy in the system as well as adapt the control and steering laws. Experiments must be performed to systematically analyse the performance of the system as the actuation capabilities of the CMGs diminish together with the energy stored and also investigate the time taken to recharge the energy in the flywheels. This information should be used to determine the time and energy available for safe continuous operation of the robot and also determine the minimum turnaround time between successive deployments.

Zero-G Class AUVs have the potential to perform missions that have so far eluded existing classes of AUV. However, to achieve this it is necessary to equip perceptional sensors for navigation. Owing to restrictions on the mass, space and power available it is suggested that a small, versatile, multipurpose sensor, such as a stereo-vision camera, should be used for real-time navigation, target tracking, obstacle avoidance and data acquisition [7, 9, 75]. Such a single sensor would allow Zero-G Class AUVs to perform detailed visual inspections of targets located prior to deployment. Examples of such missions could include tracking the dives of mobile marine creatures such as whales, turtles and penguins for scientific research or for industrial and archeological applications operating in geometrically complicated, cluttered and even enclosed environments to survey man-made structures such as oil rigs, subsea oil wells, submerged ruins and even the inside of sunken wrecks. The prototype Zero-G IKURA forms a unique platform with which to explore these new fields of underwater research.

Appendix A

CAD drawings

This appendix contains CAD drawings and images to illustrate the design of IKURA and its components:

Fig. A.1: General arrangement of IKURA

Fig. A.2: Design of the CMG pyramid

Fig. A.3: Design of a CMG unit

Fig. A.4: Photo of a CMG unit

Fig. A.5: Photo of flywheel in gimbal frame

Fig. A.6: Design of the thruster unit

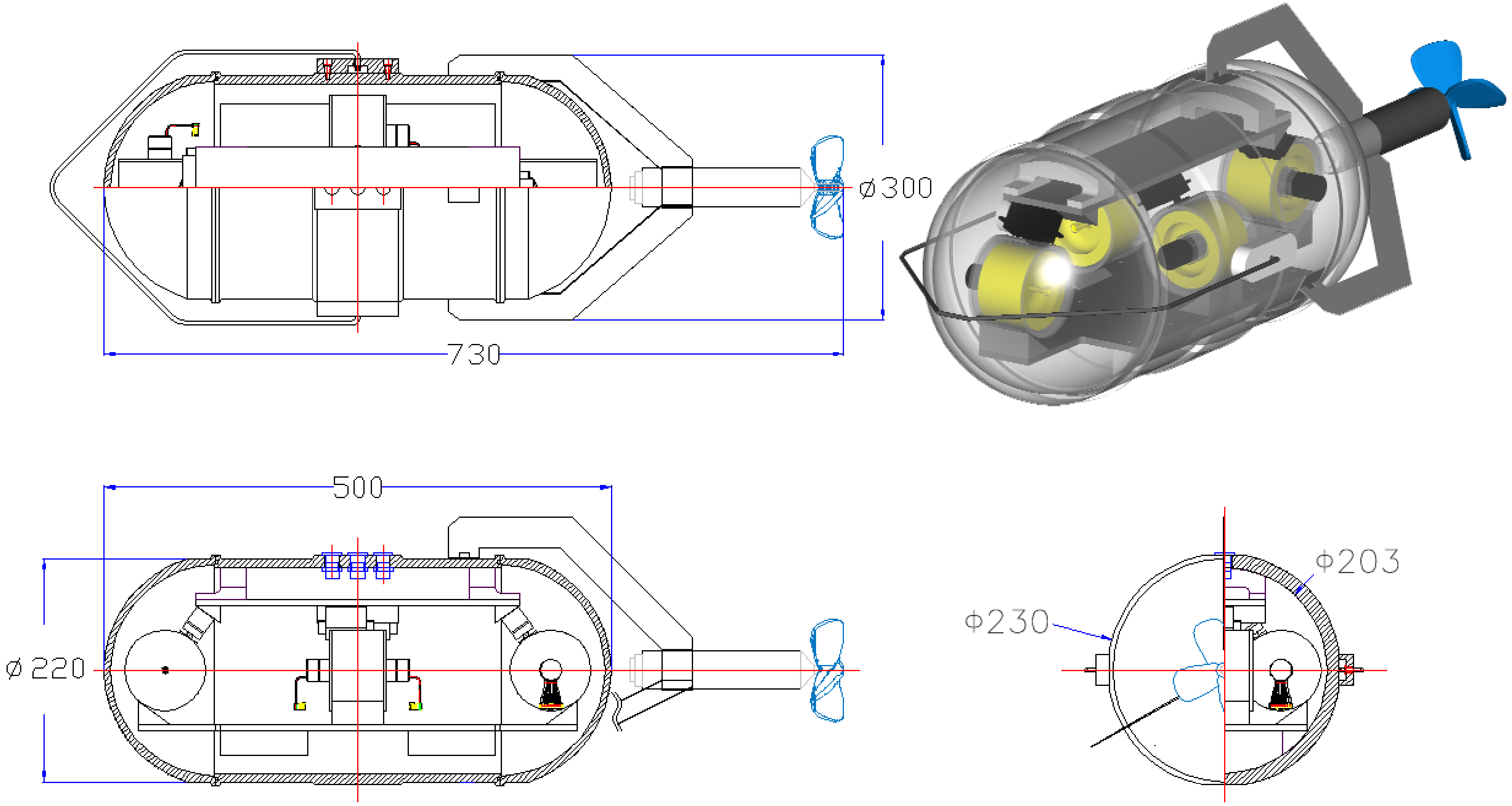

Dimensions in mm

Figure A.1: General arrangement of IKURA

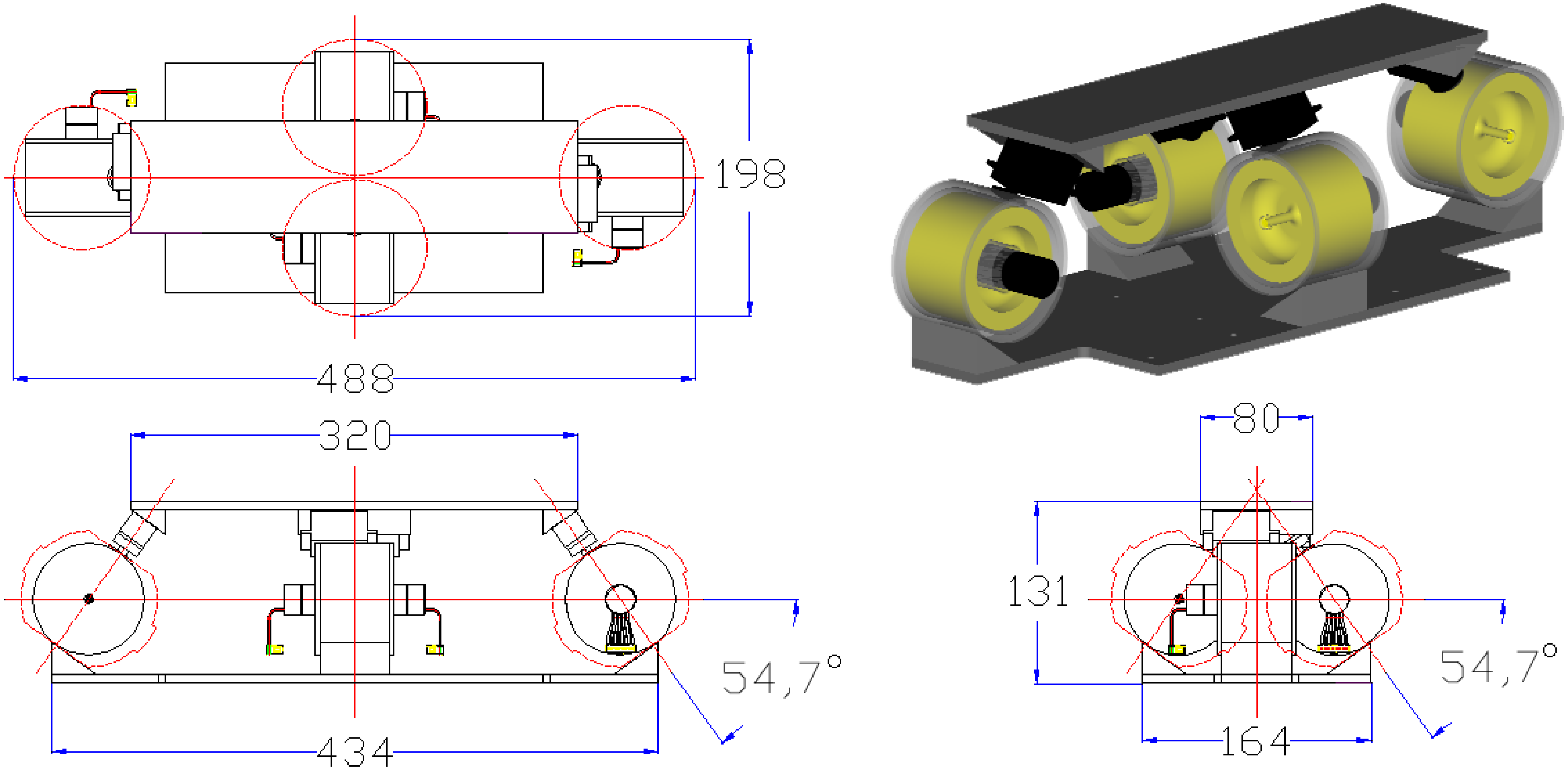

Dimensions in mm

Figure A.2: Design of the CMG pyramid

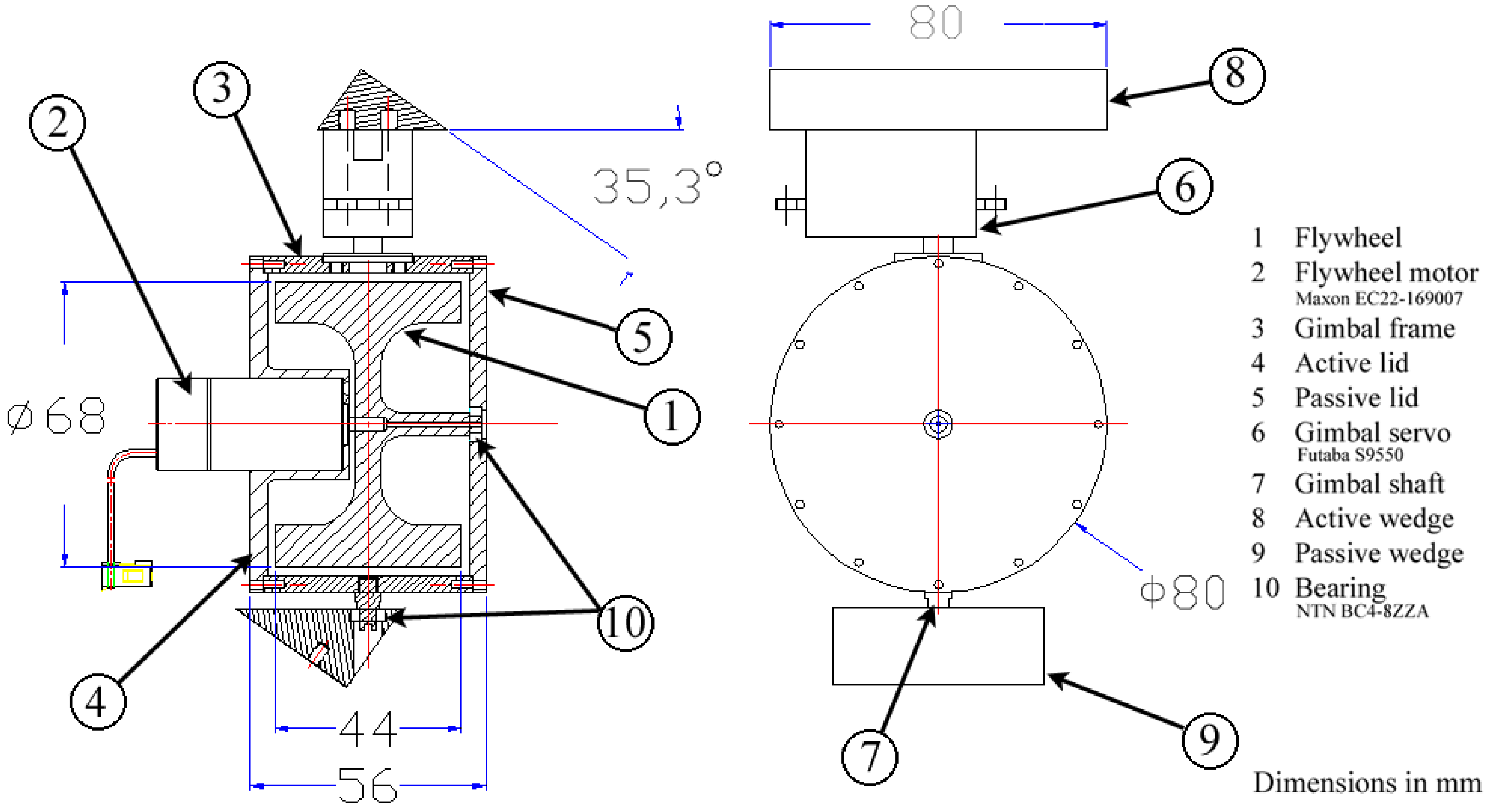

Figure A.3: Design of a CMG unit

Figure A.4: Photo of a CMG unit

Figure A.5: Photo of flywheel in gimbal frame

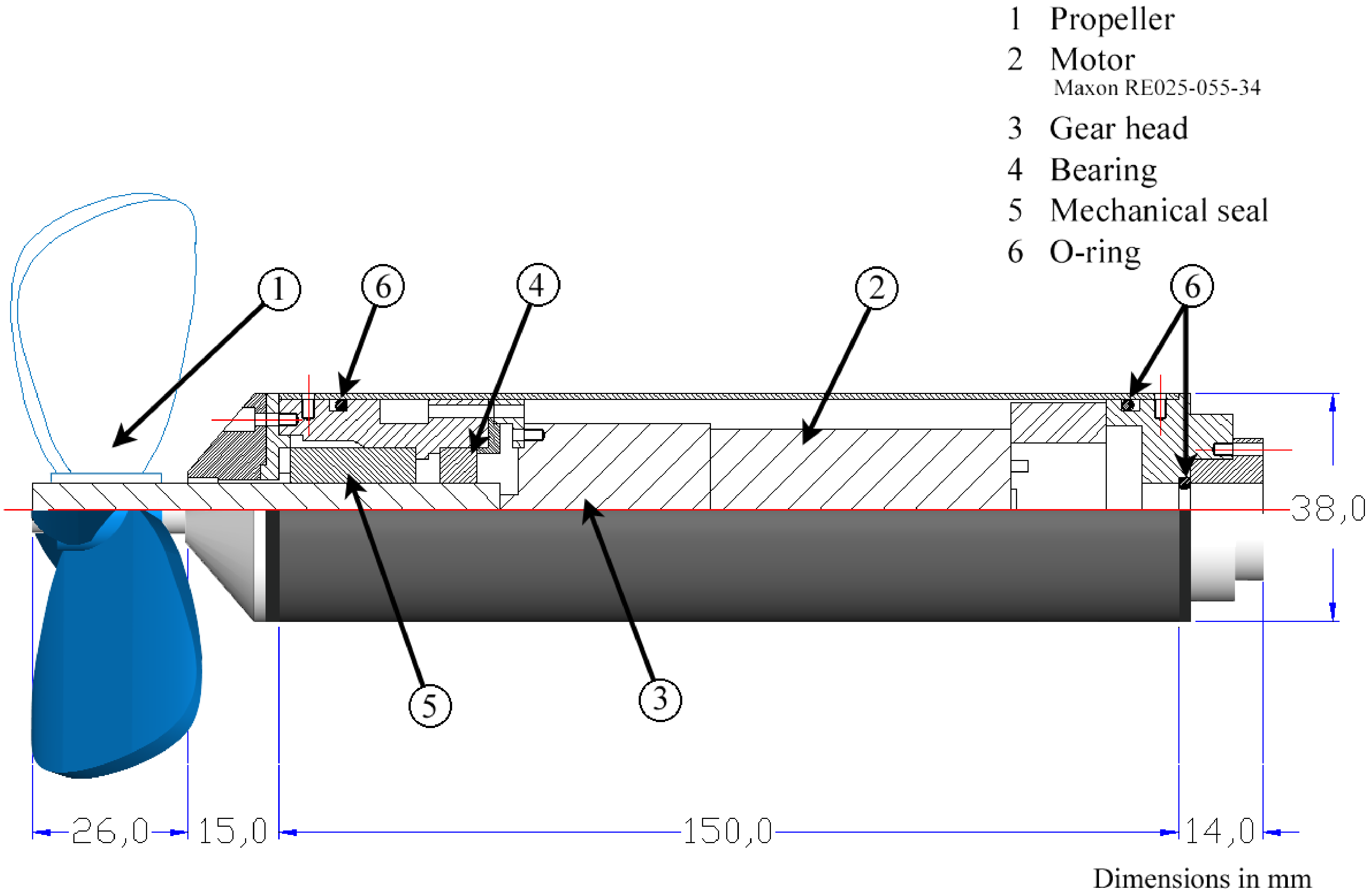

Figure A.6: Design of the thruster unit

Appendix B

Electronics and control

This appendix details the electronics and control architecture of the underwater robot IKURA. Fig. B.1 illustrates the overall arrangement of the electronics in the hull and an exploded view of the CPU stack. Fig. B.2 shows the electrical signals of the sensors and actuators. Section B.1 describes in further detail the signals of the AHRS, flywheel motors, gimbal servos and thruster unit. Where appropriate the circuitry used to generate the signals and the experiments to determine the input output relationships of the components are described. Section B.2 gives the specification of each electrical component.

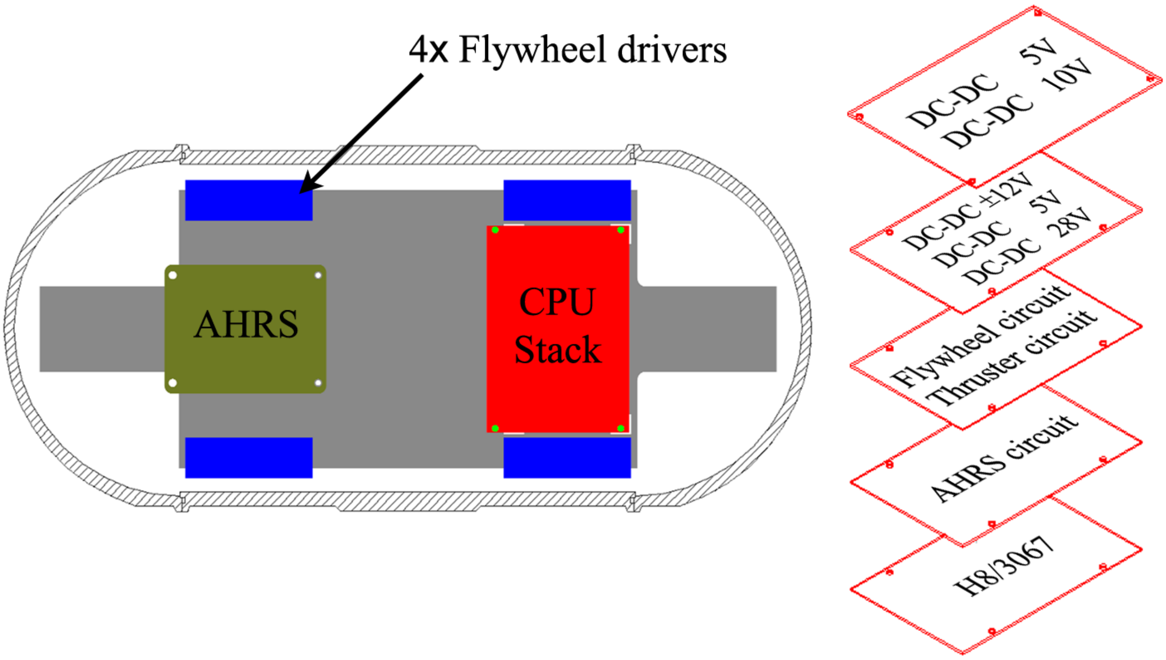

Figure B.1: Arrangement of electronics inside the main pressure hull

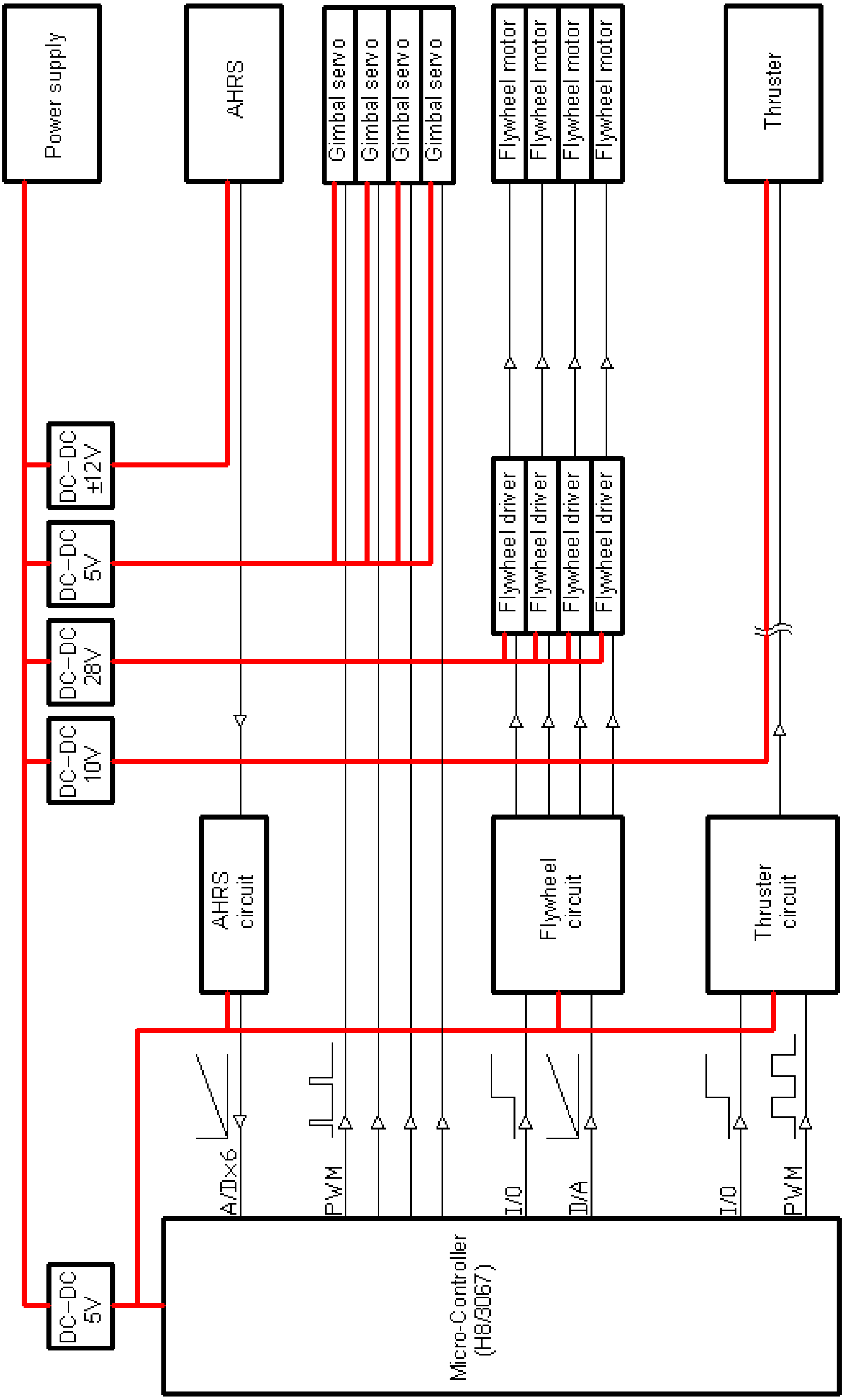

Figure B.2: Electrical architecture and control signals

B.1 Control signals

AHRS measurements

The three-axis attitude and angular rate measurements of the AHRS are output as 12 bit analogue signals between ±4.096 V. The circuit illustrated in Fig. B.3 is used to convert these signals as shown in Fig. B.4 so that they can be read by the 10 bit 0 - 5 V A/D convertors of the micro-controller. The average of five readings is taken at 10 Hz in order to filter out noise. It has been verified that the rotation of the brass flywheels and steering of the gimbals do not effect the measurements of the sensor.

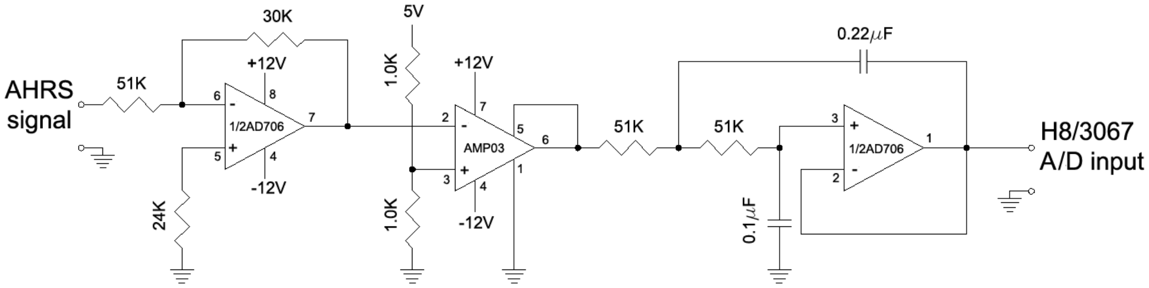

Figure B.3: Circuit to convert the output measurement signals of the AHRS

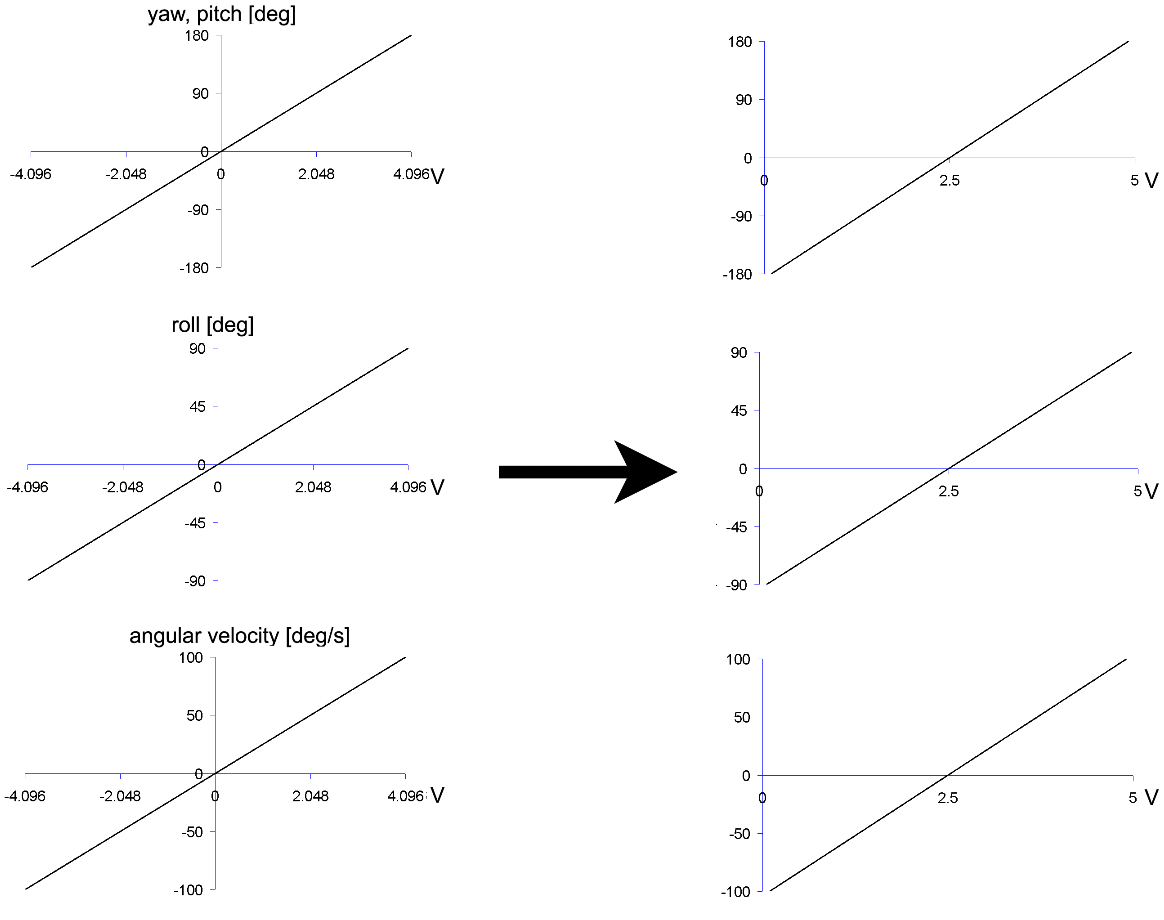

Figure B.4: AHRS signals before and after conversion

Flywheel motor

The speed of the flywheels is controlled by an 8 bit 0 - 5 V analogue signal that is generated by the micro-controller and an I/O signal that engages an electronic brake. These are distributed through the circuit in Fig. B.5 where each of the flywheels is individually monitored by a closed-loop 1-Q-EC DEC 50/5 (230572) digital driver that uses three Hall sensors in the motor to regulate its speed. The relationship between the speed of each flywheel and the input signal plotted in Fig. B.6 was measured using a variable frequency strobe and a voltmeter. Measurements could only be made up to 10,000 rpm as this was the maximum frequency of the strobe used. This data has been extrapolated assuming a linear relationship.

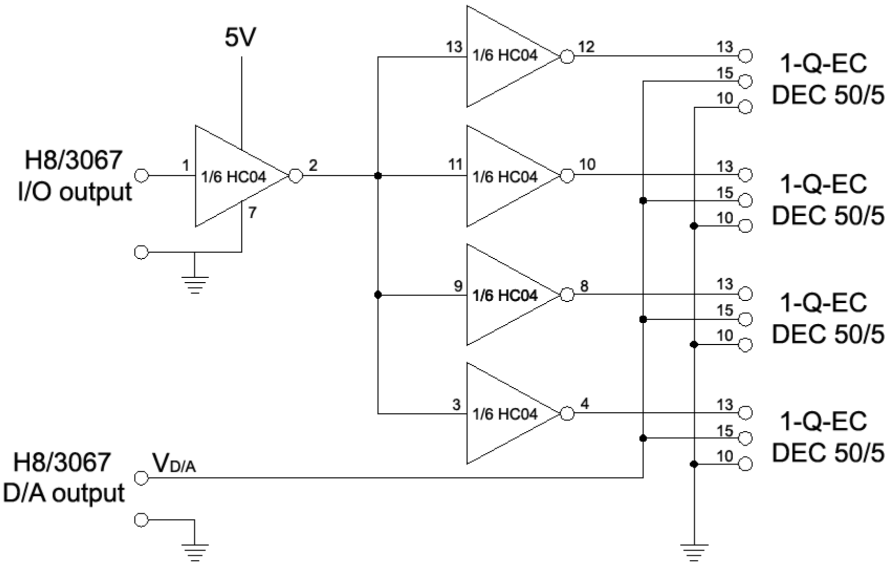

Figure B.5: Circuit to distribute the flywheel control signals

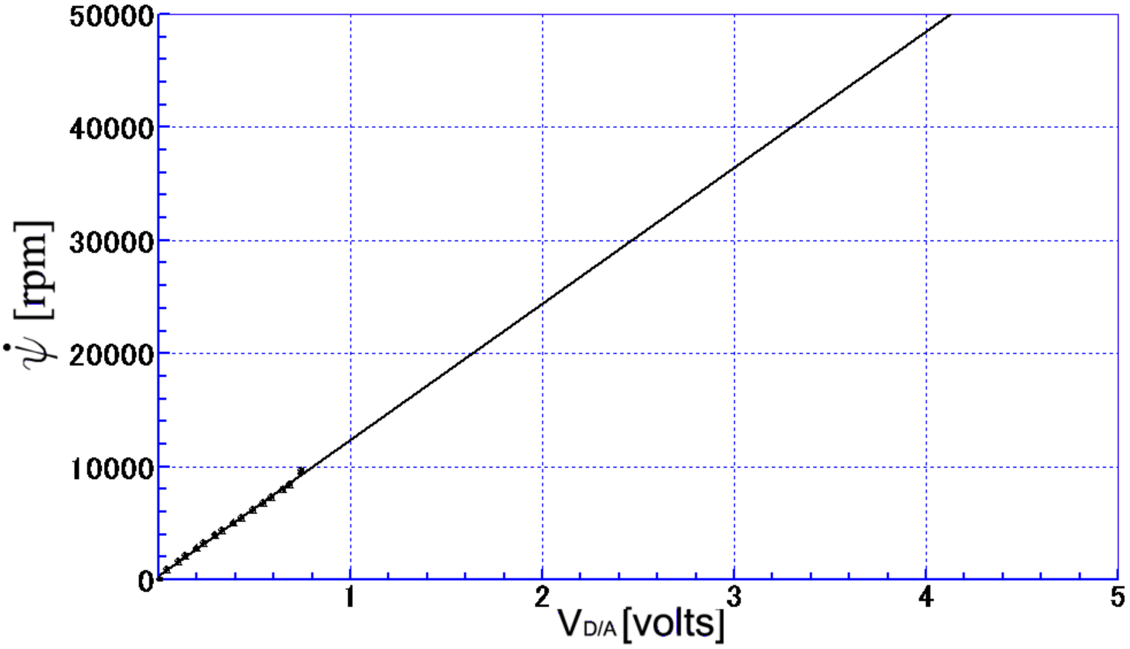

Figure B.6: Measured flywheel speed and D/A input with a supply of 28 V

Gimbal servo

Each of the gimbal servos are controlled by a 16 bit PWM signal generated by the microcontroller. The servo angle is controlled by the width of a pulse that is sent every 22 ms as illustrated in Fig. B.7. The relationship between the pulse width and the angle of the servos was measured using an oscilloscope and this is plotted in Fig. B.8.

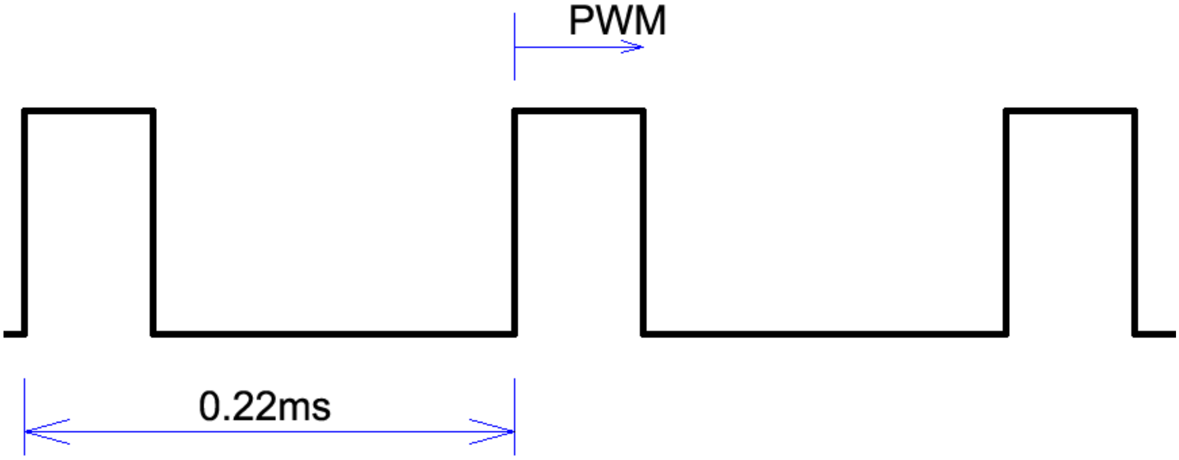

Figure B.7: Gimbal servo PWM control signal

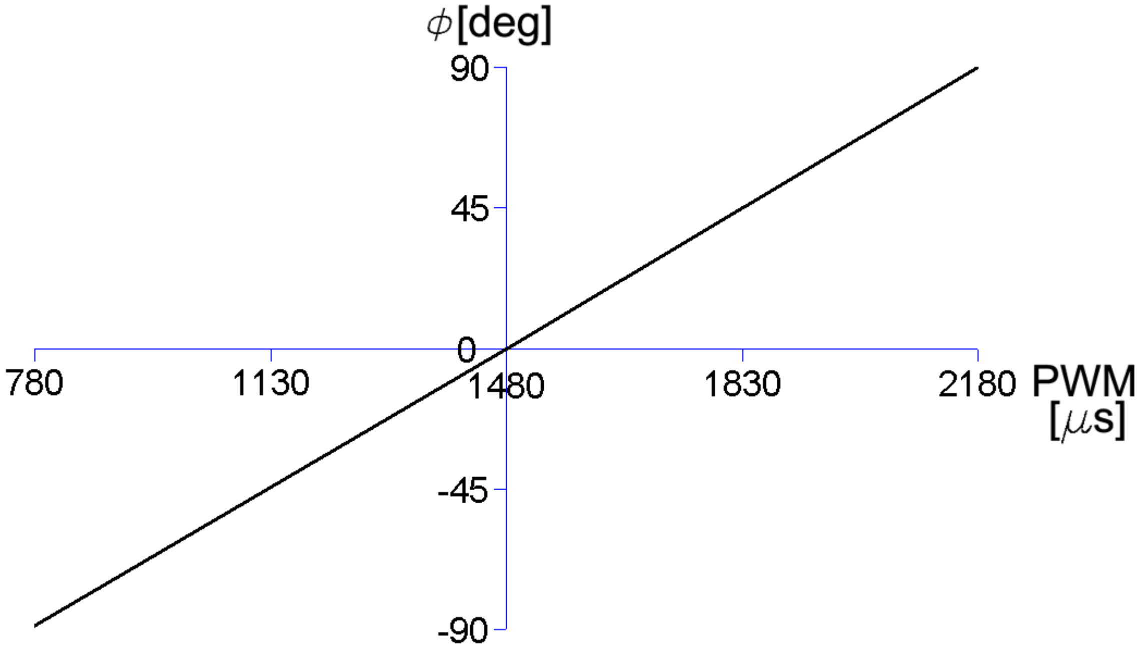

Figure B.8: Measured relationship between angle of servo and input pulse width

Thruster

The rotational rate and direction of the thruster are controlled by an 8 bit PWM signal and an I/O signal respectively. These are used to generate the appropriate pulse input to the thruster through the circuit in Fig. B.9. The diodes are used to protect against back-electromagnetic fields and the **CR** low pass filter is introduced to reduce noise. The relationship between the rotational rate of the submerged thruster and the normalised input pulse width plotted in Fig. B.10 was measured using a variable frequency strobe and an oscilloscope.

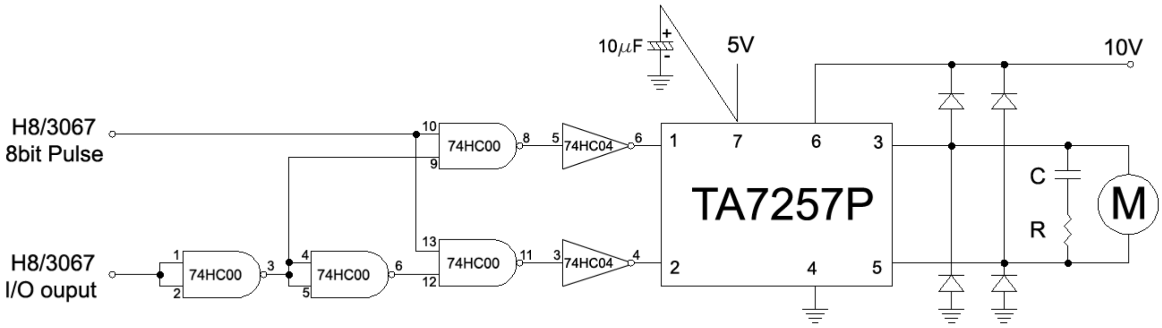

Figure B.9: Circuit to generate thruster signal

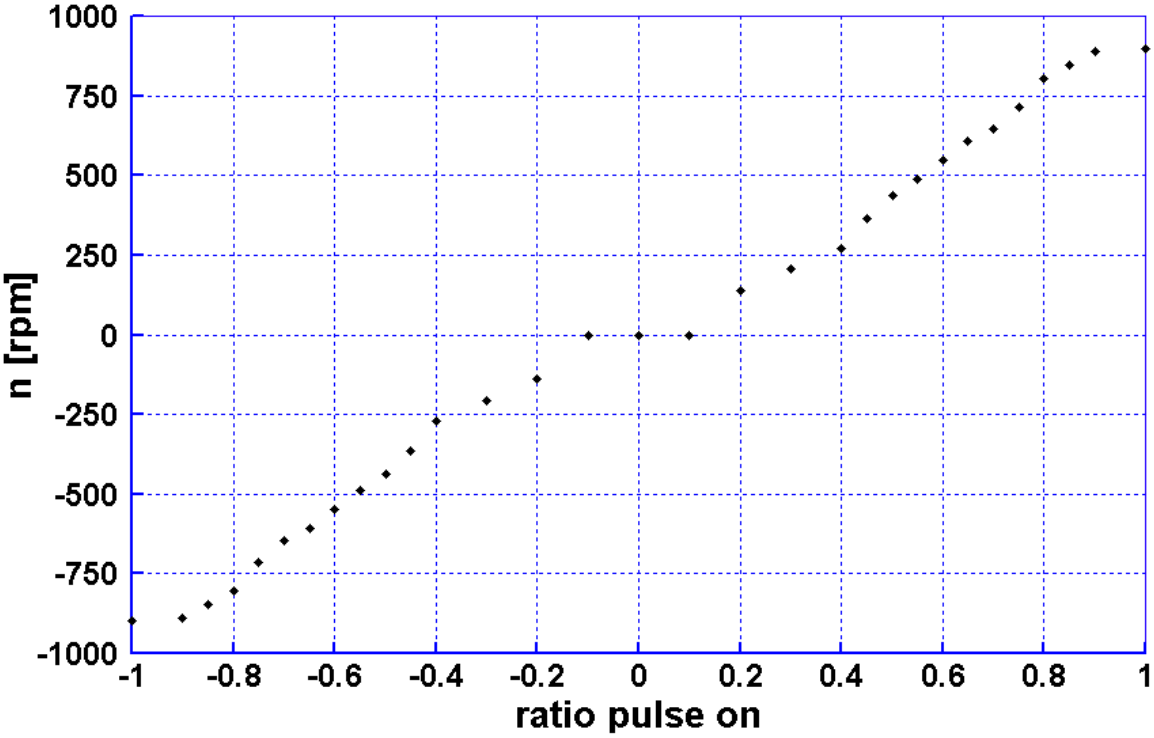

Figure B.10: Measured thruster rate and normalised input pulse width

B.2 Electrical specification

Table B.1 details the specification of the electrical hardware used in IKURA. This shows the peak power consumption for the maximum acceleration of the flywheels and the thruster, and the operational power consumption for a constant flywheel rate of $\dot{\psi} = 10,000$ rpm and steady propulsion with the thruster rotating at 450 rpm.

Component	Manufacturer serial no.	Voltage	Current	Power
Sensor	Cross-Bow AHRS-400CA	12 V	250 mA	3 W
CPU	Hitachi H8/3067	5 V	200 mA	1W
Gimbal servo	Futaba S9550	5V	100 mA ×4	0.5 W ×4
Flywheel motor	Maxon EC22-169007	28 V	110 mA ×4 max.700mA ×4	3 W ×4 max.20 W ×4
Thruster motor	Maxon RE025-055-34	10 V	200 mA max.1 A	2 W max.10 W
			TOTAL	20 W max.~100 W

Table B.1: Electrical specification of each component

Appendix C

Numerical modelling

This appendix describes the various parameters of the dynamic model that are specific to the underwater robot IKURA and its subsystems. These are used for design, simulation and control purposes. First, mass and inertia calculations are carried out for the complete system and the hydrodynamic added mass and viscous drag coefficients are derived theoretically. Next, the sizing of the CMG momentum in order to meet the requirements of the specification is discussed. Finally, the external forces and moments of the system are detailed, with the development of thruster equations and modelling of the disturbances due to bearing friction and the hydrostatic effects of the non-coincident centres of gravity and buoyancy.

C.1 Mass and inertia

Table C.1 shows the mass and rigid body inertia distribution of IKURA with the CMGs locked at zero excursion angles. The origin is taken at the centre of the CMG pyramid.

Components	**Mass (kg)**	**Centroid (mm)**			**Moment (Nm)**			**Moment of inertia (kgm^2)**		
	m	**x**	**y**	**z**	m**x**	m**y**	m**z**	**Jx**	**Jy**	**Jz**
Pyramid frame	1.650	0.0	0.0	-11.5	-1.36E-04	0.00E+00	-1.86E-01	7.98E-03	2.38E-02	2.07E-02
Gimbal servo 1	0.054	157.7	10.8	46.0	8.36E-02	5.74E-03	2.44E-02	1.32E-04	1.46E-03	1.36E-03
Gimbal servo 2	0.054	-10.8	22.7	46.0	-5.74E-03	1.20E-02	2.44E-02	1.48E-04	1.32E-04	4.48E-05
Gimbal servo 3	0.054	-157.7	-10.8	46.0	-8.36E-02	-5.74E-03	2.44E-02	1.32E-04	1.46E-03	1.36E-03
Gimbal servo 4	0.054	10.8	-22.7	46.0	5.74E-03	-1.20E-02	2.44E-02	1.48E-04	1.32E-04	4.48E-05
CMG unit 1	1.145	190.3	0.0	0.0	2.14E+00	0.00E+00	0.00E+00	8.65E-04	4.25E-02	4.23E-02
CMG unit 2	1.145	0.0	55.3	0.0	0.00E+00	6.22E-01	0.00E+00	4.50E-03	8.65E-04	4.37E-03
CMG unit 3	1.145	-190.3	0.0	0.0	-2.14E+00	0.00E+00	0.00E+00	8.65E-04	4.25E-02	4.23E-02
CMG unit 4	1.145	0.0	-55.3	0.0	0.00E+00	-6.22E-01	0.00E+00	4.50E-03	8.65E-04	4.37E-03
Flywheel drivers	0.670	0.1	0.0	-1.1	4.82E-04	0.00E+00	-7.35E-03	4.24E-03	6.63E-03	1.01E-02
CPU stack	0.200	-92.6	0.0	0.7	-1.82E-01	0.00E+00	1.43E-03	4.83E-04	2.02E-03	2.15E-03
AHRS	0.723	95.9	0.0	-1.8	6.80E-01	0.00E+00	-1.30E-02	1.01E-03	7.66E-03	7.35E-03
CMG pyramid subtotal	**8.040**	**6.321844**	**0.0**	**-1.35989**	**4.99E-01**	**0.00E+00**	**-1.07E-01**	**2.50E-02**	**1.30E-01**	**1.37E-01**
Presure hull	4.515	0.0	0.0	-0.4	0.00E+00	0.00E+00	-1.86E-02	4.55E-02	1.02E-01	1.01E-01
Cradle mechanism	0.166	0.0	0.0	0.0	0.00E+00	0.00E+00	0.00E+00	2.40E-03	8.85E-05	2.47E-03
Thruster mount	0.253	-215.0	0.0	0.0	-5.33E-01	0.00E+00	0.00E+00	2.71E-03	1.45E-02	1.45E-02
Thruster	0.517	-375.6	0.0	0.0	-1.90E+00	0.00E+00	0.00E+00	1.53E-04	7.47E-02	7.47E-02
Ballast	3.47	54.2	0.0	3.7	1.85E+00	0.00E+00	1.26E-01	4.73E-02	1.02E-02	1.02E-02
IKURA total	**16.960**	**-54.6**	**0.0**	**0.0**	**-9.25E-02**	**0.00E+00**	**0.00E+00**	**1.23E-01**	**3.31E-01**	**3.39E-01**
Total buoyancy	**16.968**	**-54.6**	**0.0**	**0.0**	**-9.27E-02**	**0.00E+00**	**0.00E+00**			

Table C.1: Mass, buoyancy and rigid body inertia of IKURA

Table C.2 shows the inertia components of the moving parts of each CMG unit about its flywheel, gimbal and transverse axes.

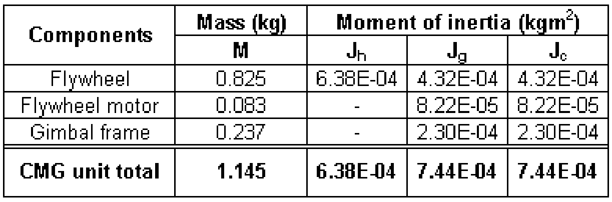

Components	Mass (kg)	Moment of inertia (kgm^2)		
	M	J_h	J_g	J_c
Flywheel	0.825	6.38E-04	4.32E-04	4.32E-04
Flywheel motor	0.083	-	8.22E-05	8.22E-05
Gimbal frame	0.237	-	2.30E-04	2.30E-04
CMG unit total	**1.145**	**6.38E-04**	**7.44E-04**	**7.44E-04**

Table C.2: Inertia components of each CMG unit

C.2 Hydrodynamic effects

The hydrodynamic interactions of the body are modelled as added mass, added inertia and viscous drag, all of which are dependant on the external shape of the body. The hydrodynamic parameters computed for IKURA are presented in Table C.3.

C.2.1 Added mass and inertia

Added mass and added inertia describe the fluid motion induced by the acceleration of a body through it. It is assumed that the robot operates at a large enough depth that these coefficients can be considered constant and strictly positive. In order to model this, the hull form is approximated to an ellipsoid of revolution, as illustrated in Fig. C.1.

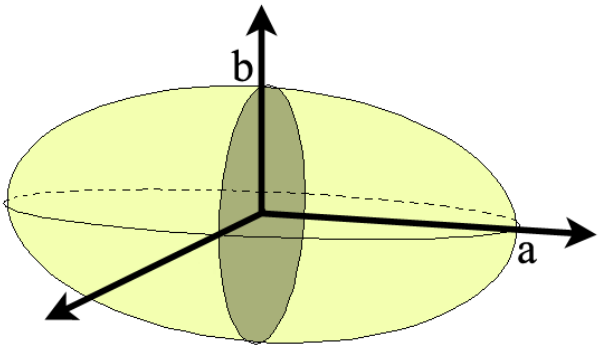

Figure C.1: Ellipsoid of revolution with major and minor semi-axes a and b

The three-planes of symmetry of this shape means that the added mass and inertia matrices are diagonal and so uncoupled between the different degrees. Imlay [76] gives the following expressions to describe these terms:

$$\begin{aligned}
M_{A_x} &= -\frac{\alpha_0}{2-\alpha_0}m \\
M_{A_y} &= M_{A_z} = -\frac{\beta_0}{2-\beta_0}m \\
J_{A_x} &= 0 \\
J_{A_y} &= J_{A_z} = -\frac{1}{5}\frac{(b^2-a^2)^2(\alpha_0-\beta_0)}{2(b^2-a^2)+(b^2+a^2)(\beta_0-\alpha_0)}m
\end{aligned}$$

where the m is the mass of the ellipsoid and the constants β_0 and α_0 are obtained as:

$$\alpha_0 = \frac{2(1-e^2)}{e^3}\left(\frac{1}{2}ln\frac{1+e}{1-e} - e\right)$$
$$\beta_0 = \frac{1}{e^2} - \left(\frac{1-e^2}{2e^3}ln\frac{1+e}{1-e}\right)$$

The eccentricity e is defined as $e = 1 - (b/a)^2$.

C.2.2 Viscous drag

The viscous forces that act on the robot are highly dependent on the type of flow regime. This can be predicted based on non-dimensional analysis using the Reynolds number $R_n = \frac{ul}{\nu}$ where u is the flow velocity, l is the characteristic length of the body and ν is the fluid kinematic viscosity, which for water at $15\,^{o}\mathrm{C}$ is $1.14 \times 10^{-6}\,\mathrm{m}^2/\mathrm{s}$. This gives the Reynolds number of IKURA at a surge velocity of $0.5\,m/s$ as $R_n = 2.2 \times 10^5$, which for a smooth body lies in the transition zone between laminar and turbulent flow. However, the hull profile of IKURA is broken up by clamped couplings where the hemispherical ends join the main cylinder, see Fig. A.1, and it is considered that these will trip the flow into a turbulent regime. The drag coefficient of the robot is calculated based on the various three-dimensional shapes that make up its hull [69, 77]. The non-diagonal terms of the drag coefficient matrix are assumed to be zero and so the drag experienced is uncoupled between different degrees.

The drag coefficient in surge is obtained by approximating the hull to a round nosed cylinder. The coefficients of drag in sway and heave are determined by taking the drag coefficient of individual parts of the robot. The main body is modelled as a circular cylinder with two hemispherical ends and the thruster is modelled as a circular cylinder with the thruster mounting modelled as a flat plate with its projected area normal to the flow.

The roll drag coefficient of the main hull is obtained by calculating the ITTC skin friction for the flow over the surface of the robot:

$$C_F = \frac{0.075}{(\log R_n - 2)^2}$$

The roll, pitch and yaw drag coefficients are obtained by separating the main body of the hull into cylindrical and hemispherical components with the thruster and thruster mount modelled as a cylinder and a flat plate as in the heave and sway models.

	M_A	C_D
Surge	6.64 kg	1.10
Sway	21.14 kg	1.06
Heave	21.14 kg	1.11
	J_A	$\sum C_{D_i} r_i^3$
Roll	0.00 kgm	$2.20 \times 10^{-3}\,\mathrm{m}^3$
Pitch	0.24 kgm	$0.92 \times 10^{-2}\,\mathrm{m}^3$
Yaw	0.24 kgm	$1.09 \times 10^{-2}\,\mathrm{m}^3$

Table C.3: Hydrodynamic properties of IKURA

C.3 Momentum sizing of the CMGs

The momentum required in each CMG to meet the specification was determined based on the predictions of numerical simulations using the dynamic model (3.12). The response of the system is simulated with an optimised bang-bang control law of the form:

$$\tau_u = \pm\tau_k$$

where τ_k is a constant torque. The most demanding specification in terms of the momentum required is the pitch manoeuvre that states the CMG system must provide sufficient control authority from the nominal state so that the robot can rotate ±90° in pitch, starting and finishing at rest in 3 s. Fig. C.2 shows the simulated pitch response with $\tau_k = 0.47$ Nm, which was determined to be the minimum torque required to meet the specification.

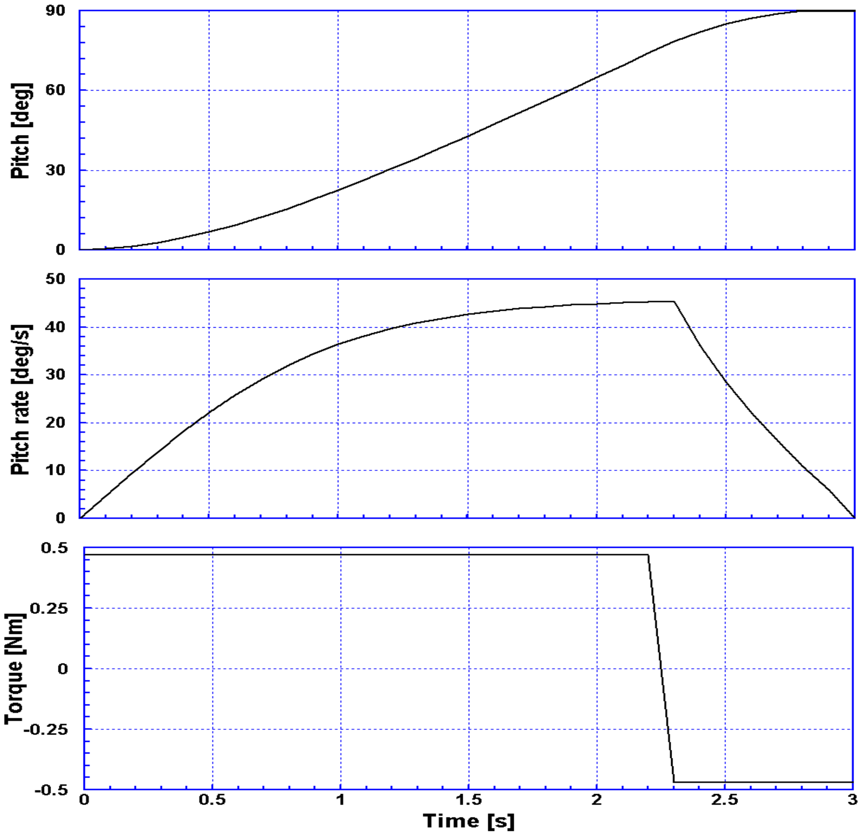

Figure C.2: Simulated pitch response with an optimised bang-bang control law

The minimum momentum change required in the CMG system to perform this manoeuvre is $H_{ymin} = 1.10$ Nms in the y-direction. From (3.4) and (6.5) the momentum required in each CMG unit to achieve this manoeuvre whilst remaining within the boundary of the constrained workspace illustrated in Fig. 6.11 can be computed as:

$$\mathbf{J}_h\dot{\psi} = \frac{H_{ymin}}{2c*}$$

This gives the minimum momentum required in each CMG unit to meet the design specification as 0.95 Nms and thus the total momentum required in the CMG pyramid is 3.80 Nms.

C.4 External forces and moments

Although not used directly in the attitude control law, it is necessary to model the external actuating force of the thruster and any disturbances in order to quantify their effects on the dynamics of the robot.

C.4.1 Thruster model

A single thruster is used to actuate the robot's surge motion. Under bollard-pull conditions, the steady state thrust generated can be modelled in the following manner:

$$F_t = f_t n|n|$$

where f_t is the thrust coefficient. The coefficients for the propeller used were determined experimentally in Suto [78] and these values are given in Table C.4.

	f_t
Forwards	$5.33 \times 10^{-4}\,\mathrm{Ns^2/rad^2}$
Reverse	$4.13 \times 10^{-4}\,\mathrm{Ns^2/rad^2}$

Table C.4: Thrust coefficients

C.4.2 Bearing friction

The friction in the bearing is modelled using the following classical form [79]:

$$\tau^* = \begin{cases} \tau_e^* & \text{if } |\omega| < \omega_s \text{ and } |\tau_e^*| < \tau_s^* \\ \tau_s^* \frac{\tau_e^*}{|\tau_e^*|} & \text{if } |\omega| < \omega_s \text{ and } |\tau_e^*| \geq \tau_s \\ \tau^*(\omega) & \text{if } \omega \geq \omega_s \end{cases}$$

The first condition describes friction below a threshold rotational rate ω_s that counteracts the external torque τ_e^* below a static breakaway value of τ_s^*. At this condition the bearing is effectively stuck. A simple model for the dynamic friction $\tau^*(\omega)$ is given as:

$$\tau_e^* = \tau_c^* \frac{\omega}{|\omega|} + (\tau_s^* - \tau_c^*) e^{-|\omega/\omega_s|} + \tau_v^* \omega|\omega|$$

C.4.3 Hydrostatic restoring moments

For a neutrally buoyant submerged body the weight $f_g = mg$ is equal in magnitude to the buoyancy $f_b = \rho g \nabla$. If the centre of gravity r_g and the centre of buoyancy r_b do not coincide the downward pointing gravitational and the upward pointing buoyancy force create a hydrostatic restoring moment:

$$\tau_{righting} = r_g \times f_g + r_b \times f_b$$

Although it is difficult to achieve exactly coincident centres of gravity and buoyancy in any real application, underwater robots are typically trimmed so that r_g lies directly below r_b. In the case of IKURA this distance was experimentally determined to be 0.4 mm.

Appendix D

IKURA DVD Video

This appendix provides a guide to the media DVD that can be found at the back of this thesis. The DVD contains experimental video footage and also includes a cinematic trailer that illustrates the Zero-G concept, a poster describing IKURA and still images of the robot and its components. A complete list of the contents is included at the end of this appendix.

D.1 Viewing the DVD

Upon inserting the DVD into a media player, a brief trailer will start after which the DVD jumps to the main menu. On each menu screen the user is presented with a number of options that can be selected by moving the cursor over the desired choice. This will highlight the option with a blue bar that will appear immediately next to each of the options. Once highlighted the option can be selected by clicking the appropriate button on the mouse or remote control.

D.2 Main menu

The DVD main menu is illustrated in Fig. D.1. There are three options available:

1. Play All
2. Video Menu
3. Picture Menu

In the figure 'Play All' is highlighted. Selecting this option will play all the video media contained in the DVD. This consists of seven clips that can be accessed individually by selecting 'Video Menu'. There are also a number of still images contained in the DVD that can be accessed by selecting 'Picture Menu'.

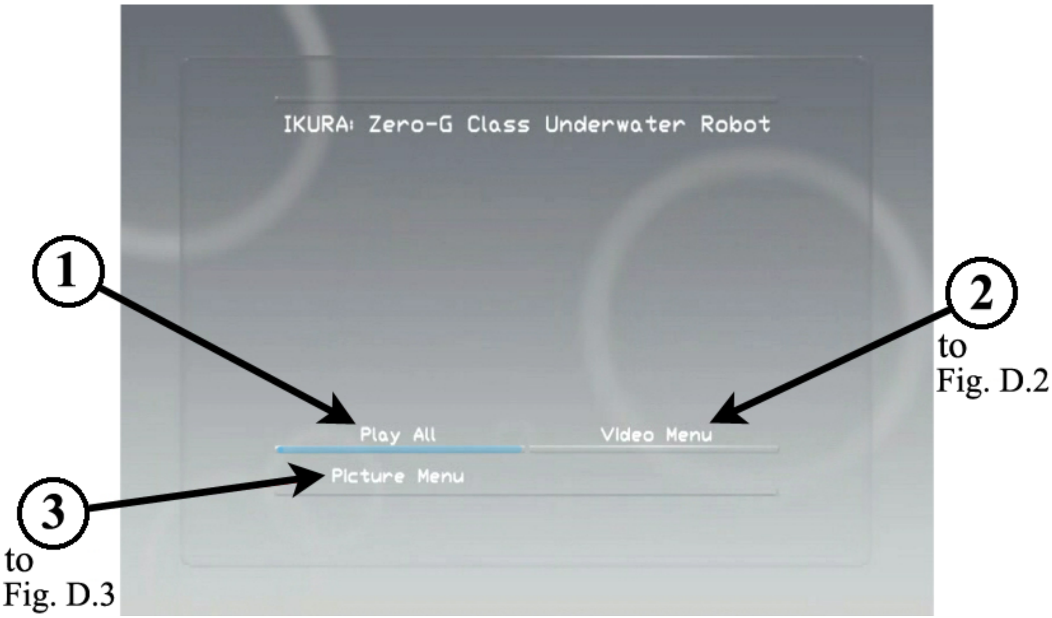

Figure D.1: DVD main menu

D.3 Video menu

The video menu consists of two pages as shown in Fig. D.2. There are a total of seven clips that can be viewed by selecting the appropriate media windows. These are briefly described in the DVD contents at the end of this appendix. It is possible to navigate between the two pages and back to the main menu by selecting the arrows highlighted in the figure.

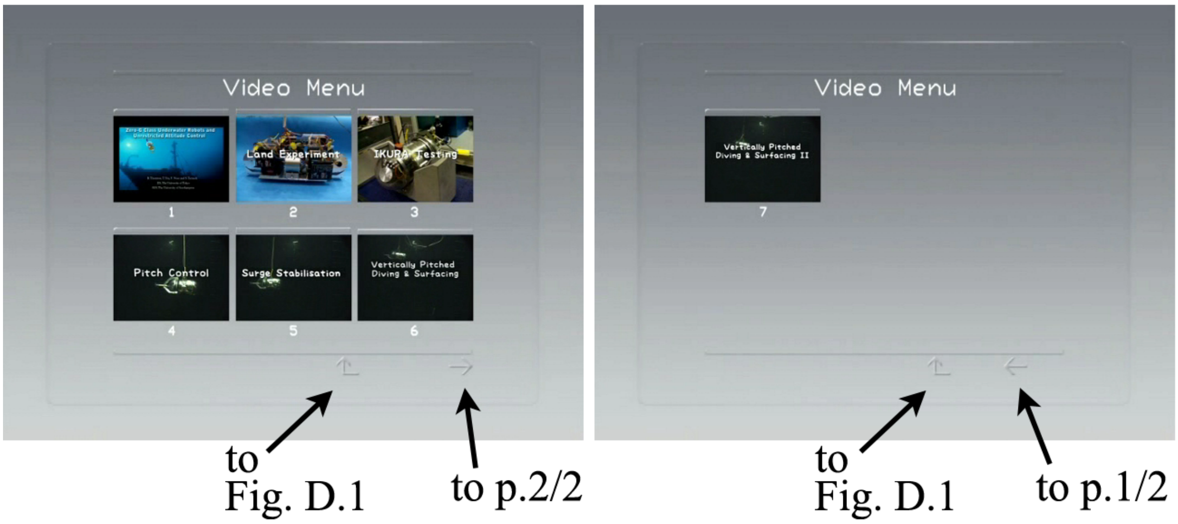

Figure D.2: DVD video menu: Left p.1/2 and right p.2/2

D.4 Picture menu

The picture menu consists of two pages as shown in Fig. D.3. Selecting 'Slideshow' on the first page will flick through a poster and five images of IKURA and its components. These can be accessed individually by selecting 'Pictures' that will jump to the second page.

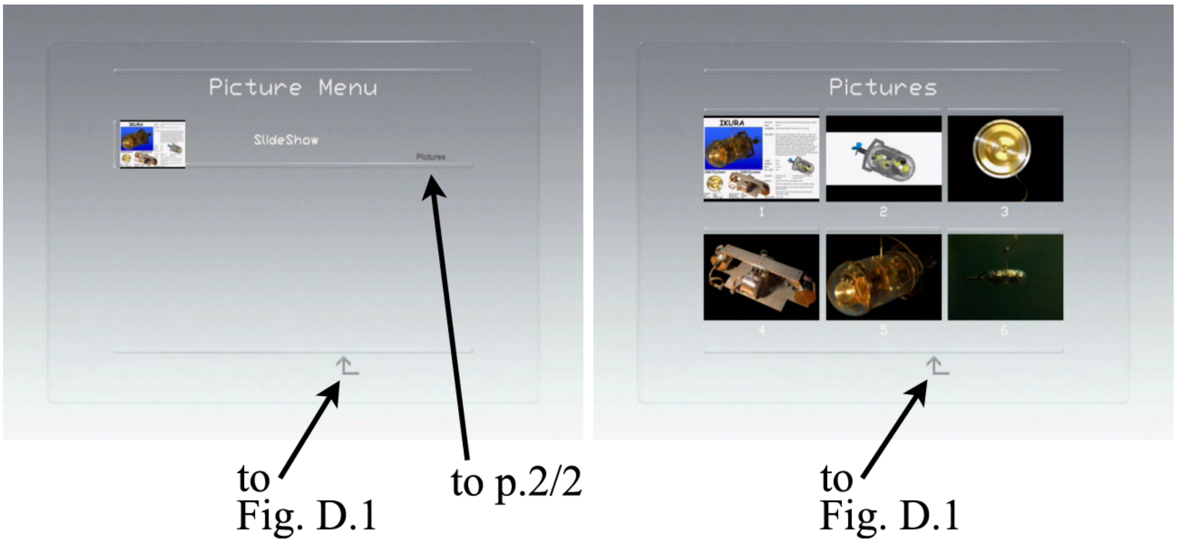

Figure D.3: DVD picture menu: Left p.1/2 and right p.2/2

Contents of DVD

This DVD is encoded in NTSC format and can be viewed on a computer monitor or television screen using any standard DVD player. The quality of the image on a computer monitor is typically superior to that of a television screen and it is possible that some televisions may crop the edges of the media.

Video menu

1. Zero-G Class Underwater Robots and Unrestricted Attitude Control: A cinematic trailer that illustrates the concept of this new class of underwater robot. This contains computer animations and experimental video footage.
2. Land Experiment: Footage of a dry-land CMG experiment with the setup described in Section 8.2.
3. IKURA Testing: Hardware check with IKURA fixed in its mount. The CMGs are set to their initial angles, the gimbal servos steer to perform what would be a yaw command and the thruster is tested.
4. Pitch Control: Footage of the vertical pitch experiment described in Section 9.1.
5. Surge Stabilisation: Footage of the horizontal surge stabilisation experiment described in Section 8.3.3. The actively stabilised and passive response of the robot to a horizontal surge manoeuvre are shown. This is repeated with the calculated position, measured attitude and CMG momentum data shown clockwise from the top right window.
6. Vertically Pitched Diving & Surfacing: Footage of the vertically pitched diving and surfacing manoeuvre described in Section 9.2. The small window shows a plan view of the experiment. The raw footage is repeated with the position, attitude and momentum data shown as described above.
7. Vertically Pitched Diving & Surfacing II: Same as above with raw footage only. In this experiment IKURA surfaces too fast and breaches the surface of the water.

Picture menu

1. Poster of IKURA
2. Simplified computer generated image of IKURA
3. Flywheel inside an open CMG unit
4. CMG pyramid
5. Zero-G Class underwater robot IKURA
6. IKURA in test pool facility of the URA Laboratory at the University of Tokyo

References

[1] N. W. Millard, S. D. McPhail, P. Stevenson, M. Pebody, J. Perrett, M. Squires and G. Griffiths, *Measurements of the sea ice Thickness Distribution and Icebergs Using the Autonomous Underwater Vehicle Autosub 2 in Antarctica*, AGU Fall Meeting Abstracts, pp.B471+, Dec. 2001.

[2] A. S. Brierley, P. G. Fernandes, M. A. Brandon, F. Armstrong, N. W. Millard, S. D. McPhail, D. Steven, P. Stevenson, M. Pebody, J. Perrett, M. Squires, D. Bone and G. Griffiths, *Antarctic Krill Under Sea Ice: Elevated Abundance in a Narrow Band Just South of Ice Edge*, Science, **295**(5561), pp.1890-1892, 2002.

[3] H. Iwakami, T. Ura, K. Asakawa, T. Fujii, Y. Nose, J. Kojima, Y. Shirasaki, T. Asai, S. Uchida, N. Higashi and T. Fukuchi, *Approaching Whales by Autonomous Underwater Vehicle*, Marine Technology Society Journal, **36**(1), pp.80-85, 2002.

[4] K. Nagahashi, T. Obara and T. Ura, *Exploration of Underwater Volcano Teisi by Autonomous Underwater Vehicle 'R-One' Robot*, Journal of Robotics and Mechatronics, **14**(2), pp.157-161, 2002.

[5] K. Okamura, K. Yanai, Y. Sohrin, J. Ishibashi, M. Watanabe and T. Ura, *In Situ Observations of Dissolved Manganese in Hydrothermal Vent Plumes at Mariana Trough*, AGU Fall Meeting Abstracts, pp.B1391+, Dec. 2004.

[6] D. M. Crimmins, E. K. Hinchey, M. C. Chintala, G. Cicchetti, C. Deacutis, and D. Blidberg, *Use of a Long Endurance Solar Powered Autonomous Underwater Vehicle (SAUV II) to Measure Dissolved Oxygen Concentrations in Greenwich Bay, Rhode Island, U.S.A.*, In Proc. IEEE Oceans'05-Europe, Brest, France, 2005.

[7] B. A. A. P. Balasuriya, M. Takai, W. C. Lam, T. Ura and Y. Kuroda, *Vision Based Autonomous Underwater Vehicle Navigation: Underwater Cable Tracking*, In Proc. Oceans'97 Vol.1, pp.1418-1424, 1997.

[8] H. Kondo T. Maki T. Ura and T. Sakamaki, *Observation of Breakwaters and their Rock Mound by AUV 'Tri-Dog 1' at Kamaishi Bay*, In Proc. IEEE Oceans'05-Europe, Brest, France, 2005.

[9] Y. Epars, Y. Nose and T. Ura, *Autonomous Underwater Sampling using a Manipulator and Stereovisual Servoing*, In Proc. IEEE Oceans'05-Europe, Brest, France, 2005.

[10] K. Kawaguchi, T. Ura, Y. Tomoda, and H. Kobayashi, *Development and sea trials of a shuttle type AUV 'ALBAC'*, In Proc. 8th International Symposium on Unmanned Untethered Submersible Technology, pp.7-13, 1993.

[11] D. C. Webb and P. J. Simonetti, *The SLOCUM AUV: An environmentally propelled underwater glider*, In Proc. 11th International Symposium on Unmanned Untethered Submersible Technology, pp.75-85, 1999.

[12] N. Kato, *Control performance in the horizontal plane of a fish robot with mechanical pectoral fins*, IEEE Journal of Oceanic Engineering, **25**(1), pp.121-129, Jan. 2000.

[13] K. A. McIsaac and J. P. Ostrowski, *Experimental Verification of Open-loop Control for an Underwater Eel-like Robot*, Int. Journal of Robotics Research, **21**(10-11), pp.849-859, 2002.

[14] T. Ura, *Development of autonomous underwater vehicles in Japan*, Advanced Robotics, **16**(1), pp.3-15, 2002.

[15] G. Griffiths, *Technology and Applications of Autonomous Underwater Vehicles*, Taylor & Francis (ISBN:0415301548), 360p., 2002.

[16] G. Roberts and R.Sutton, *Advances in Unmanned Marine Vehicles*, Institution of Engineering and Technology (ISBN:0863414508), 650p., 2005.

[17] N. E. Leonard and C. A. Woolsey, *Internal actuation for intelligent underwater vehicles*, In Proc. Tenth Yale Workshop on Adaptive and Learning Systems, New Haven, CT, pp.295-300, 1998.

[18] C. A. Woolsey and N. E. Leonard, *Underwater vehicle stabilization by internal rotors*, In Proc. American Control Conference, San Diego, CA, pp.3417-3421, 1999.

[19] C. A. Woolsey and N. E. Leonard, *Global asymptotic stabilization of an underwater vehicle using internal rotos*, In Proc. 38th IEEE Conf. Decision and Control, Pheonix, AZ, pp.2527-2532, 1999.

[20] C. Woolsey, *Energy Shaping and Dissipation: Underwater Vehicle Stabilisation using Internal Rotors*, PhD Thesis, Princeton University, 2001.

[21] C. A. Woolsey and N. E. Leonard, *Stabilizing underwater vehicle motion using internal rotors*, Automatica, **38**(12), pp.2053-2062, 2002.

[22] C. Schultz and C. A. Woolsey, *An experimental platform for validating internal actuator control strategies*, IFAC Workshop on Guidance and Control of Underwater Vehicles, Newport, Wales, pp.209-214, 2003.

[23] Bendix Corp., *Control Moment Gyroscope Gimbal Actuator Study*, AFFDL-TR-66-158, 210p., 1966.

[24] L. A. Morine and B. J. O'Conner, *The Description of the CMG and its Application to Space Vehicle Control*, Bendix Corp. Publication No. 674-7, 37p., 1967.

[25] B. J. O'Conner and L. A. Morine, *A Description of the CMG and its Application to Space Vehicle Control*, AIAA Guidance, Control and Flight Dynamics Conference, AIAA No.67-589, 1967.

[26] W. B. Chubb, D. N. Schultz and S. M. Seltzer, *Attitude Control and Precision Pointing of the Apollo Telescope Mount*, AIAA Guidance, Control and Flight Dynamics Conference, AIAA No.67-534, 1967.

[27] D. J. Liska, *A Two-degree-of-freedom Control Moment Gyro for High-Accuracy Attitude Control*, Spacecraft, pp.75-83, 1968.

[28] R. G. Kyle, *Optimal Feedback control for Nonlinear Control Moment Gyro Systems*, PhD Thesis, Virginia University, NASA-TM-X-67790, 119p., 1969.

[29] P. S. Cramer and J. T. Josephson, *CMG Assembly Life Test and Engineering Evaluation Test M-509 Experiment*, NASA-CR-115280, 35p., 1970.

[30] G. F. Ausclair and R. C. Wells, *Control Moment Gyro Selection and Design Criteria*, AIAA Guidance, Control and Flight Dynamics Conference, AIAA No.70-976, 10p., 1970.

[31] E. H. Fikes, *Control Moment Gyro for Skylab*, NASA-TM-X-64586, 22p., 1971.

[32] NASA MSFC, *A Comparison of CMG Steering Laws for High Energy Astronomy Observatories (HEAOs)*, NASA-TM-X-64727, 127p., 1972.

[33] J. W. Crenshaw, *2-Speed, a Single Gimbal CMG Attitude Control System*, TR-243-1139 (NASA-CR Northrop Services Inc.), 38p., 1972.

[34] Bendix Corp., *Study to Definite Logic Associated with CMGs to Maneuver and Stabilize an Orbiting Spacecraft - Final Report*, NASA-CR-134207, 511p., 1973.

[35] B. D. Elrod and G. M. Anderson, *Equilibrium Properties of the Skylab CMG Rotation Law - Case 620*, NASA-CR-126140 (Bellcomm TM-72-1022-2) 79p., 1972.

[36] T. Yoshikawa, *A Steering Law for Three Double Gimbal Control Moment Gyro System*, NASA-TM-X-64926, 1975.

[37] H. F. Kennel, *Steering Law for Parallel Mounted Double-Gimbaled Control Moment Gyros*, NASA-TM-X-64930, 34p., 1975.

[38] H. F. Kennel, *Steering Law for Parallel Mounted Double-Gimbaled Control Moment Gyros Revision A*, NASA-TM-X-82390, 22p., 1981.

[39] Bendix Corp., *ATM CMG/EPEA*, NASA-CR-120760, 188p., 1975.

[40] T. R. Coon and J. E. Irby, *Skylab Attitude Control System*, IBM Journal of Research Development, pp.58-66, 1976.

[41] G. Margulies and J. N. Aubrun, *Geometric Theory of Single-Gimbal Control Moment Gyro Systems*, Journal of Astronautical Sciences, **26**(2), pp.159-191, 1978.

[42] E. N. Tokar, *Efficient Design of Powered Gyrostabilizer Systems*, Cosmic Research, pp.16-23, 1978 (original: Kosmicheskie Issledovaniya Vol.16, No.1, pp.22-30, 1978).

[43] E. N. Tokar, *Problems of Gyroscopic Stabilizer Control*, Cosmic Research, pp.141-147, 1978 (original: Kosmicheskie Issledovaniya Vol.16, No.2, pp.179-187, 1978).

[44] E. N. Tokar, *Effect of Limiting Supports on Gyro Stabilizer*, Cosmic Research, pp.413-420, 1979 (original: Kosmicheskie Issledovaniya Vol.16, No.4, pp.505-513, 1978).

[45] E. N. Tokar and V. N. Platinov, *Singular Surfaces in Unsupported Gyrodyne Systems*, Cosmic Research, pp.547-555, 1979 (original: Kosmicheskie Issledovaniya Vol.16, No.5,pp.675-685, 1978).

[46] V.N. Branets, D.M. Weinberg, V.P. Verestchagin, N.N. Danilov-Nitusov, V.P. Legostaev, V.N. Platonov, Yu.P. Semyonov, V.S. Semyachkin, B.E. Chertok and N.N. Sheremetyevsky, *Development Experience of the Attitude Control System Using Single-Axis Control Moment Gyros for Long-Term Orbiting Space Stations*, 38th Congress of the International Astronoutical Federation, IAF-87-04, 8p., 1987.

[47] D. E. Cornick, *Singularity Avoidance Control Laws for Single Gimbal Control Moment Gyros*, In Proc. AIAA Guidance and Control Conference 79-1698, pp.20-33, 1979.

[48] T. Yoshikawa, *Steering Law for Roof Type Configuration Control Moment Gyro System*, Automatica Vol. 13, pp.359-368, 1979.

[49] R. D. Hefner and C. H. Mckenzie, *A technique for maximizing the torque capability of control moment gyro systems*, Astrodynamics Vol.54 (Proceedings of AAS/AIAA Astrodynamics Conference Vol.2), pp.905-920, 1983.

[50] H. Kurokawa, N. Yajima and S. Usui, *A CMG Attitude Control System for Balloon Use*, In Proc. 14th International Symposium on Space Technology and Science (ISTS), pp.1211-1216, 1984.

[51] H. Kurokawa, N. Yajima and S. Usui, *A New Steering Law of a Single gimbal CMG System of Pyramid Configuration*, In Proc. IFAC Automatic Control in Space, pp.251-257, 1985.

[52] H. Kurokawa and N. Yajima, *A Study of Single Gimbal CMG System*, In Proc. 15th International Symposium on Space Technology and Science (ISTS), pp.1219-1224, 1986.

[53] H. Kurokawa, *A Study of CMG Systems - for Selection and Evaluation*, In Proc. 16th International Symposium on Space Technology and Science (ISTS), pp.1243-1249, 1988.

[54] S. R. Bauer, *Difficulties Encountered In Steering Single Gimbal CMG's*, Space Guidance and Navigation Memo No.10E-87-09, The Charles Stark Draper Laboratory, Inc., 1987.

[55] S. R. Vadali and H. S. Oh, *Preferred Gimbal Angles for Single Gimbal Control Moment Gyros*, Journal of Guidance, Control and Dynamics, **13**(6), pp.1090-1095, 1990.

[56] J. Paradiso, *A Search Based Approach to Steering Single Gimballed CMGs*, CSDL-R-2261, 183p., 1991.

[57] J. Paradiso, *Global Steering of Single Gimballed Control Moment Gyroscopes Using a Directed Search*, AIAA Journal of Guidance, Control and Dynamics, **15**(5), pp.1236-1244, 1992.

[58] N. S. Bedrossian, *Steering Law Design for Redundant Single Gimbal Control Moment Gyro Systems*, Master's Thesis, Massachusetts Institude of Technology CSDLT-965, NASA-CR-172008, 138p., 1987.

[59] N. S. Bedrossian, J. Paradiso, E. V. Bergmann and D. Rowell, *Redundant Single Gimbal Control Moment Gyroscope Singularity Analysis*, AIAA Journal of Guidance, Control and Dynamics, **13**(6), pp.1096-1101, 1990.

[60] H. S. Oh and S. R. Vadali, *Feedback Control and Steering Laws for Spacecraft Using Single Gimbal Control Moment Gyros*, The Journal of Astronautical Sciences, **39**(2), pp.183-203, 1994.

[61] K. A. Ford and C. D. Hall, *Singular Direction Avoidance Steering for Control-Moment Gryos*, Journal of Guidance, Control and Dynamics, **23**(4), pp.648-664, 2000.

[62] H. Kurokawa, *Exact Singularity Avoidance Control of the Pyramid Type CMG System*, In Proc. AIAA Guidance and Control Conference, pp.170-180, 1994.

[63] H. Kurokawa, *Constrained Steering Law of Pyramid-Type Control Moment Gyros and Ground Tests*, AIAA Journal of Guidance, Control, and Dynamics, **20**(3), pp.445-449, 1997.

[64] H. Kurokawa, *A Geometric Study of Single Gimbal Control Moment Gyros - Singularity Problem and Steering Law*, Technical Report of Mechanical Engineering Laboratory No.175, Agency of Industrial Technology and Science, Ministry of International Trade and Industry, Japan, 108p., 1998.

[65] H. Lamb, *Hydrodynamics*, Cambridge University Press (ISBN:0486602567), 764p., 1932.

[66] L. M. Milne-Thompson, *Theoretical Hydrodynamics*, Dover Publications Inc. (ISBN:0486689700), 768p., 1968.

[67] T. I. Fossen, *Guidance and Control of Ocean Vehicles*, John Wiley and Sons (ISBN:0471941131), 494p., 1994.

[68] L. Prandtl, *Über Flüssigkeitsbewegung Bei Sehr Kleiner Reibung*, In Proc. Third Int. Math. Congress, Heidelberg, 1904.

[69] F. M. White, *Fluid Mechanics*, McGraw-Hill Book Company (ISBN:0070696675), 700p., 1979.

[70] O. Fjellstad, *Control of Unmanned Underwater Vehicles in Six Degrees of Freedom A Quaternion Feedback Approach*, DEng Thesis, University of Trondheim, 1994.

[71] J. E. Slotine and W. Li, *Applied Non-Linear Control*, Prentice-Hall Inc. (ISBN:0130408905), 352p., 1991.

[72] Y. Nakamura and H. Hanafusa, *Inverse Kinematic Solutions with Singularity Robustness for Robot Manipulator Control*, Journal of Dynamic Systems, Measurement and Control, **108**(3), pp.153-171, 1986.

[73] J. B. Roes, *An Electro-Mechanical Energy Storage System for Space Applications*, Energy Conversion for Space Power 3. Progress in Astronautics and Rocketry, edited by N. W. Snyder. New York: Academic Press, pp.613-622, 1961.

[74] R. W. Will, C. R. Keckler and K. L. Jacobs, *Description and Simulation of an Integrated Power and Attitude Control System Concept for Space-Vehicle Application*, Technical Report TN D-7459, NASA, 1974.

[75] V. S. Ila, *VLSI Architecture for Motion Estimation in Underwater Imaging*, PhD Thesis, The University of Girona, 150p., 2005.

[76] F. H. Imlay, *The Complete Expressions for Added Mass of a Rigid Body Moving in an Ideal Fluid*, Technical Report DTMB 1528, David Taylor Model Basin, Washington D.C., 1961.

[77] J. E. A. John and W. L. Haberman, *Introduction to Fluid Mechanics*, Prentice Hall Inc. (ISBN:0134839412), 587p., 1980.

[78] T. Suto, *In Japanese: Self-Generation of a Controller for a Cruising Class Underwater Robot*, PhD Thesis, The University of Tokyo, 1996.

[79] H. Olsson, K. J. Astrom, C. C. de Wit, M. Gafwert and P. Lischinsky, *Friction models and friction compensation*, European Journal of Control, **4**(3), pp.176-195, 1998.